

# Plume dispersion of low-density clayey suspension turbidity currents created by deep-sea mining

D.H.B. Enthoven

Master of Science Thesis

# Plume dispersion of low-density clayey suspension turbidity currents created by deep-sea mining

by

D.H.B. Enthoven (4165411)

June 14, 2021

**Thesis committee:**

Prof. dr. ir. C. van Rhee

Dr. ir. R.L.J. Helmons

Dr. ir. C. Chassagne

Ir. M. Elerian



# Abstract

With an increasing demand for raw materials like cobalt and nickel, there is an interest to mine polymetallic nodules from the deep-sea. These nodules are abundantly distributed along the abyssal plains, e.g., the Clarion Clipperton Zone (CCZ) in the North East Pacific. These nodules lay spread on top of a seabed consisting of very fine clayey sediment and will be collected by a seafloor mining tool (SMT). During the operation, the seabed will be disturbed, resulting in a suspended sediment plume discharged by the SMT. This plume can have a significant environmental impact through a blanketing effect on the abyssal fauna and create a disturbance in the water column affecting the entire food web structure. Hence, identifying the critical processes and quantification of sediment plume dispersion is essential to predict the potential environmental impact better and determine what technologies would enable a lower ecological impact.

Spearman et al. (2020) investigated turbidity plumes generated by deep-sea mining experiments and discovered faster settling velocity than the theory described. They hypothesize that this is due to flocculation. The settling speed depends on the density, concentration, shape, and cohesive properties of the sediment. Flocculation in the deep-sea can occur in two ways, by salinity or by organic matter. Gillard et al. (2019) showed that the flocculation response of CCZ sediment strongly depends on the concentration and applied shear rate. To analyze to what extent aggregation could influence the plume dispersion, experiments are conducted in which the effect of aggregation can be adjusted selectively. Lock exchange experiments are used to analyze the impact of aggregation by comparing results with illite based on freshwater, saltwater, pre-existing bed, and added flocculant. Additional experiments with artificial CCZ sediment are done to ensure that the illite experiments are not too idealized.

To prove that the settling velocity is increasing in saltwater, settling velocity tests have been performed. I performed experiments with illite suspensions in a settling column. An increase in settling velocity is observed due to the rise in salinity up to 75 g/L of illite. Lock exchange experiments are performed to mimic the particle-driven currents. The lock experiments involve a lock release of a fixed volume suspension of sediment from the mixing section into the outflow section.

Similar observations were made by doing lock exchange experiments. A decrease in average head velocity is shown for all experiments up to 75 g/L of illite in saltwater. To further induce flocculation and mimic organic matter in the water column, experiments with flocculant were done. Mixing the flocculant, Zetag 4120 or Zetag 8125, in the mixing section will further decrease average head velocity compared to saltwater. Zetag 4120 even ensures very fast settling as the end of the tank will not be reached.

For low concentrations in saltwater, flocculation is shown as the tail decreases more rapidly than freshwater. Flocculation with higher mass concentrations of illite is shown when flocculant is added to the mixing section. Adding Zetag 4120 to saltwater makes the current even settle quicker.

The SMT will move over a pre-existing bed, experiments were done to see if a pre-existing clay bed has consequences for the behavior of the flow. A clay bed has been made by running a lock exchange experiment with a concentration of 100g/L. This test then had, depending on the next experiment, one day or two days settling time before it was used for the new experiment. One-day bed experiments overall encountered a decrease in average head velocity. Two-day bed experiments overall experienced an increase in average head velocity.

To mimic the existing sediment in the CCZ and determine if illite experiments are not too idealized, experiments were done with artificial CCZ sediment. The currents behaved differently compared to illite, as they produced more coherent flows for low concentration. Also, it showed better effects on lowering the ecological impact when looked at mass concentrations of 100g/L of artificial CCZ sediment as gelling occurred.

To minimize the environmental impact created by deep-sea mining, the SMT should produce a discharge between the 50 and 100 g/L of artificial CCZ sediment. Gelling will occur, which has a positive effect on minimizing the minimizing the plume dispersion.

# Acknowledgements

This thesis is performed as a final part of my Master of Science in Dredging & Offshore engineering at the Delft University of Technology. This report presents my scientifically based insights into the minimization of plume dispersion created by low-density clayey suspensions created by deep-sea mining.

I was engaged in researching this thesis from June 2021 to June 2021. During this period, several people contributed academically, practically, and most of all supportive. First and foremost, I would like to thank Dr. Ir. R.L.J. Helmons for being my mentor and providing insights into the world of deep-sea mining. Additionally, I would like to thank Prof.Dr.Ir. C. van Rhee and Dr. Ir. C. (Claire) Chassagne for their guidance during my final year and playing a vital role in the decisions that needed to be made regarding my research. I would also like to thank W. Ali, PhD researcher at the TU Delft, for helping me with the experiments and knowledge regarding flocculant.

Furthermore, I would like to thank the TU Delft dredging laboratory staff Ed Stok and Andre van den Bosch for helping with the equipment and materials.

# Contents

List of Figures	v
List of Tables	ix
List of Abbreviations	x
Nomenclature	xi
1 Introduction	1
1.1 General aspects of deep-sea mining	2
1.1.1 Polymetallic nodules	2
1.1.2 Clarion Clipperton zone	2
1.1.3 Procedure of deep-sea mining	3
1.1.4 Plume	3
1.2 Problem definition	4
1.2.1 Environmental impact	4
1.2.2 Plume behaviour	4
1.2.3 Research questions	5
2 Theory	6
2.1 Seabed conditions	6
2.1.1 Conditions in the Clarion Clipperton zone	6
2.1.2 Sediment in the Clarion Clipperton zone	6
2.2 Settling velocity	7
2.2.1 Settling velocity of a single part	8
2.2.2 Shape	9
2.2.3 Hindered settlement	10
2.3 Flocculation	11
2.3.1 Flocculation process	12
2.3.2 Electro-chemical properties of cohesive minerals	12
2.3.3 Salinity	14
2.3.4 Cohesive sediment	14
2.3.5 Flocculant	15
2.4 Turbidity/gravity currents	15
2.4.1 Turbidity current	15
2.4.2 Anatomy of turbidity currents	17
2.4.3 Mean flow properties of gravity currents	19
2.4.4 Lock exchange experiments	19
2.4.5 Particle-driven gravity currents	21
3 Experimental methodology	25
3.1 Introduction	25
3.2 Sediment characterization	25
3.3 Experimental setup of the settling column	26
3.3.1 Setup settling column	26
3.3.2 Settling column experiments	27
3.3.3 Experimental measurement settling column	28
3.4 Experimental set-up for the lock exchange experiments	29
3.4.1 Setup lock exchange	29
3.4.2 Lock exchange experiments	30
3.5 Experimental procedure for calibration	33
3.5.1 Experimental measurement lock exchange	35

3.6	Experimental difficulties . . . . .	37
3.6.1	Experimental difficulties settling column . . . . .	37
3.6.2	Experimental difficulties lock exchange . . . . .	37
4	Experimental results . . . . .	39
4.1	Settling column experiments . . . . .	39
4.2	Lock exchange experiments . . . . .	43
4.2.1	Head velocities . . . . .	43
4.2.2	Mass calculation . . . . .	57
4.3	Discussion . . . . .	63
4.3.1	Settling column experiments . . . . .	63
4.3.2	Lock exchange experiments . . . . .	63
5	Conclusion and recommendations . . . . .	65
5.1	Conclusions . . . . .	65
5.2	Recommendations . . . . .	66
	References . . . . .	67
	Appendices . . . . .	73
A	Sediment properties of illite and bentonite . . . . .	74
A.1	Illite . . . . .	74
A.2	Bentonite . . . . .	76
B	Head velocities . . . . .	77
C	Froude plots . . . . .	80
D	Color maps . . . . .	83
D.1	Additional experiments with preexisting bed . . . . .	86
D.2	Additional experiments with flocculant . . . . .	87
E	Mass over time . . . . .	90
F	Mass over time compared with comparable experiments . . . . .	99
F.1	Total mass . . . . .	99
F.2	Part 1 . . . . .	102
F.3	Part 2 . . . . .	105
F.4	Part 3 . . . . .	108
F.5	Part 4 . . . . .	111
F.6	Part 5 . . . . .	114
G	Average height head . . . . .	117
H	Height profiles head . . . . .	119
I	Calibration curves . . . . .	125
J	Logbook of experiments . . . . .	128
J.1	Settling column experiments . . . . .	128
J.2	Lock exchange experiments . . . . .	129
K	Used equipment and materials . . . . .	131
L	Camera settings . . . . .	134
M	Python script settling column experiments . . . . .	135

# List of Figures

1.1	World map showing the location of the three main marine mineral deposits: polymetallic nodules; polymetallic or seafloor massive sulfides; and cobalt-rich ferromanganese crusts. (Wang, 2019) . . . . .	2
1.2	Polymetallic nodule mining operation (Wikipedia, n.d.) . . . . .	3
1.3	Different areas of interest in horizontal plume discharging (Elerian et al., n.d.). . . . .	4
2.1	Force balance on a solid body submerged in a quiescent liquid (Matousek, 2004) . . . . .	9
2.2	Drag coefficient as a function of particle Reynolds number. . . . .	9
2.3	The shape factor, $\xi$ , as a function of the dimensionless particle diameter $d^*$ and the volumetric form factor $K$ (Matousek, 2004). . . . .	10
2.4	Hindered settling (Winterwerp, 2002). . . . .	12
2.5	Electrical double layer & zeta potential. . . . .	13
2.6	(a) schematic representation of the electric double layer surrounding the particles. (b) Qualitative representation of the $\xi$ -potential as a function of the distance from the surface of the particle. (c) Potential energy corresponding to the double layer interaction for two approaching particles, where $V_R$ and $V_A$ are the potential energies associated with repulsion and attraction respectively, with $\Delta V$ the electrical barrier (Valioulis, 1983) . . . . .	13
2.7	Variation of zeta potential with electrolyte concentration for kaolinite and bentonite at constant pH. All samples: KCl-treated, 0.1 g-clay/l suspensions in KCl solutions at 25°C and pH = 5.9 + 0.2. 14	14
2.8	Visualization of a gravity current with physical quantities defined. . . . .	16
2.9	Key anatomical components of a typical sediment-laden gravity flow through an interstitial fluid. Fluid is entrained into the current via overlapping at the current front and Kelvin-Helmholtz instabilities at the back of the head (Wilson et al., 2017; Middleton, 1993) . . . . .	17
2.10	Quasi two-dimensional image of the head and body of a saline gravity current illustrating well-developed Kelvin±Helmholtz billows (side view); modified from Simpson (1969). Inset shows schematic view of lobes and clefts seen from below. upper . . . . .	18
2.11	Schematic diagram of the head and body of a gravity current, showing a typical downstream velocity profile (B. Kneller and Clare Buckee, 2000) . . . . .	19
2.12	Schematic diagram showing various characteristic density/concentration profiles (dashed lines) in density currents; the same downstream velocity profile (solid line) has been used in each case for reference. (a) A two-layer model type concentration profile, dividing the flow into a constant density lower region and an upper region of fluid detrained from the head. (b) A smooth profile, characteristic of low-concentration, weakly depositional flows. (c) A stepped concentration profile observed in erosional flows. (d) A Rouse-type distribution of sediment grain-sizes observed in turbidity currents, in which coarse material is concentrated towards the lower part of the flow whereas fine-grained material is more evenly distributed throughout the depth of the flow (B. Kneller and Clare Buckee, 2000) . . . . .	20
2.13	Schematic illustrations of the collapse of a volume of heavy fluid with $h_0/H = 1$ at four successive times after release. (a), (b) and (c) are in the adjustment phase, and (d) is at the beginning of the inviscid self-similar phase (Rottman and John Simpson, 1983). . . . .	20
2.14	The front position and bore position as functions of time after release with $h_0/H = 1$ (Keulegan, 1957; Huppert and Simpson, 1980). . . . .	21
2.15	Photographs of the different phases in a particle driven current(Bonnecaze et al., 1993). . . . .	22
2.16	Maximum head velocity. . . . .	23
2.17	Summary of flow and deposit properties. Dimensionless height is relative to the maximum thickness of the deposit. Dimensionless distance is relative to the run out distance (Baker et al., 2017) . . . . .	24
3.1	Schematic view of settling column setup. . . . .	26

3.2	Order of making the videos . . . . .	26
3.3	Order of python script steps . . . . .	28
3.4	Settling column test. Cropped, subtracted, tresh and mask pictures . . . . .	29
3.5	Schematic representation of the tank. . . . .	29
3.6	Schematic representation of the total tank setup. . . . .	30
3.7	Order of making the videos . . . . .	30
3.8	Increasing $d_{50}$ over time with different concentrations of flocculant, s stands for is saltwater. . . . .	32
3.9	Shades of grey for 10 mM, volume percentage per picture. . . . .	34
3.10	Pixel calibration curve . . . . .	35
3.11	Color map of a calibrated current of experiment 1 . . . . .	35
3.12	Order of analysing video's to find the speed . . . . .	35
3.13	Order of analysing video's to find the speed . . . . .	36
3.14	Velocity over time for 10g/L illite in fresh water . . . . .	36
3.15	Start point measurements . . . . .	38
4.1	Relationships of mud-line height for illite clay as a function of salt type and concentration . . . . .	40
4.2	Schematized settling curve with indication of start and end of consolidation phases. The inserted photos correspond with the start of the consolidation phase, the point of contraction at $t=t_c$ and the end of the consolidation phase at $t=t_\infty$ . The consolidation phase itself is divided into two phases, C-I and C-II. The x-axis is not to scale. . . . .	40
4.3	Relationships of velocity for illite clay as a function of salt type and concentration: . . . . .	41
4.4	Settling columns experiments, $t=50$ minutes. . . . .	42
4.5	Comparison settling column experiments of 10 g/L of bentonite . . . . .	43
4.6	Filtered velocity of experiment 1 . . . . .	44
4.7	Comparison of head velocities for 10 g/L illite without added $CaCl_2$ . . . . .	44
4.8	Head velocities experiment 1 up to 24 . . . . .	46
4.9	Head velocities experiments: 10, 50 and 100 g/L of illite with different salinity's . . . . .	47
4.10	Head velocities of experiments with pre-existing bed . . . . .	48
4.11	Initial transparency of illite in the tank before test is done . . . . .	49
4.12	Distance travelled of the current created with flocculant mixed in the mixing section. Experiments: 33, 34, 35,36,39 and 40 . . . . .	50
4.13	Head velocities of experiments with added flocculant . . . . .	51
4.14	Distance travelled of the current with Clarion Clipperton zone (CCZ) sediment. Experiment: 43, 44, 45, 46, 47 and 48. . . . .	52
4.15	Head velocities of artificial CCZ mixture . . . . .	53
4.16	Densimetric Froude number experiments with artificial CCZ sediment. Exp 43 up to 48. . . . .	54
4.17	Velocities of flocculant mixed in the outflow section . . . . .	57
4.18	Results for mass measurement . . . . .	57
4.19	Color maps of 10 g/L. Exp 1, 9 and 17. . . . .	58
4.20	Mass in 3 parts for 10 and 50 g/L with different salinity's . . . . .	58
4.21	Color maps of 100 g/L with pre-existing beds. Exp 27, exp 27-2, exp 30 and exp 30-2 . . . . .	59
4.22	Color maps of 10 g/L illite mixed in outflow section. Exp 1, exp 31, exp 37 and exp 41 . . . . .	59
4.23	Color maps of 100 g/L illite mixed in outflow section. Exp 7, exp 32, exp 38 and exp 42 . . . . .	60
4.24	Color maps of 10 g/L illite mixed in mixing section. Exp 33, exp 35 and exp 39 . . . . .	60
4.25	Color maps of 100 g/L illite mixed in mixing section. Exp 34, exp 36 and exp 40 . . . . .	61
4.26	Color maps of 10 g/L artificial clay. Exp 43 and exp 46 . . . . .	61
4.27	Color maps of 50 g/L artificial clay. Exp 44 and exp 47 . . . . .	61
4.28	Color maps of 100 g/L artificial clay. Exp 45 and exp 48 . . . . .	62
4.29	Color maps of 100 g/L artificial clay. Exp 45 and exp 48 . . . . .	62
A.1	Zeta potential illite . . . . .	74
A.2	Particle size distribution illite . . . . .	74
A.3	Settling velocity with increased grain size. Blue line is size illite used . . . . .	75
A.4	Settling velocity with hindered settlement. Blue line is mass concentration of 10 g/L of illite. . . . .	75
A.5	Zeta potential bentonite . . . . .	76
A.6	Particle size distribution bentonite . . . . .	76

B.1	Head velocities experiments: 1, 2, 9, 10, 17 and 18 . . . . .	77
B.2	Head velocities experiments: 3, 4, 5, 11, 12, 13, 19, 20 and 21 . . . . .	78
B.3	Head velocities experiments: 6,7,8, 14, 15, 16, 22, 23 and 24 . . . . .	79
C.1	Densimetric Froude number, experiment 1 up to 8 . . . . .	80
C.2	Densimetric Froude number, experiments 9 up to 16 . . . . .	80
C.3	Densimetric Froude number, number experiments 17 up to 24 . . . . .	81
C.4	Densimetric Froude number, experiments 25 up to 27-2 . . . . .	81
C.5	Densimetric Froude number, experiments 28 up to 30-2 . . . . .	81
C.6	Densimetric Froude number, experiments 43 up to 48 . . . . .	82
C.7	Densimetric Froude number, experiments 33, 34, 35, 36, 39 and 40 . . . . .	82
C.8	Densimetric Froude number, experiments 31, 32, 37, 38, 41 and 42 . . . . .	82
D.1	Color maps of experiments: 1, 2, 9, 10, 17 and 18 . . . . .	83
D.2	Color maps of experiments: 3, 4, 5, 11, 12, 13, 19, 20 and 21 . . . . .	84
D.3	Color maps of experiments: 6,7,8, 14, 15, 16, 22, 23 and 24 . . . . .	85
D.4	Color maps of experiments with preexisting bed . . . . .	86
D.5	Color maps 100 g/L of Illite with preexisting bed. Exp 27-1, 27-2, 30-1 and 30-2 . . . . .	87
D.6	Color maps of experiments with flocculant mixed in outflow section . . . . .	87
D.7	Color maps of experiments with flocculant mixed in mixing section . . . . .	88
D.8	Color maps of experiments with artificial CCZ sediment . . . . .	89
E.1	Mass over time experiments 1 and 2 . . . . .	90
E.2	Mass over time experiments 3, 4 and 5 . . . . .	91
E.3	Mass over time experiments 6, 7 and 8 . . . . .	92
E.4	Mass over time experiments 9, 10 and 11 . . . . .	93
E.5	Mass over time experiments 12, 13 and 14 . . . . .	94
E.6	Mass over time experiments 15, 16 and 17 . . . . .	95
E.7	Mass over time experiments 18, 19 and 20 . . . . .	96
E.8	Mass over time experiments 21, 22 and 23 . . . . .	97
E.9	Mass over time experiments 24 . . . . .	98
F.1	Total mass of experiments: 1, 2, 9, 10, 17 and 18 . . . . .	99
F.2	Total mass of experiments: 3, 4, 5, 11, 12, 13, 19, 20 and 21 . . . . .	100
F.3	Total mass of experiments: 6,7,8, 14, 15, 16, 22, 23 and 24 . . . . .	101
F.4	Mass part 1 of experiments: 1, 2, 9, 10, 17 and 18 . . . . .	102
F.5	Mass part 1 of experiments: 3, 4, 5, 11, 12, 13, 19, 20 and 21 . . . . .	103
F.6	Mass part 1 of experiments: 6,7,8, 14, 15, 16, 22, 23 and 24 . . . . .	104
F.7	Mass part 2 of experiments: 1, 2, 9, 10, 17 and 18 . . . . .	105
F.8	Mass part 2 of experiments: 3, 4, 5, 11, 12, 13, 19, 20 and 21 . . . . .	106
F.9	Mass part 2 of experiments: 6,7,8, 14, 15, 16, 22, 23 and 24 . . . . .	107
F.10	Mass part 3 of experiments: 1, 2, 9, 10, 17 and 18 . . . . .	108
F.11	Mass part 3 of experiments: 3, 4, 5, 11, 12, 13, 19, 20 and 21 . . . . .	109
F.12	Mass part 3 of experiments: 6,7,8, 14, 15, 16, 22, 23 and 24 . . . . .	110
F.13	Mass part 4 of experiments: 1, 2, 9, 10, 17 and 18 . . . . .	111
F.14	Mass part 4 of experiments: 3, 4, 5, 11, 12, 13, 19, 20 and 21 . . . . .	112
F.15	Mass part 4 of experiments: 6,7,8, 14, 15, 16, 22, 23 and 24 . . . . .	113
F.16	Mass part 5 of experiments: 1, 2, 9, 10, 17 and 18 . . . . .	114
F.17	Mass part 5 of experiments: 3, 4, 5, 11, 12, 13, 19, 20 and 21 . . . . .	115
F.18	Mass part 5 of experiments: 6,7,8, 14, 15, 16, 22, 23 and 24 . . . . .	116
H.1	Height heads experiments: 1, 2, 9, 10, 17 and 18 . . . . .	119
H.2	Height heads experiments: 3, 4, 5, 11, 12, 13, 19, 20 and 21 . . . . .	120
H.3	Height heads experiments: 6,7,8, 14, 15, 16, 22, 23 and 24 . . . . .	121
H.4	Height heads experiments: 1 up to 24 . . . . .	122
H.5	Height heads experiments with pre-existing bed: 25 up to 30 <sub>2</sub> . . . . .	123
H.6	Height heads experiments with flocculant: 31 up to 42 . . . . .	123

---

H.7	Height heads experiments with artificial mixture: 43 up to 48 . . . . .	124
I.1	Calibration curve without $CaCl_2$ . . . . .	125
I.2	Calibration curve with 10 mM $CaCl_2$ . . . . .	126
I.3	Calibration curve with 100 mM $CaCl_2$ . . . . .	127
K.1	Mixing rod settling column experiments . . . . .	131
K.2	Left: Fastec camera. Right: Mixing rod lock exchange experiments . . . . .	132
K.3	Left:Elmetron pH/ Conductivity meter. Right:Vos stirrer . . . . .	132
K.4	Left: Illite/ Right: $CaCl_2$ . . . . .	133
L.1	Camera settings . . . . .	134



# List of Tables

2.1	Conditions in the CCZ:(1)(Park, 2011);(2)(Gollner et al., 2017);(3,5)(Gillard, 2019);(4)(Federal Ministry for Economic Affairs and BGR Energy, 2018);(6)(Zawadzki et al., 2020);(7)(Gillard et al., 2019);(8) (GSR, 2018).	6
2.2	Fraction distribution of sediments.	7
2.3	Percentages of mineral groups in clay (Maciag and Harff, 2020; Bischoff et al., 1979; GSR, 2018; Zawadzki et al., 2020).	7
2.4	Typical values of thickness, planar diameter, specific surface area, and cation exchange capacity of common clay minerals. The clay minerals are sorted from small to large. Modified after (Hillel, 2003; Yong et al., 2012)	15
3.1	Properties illite & bentonite	25
3.2	Elmetron accuracy. TDS: total dissolved salts	27
3.3	Summary of experiments, [mM] stands for mol/m <sup>3</sup> .	28
3.4	Summary of experiments.	31
3.5	Summary of experiments	31
3.6	Summary of experiments with flocculant	32
3.7	Summary of experiments with mixture	33
3.8	Properties artificial CCZ sediment	33
3.9	Sediment concentration ranges and steps within	33
4.1	Summary of experiments.	40
4.2	Increased density water due to salinity	41
4.3	Viscosity's experiments with 10 g/L of illite (1, 9 and 17)	42
4.4	Standard deviations for three experiments.	45
4.6	Experimental details experiments 1 up to 24	45
4.7	Comparison time to reach end and maximum head velocity of experiments 1 to 24	47
4.8	Density different mixing section with outflow section for illite	47
4.9	Experimental details pre-existing bed. With _1 indicates 24 hours and _2 indicates 48 hours.	48
4.10	Comparison time to reach end and maximum velocity of experiments 25 to 30	49
4.11	Experimental details experiments with flocculant.	50
4.12	Comparison time to reach end and maximum velocity of mixed in mixing section	51
4.13	Comparison time to reach end and maximum velocity of mixed in outflow section	52
4.14	Experimental details CCZ sediment	52
4.15	Comparison time to reach end and maximum velocity of the CCZ sediment	53
4.16	Density different mixing section with outflow section for artificial CCZ clay	53
4.17	Time to reach end [s]	55
4.18	Time to reach end, compared with benchmark settings of 0 mM CaCl <sub>2</sub> . Green: positive effect on plume dispersion, red: negative effect on dispersion, yellow: undecided effect as it lays in the standard deviation zone.	55
4.19	Maximum head velocities illite [m/s]	56
4.20	Maximum head velocities illite, compared with benchmark settings of 0 mM CaCl <sub>2</sub> . Green: positive effect on plume dispersion, red: negative effect on dispersion, yellow: undecided effect as it lays in the standard deviation zone.	56
G.1	Average height head [m]	118
G.2	Average height head [m], compared with benchmark settings of 0 mM CaCl <sub>2</sub>	118

# List of Abbreviations

CCZ	Clarion Clipperton zone
CHG	Climate and Greenhouse Gas
GSR	Global Sea Mineral Resources
IOM	Interoceanmetal Joint Organization
ISA	International Seabed Authority
LDTCs	Low-Density Turbidity Current
NTNU	Norwegian University of Science and Technology
ppt	Parts per Thousand
SMT	Seafloor Mining Tool
SSA	Specific Surface Area

# Nomenclature

## Greek symbols

$\eta$	Displacement of the free surface [ $m$ ]
$\mu$	Dynamic viscosity of the fluid [ $Pa\cdot s$ ]
$\mu_f$	Dynamic viscosity [ $Pa * s$ ]
$\rho$	Density of liquid [ $kg/m^3$ ]
$\rho_1$	Constant density of upper fluid [ $kg/m^3$ ]
$\rho_2$	Density of the current [ $kg/m^3$ ]
$\rho_a$	Constant density of lower fluid [ $kg/m^3$ ]
$\rho_c$	Density of the ambient fluid [ $kg/m^3$ ]
$\rho_f$	Density of liquid [ $kg/m^3$ ]
$\rho_s$	Density of solid particle [ $kg/m^3$ ]
$\Delta$	Specific density [-]
$\nu$	Kinematic viscosity [ $Ns/m^2$ ]
$\xi$	Shape factor of a solid particle [ $kg/m^3$ ]

## Latin symbols

$c$	Volumetric concentration [-]
$C_D$	Drag coefficient [-]
$c_j$	Concentration of fraction j [-]
$d$	Diameter of a particle [ $m$ ]
$d$	Hydraulic mean depth [ $m$ ]
$F_B$	Buoyancy force [ $N$ ]
$F_D$	Drag force [ $N$ ]
$F_G$	Gravity force [ $N$ ]
$F_{Gp}$	Gravitational force on a spherical particle [ $N$ ]
$Fr$	Froude number [-]
$g$	Gravitational acceleration [ $m/s^2$ ]
$H$	Mean total depth [ $m$ ]
$h_0$	Height of the head current [ $m$ ]
$N$	Amount of different fractions [-]
$n$	Hindered settling exponent [-]

---

$n_i$	Hindered settling exponent of fraction i [-]
$p_1$	Total pressure in the upper layer [Pa]
$p_2$	Total pressure in the lower layer [Pa]
$Re$	Reynolds number [-]
$Re_p$	Particle Reynolds number [-]
$U$	Local flow velocity [m/s]
$u$	Flow speed [m/s]
$U_0$	Velocity of the head $h_0$ [m/s]
$v_0$	Settling velocity for a single sphere [m/s]
$v_r$	Relative velocity [m/s]
$v_s$	Slip velocity [m/s]
$v_t$	Terminal settling velocity of a non-spherical solid particle [m/s]
$v_w$	Water velocity [m/s]
$v_{0,i}$	Settling velocity of fraction i [m/s]
$v_{0,s}$	Settling velocity for a single sphere in a multi-sized mixture [m/s]
$v_{s,i}$	Slip velocity of a particle with fraction i [m/s]
$v_{s,j}$	Slip velocity of a particle with fraction j [m/s]
$v_{ts}$	Terminal settling velocity of a spherical solid particle [m/s]
$z$	Thickness of the bottom current [m]
$g'$	Reduced gravity [-]

# 1

## Introduction

Due to the growth of the world population and the increase in economic activity, the demand for minerals and metals is rising. Especially an excessive rise in demand for metals and minerals, which can be used in the transition to green energy. In 2015 the Paris Agreement on climate change had been agreed upon. This agreement indicates a global resolve to embark on development patterns that would significantly be less Climate and Greenhouse Gas (CHG) intensive. This report suggests that for the coming 30 years (till 2050), the demands for widely used metals will rise (The World Bank, 2017). The most important metals are probably: aluminum, cobalt, copper, iron, lead, lithium, nickel, manganese, rare earth metals, including cadmium, molybdenum, neodymium, indium—silver, steel, titanium, zinc, and the platinum group of metals.

Land-based resources are limited, and access to these resources can be difficult. China, responsible for more than 70% of the world's supply of these metals, prioritizes its economy before exporting these elements. Also, political problems may arise due to the work circumstances of mining. For example, cobalt mining in the Congo's copper belt, where 64% of the world's land-based cobalt is present, is problematic. Especially child labor in the Republic of Congo is controversial (Hein et al., 2020; Gonda et al., 1990).

Many metals required for the transition to green energy are abundant in the deep-sea. Polymetallic nodules, which are rich in metals, lie in the deep-sea on abyssal planes. Many of the areas where polymetallic nodules are found are located in international waters. The Clarion Clipperton Zone CCZ in the North Pacific, between Mexico and Hawaii, is the largest area with adjacent polymetallic nodules. The deep-sea is defined as the area which is covered with >200m depth of seawater. It covers an area of more than 65% of the earth's surface (Halbach and Fellerer, 1980; Thistle, 2003). In the deep-sea, the polymetallic nodules may occur on the abyssal seafloor of every ocean at a depth between 4000 and 6000 m (Gillard, 2019).

Mining of the polymetallic nodules will take place with a seafloor mining tool (smt) which will be deployed from a ship. The Seafloor Mining Tool (SMT) will be moved down to the seabed, where it will loosen the top 10 centimeters of the seabed. This will create plumes of which can be hazardous for the deep-sea environment. The plume will be carried far away from the collector vehicle by ocean currents. Polymetallic nodule mining at abyssal depths in the CCZ will have an unknown impact on one of the most remote and least known environments on earth (Vanreusel et al., 2016).

In 1994 the International Seabed Authority (ISA) was founded. The ISA is mandated to regulate and control all mineral-related activities in international waters. This authority has issued regulations on Prospecting and Exploration for polymetallic sulphides in the area. One of the regulations is: "Each prospector shall take necessary measures to prevent, reduce and control pollution and other hazards to the marine environment arising from prospecting, as far as reasonably possible, applying a precautionary approach and best environmental practices" (International Seabed Authority, 2014).

As reported, the increasing demand for minerals for the growing world population is evident. Deep-sea mining may contribute to the solution of this problem. Protection of the sea-bed environment has to be taken into account, as has been stated by the ISA. Taken into account the technical procedure of deep-sea mining and the regulations of the ISA it seems crucial to focus on minimization of the spread of the sediment plume (Miller et al., 2018).

## 1.1. General aspects of deep-sea mining

### 1.1.1. Polymetallic nodules

Polymetallic nodules were discovered in 1868 in the Kara Sea, in the Arctic Ocean off Siberia. The scientific expedition of the H.M.S Challenger in 1872-1876 found polymetallic nodules in most of the world's oceans; see figure 1.1. Polymetallic nodules are potato-like in shape. They have a diameter between 1 and 15 centimeters and lie on top or within the first 10 cm of the deep-sea sediments. The name polymetallic nodules point to the fact that the nodules consist of multiple metals. They contain especially manganese, nickel, copper, and cobalt, but they also harbor interesting amounts of molybdenum, titanium, and lithium (Sharma, 2017). The chemical and physical properties of a nodule depend on the location of the specific site (Halbach and Fellerer, 1980).

Nodules expand at a rate of a few centimeters per million years by collecting metals, either out of cold ambient seawater (hydrogenetic) or out of pore water in sediments (diagenetic). Nodules can grow solely hydrogenetic, solely diagenetic, but mostly a combination of the two. Nodules formed by diagenetic have the highest Ni, Cu, and Li concentrations. The rate of expansion also differs, hydrogenetic growth is at 1 to 5 mm/10<sup>6</sup> year and diagenetic growth is at 250 mm/10<sup>6</sup> year (Halbach and Fellerer, 1980; Hein et al., 2020).

### 1.1.2. Clarion Clipperton zone

The CCZ is the region with the largest adjacent occurrence polymetallic nodules fields, which is a tremendous economic advantage. The region is found in the North Pacific, between Mexico and Hawaii, and contains an area of six million km<sup>2</sup>, with depths between 4000 and 6000 m. The estimation is that in the CCZ an abundance of 21 billion tons of polymetallic nodules is present (Kuhn et al., 2017). The ground coverage of nodules depends on the site in the CCZ, and even in these sites, the coverage can change quickly. The amount of Mn, Co, Ni, Te, Ti, and Y estimated to be present in the CCZ is larger than the total land-based reserves and resources (Peukert et al., 2018).

The ISA handed out exploration contracts to eighteen contractors in the period from 2001 till 2019. An exploration contract contains the right to explore an area of 75,000 km<sup>2</sup>. The ISA also assigned nine regions in the CCZ where exploration is forbidden, the Areas of Particular Environmental Interest.

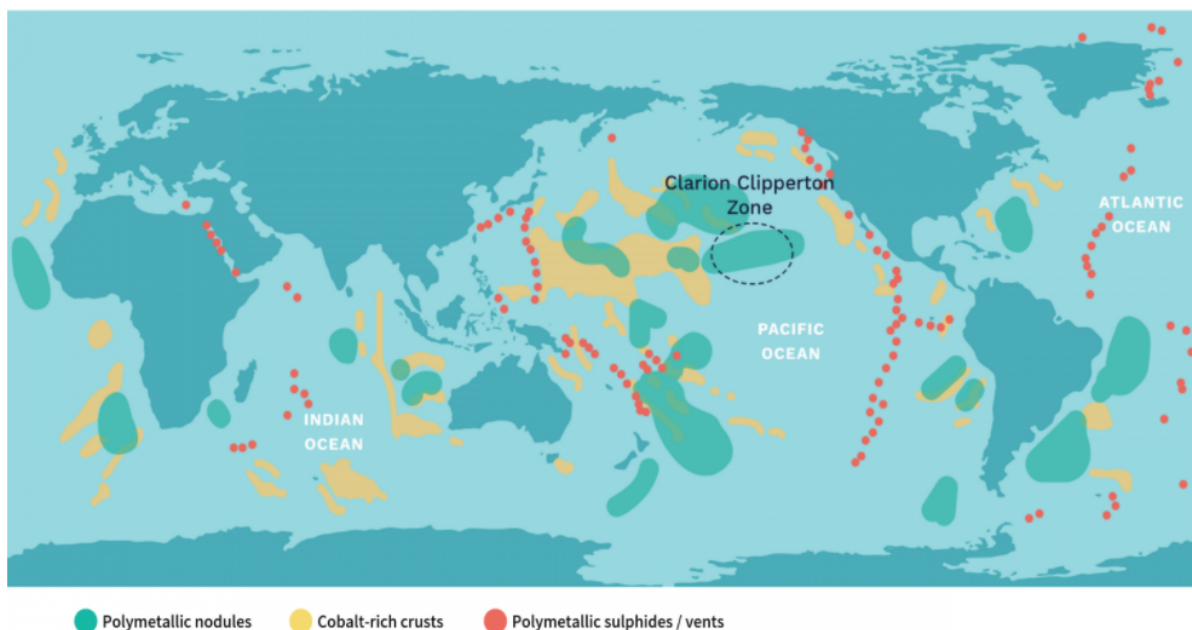


Figure 1.1: World map showing the location of the three main marine mineral deposits: polymetallic nodules; polymetallic or seafloor massive sulfides; and cobalt-rich ferromanganese crusts. (Wang, 2019)

The composition of the sediment in the CCZ depends on the location in the CCZ. Bischoff et al. (1979) investigated three sites in the CCZ and found sediment specimens, which predominantly consist of pelagic clay, sea salts, and hydrogenous materials.

### 1.1.3. Procedure of deep-sea mining

Mining in the deep-sea is a challenging task. Currently, the most effective system to mine polymetallic nodules is represented in figure 1.2. The Seafloor mining tool (smt) will move with a speed of 0.5 m/s. The nodules, laying on top or within the first 10 centimeters of the sea-bed, will presumably be harvested using a hydraulic collector (Lang et al., 2019).

In the SMT these nodules are separated from the sediment, and 90% of the sediment is successively discharged at the back of the SMT, forming the sediment plume. The remaining 10% sediment with nodules is pumped up through the vertical transport system to the mining platform, where the rest of the sediment is separated and discharged through the discharge pipe, forming a plume called the tailings discharge (Gillard, 2019). The simultaneous transport of the sediment and the nodules to the mining platform is a necessary disadvantage. Ideally, no sediment is transported, but with the present method, it is inevitable. It is expensive, and the tailing discharge harms the environment.

The sediment plume is discharged through a diffuser at the rear of the SMT. The SMT will discharge 725 tons of dry sediment an hour, equivalent to  $290 \text{ m}^3/\text{h}$ . With the sediment, it will discharge  $21317 \text{ m}^3/\text{h}$  of water. (Lang et al., 2019; Mohn et al., 2019).

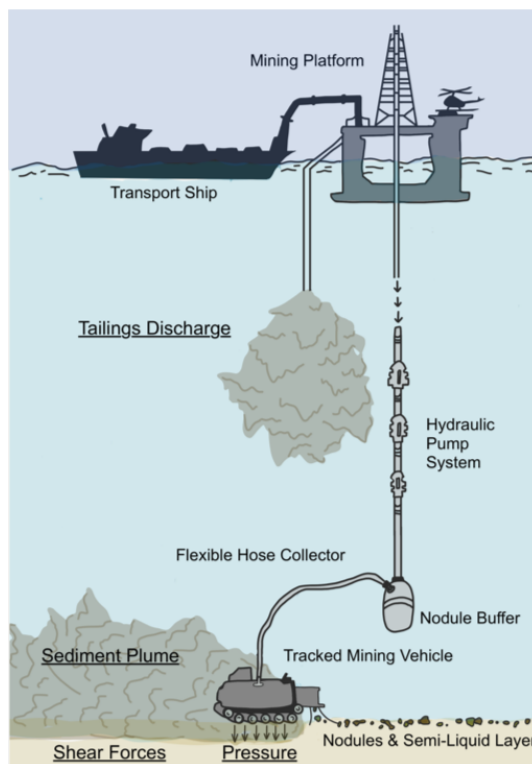


Figure 1.2: Polymetallic nodule mining operation (Wikipedia, n.d.)

### 1.1.4. Plume

Three plumes are created by using an SMT. The first one is a plume created by the disturbance due to the operations of the SMT for example, the movement and the landing of the SMT. This one is known as the least harmful for the deep-sea environment. The sediment plume and the tailing discharge are discussed above and are harmful to the local habitat. The tailings discharge and the sediment plume cause turbidity plumes, which can travel hundreds of kilometers from where the mining operation occurs. To reduce the effect of the plume on the marine environment, it seems essential to limit the spread of the plume (Elerian et al., n.d.; Kyrrousi et al., 2018).

The sediment plume will be discharged horizontally out of the SMT, and consist of four main parts of focus, see fig 1.3. The first part is the discharging region; this is the region where the sediment is released from the SMT. Here the discharge contains the initial conditions created by the SMT e.g., momentum, flow rate, and concentration of the discharge. This could be altered by redesigning the SMT for example, the collection and separation method. The second part, the jet-plume transition, transitions from a momentum-dominated plume to a buoyancy-dominated plume, which is caused by entrainment. This plume will then interact with the seabed, the impingement area. Here deposition and erosion can occur due to interaction. After this interaction, the plume will travel as a turbidity current along the seabed (Elerian et al., n.d.). The sediment volume concentration of the turbidity current is estimated as 2% (Personal communication with Dr.Ir. R.L.J. Helmons).

Sharma (2017) says that the critical factor in plume dispersion is the high proportion of clay that can remain in suspension over long periods of time, whereas nodule debris will settle faster. Even in areas with an abundance of nodules, it would be desirable to screen out sediment before lifting the nodules and, in that way minimizing environmental impact.

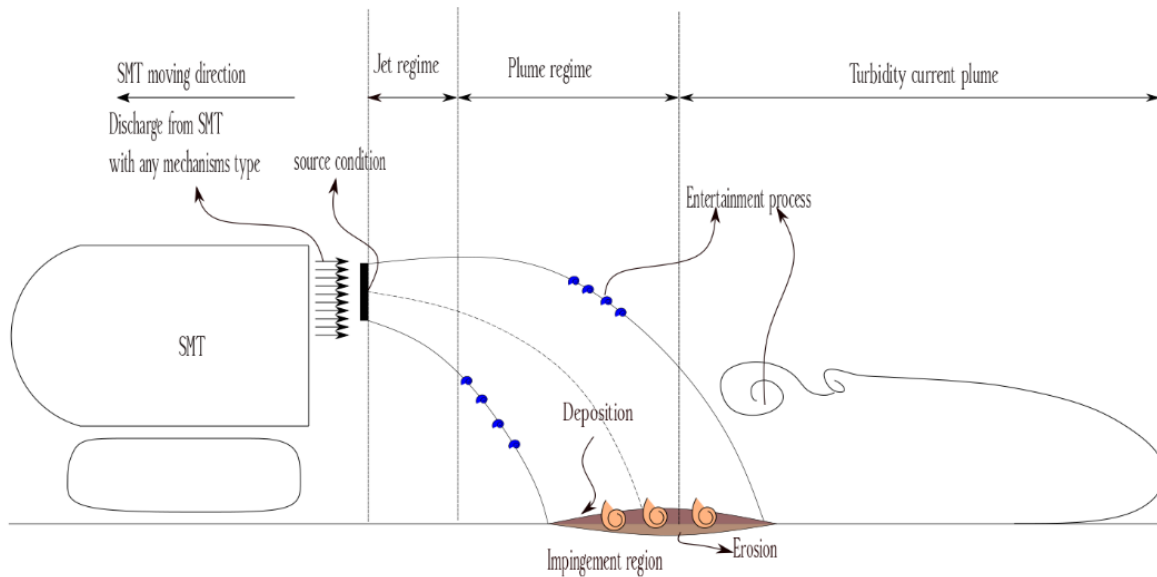


Figure 1.3: Different areas of interest in horizontal plume discharging (Elerian et al., n.d.).

## 1.2. Problem definition

### 1.2.1. Environmental impact

The SMT has considerable effects on the deep-sea environment. Especially three plumes play a role in these effects. This study will be confined to the impact of the sediment plume.

The stirring of the seabed, the discharge of the sediment out of the collector, and the forming of the sediment plume would lead to significant alterations of the seafloor and benthic habitat. All the abyssal fauna live on the seafloor or within the upper few centimeters of the seabed. The cloud of resuspended sediment created at the collector's back spread two ways, locally, called near field, and remote, called far-field. The sediment plume will have a blanketing effect on the abyssal fauna, which causes an indirect disturbance or deletion of the benthos (Roels, 1974; Oebius et al., 2001). The dissolved nodules particles can act as a source of potentially toxic metal (Koschinsky et al., 2001; Hein et al., 2020). The reduction of the widespread toxic blanketing effect can be achieved by lowering the spreading effect of plumes (Miller et al., 2018). To minimize the impact from nodule mining, Helmons (2019) writes: "The highest reduction of the environmental impact is expected through optimization of the mixture flows and reduction of the clean water intake, allowing to discharge the sediment at a higher concentration"

### 1.2.2. Plume behaviour

Gillard et al. (2019) investigated the impact of collector tests in the eastern section of the German license area of the CCZ. They performed experiments with the real sediment, with different concentrations (35, 105, 175, 500  $mg/L$ ) and different shear rates (2.4, 5.7, 10.4  $s^{-1}$ ). Concentration with 500  $mg/L$  with the shear rate of 2.4  $s^{-1}$  will lead to high settling flux, presumably due to flocculation. Optimizing the discharge condition in terms of concentration and shear rate (turbulence level) is highly needed (Elerian et al., n.d.). For further research, they suggest investigating higher discharge concentrations and also the hindered settling process. The settling velocities used by Gillard et al. (2019) were based on the sediment particle size distribution, but Spearman et al. (2020) found much lower settling velocities.

Spearman et al. (2020) tested the hypothesis that sediment plumes generated at the sea bed by deep-sea mining will be limited in spatial extent due to a combination of effects of sediment flocculation and dispersion to levels below the natural variation in the background suspended sediment signal. These studies identify the behavior of deep-sea benthic plumes on the Tropic Seamount near the Canary Islands. The authors investigated the turbidity plume with a sediment concentration of 20 and 100  $mg/L$  (dry weight). Just like Gillard et al. (2019) rapid flocculation of fine to coarse silts was presumably observed, resulting in faster settling velocities. These higher settling velocities are considered to result from the flocculation enhancing role of the extra-cellular polymers and bacteria occurring in natural seawater, the electrostatic properties of



crust particles, and the ability of fine sediment to flocculate with larger sand-sized particles.

### 1.2.3. Research questions

Numerical modeling of sediment plumes is being applied to determine the behavior. This behavior is essential to predict how it will impact the environment. The existing numerical models depend on experimental validation data produced by scaled experiments or field observations. The current models for plume dispersion don't account for the increased settling velocity by flocculation. Gillard et al. (2019) investigated the turbidity plume and discovered faster settling velocity than the existing numerical models describe and suggested it was caused by flocculation but was not proven.

The collector discharges 90% of the sediment out of the diffuser, and a turbidity current with a volume percentage of around 2% arises. It is crucial to find out the ideal concentration of sediment in the sediment plume to minimize the plume's environmental impact. The volume percentage of the turbidity current can be slightly altered by the design of the SMT and is expected to be between the 1 and 3%. The main objective of this project is to determine if there is an optimal concentration of particles that give the most negligible dispersion of the turbidity current at a similar sediment flux.

#### Research objective

- Is there a difference in plume scatter when comparing fresh and saltwater with mass concentration of ( $1\% \leq C \leq 12.5\%$ ) sediment due to flocculation?
- Is the plume influenced by the seabed?
- Is there an opportunity to increase the flocculation using additives?
- Is there an optimum mass sediment concentration ( $1\% \leq C \leq 12.5\%$ ) of CCZ sediment, in saltwater where the plume scatter is minimal?

# 2

## Theory

This chapter discusses the known literature available about the seabed conditions, the settling velocity, flocculation, and gravity currents. The goal of this chapter is to obtain more insight about gravity currents in the CCZ.

### 2.1. Seabed conditions

This paragraph discusses the seabed conditions in the CCZ. These conditions are of great importance; for example, the sediment type and size significantly affect the plume. The seabed conditions have a lot of constants but also a few variables dependent on geographic location.

#### 2.1.1. Conditions in the Clarion Clipperton zone

As the marine environment accounts for 65% of the earth's surface and 95% of the global biosphere, there is a lot to discover. The conditions in the CCZ are shown in table 2.1. The acidity in the deep-sea has a pH value of around 7.9. This means that the sea here is base. With a slow sedimentation rate and low current velocity, the environment in the CCZ is very stable (Gillard, 2019). As the slope predicts, the CCZ is called an abyssal plane; they are among the flattest, smoothest regions on earth. The oxygen level of the seabed is declining by depth till about 2-3 meters below the seabed. (Gillard, 2019).

	Value	Unit
Acidity (1)	7.9	pH
Current velocity (2)	3.8	cm/s
Depth (3)	4000 to 5000	m
Salinity (4)	35	ppt
Sedimentation rate (5)	35	mm/kyr
Slope (6)	<0.57	°
Temperature (7)	1.5	° C
Seawater density (8)	1048	$kg/m^3$

Table 2.1: Conditions in the CCZ:(1)(Park, 2011);(2)(Gollner et al., 2017);(3,5)(Gillard, 2019);(4)(Federal Ministry for Economic Affairs and BGR Energy, 2018);(6)(Zawadzki et al., 2020);(7)(Gillard et al., 2019);(8) (GSR, 2018).

#### 2.1.2. Sediment in the Clarion Clipperton zone

##### Sediment distribution in the CCZ

Sediments in the deep-sea are mechanical mixtures of several fractions. These fractions can consist: biogenic ooze, terrigenous or pelagic clay, volcano debris, hydrogenous material, and metalliferous sediment. The predominance of the fraction depends on the differences in relative rates of supply to the seafloor. This variation can be seen in the chemical composition in the sediment (Bischoff et al., 1979).

According to the data from the Global Sea Mineral Resources (GSR) (Lang et al., 2019), the Norwegian University of Science and Technology(NTNU)(Lang et al., 2019) and the Interoceanmetal Joint Organization

(IOM) (Zawadzki et al., 2020) the sediment in the CCZ typically consists of particles with a size mostly in the range of silts. The GSR and IOM both have an exploration area assigned by the ISA. The NTNU uses samples from the GSR exploration area. Table 2.2 gives an overview of the distribution of particle sizes in these areas. These percentages are measured as diameter, not a percentage of clay, silt, or sand. It is shown that more than 70% of the sediment is between 2 $\mu$ m and 63 $\mu$ m.

Name of sediment fraction	Diameter limits ( $\mu$ m) WRB classification	GSR data Average (%)	NTNU data BC062 (%)	NTNU data BC064 (%)	IOM data Average (%)
Clay	<2	12.0	11.3	14.5	23.24
Silt	2-63	76.2	85.7	82.5	70.36
Sand	63-2000	11.8	3	3	6.13

Table 2.2: Fraction distribution of sediments.

There are four main groups of clays: kaolinite, chlorite, illite and smectites or montmorillonites. As the sediment type in the CCZ is dependable on the location, the percentages of the groups in clay also depend on the location, see table 2.3. It is clear that in all the different sites, smectite and illite are the most present clay groups. Surface sediments in areas A and B are clay-bearing siliceous oozes with a clay content ranging from 25 to 70 percent. Sediments at site C is siliceous pelagic clay and contains a more significant clay fraction ranging from 70 to 100 percent (Bischoff et al., 1979). In the GSR area, more than 50% of the sediment consists of a biogenic siliceous clayey mud (GSR, 2007).

Lithologically, sediments of the CCZ are represented by two classes of biogenic sediments. Namely (i) carbonate sediments (e.g., carbonate silts, clays, and oozes), and (ii) siliceous sediments (e.g. red clays, siliceous silts, clays, and oozes). Mixtures of these two are predominant across the majority of the CCZ seabed (GSR, 2007).

	IOM 1	IOM 2	IOM3	Site A	Site B	Site C	GSR	IOM
Smectite [%]	12.71	17.33	16.49	52	38	40	36.41	16.3
Illite [%]	13.82	12.05	14.25	31	42	50	48.34	13.2
Kaolinite [%]	0.65	0.43	0.54	17	20	10	10.33	1
Chlorite [%]	1.70	1.85	2.35				4.92	1.5
Amorphous [%]	50.47	47.09	44.42					

Table 2.3: Percentages of mineral groups in clay (Maciag and Harff, 2020; Bischoff et al., 1979; GSR, 2018; Zawadzki et al., 2020).

### Organic matter

The ocean constitutes the second-largest carbon sink on earth (Le Quéré et al., 2018). The exchange of carbon dioxide between various pools within the oceans as well as between the atmosphere, earth interior, and the seafloor is called the carbon cycle. Living things in the sea move carbon from the atmosphere into surface waters then into the deeper ocean. The carbon cycle consists of organic carbon, which is carbonated into marine organisms, or inorganic carbon, as  $CO_2$ .

The bulk of the organic matter, sinking from the surface water that supplied the deep-sea with energy, is restricted as the water column in the CCZ is recognized as an oligotrophic environment, with low primary productivity and a consequently poor food network. The relatively low productivity at the surface is translated to low particulate organic carbon flux at the seafloor; the pelagic clay will so receive little organic carbon (Lutz et al., 2007; GSR, 2018). The upper few centimeters of the sediment in the CCZ have a carbon content of less than 0.5 % of the mass of the sediment. Below 30 centimeters, this declines to 0.1 % of the mass of the sediment (Volz et al., 2018). As a consequence of weak ocean ventilation, caused by the current velocity and low sedimentation rate, a pronounced oxygen minimum zone persists in the CCZ (Wishner et al., 1995). Considering that the low particulate organic carbon flux limits benthic communities at the seafloor, biodiversity in the CCZ is surprisingly high (Glover et al., 2002).

## 2.2. Settling velocity

This paragraph will explain the settling velocity and how to calculate it. The settling velocity of one particle is different from that of a multi-size mixture. This multi-size mixture can also be influenced by the shape of the particles and by hindered settlement.

### 2.2.1. Settling velocity of a single part

An accurate assessment of the settling velocity of sediment particles during deep-sea mining is fundamental for the feasibility of deep-sea mining. The settling velocity of a sphere in a fluid at rest can be estimated by solving the balance between the gravitational force minus the buoyancy force and the drag resistance, see equation 2.1 (Jiménez and Madsen, 2004; Matousek, 2004).

$$F_G - F_B = F_D \quad (2.1)$$

The submerged weight is dependent on the density of the particle. If a particle has a higher density than the fluid, it will sink; if it has a lower density, it will float.

The gravity force and the buoyancy force are determined by the volume and its density. The force on a spherical solid particle due to gravitation is determined by equation 2.2 (Matousek, 2004).

$$F_{Gp} = \rho_s g \frac{\pi d^3}{6} \quad (2.2)$$

According to Archimedes law, the weight of a submerged solid particle is reduced in the carrying medium by the buoyancy effect. The submerged weight of a spherical particle is determined by equation 2.3 (Matousek, 2004).

$$F_{wp} = (\rho_s - \rho_f) g \frac{\pi d^3}{6} \quad (2.3)$$

Here,

$F_{WP}$	: Submerged weight of a spherical particle	[N]
$\rho_s$	: Density of solid particle	[kg/m <sup>3</sup> ]
$\rho_f$	: Density of liquid	[kg/m <sup>3</sup> ]
$g$	: Gravitational acceleration	[m/s <sup>2</sup> ]
$d$	: Diameter of a particle	[m]

When the surrounding fluid moves relative to a solid particle, an additional force is exerted from the fluid onto the particle. The drag force,  $F_D$ , acts in the direction of the relative velocity between the liquid and the solid particle. The relative velocity is calculated as  $v_r = v_f - v_s$ , where  $v_f$  is the fluid speed and  $v_s$  is the particle speed. The magnitude of the drag force is expressed in terms of the drag coefficient  $C_D$  (Matousek, 2004).

$$F_D = \frac{1}{8} C_D \pi d^2 v_r |v_r| \rho_f \quad (2.4)$$

Here,

$F_D$	: Drag force	[N]
$C_D$	: Drag coefficient	[-]
$d$	: Diameter of a particle	[m]
$v_r$	: Relative velocity	[m/s]
$\rho_f$	: Density of fluid	[kg/m <sup>3</sup> ]

The drag coefficient  $C_D$  is sensitive to a regime of the liquid flow round the settling solid particle and this can be expressed by a relationship  $C_D = fn(Re_p)$ .

$$Re_p = \frac{\rho_f |v_r| d}{\mu_f} \quad (2.5)$$

A balance of the gravitational, buoyancy and drag forces on the submerged solid body determines a settling velocity of the body, see figure 2.1

For single particles or dilute suspensions, the settling velocity can be accurately predicted. The settling velocity depends on the drag coefficient. The drag coefficient depends on the particle Reynolds number; see figure 2.2. This number is used to determine if the flow is in the laminar ( $Re_p < 0.1$ ), turbulent ( $Re_p > 500$ ) or transition regime. The settling velocity of a single particle can be calculated with the equation of 2.6 (Ferguson and Church, 2004; Matousek, 2004). It shows that with increasing size, the settling velocity increases.

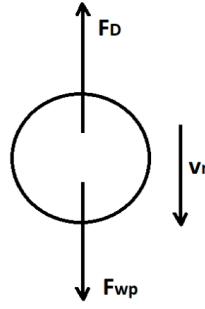


Figure 2.1: Force balance on a solid body submerged in a quiescent liquid (Matousek, 2004)

$$v_0 = \frac{\Delta g d^2}{C_1 v + \sqrt{0.75 C_2 \Delta g d^3}} \quad (2.6)$$

In this equation, the value for  $C_1=18$  and  $C_2=1$  for natural sands and  $C_2=0.44$  for spheres where the specific density is defined as:

$$\Delta = \frac{\rho_s - \rho_f}{\rho_f} \quad (2.7)$$

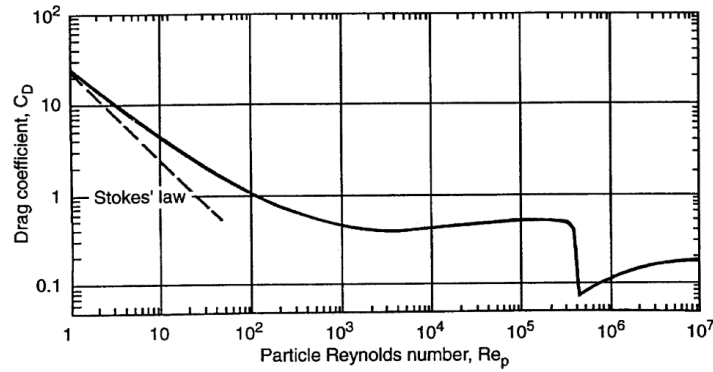


Figure 2.2: Drag coefficient as a function of particle Reynolds number.

### 2.2.2. Shape

To calculate the settling velocity of sediment particles, two different approaches are often used: an idealized one in which particles are assumed to be a sphere and the second one in which the shape is considered natural. The shape of a natural sediment particle differs from a sphere. One of the consequences of this difference is that the settling velocity will be lower than that of a sphere with the nominal diameter (Jiménez and Madsen, 2004).

The reduction of the settling velocity due to a non-spherical shape of a solid particle can be determined by the velocity ratio 2.8 (Matousek, 2004).

$$\xi = \frac{v_t}{v_{ts}} \quad (2.8)$$

Here,

- |          |  |            |
|----------|--|------------|
| $\xi$    | : Shape factor of a solid particle                             | $[kg/m^3]$ |
| $v_t$    | : Terminal settling velocity of a non-spherical solid particle | $[m/s]$    |
| $v_{ts}$ | : Terminal settling velocity of a spherical solid particle     | $[m/s]$    |

The Grace method can be used to determine the shape factor  $\xi$ . The shape factor can be determined with figure 2.3. Here the volumetric form factor  $K$  is 0.26 for sand and gravel. The dimensionless particle diameter can be calculated with equation 2.9 (Matousek, 2004). In the case of sand it reduces the terminal settling velocity to 50-60% of the initial terminal settling velocity.

$$d^* = \sqrt[3]{\frac{\rho_f(\rho_s - \rho_f)g}{\mu_f^2} d} \quad (2.9)$$

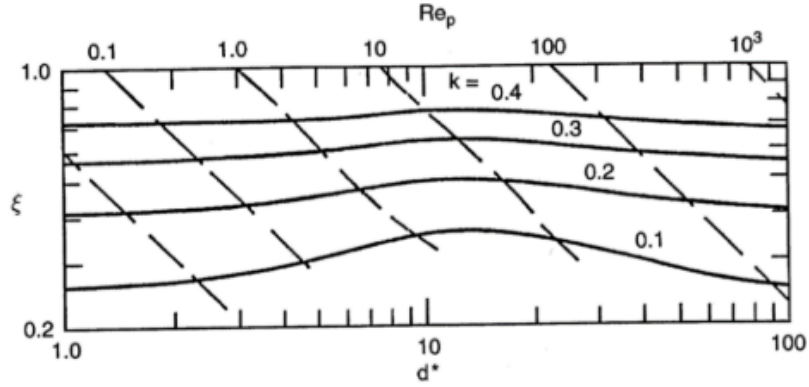


Figure 2.3: The shape factor,  $\zeta$ , as a function of the dimensionless particle diameter  $d^*$  and the volumetric form factor  $K$  (Matousek, 2004).

### 2.2.3. Hindered settlement

#### Multi-sized mixture of particles

Natural sediments consist of different particle sizes, which in turn will have mutual influence during settling. With particles descending in a fluid, it will have an inevitable slip velocity relative to the surrounding water velocity. This velocity is created by the water displacement of the descending particle. When looking at one particle, the settling velocity in a multi-sized mixture can be calculated with equation 2.10. 2.10.

$$v_{0,s} = v_w + v_s \quad (2.10)$$

In this equation the settling velocity  $v_{0,s}$  is the sum of the water velocity  $v_w$  and the slip velocity  $v_s$ . Since water is incompressible, the total volume displacement is zero, hence:

$$v_w = \frac{c}{1-c} v_{0,s} \quad (2.11)$$

Here,  $c$  is the volumetric concentration. Combined this could be written as 2.12

$$v_s = v_0(1-c)^{n-1} \quad (2.12)$$

When looking at a mixture of particles with different sizes, the slip velocity of a particle with fraction  $i$  can be calculated with equation 2.13

$$v_{s,i} = v_{0,i}(1-c)^{n_i-1} \quad (2.13)$$

Here,

$v_{s,i}$	: Slip velocity of a particle with fraction $i$	[~ / s]
$v_{0,i}$	: Settling velocity of fraction $i$	[m / s]
$c$	: Total volumetric concentration	[%]
$n_i$	: Hindered settling exponent of fraction $i$	[-]

During one-dimensional settling the total volume displaced is zero hence:

$$\sum_{j=1}^N c_j v_{s,j} + \left(1 - \sum_{j=1}^N c_j\right) v_w = 0 \quad (2.14)$$

Combining 2.10 and 2.14 gives:

$$v_{s,i} = - \sum_{j=1}^N c_j v_{s,j} + v_{s,i} \quad (2.15)$$

Here,

$N$	: Amount of different fractions	[-]
$c_j$	: Concentration of fraction j	[%]
$v_{s,j}$	: Slip velocity of a particle with fraction j	[m/s]
$v_{s,i}$	: Slip velocity of a particle with fraction i	[m/s]

### Interference during settling

A single sediment particle settling in still water has a specific settling velocity, which is a function of its shape, size, density, and fluid viscosity. When the concentration of particles is increased, the particles start to interfere and hinder each other. Thereby reducing the particle settling speed. Increasing the concentration further will result in particles that are in constant contact with each other (Dankers and Winterwerp, 2007; Richardson and Zaki, 1997). The effective settling velocity can be calculated with equation 2.16.

$$v_{0,s} = v_0(1 - c)^n \quad (2.16)$$

Here,

$v_{0,s}$	: Effective settling velocity	[m/s]
$v_0$	: Settling velocity of a single particle	[m/s]
$c$	: Volume concentration	[%]
$n$	: Hindered settling exponent	[-]

The hindered settling exponent is a function of the particles Reynolds number and varies between 2.4 for coarse particles and 4.65 for fine particles. The hindered settling component can be computed by equation 2.17 (Rowe, 1987).

$$n = \frac{4.7 + 0.41Re_p^{0.75}}{1 + 0.175Re_p^{0.75}} \quad (2.17)$$

Hindered settling already takes place at sediment concentrations  $\geq 2-3 \text{ kg/m}^3$  and the gelling effect of cohesive sediment could take place at sediment concentration  $\geq 40 \text{ kg/m}^3$ , depending on the sediment composition, see fig 2.4 (Winterwerp, 2002; Camenen and Bang, 2011). As the volume concentrations during deep-sea mining are around 2%. The concentrations are deemed sufficiently small that the particles should fall initially without being influenced by surrounding particles. As the settling continues near the bottom, the particle concentration there would increase, and the settling of each particle would be subjected to hindered settlement (Sutherland et al., 2014).

Hindered settlement occurs when particles interfere with each other; this interference can also induce a faster settling velocity speed through flocculation. Flocculation is the result of a mutual collision of, and subsequent adherence between, particles of cohesive sediment (Winterwerp and Kesteren, 2004).

## 2.3. Flocculation

Flocculation is the formation and breakup of flocs of cohesive sediment. It results from a mutual collision of and subsequent adherence between particles of cohesive sediment. Break-up is caused by turbulent stresses and mutual collisions (Winterwerp and Kesteren, 2004; Winterwerp, 2002). Cohesive sediment implies a mixture of silt and clay with a diameter less than  $50 \mu\text{m}$  and as small as a fraction of  $1 \mu\text{m}$  with various degrees of organic matter (Partheniades, 2009b). The sediment properties and the environmental conditions affect the settling velocity through the process of flocculation. The rate at which particles bond and the size they become depends on hydrodynamic conditions, residence time, sediment properties, pH, and salinity (Francesca Mietta et al., 2009).

Cohesive sediment consists predominantly of clayey particulate matter subjected to aggregation, breakup, deposition, and erosion processes. Through random motion, different settling velocities, or turbulent mixing of the fluid, the suspended aggregates contact each other, inducing further aggregation and inducing the growth of aggregates. Breaking can occur simultaneously; it happens when the fluid stresses disrupt those aggregates that cannot withstand the shear stresses. The mechanism of most importance for particle aggregation is the collision amongst particles. The distribution of the floc size is fundamental to characterize a cohesive suspension because it is correlated to the residence time of the sediment in the water column, as the settling velocity scales with a power of the floc size (Maggi, 2005).

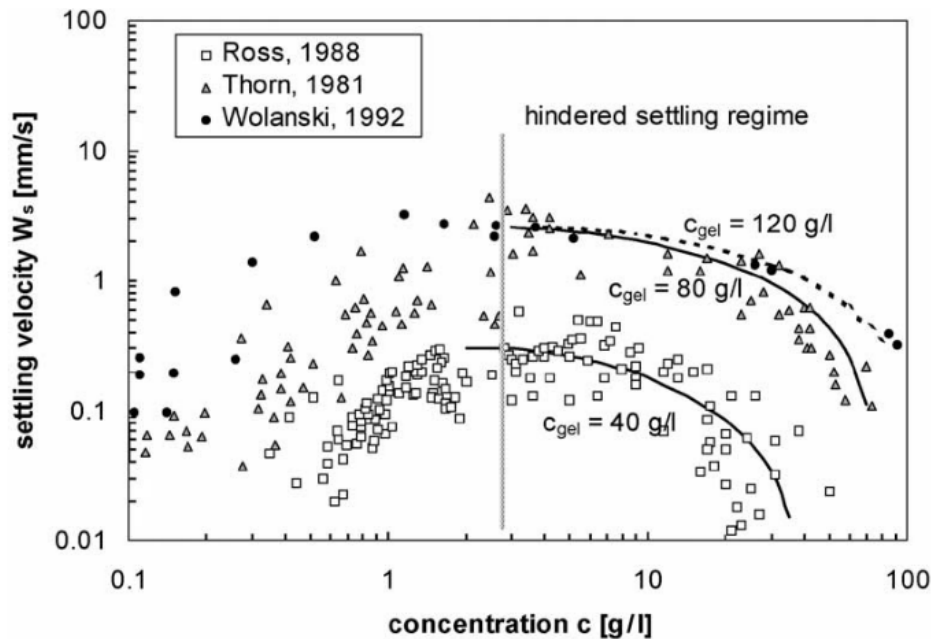


Figure 2.4: Hindered settling (Winterwerp, 2002).

Flocculation and, in particular, the settling velocity is affected by several factors. Manning and Dyer (2002) found that particulate systems consisting of a collection of massive, cohesive particles interacting with each other show intriguing behavior. Large flocs generally have a higher settling velocity than small flocs. However, it is observed that flocs with similar sizes differ in settling velocity due to the differences in relative density. This implies that the settling velocity also depends on the geometrical structure of the flocs. Not only the geometry depends on the flocculation, but also the mineralogy and the electrochemical properties, which in turn can be altered by the salinity (Winterwerp and Kesteren, 2004). Flocs can be formed by the addition of flocculating agents, which are classified as (i) inorganic salts and (ii) organic/carbon-based polymers, defined as flocculants.

### 2.3.1. Flocculation process

The formation of aggregates is governed by three processes: (i) Brownian motions, random motion of particles suspended in a medium, cause the particles to collide, resulting in the formation of aggregates. (ii) Particles with a more significant settling velocity will overtake those with a smaller settling velocity. Aggregates can form by collisions of these particles. (iii) Turbulent motions will cause collisions of particles, causing aggregations or breakup of aggregations due to turbulent shear (Winterwerp and Kesteren, 2004).

Clays have a plate-like structure. This structure is divided into the face surface and the edge surface. The interior of the crystallite has a net negative charge due to isomorphous lattice substitutions. In the presence of water, the negative charge from the interior is compensated by positive counter ions, which are absorbed on the face surface. At the edges of the plate, a bond surface is exposed due to a disrupted lattice. Here an electrical double layer of the constant potential type is created. The double-layer on the edge is considered negative, see figure 2.5 (Olphen, 1964; Partheniades, 2009a). This layer neutralizes the negative charge of the minerals so that the particles have the opportunity to form bonds when the particles move close enough for the Van der Waals force to be working (Dankers, 2006).

The aggregation process of the plate-like particles can take place in three ways: face to face, edge to face, and edge to edge. Face to face leads to the formation of thicker plates. Edge to face and edge to edge result in voluminous flocs or gels or voluminous card house matrix. Edge to face and edge to edge will be accompanied by the appearance of real flocs and should be described as flocculation (Olphen, 1964).

### 2.3.2. Electro-chemical properties of cohesive minerals

The electrical charge on the particles determines the rate of aggregation and the strength of flocs. This charge is called the electric potential and is defined as  $\xi$ . The clay has a negative surface charge, shown in figure 2.5



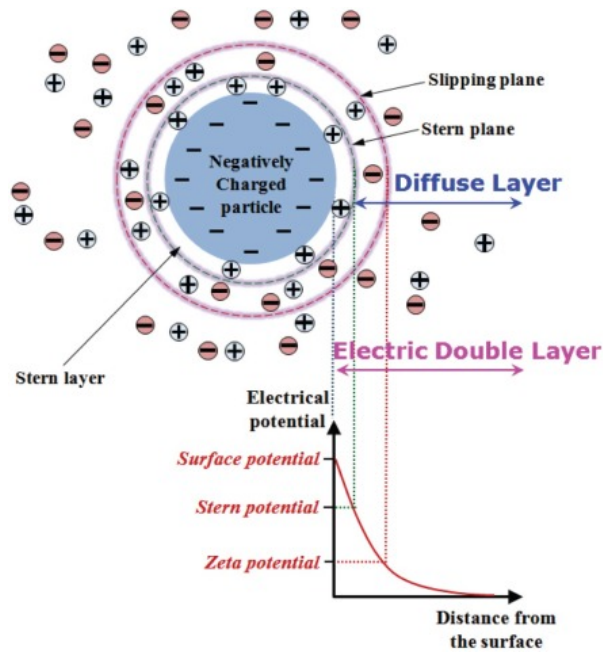


Figure 2.5: Electrical double layer & zeta potential.

and 2.6a(Kruyt 1983). This negative surface may surround itself with a cloud of cations, which are positively charged ions whose concentration is very high in the stern layer. The adjacent layer to the surface, the Gouy or diffuse layer, where the positive and negative charges meet, is called the double layer. The double-layer is characterized by the  $\xi$ -potential  $\xi_0$  at the water particle interface, which decreases proportionally to the ion concentration, see figure 2.6b. Van Leussen (1994) says that "The thickness of the double layer can vary largely for different minerals and ion concentration in the medium, and also according to the balance between attractive electrical forces and diffusion within the medium". The aggregation of two particles depends strongly on the interaction of their double layers. First, the repulsive electrical force tends to separate the particles, if this is overcome at a certain distance, then the collision of the particles may occur, and aggregation could be possible, see figure 2.6c (Maggi, 2005).

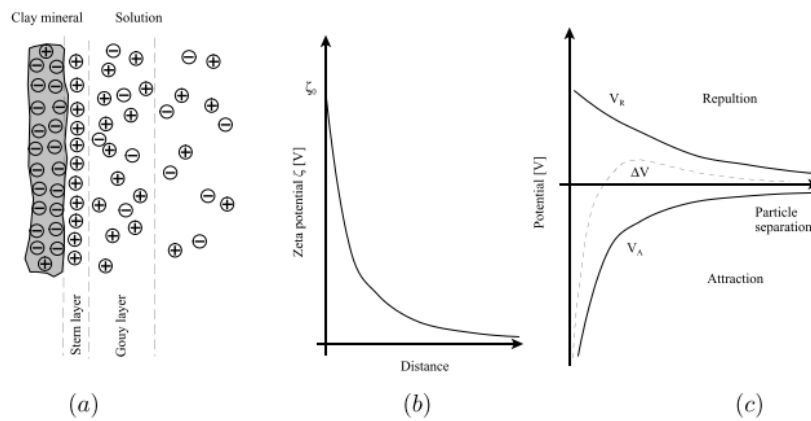


Figure 2.6: (a) schematic representation of the electric double layer surrounding the particles. (b) Qualitative representation of the  $\xi$ -potential as a function of the distance from the surface of the particle. (c) Potential energy corresponding to the double layer interaction for two approaching particles, where  $V_R$  and  $V_A$  are the potential energies associated with repulsion and attraction respectively, with  $\Delta V$  the electrical barrier (Valioulis, 1983)

The relationship between the surface charge of particles and their  $\xi$  potential is complex (Chassagne et al., 2009). Uniformly charged particles with a low  $\xi$  potential are considered to form aggregates more likely than particles with a high  $\xi$  potential (Francesca Mietta et al., 2009). Particles with a high zeta-potential (in

absolute value) will have less tendency to aggregate than those with low zeta-potential (Mietta et al., 2009).

### 2.3.3. Salinity

As individual clay particles are plate-shaped with a negative charge, see section 2.3.1, this arrangement is such that plates repel each other when dispersed in freshwater. However, if the water is saline, sodium and chlorine ions act to neutralize the repulsive forces so that the plates may flocculate (Sutherland et al., 2014).

An increase in salt concentration would lead to an increase of flocculation, and so to an increase in the floc size and settling velocity (Sutherland et al., 2014). Floccs created in fresh water are smaller than floccs in seawater (Burban et al., 1989). An average salinity of 2 parts per thousand (ppt) can already increase mineral cohesion and allow aggregation (Drake, 1967). Leussen (1994) and McAnally (1999) suggested different salinities for different minerals. For kaolinite they suggested 0.6 ppt and for illite 1.1 ppt and 2.4 ppt for montmorillonite. However Vane and Zang (1997) clearly shows that the  $\xi$  potential of kaolinite can be related to the salt concentration, see figure 2.7. The electrolytic levels can be affected by the salinity Krone (1963) which can in turn alter the  $\xi$  potential (Chassagne et al., 2009). Krone (1963), Migniot (1968) and Francesca Mietta et al. (2009) observed that aggregation with a salinity larger than 15 ppt varies very little.

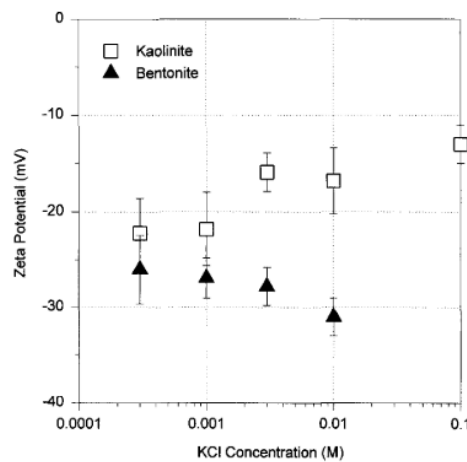


Figure 2.7: Variation of zeta potential with electrolyte concentration for kaolinite and bentonite at constant pH. All samples: KCl-treated, 0.1 g-clay/l suspensions in KCl solutions at 25°C and pH = 5.9 ± 0.2.

The history of the floccs influences the effect of salinity. Leussen (1994) performed experiments of natural sediments at different salinities; the experiments concluded that mud flocculation had not been related to the electrokinetic properties ( $\xi$  potential) of the sediment in a systematic way. The in situ salinity variations depend strongly on the shear rate, sediment concentration, and organic matter content. Therefore it isn't easy to establish the effect of each physical quantity independently. Moreover, the history of the floccs has a strong influence on the impact of salinity on aggregations (Francesca Mietta et al., 2009).

### 2.3.4. Cohesive sediment

As pointed out in section 2.3, cohesive sediment or mud implies a mixture of silt and clay with particle diameter less than 50  $\mu\text{m}$  and as small as a fraction of 1  $\mu\text{m}$  with various degrees of organic matter, water, and sometimes gas (Partheniades, 2009b). Clays are the most minor solid constituents of mud, and together with organic bounds, they are responsible for the cohesion properties. Sand and silt particles have, in contrast to clay, no effect on cohesion (Maggi, 2005).

Various clay minerals have different shapes, sizes, layer charges, exchangeability of cation, edge charge densities, and structures of the particle edges, which in turn control the rheological and cohesive properties of the clay flow (Lagaly, 1989). Some of these properties are also influenced by the pH and the available ions in the medium (Luckham and Rossi, 1999). As the deep-sea has a constant pH value, this variable is disregarded.

There are four main groups of clays: kaolinite, chlorite, illite and smectites or montmorillonites. Kaolinite is weakly cohesive, and montmorillonite is strongly cohesive because of differences in chemical and physical properties, see table 2.4. As shown in section 2.1.2 clays in the CCZ mainly consist of smectite (montmorillonite) and illite. Smectite particles are relatively small and have a large Specific Surface Area (SSA), which is the ratio of the surface area of a material to either its volume or its mass (Baker et al., 2017). The SSA of

the particle controls the magnitude of the interparticle forces, with a larger SSA allowing greater interparticle forces (Atkinson, 2007). The SSA from smectite is further increased by the ability of smectite to absorb water into its chemical structure (Yong et al., 2012).

The cation exchange capacity (CEC) is a measure of the potential chemical activity of a clay mineral, which in turn is directly related to the cohesive forces. The higher the CEC, the more plastic the clay will behave, and also higher cohesive and adhesive shear strengths may be expected (Baker et al., 2017; Kooistra et al., 1998).

Edge view	Typical Thickness (nm)	Planar Diameter (nm)	Specific Surface Area (SSA) (m <sup>2</sup> /kg)	Cation Exchange Capacity (CEC) (mEq/100g)
Montmorillonite	2	10-1,000	700-800	80-100
Illite	20	100-2,000	80-120	10-40
Chlorite	30	100-2,000	70-90	10-40
Kaolinite	100	10-1,000	10-15	3-15

Table 2.4: Typical values of thickness, planar diameter, specific surface area, and cation exchange capacity of common clay minerals. The clay minerals are sorted from small to large. Modified after (Hillel, 2003; Yong et al., 2012)

### 2.3.5. Flocculant

Flocs can be formed by the addition of flocculation agents, inorganic salt or/and organic/carbon-based polymers, called flocculants. Anionic flocculants are quite common in nature and synthetic organic flocculants are widely used in industry for solid-liquid separation (Shakeel et al., 2020; Tan et al., 2012). Aggregations are mainly formed by a combination of two groups of processes: (i) those bringing particles together, and (ii) those keeping them together. The first one was explained in 2.3.1, the second one is related to the formation of sticky organic matter by a variety of organisms. As microflocs consist of mineral particles and organic matter, their formation is strongly related to the origin of the organic matter (Eisma, 1986).

Organic matter consists mainly of polymers (Winterwerp and Kesteren, 2004). These polymers are a major factor responsible for mud flocculation since it can adhere particles modifying their surface charge. These polymers exhibit different polarities, such as cationic, anionic, and neutral, and hence are chemically active or reactive in solution or suspension (Tan et al., 2012). The choice of the best flocculant is related to multiple factors, one of these factors is the mineral composition of the particle. The desired efficiency of the flocculant and type of flocculation depends on the flocculant structure, molecular weight, charge and dose.

The difference between cationic and anionic is that cationic has a positive charge and anionic has a negative charge. As cationic is positively charged, electrostatic attraction is the main driving mechanism between cationic polymers and negatively charged clay. The use of cationic polymers ensures for larger aggregates than those created by the aggregation by salt. Anionic polymers which are negatively charged need a cationic agent to ensure flocculation. This cationic agent can be provided by the use of salt (Shakeel et al., 2020).

## 2.4. Turbidity/gravity currents

As told in paragraph 1.1.4, the plume will travel as a turbidity current. This paragraph will first explain what a turbidity current is, what it looks like, and what velocity and concentration profiles look like. Further, it will give insight into saline lock exchange and particle-driven gravity currents.

### 2.4.1. Turbidity current

Turbidity currents are the best-understood mode of sediment gravity flows (Parsons et al., 2009). The buoyancy or gravitational force driving the motion may be due to differences in composition or temperature between the gravity current and the ambient fluid. The two fluids may even be physically different liquids. A density difference can also arise from the suspension of particles in the fluid forming the current. The bulk density of such a suspension may be greater than its surroundings, resulting in a gravity current (Bonnetze et al., 1993).

Sediment gravity flows, or gravity currents are primarily horizontal currents, which consist of one fluid within another when this flow takes place because of relatively small differences in density between the fluids (Middleton, 1993). They occur as either top or bottom boundary currents or as intrusions at some intermediate level (D'Alessio et al., 1996). These turbidity currents are gravity currents in which the excess density or

unit weight providing the driving buoyancy forces is due to the presence of sediment being held in suspension by fluid turbulence (Moodie et al., 1998).

B. Kneller and Clare Buckee (2000) say that a turbidity current is a suspension current in which the interstitial fluid is a liquid (generally water). These currents are dilute mass concentrations, with a mass concentration of less than  $10 \text{ kg/m}^3$ , fully turbulent flows of poorly sorted sediment ( $Re > 10^4$ ). The Reynolds number  $Re$  can be calculated by equation 2.18.

$$Re = \frac{\rho u_0 L}{\mu} \quad (2.18)$$

These currents can flow with speeds larger than 0.3 m/s for minutes or as long as a couple of days (Parsons et al., 2009). Although turbidity currents transport material everywhere they travel, the material deposit will only take place in areas of reduced bed shear (B. Kneller, 1995).

Lock-exchange experiments or fixed volume gravity currents are caused by the release of dense material in a fixed volume. These experiments approach continuous flows asymptotically. Continuous turbidity currents are currents where the supply of sediment is continuous, like in deep-sea mining operations (Parsons et al., 2009).

### Composition driven flows

A visualization of a gravity current is shown in figure 2.8. In figure 2.8  $\eta(x, y, t)$  represents the displacement of the free surface from its undisturbed configuration,  $u=(u; v; w)$  is the fluid velocity in Cartesian coordinates with position vector  $x=(x; y; z)$ ,  $H$  is the mean total depth,  $h(x; y; t)$  is the thickness of the near bed current, and  $\rho_1, \rho_2$  ( $\rho_1 < \rho_2$ ) represent the constant densities of the upper and lower fluids, respectively (Moodie, 2002; D'Alessio et al., 1996).

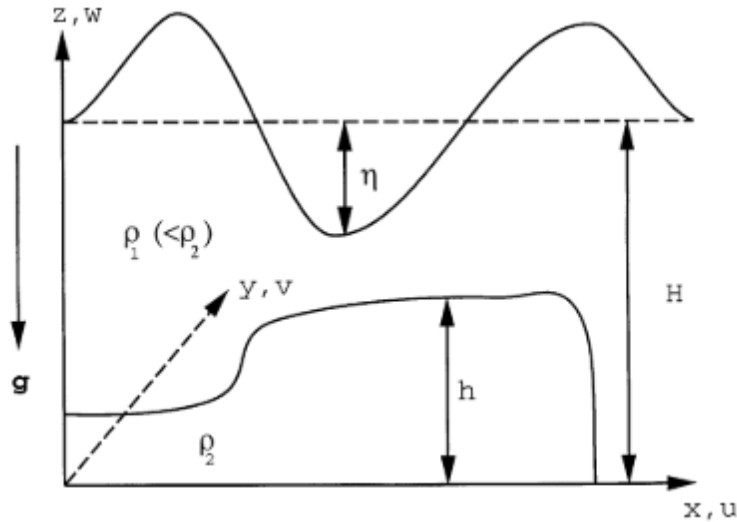


Figure 2.8: Visualization of a gravity current with physical quantities defined.

The flow following the release is a gravity current of finite volume that will have spread sufficiently that its length is much larger than its height. The height varies over the horizontal position and in time. When the maximum surviving height of the lower-layer of the two layer flow is small compared with its length, vertical accelerations in the motion will also be small compared with horizontal accelerations. This observation led to the assumption that the pressure at any point is the same as the static pressure due to its depth below the free surface. This assumption together with the assumption that the flow is inviscid, incompressible, irrotational and horizontal gives the formula for the total pressure field in equations 2.19 and 2.20 (Moodie, 2002).

$$p_1 = \rho_1 g [(H + \eta) - z] \quad (2.19)$$

Here  $p_1$  is the total pressure in the upper layer, see figure 2.9.

$$p_2 = -\rho_2 g z + \rho_2 g' h + \rho_1 g (H + \eta) \quad (2.20)$$

Here  $p_2$  is the total pressure in the lower layer and  $g'$  is the reduced gravity. The reduced gravity can be calculated with equation 2.21. From equations 2.19 and 2.20 it follows that the horizontal pressure gradients driving the flow are independent of depth and hence also are the horizontal velocities (D'Alessio et al., 1996; Moodie, 2002).

$$g' = g(\rho_c - \rho_f) / \rho_f \quad (2.21)$$

$$\rho_c = \varphi_0 * \rho_s + (1 - \varphi) \rho_f \quad (2.22)$$

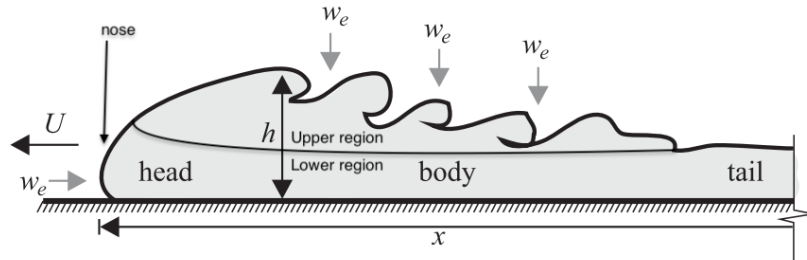


Figure 2.9: Key anatomical components of a typical sediment-laden gravity flow through an interstitial fluid. Fluid is entrained into the current via overlapping at the current front and Kelvin-Helmholtz instabilities at the back of the head (Wilson et al., 2017; Middleton, 1993)

### 2.4.2. Anatomy of turbidity currents

The anatomy of the gravity current is equal to that of a turbidity current. A turbidity current is divided into three parts: the head, the body, and the tail; see fig 2.9. A "universal profile" of a gravity current head does not exist. Even for flows into calm surroundings, the value of the excess head height above the following flow varies with the fraction of the total depth occupied by the current. The form of the head is strongly modified by opposing and following ambient flows and other physical effects (Simpson, 1982).

#### Head

The head of the density surge is considered a complex part of the current with a distinct shape and hydraulics, which differ from the region behind the head. This zone plays a vital role in the dynamics of the current as this is a zone of breaking waves and intense mixing and so sets a boundary condition for the current as a whole (Simpson and Britter, 1980a). For the head to advance, it must displace the ambient fluid, which is generally at rest (Buhler et al., 2016). Accelerating the ambient fluid produces resistance to the flow, which is larger than friction at the bed or the upper interface. Therefore the head of the current must be thicker than the current behind the head, where only frictional resistance is important (Middleton, 1993). A current flowing along a horizontal surface usually has a "nose," or foremost point raised a short distance above the ground (Simpson, 1982). The nose is a result of the no-slip condition at the lower boundary and frictional resistance at the upper boundary (Simpson and Britter, 1980b). This is one way that ambient fluid is mixed into the flow (Middleton, 1993)

At the rear of the head, a series of transverse vortices, see fig 2.10 are present, Kelvin-Helmholtz instabilities (Simpson and Britter, 1980b). Kelvin-Helmholtz instabilities are the result of a vortex-intensification process associated with shear. The Kelvin-Helmholtz instability is a flow instability in which variation of either velocity or density occurs over a finite thickness. Gerard Middleton (1966) performed experiments on the heads of turbidity currents in a laboratory and found that for low slopes (angles  $< 2^\circ$ - $3^\circ$ ), the head velocity is adequately described by equation 2.23 in with the head velocity is independent of the slope (Keulegan, 1957)

$$U_0 = Fr \sqrt{g' h_0} \quad (2.23)$$

Here,

$U_0$	: Velocity of the head $h_0$	[m/s]
$Fr$	: Froude number	[-]
$h_0$	: Height of the head current	[m]
$g'$	: Reduced gravity	[-]

Its Froude number can characterize the state of flow in an open-surface conduit. The Froude number can be calculated with equation 2.24. Benjamin (1968) found that the value of the Froude number depends on the ratio of the height of the head of the current to the depth of the ambient fluid and has a theoretical value of  $\sqrt{2}$  for a current intruding into very deep surroundings.

$$Fr = \frac{U}{\sqrt{gd}} \quad (2.24)$$

Here,

$U$  : Local flow velocity [m/s]  
 $d$  : Hydraulic mean depth [M]

The Froude number has a value of 1.0 when a flow passes through critical conditions. For sub-critical flow, the depth is greater, and the velocity is lower; therefore, the Froude number is always less than 1.0. For supercritical flow, the opposite is true, and the Froude number will always be greater than 1.0 (Brandt et al., 2015) As the flow starts to slow down, the vertical settling velocity of the grains becomes more significant than the horizontal velocity. This contraction of the flow brings the particles into closer proximity, resulting in greater frictional forces, which further reduce the forward momentum of the particles. Which in turn leads to a rapid decline in head velocity (Baker et al., 2017). The closer the Froude number is to 1.0, the more unstable the water surface becomes since minor disturbances can cause the flow to flip locally between two possible energy states. This can lead to waves and surface disturbances (Brandt et al., 2015)

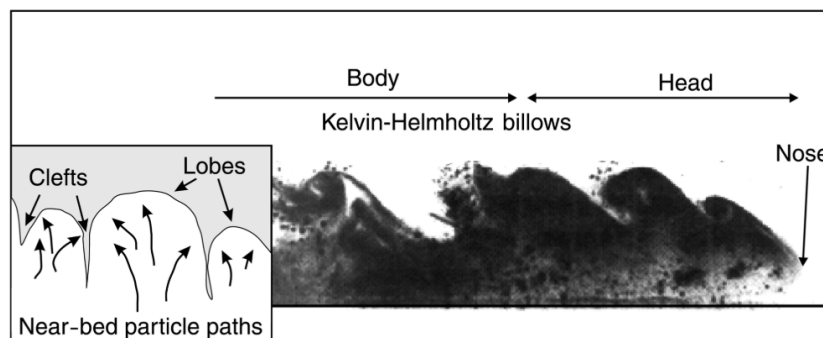


Figure 2.10: Quasi two-dimensional image of the head and body of a saline gravity current illustrating well-developed Kelvin±Helmholtz billows (side view); modified from Simpson (1969). Inset shows schematic view of lobes and clefts seen from below. upper

At the head of a gravity current moving along a horizontal surface, there is a complicated shifting pattern of lobes and clefts, believed to be caused by gravitational instability of the less dense fluid, which is overrun by the nose of the current (John Simpson, 1972). Instantaneous velocities, associated with large eddies, were found to exceed the maximum mean downstream velocity by up to 50%. The turbulence structure in the head, in which the Froude number is always less than one, is dominated by shearing at the upper interface. This is reflected in the distributions of turbulent kinetic energy and density fluctuations, both of which have a maximum at the upper boundary of the head (Best et al., 2009).

### Body

The body is a region of steady downstream velocity with a thin, dense layer of fluid near the base of the current, with increasing downstream velocity, mixes with the ambient fluid at the upper boundary as an irregular succession of large eddies (Ellison and Turner, 1959). The velocity may be up to 40% higher than the maximum mean velocity in the body, and therefore equivalent or higher than the instantaneous velocity of the head (B. Kneller and Clare Buckee, 2000). Simpson and Britter (1980b) and Simpson and Britter (1980a) used visual observations and measurements to divide gravity currents, behind the head, into two distinct regions; the body, which is the lower dense layer, and a region of less dense, mixed fluid that has been mixed out of the head of the current. A similar structure was inferred by (C. Kneller et al., 1999) based on the effect of mixing on the refractive index of brine currents. Some controversy surrounds the nature of the mixed region

above the dense layer; it has been suggested that this is not strictly part of the gravity current but should be described as a zone of clouded water entrained by the underflow (Gerard Middleton, 1966; Kuenen, 1951).

### 2.4.3. Mean flow properties of gravity currents

#### Velocity profile

Figure 2.11 shows a typical vertical profile of the downstream velocity (Hamilton, 1997; Altinakar et al., 1996; Chikita, 1990). Gravity currents have inner and outer regions divided by the velocity maximum. The inner part has a positive velocity gradient in contrast with the outer region. The thickness of the inner region is generally less than half the thickness of the outer region. The height of the velocity maximum is controlled by the ratio of the drag forces at the upper and lower boundaries (Gerard Middleton, 1967; Hiscott et al., 1997). According to Altinakar et al. (1996) and Hiscott et al. (1997) the height of the maximum velocity is found between 0.2 and 0.3 from the height of the current. This height will be raised when looking at gravity currents traveling over a rough bed (Buckee et al., 2001). Despite the variable in the height of the velocity maximum, it is possible to describe the velocity profile by using a characteristic length scale,  $y_{1/2}$ . This characteristic length scale is defined as the distance between the bed and the height in the outer region at which the downstream velocity is half the maximum downstream velocity (Buckee et al., 2001).

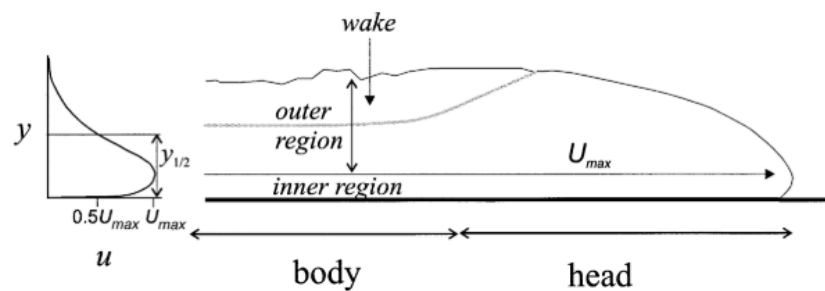


Figure 2.11: Schematic diagram of the head and body of a gravity current, showing a typical downstream velocity profile (B. Kneller and Clare Buckee, 2000)

#### Concentration profiles

Gravity currents are density stratified, having a dense lower layer of fluid and sediment, with a less dense, more homogeneous mixed region above. Two-layer models were based on visual observations of saline currents (Simpson and Britter, 1980a; Simpson and Britter, 1980b). The inflection point in the density distribution was observed to occur well above the level of the velocity maximum and divided the body of the current from the mixed fluid detrained from the head, shown in figure 2.12a.

Two main types of sediment concentration profile have been observed by (Peakall et al., 2000)). A smooth profile is shown in figure 2.12b. This profile is commonly shown in low-concentration, weakly depositional currents, and in saline gravity currents (Altinakar et al., 1996; Buckee et al., 2001). These currents are highly stratified, with a density gradient that is greatest near the base of the current and decreases rapidly around the level of the velocity maximum (B. Kneller and Clare Buckee, 2000). A stepped-concentration profile is shown in 2.12c and is commonly observed in erosional currents or currents interpreted to have a high entrainment rate at the upper boundary (GarcóÁa, 1993; Peakall et al., 2000).

According to GarcóÁa (1994) the fine-grained material is more uniformly distributed in the vertical than the coarse material, which tends to become concentrated in the lower part of the current. 2.12d shows a high near-bed concentration of suspended sediment, decaying rapidly upwards.

### 2.4.4. Lock exchange experiments

#### Smooth bed

Gravity currents have been studied extensively in the laboratory through lock-exchange experiments, which consist of the instantaneous release of a fixed volume of dense fluid into another fluid of slightly lower density. Nogueira et al. (2013) calls the lock-exchange set up a simple and convenient way to investigating the flow features of gravity currents. Gravity currents produced by lock-exchange experiments over a smooth bed present two or even three distinct phases. Namely the adjustment phase, the self-similar phase, and viscous phase (Rottman and John Simpson, 1983). The initial adjustment phase, during which the initial conditions

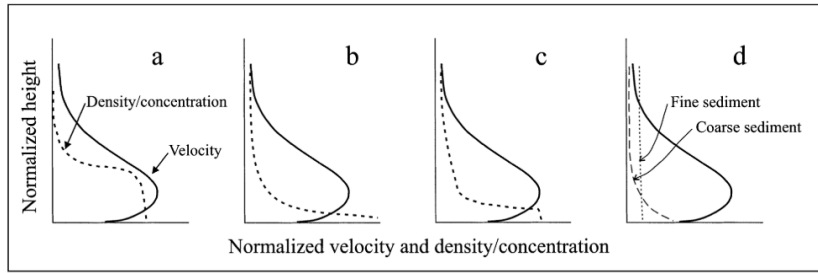


Figure 2.12: Schematic diagram showing various characteristic density/concentration profiles (dashed lines) in density currents; the same downstream velocity profile (solid line) has been used in each case for reference. (a) A two-layer model type concentration profile, dividing the flow into a constant density lower region and an upper region of fluid detrained from the head. (b) A smooth profile, characteristic of low-concentration, weakly depositional flows. (c) A stepped concentration profile observed in erosional flows. (d) A Rouse-type distribution of sediment grain-sizes observed in turbidity currents, in which coarse material is concentrated towards the lower part of the flow whereas fine-grained material is more evenly distributed throughout the depth of the flow (B. Kneller and Clare Buckee, 2000)

are essential, at this phase, the front advances with approximately constant velocity (Huppert and Simpson, 1980). In the self-similar phase, the front speed decreases as  $t^{-1/3}$  (where  $t$  is the time measured from release). The transition from the first to the second phase is observed to be rather abrupt. The decrease of front speed is based on the assumption that the motion is determined by a balance between the inertia and buoyancy of the fluid in the current (Rottman and John Simpson, 1983).

From the observations of Rottman and John Simpson (1983) it is clear that the current front moves steadily in the first phase and that the transition to the inviscid self-similar phase occurs when a disturbance generated at the end wall overtakes the front. If the initial depth of the heavy fluid is equal to or slightly less than the total depth of the fluid in the channel  $h_0 \leq H$ , the disturbance has the appearance of an internal hydraulic drop. Otherwise, the disturbance is a long wave of depression.

After the release of a volume of saltwater into freshwater when  $h_0 = H$ , the fluid from behind the gate forms a gravity current that moves away from the end wall at a constant speed and with constant head depth, see figure 2.13a. Intense mixing between the two fluids is confined to a region just behind the leading edge of the current, the mixed fluid being left behind the head and above the following current. When the back-flowing current meets the wall, the hydraulic drop is generated, see figure 2.13b. The backflow then propagates away from the wall, see figure 2.13c, and eventually overtakes the front, see figure 2.13d. Again, after the front has been overtaken, its speed begins to decrease roughly as  $t^{-1/3}$  until viscous effects dominate inertial effects, when the Reynolds number approaches 1, causing the front speed to decrease more rapidly. The front was observed to be ten lock lengths from the end wall when it was overtaken by the bore. From this instant, the front position advances as  $t^{2/3}$  Nogueira et al. (2013).

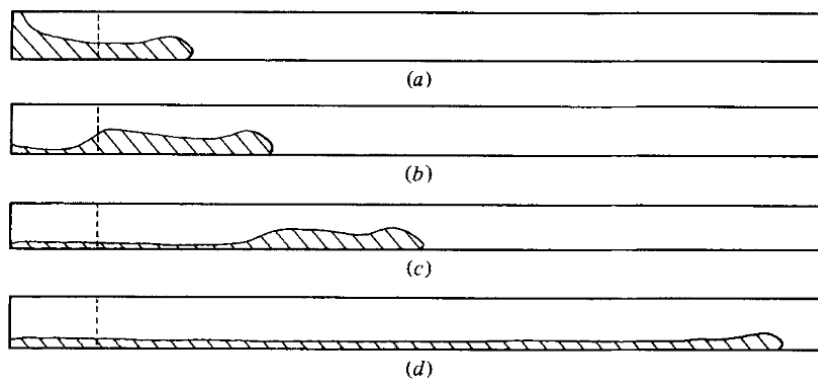


Figure 2.13: Schematic illustrations of the collapse of a volume of heavy fluid with  $h_0/H = 1$  at four successive times after release. (a), (b) and (c) are in the adjustment phase, and (d) is at the beginning of the inviscid self-similar phase (Rottman and John Simpson, 1983).

Figure 2.14 shows a plot of the front position and the bore position, for the case  $h_0/H = 1$ , as functions of time after release. The front and the bore initially travel at constant speed until the lines intersect. Here the front speed declines Rottman and John Simpson, 1983.



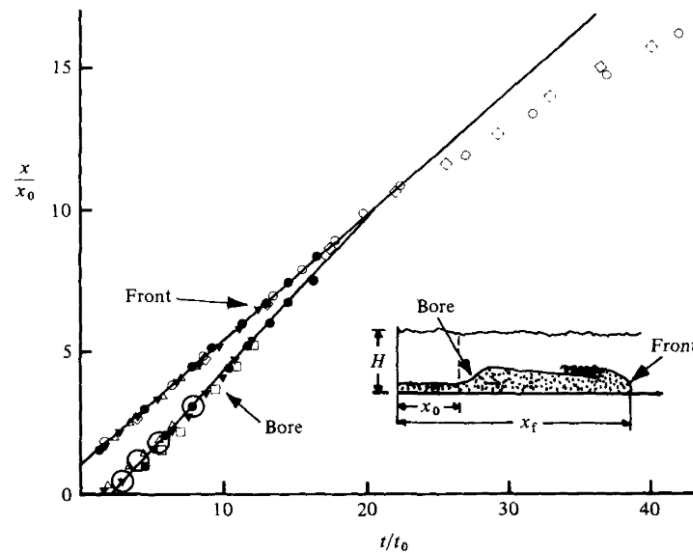


Figure 2.14: The front position and bore position as functions of time after release with  $h_0/H = 1$  (Keulegan, 1957; Huppert and Simpson, 1980).

### Rough bed

Nogueira et al. (2013) looked at the difference between lock exchange experiments with a smooth or rough bed. Seven lock exchange experiments were done with saltwater in freshwater, with variable roughness of the bottom. Nogueira et al. (2013) found that roughness of the bed plays an essential role in the current kinematics, particularly in decreasing the front velocity due to extra drag at the bed. Increasing the size of the bed materials induces a homogenizing effect throughout the current height, fewer large-scale billows being observed. This is possibly due to the turbulent production in the lower level, causing extra mixing with the current. During the self-similar phase, the front position decreases in time and is a function of  $t^{0.78}$ , approximately, which is higher than  $t^{2/3}$  described above. Increasing the bed roughness made the transition to the self-similar phase happen earlier.

Also, La Rocca et al. (2008) did experiments with fresh and saltwater where gravity currents were produced by varying the initial density of the mixture in the lock and the bed roughness of the tank. With an increase in the mean diameter of the roughness elements, the front velocity decreased. The rise of friction by larger elements precedes the beginning of the current deceleration.

### 2.4.5. Particle-driven gravity currents

If the current fluid is a mixture (suspension) of heavier particles in essentially the same interstitial fluid as the ambient, it is called a particle-driven current. While the current spreads, particles fallout and the effective driving strength of the current, compared to a homogeneous current, decays (Ungarish, 2009). Alternatively, sediment may be entrained if the current is passing sufficiently rapidly over an erodible bed, which increases the particle concentration and driving buoyancy force. Both the settling and entrainment rates depend on the velocity and dimensions of the gravity current, and so there is a strong coupling between the sediment transport and the dynamics of the flow (Bonnecaze et al., 1993). A particle-driven current can be described as a two-phase fluid or suspension due to the fact it typically contains thousands of particles per  $cm^3$  (Ungarish, 2009).

The dynamics of the particle drive current can be divided into three phases, namely the initial or starting phase, the transition phase, and a traveling shock phase, see figure 2.15. During the initial or starting phase, the initially stationary fixed volume of fluid is released and collapses, during which it approaches the self-similar solution though very few particles have yet settled out of the current. In the transition phase, the particles are removed from the rear of the current. The fluid in the tail now decelerates less rapidly than the nose. In the last phase, the traveling shock phase, a bore is developed within the current and separates a region of low concentration particles from a particle-rich gravity current region (Bonnecaze et al., 1993).

When the initially stationary fluid collapses, it creates a wave that will be reflected from the end wall a short time later and will travel towards the front of the current. Meanwhile, the current lengthens as the front

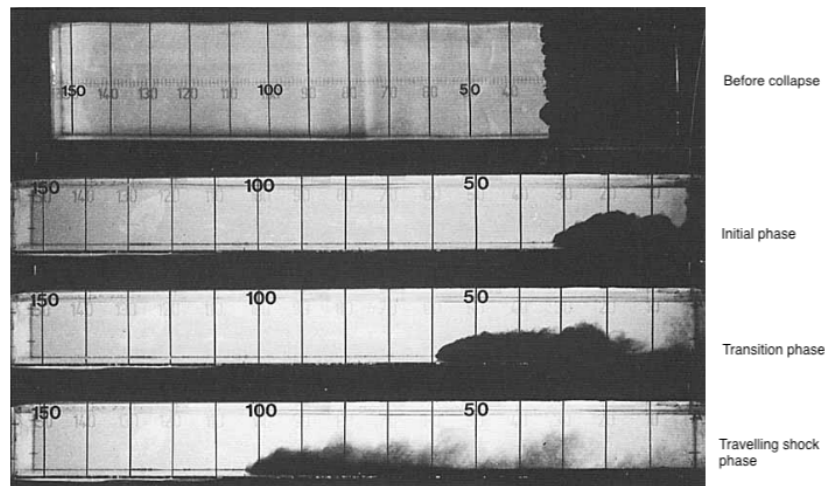


Figure 2.15: Photographs of the different phases in a particle driven current (Bonnetcaze et al., 1993).

moves to the end wall, and the height profile approaches the self-similar shape. During this initial phase, very few particles settle out. During the transition phase, the height of the nose is increasing, and the particle density is declining faster in the back of the current than in the front. Eventually, a traveling shock of bore forms, which rapidly changes the height and the velocity.

During the shock, the rear of the fluid is relatively particle-free, where the front is particle rich. The concentration of particles in the fluid varies continuously across the shock by virtue of the conservation of particles and fluid. The shock is created due to the differential settling of particles along the length of the current. As the height of the front and the tail varies, the front is higher, which establishes a pressure gradient that decelerates the fluid behind the nose. Due to the smaller height of the back of the current, the particles settle out faster than in the front. Consequently, the pressure gradient and the density in the rear are reduced. As the fluid in the rear did not decelerate enough to maintain the self-similar profile, the fluid in the rear accumulates behind the slow-moving front. The motion of the rear is like a jet due to the vanishing concentration of particles and due to the fact that the motion is due to the momentum of the particle-free fluid, and the effects of buoyancy are negligible. The front now behaves like a buoyancy-driven flow as the concentration of particles is declined since the initial value (Bonnetcaze et al., 1993).

#### **Influence of particle size distribution and deposition behavior**

To simulate the natural environment, Gladstone et al., 1998 did non-cohesive lock exchange experiments with more than one-grain size because turbidity deposits typically comprise a wide range of grain sizes. The mixing of different sizes of particles has strongly non-linear effects on both the motion of the current and the sedimentation patterns.

Adding small amounts of coarse particles to a current composed of fine particles has little effect on the dynamics of the current. Comparing this with the addition of a small number of fine particles to a dominantly coarse material has a totally different effect as the flow will travel further. The nonlinearity arises from the presence of modest amounts of fines which causes the current to maintain an excess density difference for much longer. The decay of velocity is dominated by the particles which remain in the suspension. The nonlinearity is seen in both bidisperse and polydisperse experiments. Coarse particles will travel larger distances when in a current with an increasing amount of fine particles. These coarse particles will travel further due to the fact that they are being carried by a current of fines, which has a slower decaying velocity than coarse particles. Concluding, the transport of bidisperse and polydisperse currents depend strongly on the amount of fine-grained sediment (Gladstone et al., 1998).

#### **Cohesive influence**

Marr et al. (2001) conducted an experimental study of cohesive sand-rich sub-aqueous gravity flows in a glass-walled flume, which also carried bentonite or kaolinite. Bentonite is a swelling clay composed of a significant amount of montmorillonite. Marr et al. (2001) found that between 0.7 and 5% by weight bentonite was sufficient to produce coherent flows, compared with 7% for kaolinite. They defined coherent flows as flows that resist breaking apart and becoming completely turbulent under the dynamic stress associated

with the head of a propagating debris flow. The lower concentration of bentonite is caused by the higher yield strength compared to kaolinite. Baas et al. (2016) found that the suspended sediment concentration to produce transient turbulent behavior is much lower in bentonite flows than in kaolinite flows due to the greater cohesive strength of bentonite producing flows with a significantly higher molecular viscosity and yield stress than kaolinite flows at concentrations above the gelling threshold.

Baker et al. (2017) conducted smooth bottomed lock-exchange experiments in a 5 m long, 0.2 m wide, and 0.5 m deep set up to find the effect of clay type on the properties of cohesive sediment gravity flows and their deposits, their focus was on the head of the flows. They conducted experiments with noncohesive silica flour, low coherent kaolinite, and strong, cohesive bentonite in ambient seawater. And found that bentonite flows with a volumetric sediment-water concentration of less than 10% and kaolinite flows of 15% behaved as low-density turbidity currents (LDTCs), with only yield stress on the upper boundary. The kaolinite  $C \leq 15\%$  and bentonite  $C \leq 10\%$  behave in a similar manner to that of the low concentration silica flour flows, exhibiting strong turbulent mixing, both internally and at flow boundaries, pointed semi-elliptically shaped heads with a pronounced nose, and Kelvin-Helmholtz instabilities at the upper boundary. The low concentrations of kaolinite and bentonite did not influence the flow dynamics, as can be seen by the velocities of the heads in figure 2.16 which is inferred to result from effective particle support by shear turbulence and minor particle settling. Baker et al. (2017) expect that the shape of the deposits of these LDTCs is also independent of the cohesive properties of the sediment at  $C \leq 10\%$ , although a longer lock-exchange tank is needed to test this hypothesis.

At low concentration, the dominant turbulent forces prevent electrochemical binding and frictional interaction between the particles. The kaolinite, bentonite, and silica flour produce similar behavior between flows laden with sediment of contrasting cohesive properties. The effect of the cohesive properties of the suspended sediment on deposit geometry can be ignored at  $C \leq 10\%$  (Baker et al., 2017).

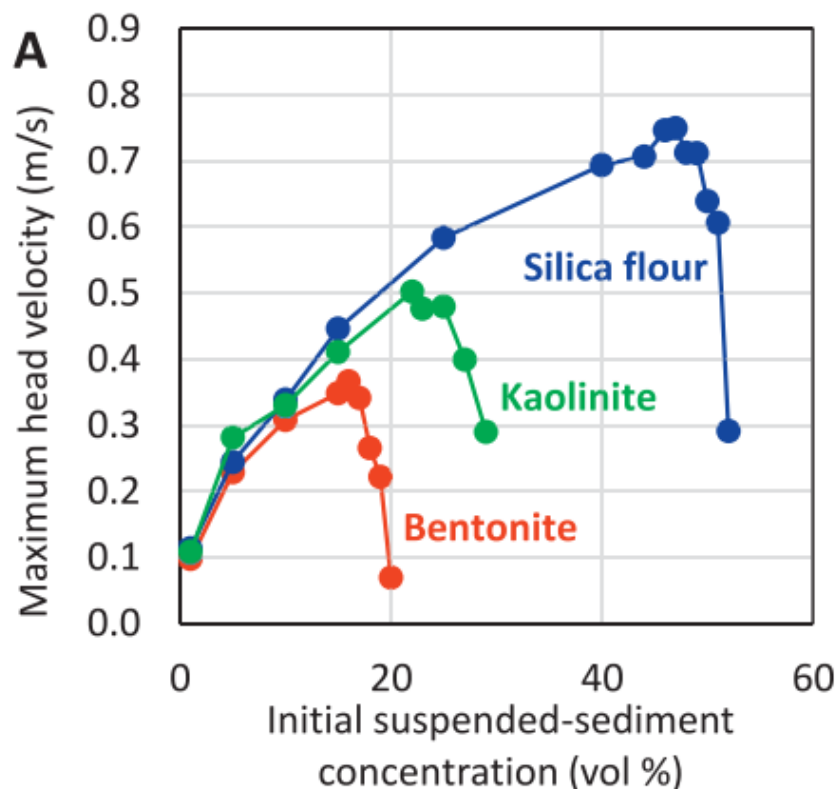


Figure 2.16: Maximum head velocity.

The visual flow properties of flows with Kaolinite  $C \leq 15\%$  and Bentonite  $C \leq 10\%$  show similarities. They are both fully turbulent and have uniform color when mixed with ambient water. Increasing the mass concentrations will give other visual properties; see figure 2.17.



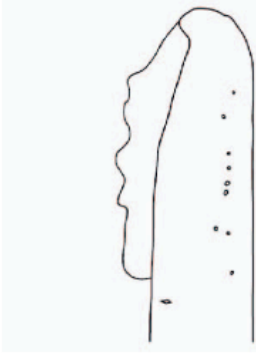
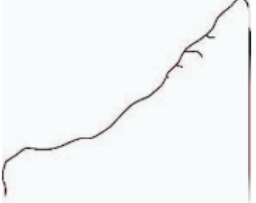

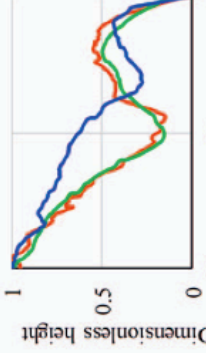
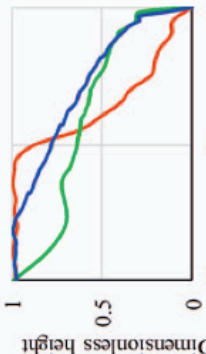
	Low-Density Turbidity Current (LDTC)	High-Density Turbidity Current (HDTC)	Cohesive and Noncohesive Mud Flow (CMF/NCMF)	Slide
<b>Visual flow properties</b>	Fully turbulent; uniform color; mixing with ambient water	Dense lower layer and dilute upper layer; mixing with ambient water	Weak to no internal turbulence; some sediment entrained at top, producing dilute sediment cloud	Coherent mass without significant internal deformation
<b>Flow shape and internal structures</b>				
<b>Deposit shape</b>	Not measured, but probably elongate, thin and wedge-shaped (cf. Amy et al. 2005)			
<b>Range of C-values</b>	Silica flour: $C \leq 44\%$ Kaolinite: $C \leq 15\%$ , Bentonite: $C \leq 10\%$	Silica flour: $46\% \leq C \leq 50\%$ Kaolinite: $22\% \leq C \leq 25\%$ Bentonite: $15\% \leq C \leq 17\%$	Silica flour: $C = 51\%$ Kaolinite: $C = 27\%$ Bentonite: $18\% \leq C \leq 19\%$	Silica flour: $C = 52\%$ Kaolinite: $C = 29\%$ Bentonite: $C = 20\%$

Figure 2.17: Summary of flow and deposit properties. Dimensionless height is relative to the maximum thickness of the deposit. Dimensionless distance is relative to the run out distance (Baker et al., 2017)

# 3

## Experimental methodology

### 3.1. Introduction

As Spearman et al. (2020) and Gillard et al. (2019) ascribed fast settling velocities to flocculation. They both tested the long-term flocculation of currents with a maximum of 0.5 g/L of sediment. But Baker et al. (2017) found that turbulent forces inhibit electrochemical binding and frictional interaction between bentonite particles or between kaolinite particles at low volume concentration  $C \leq 10\%$  in saltwater, so preventing flocculation. What will be the cause of the increased settling velocity observed by Spearman et al. (2020) and Gillard et al. (2019)? Maybe it lies in the fact that Baker et al. (2017) predominantly investigated the heads of the sediment gravity flows. He investigated the shape and velocity of the heads. Still, he did not look at the shape of the body and tail, the plume behavior, the concentration profile, and the settling velocity. The objective of these experiments is to investigate these features further.

The investigation of these features can be split into two parts. First, the difference in settling speed is investigated by doing settling column tests with altering clay concentrations in water with varying salinity. After this, lock exchange experiments will be done to see if the flocculation results of the first experiments are comparable in turbidity currents. During these experiments, there will be made use of Illite.  $CaCl_2$  was used as salt as this is a well-known salt that induced flocculation (Francesca Mietta et al., 2009).

### 3.2. Sediment characterization

Illite was used in the experiments. As told in paragraph 2.1.2, illite and bentonite were the most frequent clay in the CCZ. Bentonite was not used, as from experience with bentonite, it is tough to get a homogeneous mixture with the same characteristics. Illite is a clay with strong ionic bonds that hold back the water movement between the layers F (D. Mietta (2010). Clays containing illite show an initial significant volume decrease on drying with only minor swelling on re-wetting Yong et al. (2012).

The Illite used in the experiments was bought in dry form to ensure no water was present. It was put in the oven for 12 hours at 105 degrees Celsius. The illite used is from the brand: Argiletz laboratoires. To determine the density of illite, a determined quantity of illite was placed in a graduated cylinder filled with a determined amount of water. Subsequently, the mixture was stirred for 20 minutes to make it homogeneous. A volume change was observed from the initial water volume. With this value, the density could be calculated. The particle size was determined with a Mastersizer 2000. The  $\xi$  potential was determined by electrophoretic measurements with a Malvern Zetasizer 1000HS/ 3000HS. All the known material properties of Illite are shown in table 3.1.

	Illite	Bentonite
Density [ $kg/m^3$ ]	2750	2500
Zeta[mV]	-17,3	-20,6
d10 [ $\mu m$ ]	1,39	1,92
d50 [ $\mu m$ ]	5,32	6,35
d90 [ $\mu m$ ]	18,61	21,02

Table 3.1: Properties illite & bentonite

### 3.3. Experimental setup of the settling column

To investigate the different settling velocities created by flocculation, settling column tests were done. These tests consist of examining the settling velocity for different concentrations of clay in different concentrations of added salt. The experimental methodology was based on the effect that particles block more light than water. When the sediments settle, more light will be visible at the top of the graduated cylinder. These experiments were filmed and analyzed.

#### 3.3.1. Setup settling column

The side view and top view of the setup used are shown in Figure 3.1. From left to right, there is pictured: GoPro Nero 7 Black on a wooden block to center it to the middle of the settling column. Next, the graduated cylinder (settling column) is shown. On the right, the LED lamp is shown.

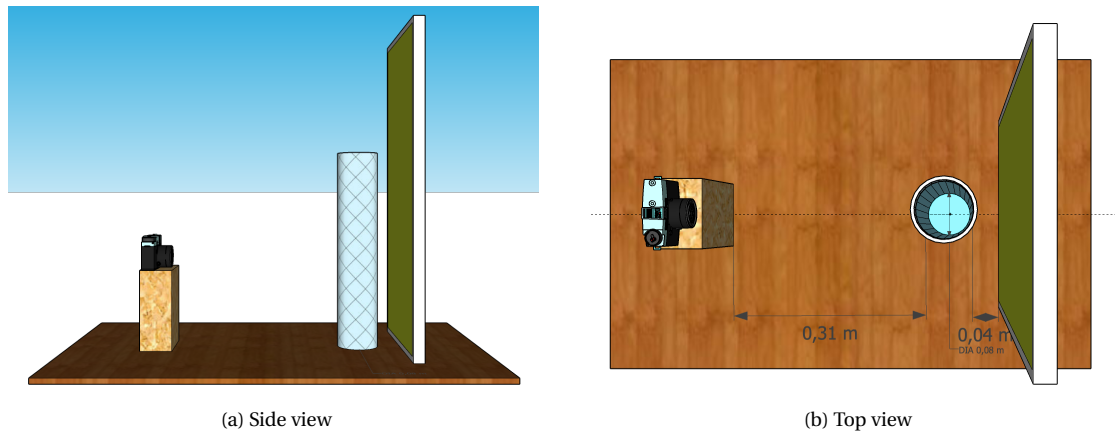


Figure 3.1: Schematic view of settling column setup.

Making the mixture was done by adding water to a predetermined quantity of clay to make a constant volume of one liter. For experiments nine up to 25, I first mixed the water with  $CaCl_2$ . Mixing was done for 20 minutes to make sure the mixture was homogeneous. The steps to make the settling videos are shown in figure 3.2. After I mixed the solution, I measured the temperature and total dissolved salts [mg/L] using an Elmetron pH/conductivity meter CPC-401. The Elmetron is a measuring tool with three separate attachments: a temperature meter, a conductivity meter, and a pH meter. Combining all three gives the most accurate outcome as the salinity affects the pH value.

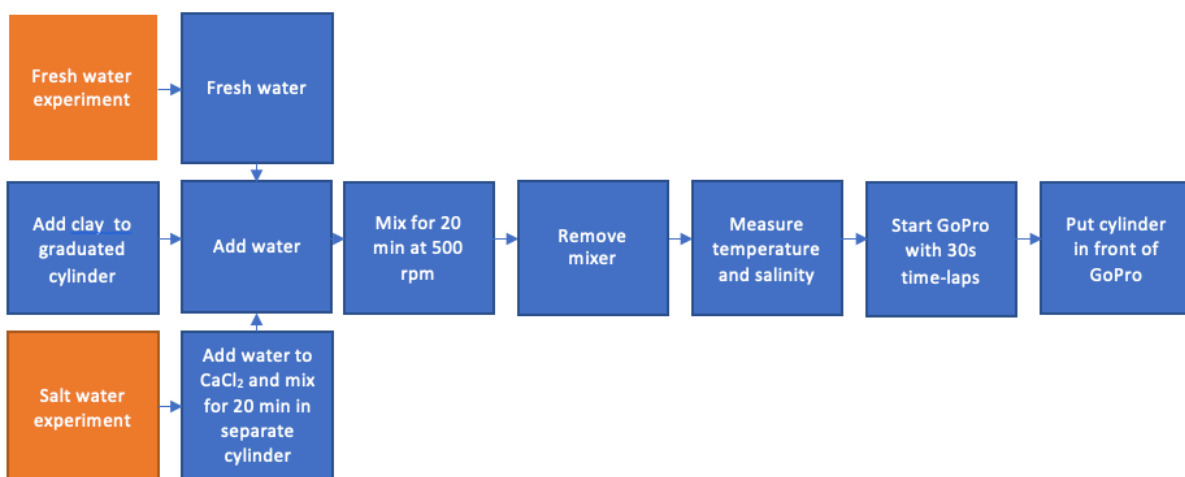


Figure 3.2: Order of making the videos

I first tested the Elmetron meter by adding  $CaCl_2$  to water. The result is shown in table 3.2. The meter is not very accurate in determining the  $CaCl_2$  concentration, especially not when the salt concentration is increased. Also, there is a difference in the accuracy shown at the two last 100g/L  $CaCl_2$ . There is at largest a difference of around the 14 %. Both can be the effect that the amount of salt was too significant to dissolve.

Added $CaCl_2$ [g/L]	Measured TDS [g/L]	Percentage of measured salt compared with added salt [%]
0	0.26	
5	3.99	0.80
10	7.31	0.71
50	28.55	0.57
100	49.07	0.49
100	42.89	0.43

Table 3.2: Elmetron accuracy. TDS: total dissolved salts

Equipment used:

- mixer: VOS-12020 overhead stirrer
- mixing rod: 4 bladed mixing rod which is placed 17cm above the bottom of the jar.
- pH/conductivity meter: Elmetron CPC-401
- mass scale: Kern with accuracy of 0.1g

### 3.3.2. Settling column experiments

The TU Delft Dredging Laboratory provided a graduated cylinder with a capacity of one liter to do settling column experiments. Twenty-four experiments were done with the use of the graduated cylinder; see table 3.3. Three different levels of salinities were chosen. Tests are done with various concentrations of clay content to investigate if salt has a similar effect on the settling speed of clay for different salinities.

#	Mass concentration Illite [g/L]	Volumetric concentration Illite [-]	Concentration $CaCl_2$ [mM]	Concentration $CaCl_2$ (mg/L)
1	10	0.00363	0	0
2	20	0.00727	0	0
3	30	0.0109	0	0
4	40	0.0145	0	0
5	50	0.0182	0	0
6	75	0.0273	0	0
7	100	0.0364	0	0
8	125	0.0455	0	0
9	10	0.00363	10	1110
10	20	0.00727	10	1110
11	30	0.0109	10	1110
12	40	0.0145	10	1110
13	50	0.0182	10	1110
14	75	0.0273	10	1110
15	100	0.0364	10	1110
16	125	0.0455	10	1110
17	10	0.00363	100	11,100
18	20	0.00727	100	11,100
19	30	0.0109	100	11,100
20	40	0.0145	100	11,100
21	50	0.0182	100	11,100
22	75	0.0273	100	11,100
23	100	0.0364	100	11,100
24	125	0.0455	100	11,100

Table 3.3: Summary of experiments, [mM] stands for  $\text{mol}/m^3$ .

### 3.3.3. Experimental measurement settling column

Illite's settling velocity was measured by using machine vision tools like Opencv and algorithms developed in Python. The time-lapse was made into a movie by using a pre-existing python script found online. The obtained video was cropped to 0.35 meters in height, so no surroundings were shown.

A subtraction procedure was used to only consider changes over time of the background, see figure 3.4. This is called the subtracted video. The subtracted movie was then thresh held. Every color in the spectrum has a pixel value. If the pixel value is smaller than the threshold, it is set to 0 (black); otherwise, it is set to a maximum value of 255 (white). The threshold was generally set on 100, with some changes at specific experiments. To determine the threshold, a good visual comparison was made to find the ideal threshold. The led light was flickering when filmed, making the color changes slightly, which makes the visual comparison required. An increase of threshold value by 25 can lead to a rise of the settling velocity by 150%. I then flipped the pixel values to make black white and vice versa, the mask. An overview of the step is shown in figure 3.3

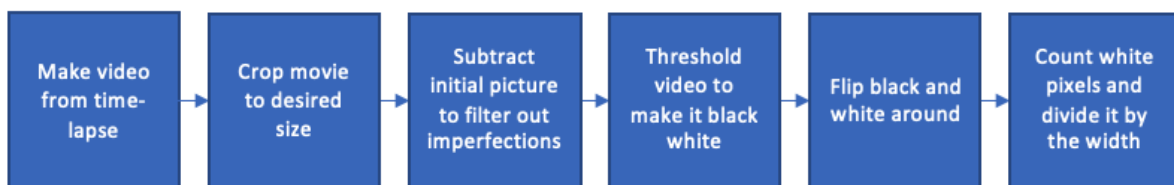


Figure 3.3: Order of python script steps

Python determined all the white pixels. The number of pixels was then divided by the width of the cropped movie. In that way, it was possible to measure the white line decreasing every 30 seconds.



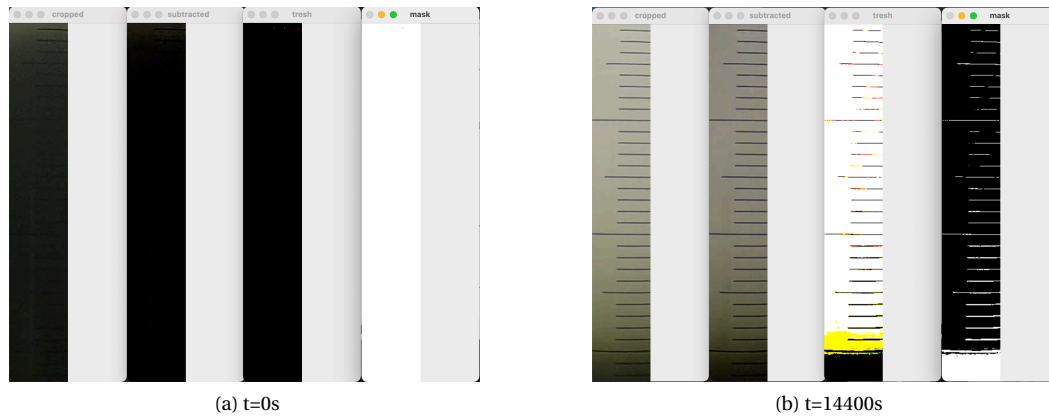


Figure 3.4: Settling column test. Cropped, subtracted, trash and mask pictures

### 3.4. Experimental set-up for the lock exchange experiments

Lock exchange experiments were performed to mimic the turbulent flows created by the SMT. The experimental methodology was based in the same way as the settling column test. This was based on the effect that particles block more light than water. When the concentration of the illite in the water decreases, more light will travel to the camera.

#### 3.4.1. Setup lock exchange

The TU Delft Dredging Laboratory provided an existing tank. This tank has a length of 3 meters, a width of 0.2m, and a height of 0.4m. The tank has a lock gate located 0.2 meters from the end; see figure 3.5. This lock was used to release the sediment mixture. The mixture was always made in the mixing section. The filmed area is shown and is 2.40 centimeters wide.

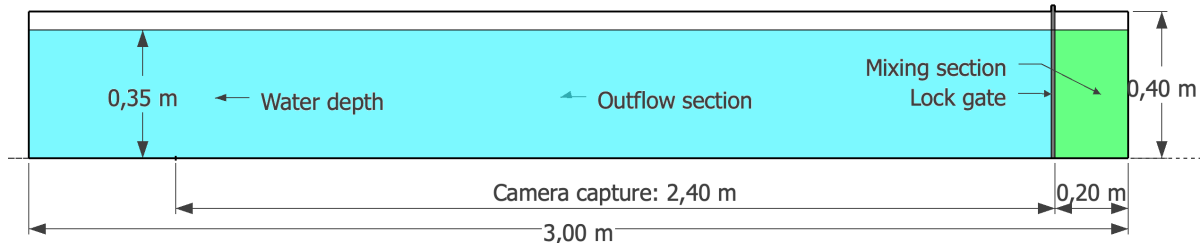


Figure 3.5: Schematic representation of the tank.

The tank was fixed to the table with two blocks; see figure 3.6. The tank was calibrated with a level to ensure no height differences between both sides. At the back of the tank, a diffuse paper was placed. This paper created as much homogeneous light throughout the length and height of the tank. Behind the diffuse paper, there is a wooden panel with three LED strips attached to it. These LED strips are positioned at 0.15 m from each other. The LED strips have the function of creating a white light throughout the length of the tank to illuminate the current.

Videos were made with an IL5HM8512D: Fastec high-speed camera with a Navitar 17mm lens. The camera and tank were placed underneath a dark cloth to make sure the outside light is blocked. The camera was placed 4.75 meters from the camera lens to the front wall of the tank and films with 130 frames per second. Images of camera settings and used tools are shown in appendix L. Be aware that the camera filmed only the 2.40 meters left from the lock. With the used lens, it was not possible to film a broader range. The camera could also not be put back further as the dark cloth hanging over the setup was limited in length.

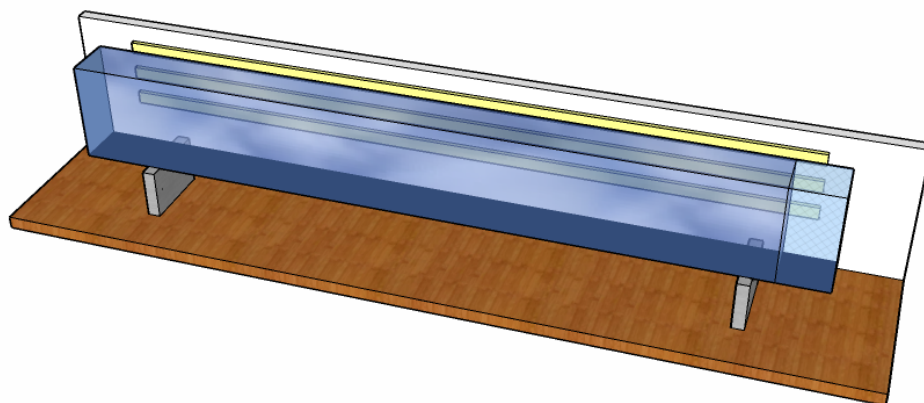


Figure 3.6: Schematic representation of the total tank setup.

Filling the tank was done in three ways, depending on the salinity of the experiment, see figure 3.7. I always filled the tank to a height of 0.35 meters, which makes the capacity 210 liters.

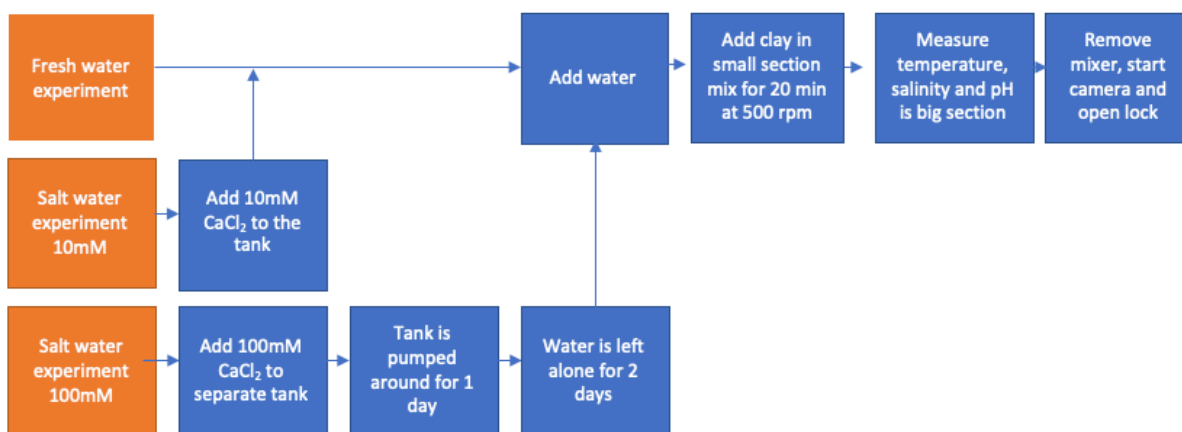


Figure 3.7: Order of making the videos

### 3.4.2. Lock exchange experiments

First off, I did 24 experiments with the lock exchange; see table 3.4. These all have the same concentration of salt and illite used as in the settling column experiments.

#	Mass concentration illite [g/L]	Concentration CaCl2 [mM]
1	10	0
2	20	0
3	30	0
4	40	0
5	50	0
6	75	0
7	100	0
8	125	0
9	10	10
10	20	10
11	30	10
12	40	10
13	50	10
14	75	10

15	100	10
16	125	10
17	10	100
18	20	100
19	30	100
20	40	100
21	50	100
22	75	100
23	100	100
24	125	100

Table 3.4: Summary of experiments.

**Additional experiments with pre-existing bed**

In addition, I did experiments to see if a pre-existing clay bed has consequences for the behavior of the flow. Before the experiment, a clay bed has been made by running a lock exchange experiment with a concentration of 100g/L. This test then had, depending on the next experiment, one day or two days settling time before it was used for the new experiment, see table 3.5. The lock was put back for these tests, and the mixing section of the tank is cleaned out. This part is then filled with either freshwater or water with added  $CaCl_2$ . The tank is left to rest for either one or two days, depending on the following experiment. The clay was added 20 minutes before the experiments and was mixed for 20 minutes at 500 rpm.

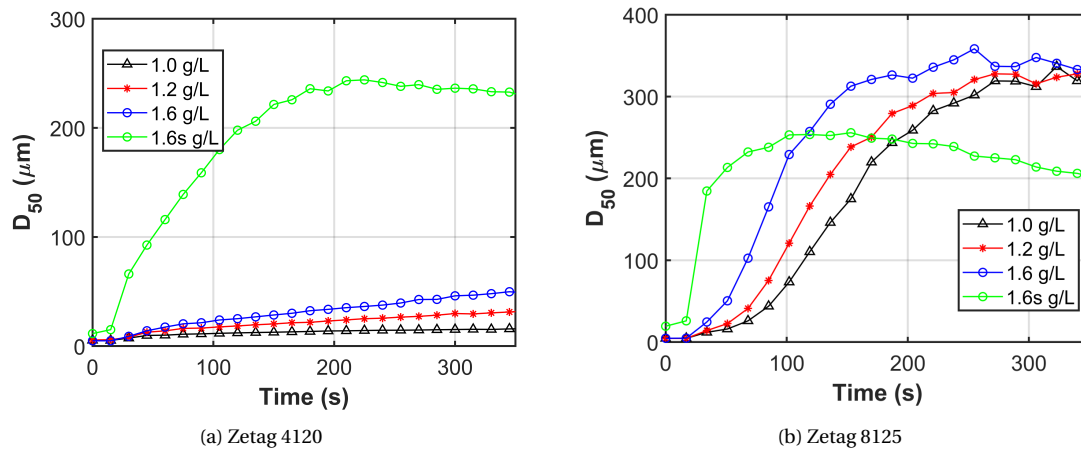
#	Mass concentration illite [g/L]	Concentration $CaCl_2$ [mM]	Pre-existing bed [days]
25_1	10	0	1
25_2	10	0	2
26_1	50	0	1
26_2	50	0	2
27_1	100	0	1
27_2	100	0	2
28_1	10	10	1
28_2	10	10	2
29_1	50	10	1
29_2	50	10	2
30_1	100	10	1
30_2	100	10	2

Table 3.5: Summary of experiments

**Additional experiments with flocculant**

After the experiments above, no quick differences were visible regarding decreasing head velocity or an increased settling velocity. So other options could be attractive. One of those options is the use of flocculant. I did twelve experiments with either Zetag 4120 or Zetag 8125. Zetag 4120 is an anionic flocculant with a medium charge and a medium molecular weight. Zetag 8125 is a cationic flocculant with a low charge and a high molecular weight. Both the flocculants have an optimum dose of 2.5mg per gram of clay used in all experiments. In figure 3.8 the abilities of the flocculant were shown to increase the  $d_{50}$ . Chosen was to use Zetag 4120 in fresh water and water with added salt to see if there is a big difference as that the  $d_{50}$  predicts. The difference shown in 3.8a, is explained as told as in 2.3.5 that anionic polymers thrive better with a cationic medium as salt. Zetag 8125 is only tested in freshwater as it has a positive charge.

I tested the effect of flocculant in two ways based on the idea that biological matter could be in the water column in the deep sea. 1. Adding the flocculant in only the outflow section, stirred for 30 seconds before the lock is opened. 2. Adding flocculant to the mixing section, mixed in with the mixture 30 seconds before the lock is opened. All these experiments are summarized in table 3.6.

Figure 3.8: Increasing  $d_{50}$  over time with different concentrations of flocculant, s stands for is saltwater.

#	Mass concentration illite [g/L]	Concentration CaCl <sub>2</sub> [mM]	Zetag 4120 Mixing section	Zetag 4120 Outflow section	Zetag 8125 Mixing section	Zetag 8125 Outflow section
31	10	0				x
32	100	0				x
33	10	0			x	
34	100	0			x	
35	10	0	x			
36	100	0	x			
37	10	0		x		
38	100	0		x		
39	10	10	x			
40	100	10	x			
41	10	10		x		
42	100	10		x		

Table 3.6: Summary of experiments with flocculant

#### Additional experiments with artificial Clarion Clipperton zone clay

In addition, I investigated artificial soil, which can be compared to CCZ sediment. I did experiments with this sediment to make sure that the experiments with Illite were not too idealized. The mixture consist of two materials:

- 1. Sibelco FT-S1 (Abidichte Ton") consisting of 64% kaolinite, 10% illite, 19% quartz and 7% various other minerals
- 2. Cebo OMCA Betonite consisting of 17% kaolinite, 17% illite and 66% montmorillonite

The percentage of the used materials is not known. The clay was made to mimic the mechanical strength of the CCZ clay. The clay was in wet form, which was put in the oven at 105 °C for 24 hours to make sure the water was evaporated. I measured the density, which came around 2600 kg/m<sup>3</sup>. Mixing it into a homogeneous mixture was more complex than with illite and took more time, see section 3.6.2. These experiments are summarized in table 3.7. Figure 3.8 shows the density and grain sizes.

#	Mass concentration mixture [g/L]	Concentration CaCl <sub>2</sub> [mM]
43	10	0
44	50	0
45	100	0
46	10	10
47	50	10
48	100	10

Table 3.7: Summary of experiments with mixture

	Mixture
Density [ $kg/m^3$ ]	2600
d10 [ $\mu m$ ]	2,49
d50 [ $\mu m$ ]	19,50
d90 [ $\mu m$ ]	75,40

Table 3.8: Properties artificial CCZ sediment

### 3.5. Experimental procedure for calibration

Making a calibration matrix would contribute to analyze the made videos. Using a calibration curve, the concentration and mass could be measured of the flow in the videos. The calibration was made by measuring how much light can travel through a specific concentration of sediment. When more sediment is added, the more opaque the mixture becomes.

To make a calibration curve, the tank was moved 20 centimeters to the left. This was done to make sure the camera stays located in the same spot. A calibration matrix was only made from illite with 0mM, 10mM, and 100mM. No calibration curve was constructed for flocculant as it would be more difficult due to time-dependent response due to time restrictions. The artificial CCZ clay was also not calibrated; as mixing the clay takes a long time, it would become a multiple days project.

The tank was filled with water till it reaches 0.35m height. Step by step, sediment was added to the mixing section. The sediment would be mixed till it was homogeneous, the mixer would be taken out, and a picture will be made before adding new sediment. As increasing the salinity makes the suspension a little white, three calibration tests are done.

Per salinity, the calibration was made for mass concentrations between specific ranges with different steps; a summary can be seen in Table 3.9. An amount of 1.4g of illite was added in every step. After adding the illite, the mixture was stirred for five minutes to ensure the mixture was homogeneous. This step was continued until a mass of 70 g is added in total to the 14 liters in the mixing section. A picture was taken after the mixing, before adding more illite. These pictures are shown in figure 3.9

Volume concentrations ranges	Steps	Mass	Steps
0.0% - 0.0051%	0.00051%	0g - 14g	1.4g
0.0051% - 0.02545%	0.00255%	14g - 70g	7g

Table 3.9: Sediment concentration ranges and steps within

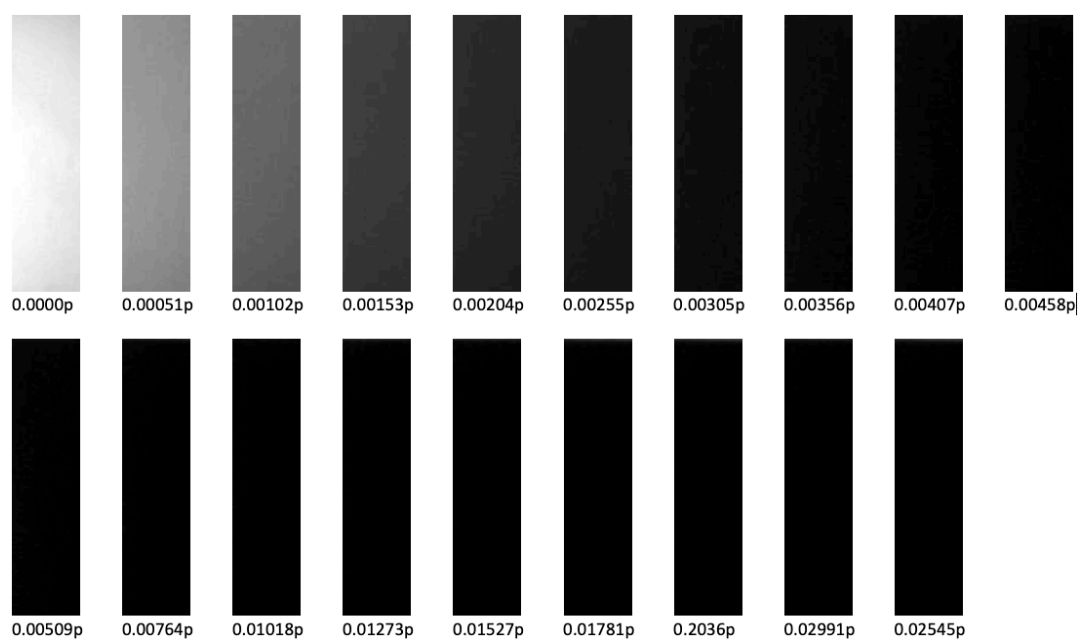


Figure 3.9: Shades of grey for 10 mM, volume percentage per picture.

A calibration curve was made by the use of a pre-existing python script (Vasquez, 2020). As computer work with color codes per color, each picture from figure 3.9 gets its value, a pixel value of 255 represent complete white, and a value of 0 represents absolute black. The calibration curve is shown in figure 3.10. It showed that at a concentration of 0.015, no more visible light was detected. This means that this was the maximum value of concentration that can be determined.

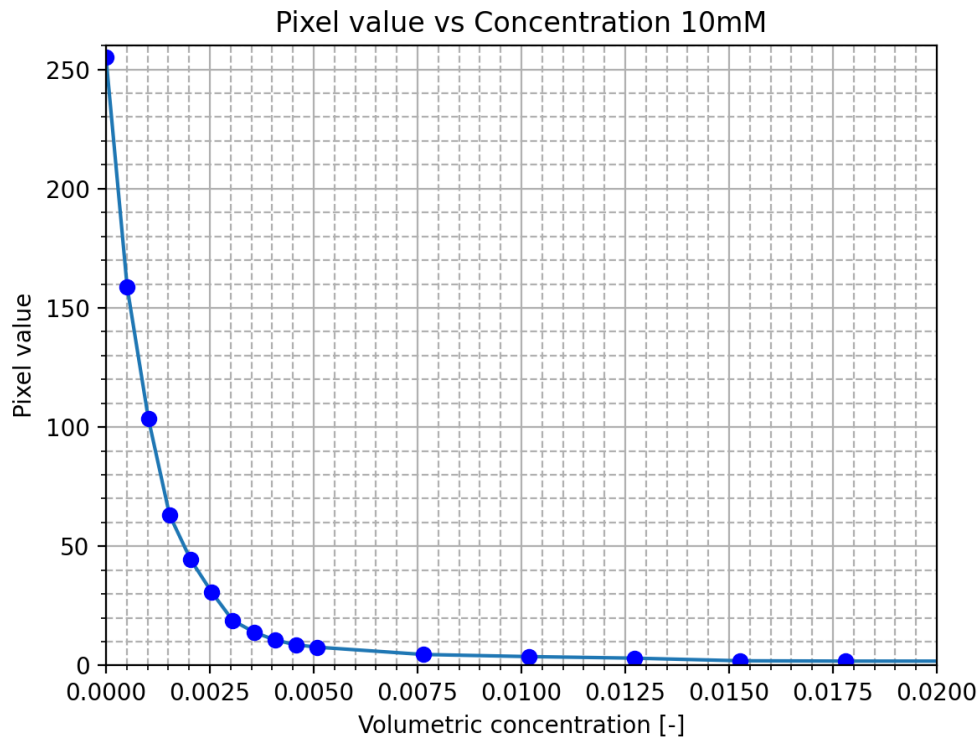


Figure 3.10: Pixel calibration curve

The grey colors could be changed to the primary colors using Opencv in Python. This would give a more precise visual representation of the concentrations and the mass, see figure 3.11. Be aware that the dark red gives a maximum value of 0.015 and could be much more significant. This was an experiment with the least amount of illite.

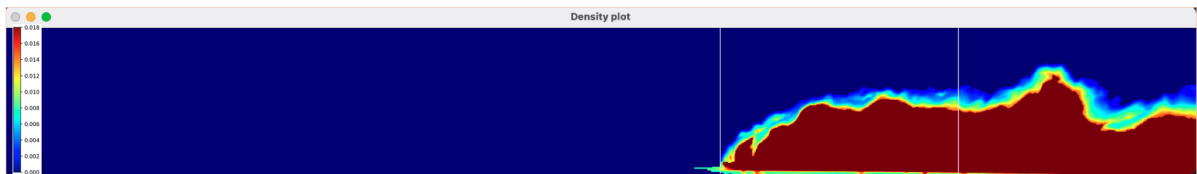


Figure 3.11: Color map of a calibrated current of experiment 1

### 3.5.1. Experimental measurement lock exchange

Velocity measurements can be done with the same principle as the velocity is measured at the settling column test; the difference is that the last step is changed. Vasquez (2020) her algorithm scans from left to right to find the first white pixel value. The other steps are still the same and are shown in figure 3.12 and 3.13. When the distance from the left wall is known, the speed can be calculated as the fps, size of the image, and size of the tank are known.

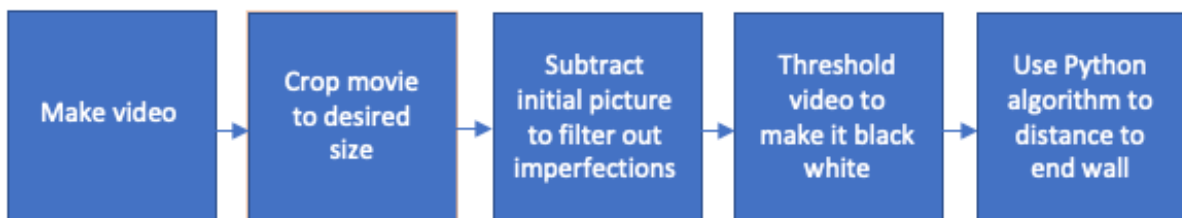


Figure 3.12: Order of analysing video's to find the speed

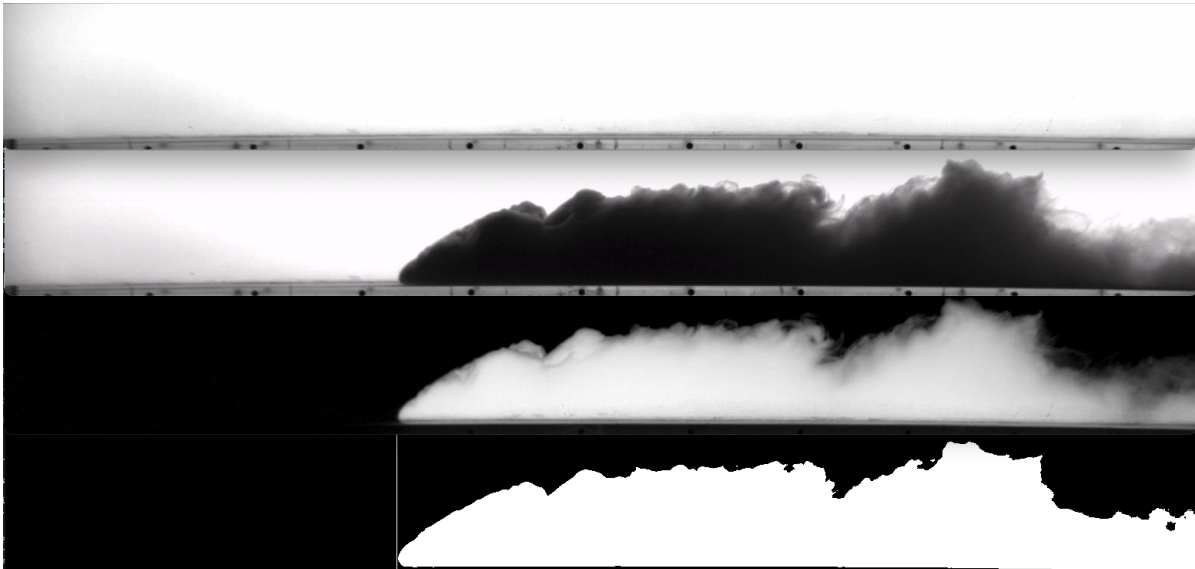


Figure 3.13: Order of analysing video's to find the speed

As in Vasquez (2020) her experiments, my experiments also experience oscillations in the velocity, see figure 3.14. This is mainly due to the way the lock is opened; more on this in 3.6. This means that the results are polluted. The impact is more extreme for low concentrations as these have a longer travel time in the tank before they reach the end.

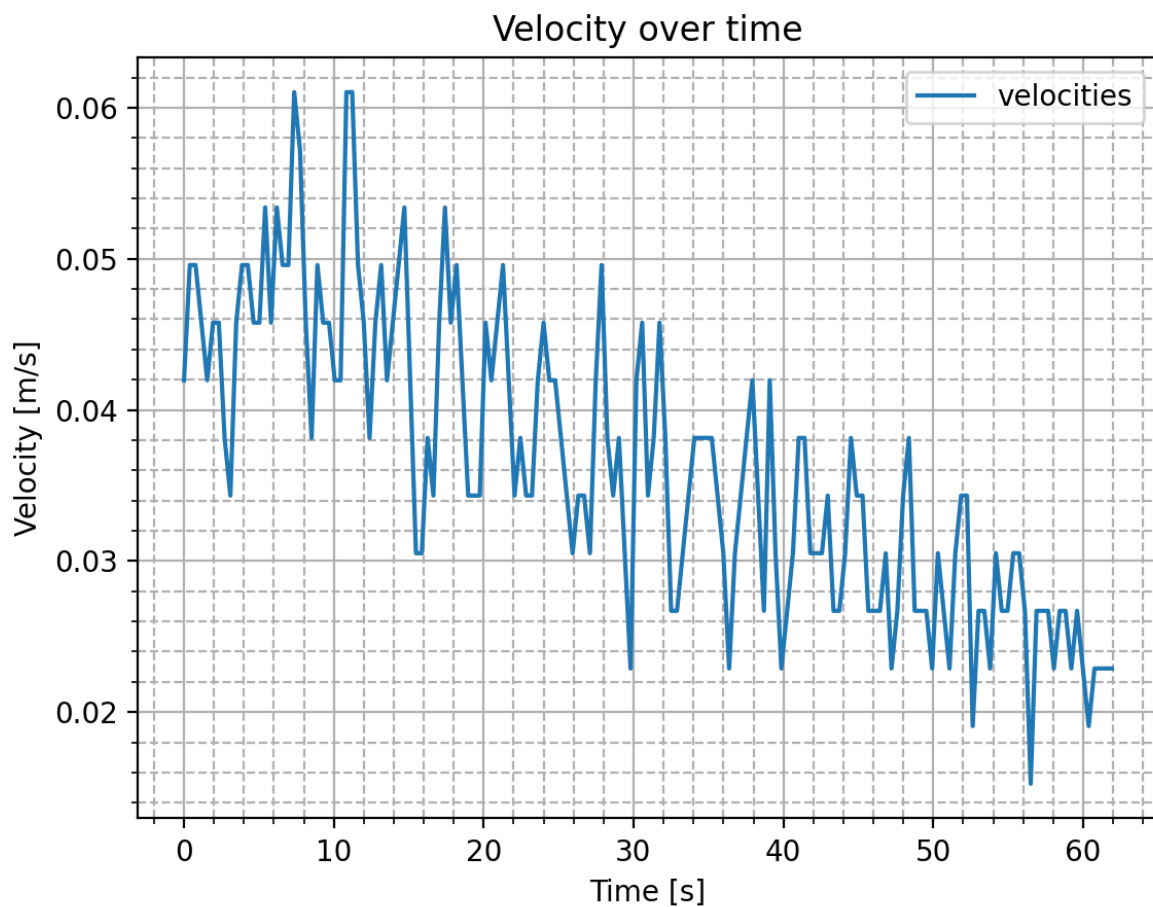


Figure 3.14: Velocity over time for 10g/L illite in fresh water



### 3.6. Experimental difficulties

Experimental difficulties were experienced with settling column tests and with lock exchange experiments. One difficulty both had, is the mixing of 100 mM of  $CaCl_2$ . The amount was not able to dissolve. In settling column experiments, nothing was done to this fact, but the water  $CaCl_2$  mixture was first prepared in a different tank for the lock exchange experiments. After one day of pumping the mixture around, the mixture got two days to settle. White flocks were shown on the bottom of the tank. Only water above 5 centimeters above the tank's lowest point was pumped to the lock exchange tank.

#### 3.6.1. Experimental difficulties settling column

Settling column test with a low concentration of illite experiences difficulties as the light visibility is blurred and will not show good contrast between the water and the mixture. This makes the low concentration mixtures less accurate than the higher concentrations used. The threshold should be altered to see what the impact is on the analysis. The led light is flickering when filmed, making it necessary to make a threshold by visual observation.

#### 3.6.2. Experimental difficulties lock exchange

##### Mixing

Before the lock gate is opened, the sediment is mixed with water. Mixing is done to make a homogeneous mixture; however, mixing induces unwanted turbulence. After mixing, the mixing tool is removed and is put aside. The time between removing the mixing device and opening the lock is around 10 seconds. For the experiments with the flocculant in the mixing section, an additional 30 seconds were added. In these 30 seconds, the flocculant was mixed in with the homogeneous mixture. The use of different kind of light is recommended.

##### Turbulence created by opening the lock

Removing the lock causes a lot of unneeded turbulence and disturbances, especially for small particle sizes; the particles follow the vortices of the generated turbulence because they are that fine that particle's drag forces can not overcome the turbulence's forces. After the transfer of energy from the turbulence on the tank to the forming wave, the turbulence will lose its momentum inside the tank. As I can not quantify these details because it is that complex, I set a benchmark position (starting of the current) for all my experiments. This benchmark is placed on the worst-case scenario I experienced, which is 146 pixels or 21 centimeters left from the lock.

The worst-case scenario is shown in figure 3.15. Clear is that there is a mixture of clay and water in the upper and lower part divided by water. The start of the experiments is taken at the point where the lower mixture is further left than the upper mixture, at  $t=0$ .



Figure 3.15: Start point measurements

#### **Mixing the artificial CCZ clay**

Mixing the artificial CCZ clay was very challenging. Especially with high concentrations, the clay was added to a square box, the mixing section of the tank, where it should be mixed. Mixing in the square box was no problem for the same concentrations of illite, but with the artificial CCZ clay, it was impossible. For the 100g/L experiments, the mixture with water was pre-made in a bucket and was mixed around for 5 hours before adding it gradually to the tank. The lock is set in place, and the mixture is added to the mixing section at the same speed; the water is filled in the outflow section to minimize leakage from the lock.

The low concentration were mixed in the mixing section and took around five hours to make sure the mixture was homogeneous.

# 4

## Experimental results

In this chapter, the results of the settling column experiments and lock exchange experiments are presented. The settling velocity is obtained by the settling column experiments. The results obtained for the lock exchange experiments depend on which experiment is done. For all the standard illite experiments with either 0 mM, 10 mM, and 100 mM, head velocity profiles and mass concentration profiles are made. Only head velocity profiles are determined for the additional test with flocculant and artificial CCZ clay. In all lock exchange experiments, I assessed if there was an increase in settling in the body or tail of the current using visual observations.

### 4.1. Settling column experiments

This section represents the result of the settling column experiments are represented. Twenty-four experiments were performed to get a better understanding of flocculation; see the experimental details in table 4.1. For experiments 1 up to 8 no  $CaCl_2$  was added, for experiments 9 up to 16 1,11 grams  $CaCl_2$  was added and for experiments 17 up to 24 11,1 grams of  $CaCl_2$  was added.

The heights were plotted over time; see figure 4.1. The experiments had a duration of 500 minutes. From left to right, an increase in salinity is shown. It is clear that with an increase of sediment, the curves become rounder in shape, which in turn tells us that the settling velocity declines.

#	Mass concentration illite [g/L]	Concentration $CaCl_2$ [mM]	Temperature [ $^{\circ}$ C]	TDS [mg/L]
1	10	0	20.2	509.4
2	20	0	20.1	498.3
3	30	0	19.9	502.1
4	40	0	20.3	500.7
5	50	0	19.8	506.4
6	75	0	18.4	491.3
7	100	0	18.0	495.2
8	125	0	17.4	554.9
9	10	10	17.5	1336
10	20	10	17.4	1157
11	30	10	16.5	1244
12	40	10	11.6	1049
13	50	10	18.8	1425
14	75	10	11.9	1040
15	100	10	14.9	1044
16	125	10	14.1	1191
17	10	100	19.6	8049
18	20	100	19.3	7900
19	30	100	19.1	7993
20	40	100	19.6	8155

21	50	100	20.2	7839
22	75	100	23.8	6208
23	100	100	23.8	7311
24	125	100	23.8	7353

Table 4.1: Summary of experiments.

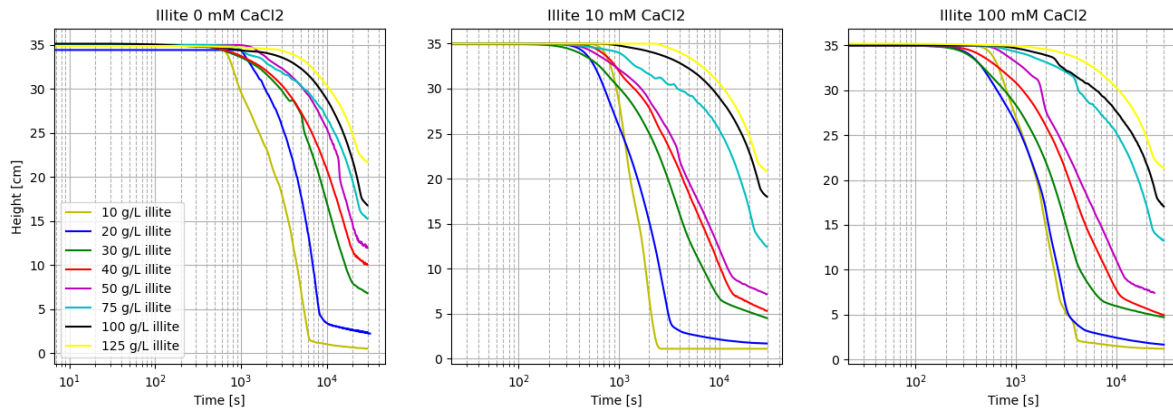


Figure 4.1: Relationships of mud-line height for illite clay as a function of salt type and concentration

Settling can be divided into two parts; see Figure 4.2. The first part from  $t = 0$  till  $t = t_c$  shows a more or less linear downward trend. The second part is the consolidation part, which means going from undrained to drained sediment. In this thesis, there will not be looked at consolidation. In the first section, the settling velocity will be calculated, and this is done by calculating the derivative of the first part.

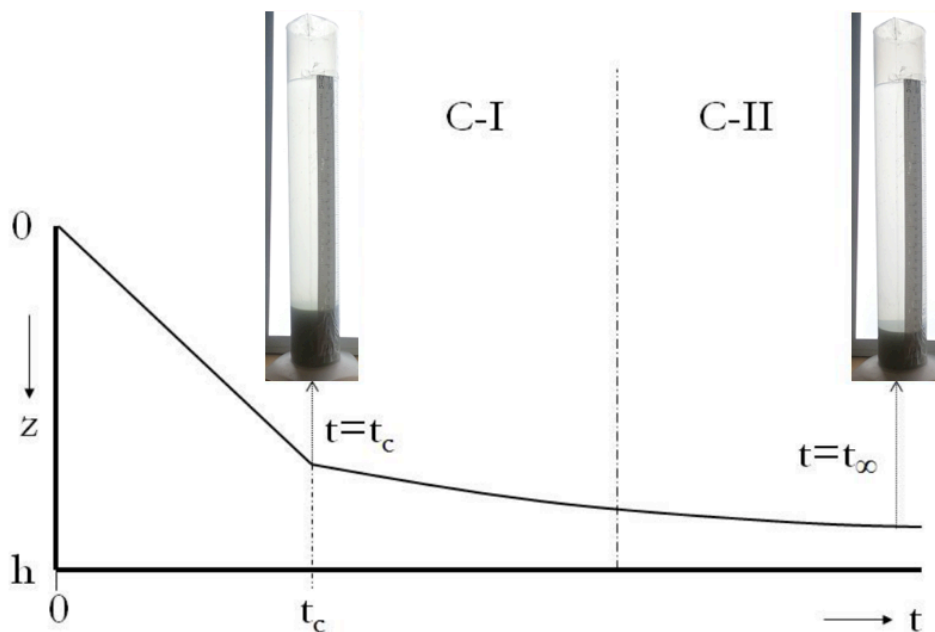


Figure 4.2: Schematized settling curve with indication of start and end of consolidation phases. The inserted photos correspond with the start of the consolidation phase, the point of contraction at  $t = t_c$  and the end of the consolidation phase at  $t = t_\infty$ . The consolidation phase itself is divided into two phases, C-I and C-II. The x-axis is not to scale.

The settling velocities were determined of all experiments and are shown in 4.3. It shows that with added  $CaCl_2$ , the settling speed increases up to a specific concentration; this concentration is in the neighborhood

of 75 gram/L of illite. There is a difference in settling velocity for experiments with 10, 20, 30, and 50 gram/L illite with 10 mM and 100 mM of  $CaCl_2$ .

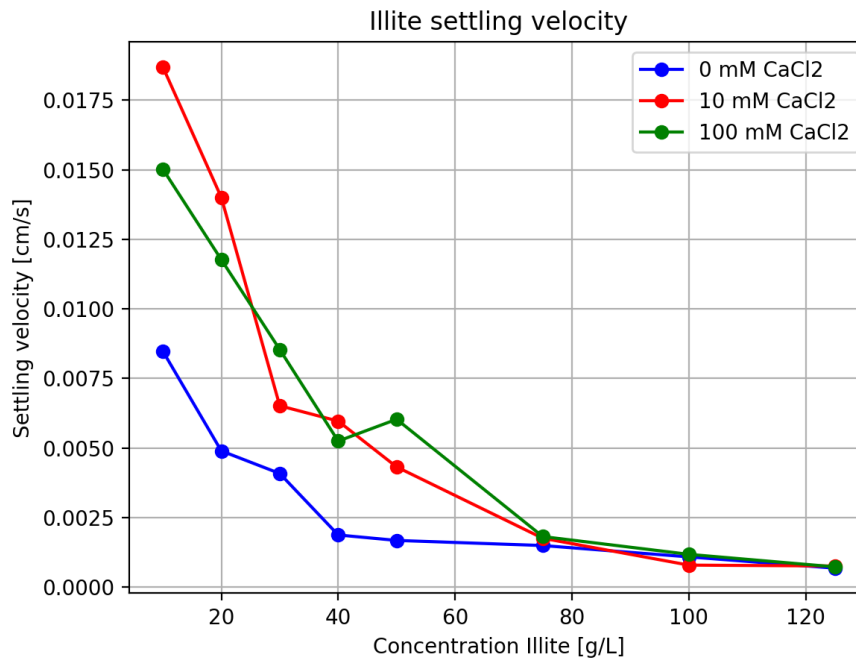


Figure 4.3: Relationships of velocity for illite clay as a function of salt type and concentration:

Salt densities were determined, no visual volume changes were observed, which means that the density can be calculated by adding the weight of salt added to freshwater, see Table 4.2. Small steps are observed from 0 mM to 10 mM.

Salinity [mM]	Density [kg/m <sup>3</sup> ]
0	1000,00
10	1001,11
100	1011,10

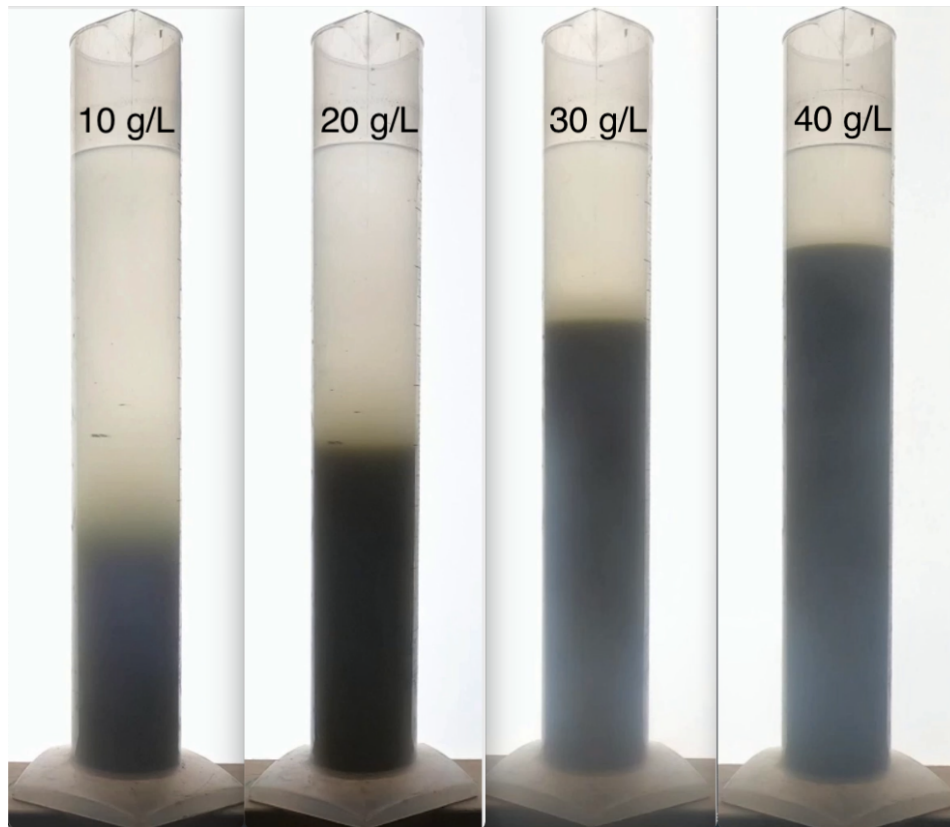
Table 4.2: Increased density water due to salinity

Hinder settlement is observed when the mass concentration of illite is increased; see fig 4.4. It shows a more clear boundary between the mixture and the water with increased mass concentration of illite as Winterwerp (2002) predicted. As told above will the settling velocities decline with increased concentrations of illite.

The kinematic viscosity was calculated with the Stokes equation for experiments with ten g/L of illite, see table 4.3. The Stokes equation is normally used to measure the settling velocity of 1 particle, but as hindered settlement takes place at sediment concentrations  $\geq 2\text{-}3 \text{ kg/m}^3$ , no hindered settlement was suspected. The viscosity of water at temperatures from experiments done should lie between  $1,028 \text{ mm}^2/\text{s}$  and  $1,067 \text{ mm}^2/\text{s}$ . This, however, is not the case because natural sediments consist of different particle sizes, which in turn will have mutual influence during settling. With particles descending in a fluid, it will have an inevitable slip velocity relative to the surrounding water velocity. Although the viscosity should not be three times lower, it should be 0.987 times lower compared to 1 particle settling according to the theory, see appendix A. The lower viscosity when salt is added can be because the particles form aggregates, and so the  $d_{50}$  increases, which lowers the viscosity.

Experiment	Viscosity [ $\text{mm}^2/\text{s}$ ]
0 mM	0,318
10 mM	0,144
100 mM	0,177

Table 4.3: Viscosity's experiments with 10 g/L of illite (1, 9 and 17)

Figure 4.4: Settling columns experiments,  $t = 50$  minutes.

As told, it was hard to get a homogeneous mixture of bentonite. It also did not behave consistently; see figure 4.5. No experiments have been done with bentonite from this point on.

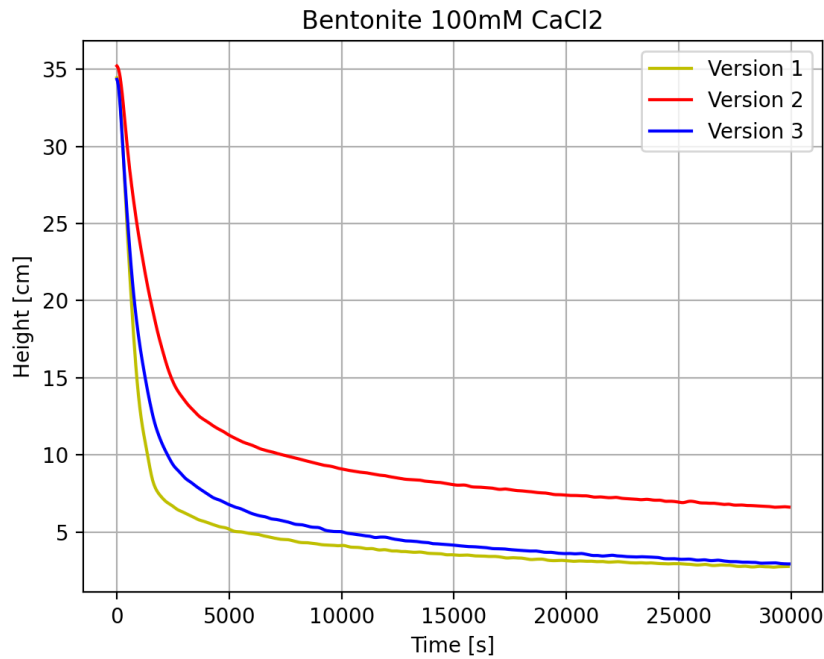


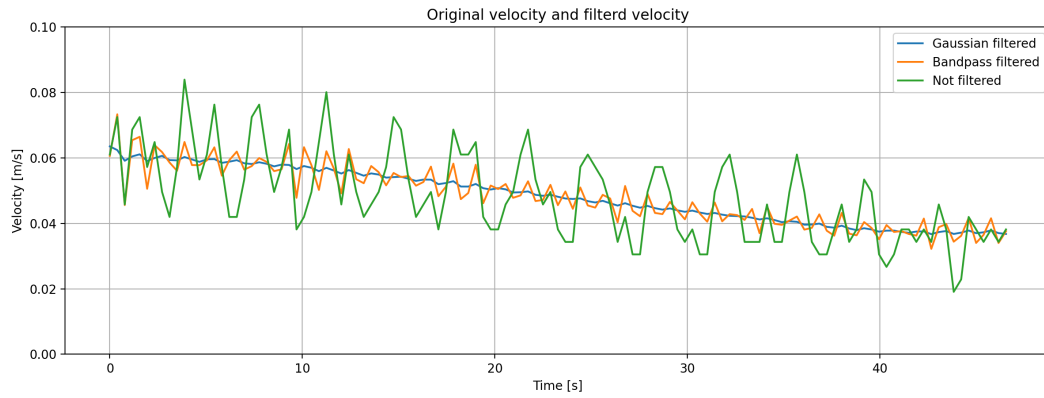
Figure 4.5: Comparison settling column experiments of 10 g/L of bentonite

## 4.2. Lock exchange experiments

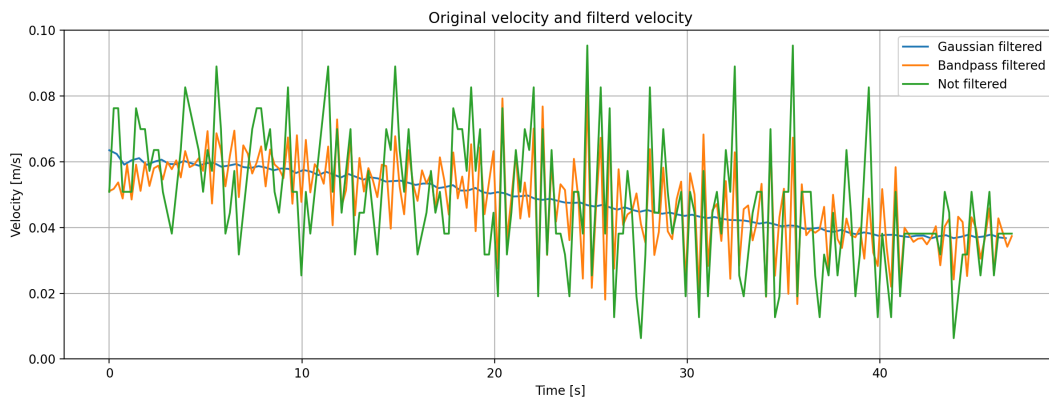
This section represents the results of all the lock exchange experiments and compares different experiments to each other. The driving force of a gravity current for the experiments is due to density difference. The bulk density of such a suspension may be greater than its surroundings, resulting in a gravity current. As stated in the introduction of Chapter 4 no mass profiles are made for the pre-existing beds, added flocculant, and the artificial CCZ clay. Experiments 1 up to 7 are used as a benchmark to compare other experiments.

### 4.2.1. Head velocities

The head velocity can be calculated with the script provided by Vasquez (2020). Depending on the concentration used, either 30 or 50 frames per measurement were used to track the head velocity. For all the experiments which used 10 up to 50 g/L of clay, 50 frames were chosen. As using fewer frames will give a cloudy result, see figure 4.6. These cloudy results result from the surface wave created when the lock gate opens to release the suspension into the outflow section. The used sampling frequency is showed in every upcoming table with details of the experiments. Vasquez (2020) filtered the velocities with a Chebychev bandpass filter type 2 with an extra filfilt function. An additional Gaussian filter type 1 is added to smooth out the spikes when comparisons need to be made.



(a) 50 Frames interval



(b) 30 Frames interval

Figure 4.6: Filtered velocity of experiment 1

Specific experiments were repeated to see if they were consistent. Figure 4.7 shows three repetitions of the first experiment. It shows that except for the first 5 seconds, the velocity profiles have the same characteristics. A very slight velocity difference is shown.

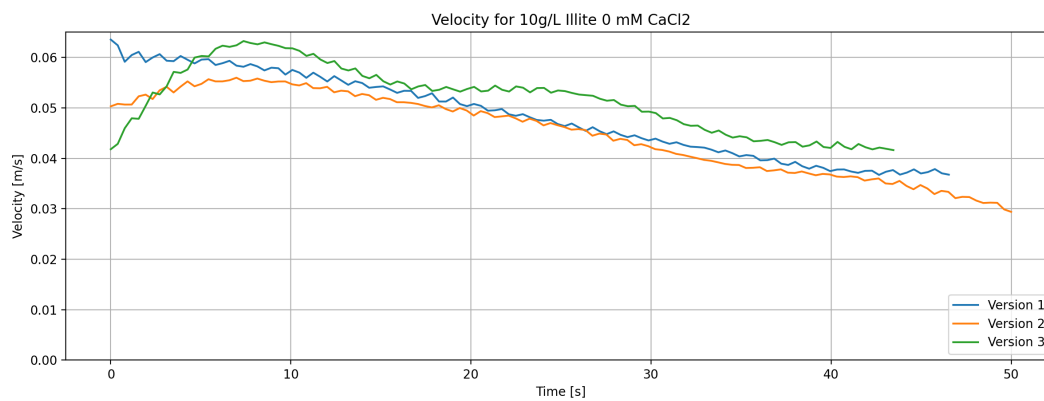
Figure 4.7: Comparison of head velocities for 10 g/L illite without added  $CaCl_2$ 

Table 4.4 shows the standard deviations from experiments 1 and 7. It shows that there is a difference when an experiment is repeated. This is due to multiple factors: (i) the fact that every experiment has a different temperature, (ii) gravity currents are stochastic.



Experiment	Times repeated	Standard deviation time to reach end [%]	Standard deviation max head velocity [%]
1	4	5	7
7	3	8	5

Table 4.4: Standard deviations for three experiments.

Table 4.5 shows the frames per measurement used for the head velocity. So, for example, for experiment 1, for every 50 frames, the head velocity is determined. Additionally, the temperature, the pH values, and the total dissolved salts are shown. An increase of pH is observed when the salinity goes from 0mM to 10mM  $CaCl_2$ . This is because a rise in salinity increases the pH. For 100 mM  $CaCl_2$ , the pH increase should be expected; however, this is not the case. As the temperature rises, molecular vibrations will increase. This results in the ability of water to ionize and form more hydrogen ions. As a result, the pH will drop.

#	Mass concentration illite [g/L]	Concentration $CaCl_2$ [mM]	Frames per measurement	Fs [Hz]	Temperature [° C]	pH	TDS [mg/L]
1	10	0	50	2,6	23,2	8,00	259
2	20	0	50	2,6	10,7	8,02	270
3	30	0	50	2,6	10,9	8,04	267
4	40	0	50	2,6	10,9	7,99	269
5	50	0	50	4,3	10,1	8,09	299
6	75	0	30	4,3	10,4	8,08	267
7	100	0	30	4,3	10,1	8,01	179
8	125	0	30	4,3	11,6	8,03	192
9	10	10	50	2,6	10,4	8,12	1538
10	20	10	50	2,6	9,4	8,00	1455
11	30	10	50	2,6	9,2	8,33	1535
12	40	10	50	2,6	9,1	8,32	1443
13	50	10	5	4,3	9,6	8,32	1476
14	75	10	30	4,3	10,7	8,31	1579
15	100	10	30	4,3	10,1	8,25	1622
16	125	10	30	4,3	11,0	8,24	1546
17	10	100	50	2,6	17,5	7,24	7205
18	20	100	50	2,6	17,3	7,74	5957
19	30	100	50	2,6	19,0	7,55	7059
20	40	100	50	2,6	19,1	7,60	7084
21	50	100	50	4,3	17,5	7,45	7106
22	75	100	30	4,3	16,3	7,19	7448
23	100	100	30	4,3	17,4	7,69	6237
24	125	100	30	4,3	16,7	7,23	7577

Table 4.6: Experimental details experiments 1 up to 24

The head velocity of all the mentioned experiments above is shown in figure 4.8. With an increase of sediment in the mixing section, a higher head velocity is created, as the theory predicted. When the head is formed, an increase in speed is shown in every experiment. The currents produced can be presented in two or even three phases. The first phase, the initial adjustment phase, starts when the lock is opened; here the density difference and height will create a current. This current will increase till it reaches its maximum velocity.

In the second phase, the self-similar phase, the head velocity will decline. The transition from the first to the second phase is observed to be rather abrupt. While the current spreads, particles fallout, and the adequate driving strength of the current, compared to a homogeneous current, decays as predicted by Ungarish (2009). Only currents with a mass concentration up to 30 g/L of illite show a constant speed after the second phase. None of the experiments experience the decrease in velocity Rottman and John Simpson (1983) described. It is more in the neighborhood of  $t^{-0.15}$ , when the  $t$  is measured from the maximum head velocity until it reaches a constant speed. All these experiments reached the end wall.

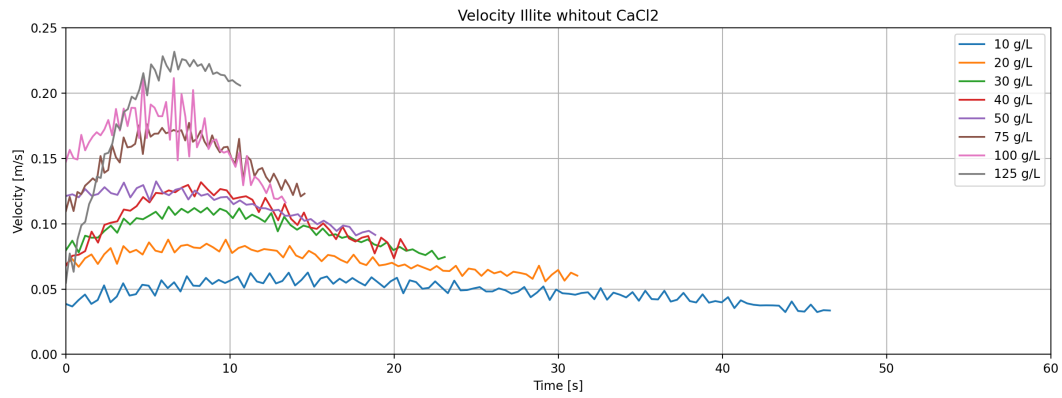
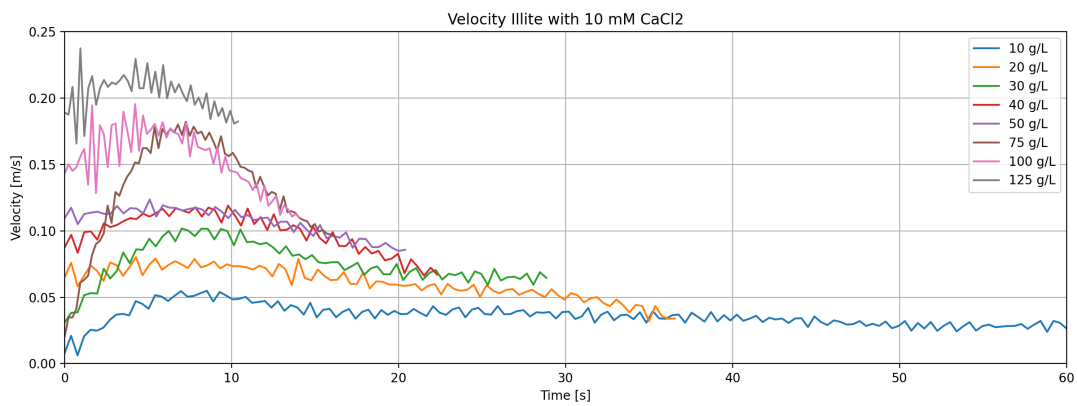
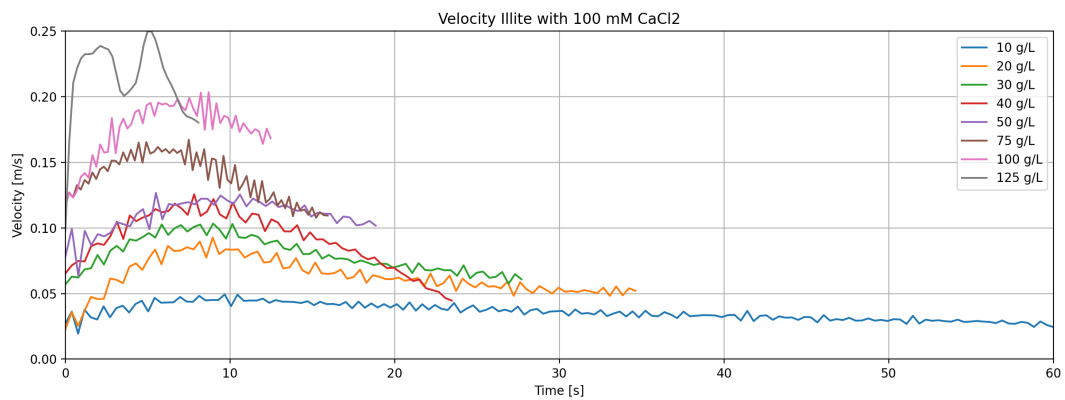
(a) Illite without  $CaCl_2$ . Experiments: 1 up to 8(b) Illite with 10 mM  $CaCl_2$ . Experiments: 9 up to 16(c) Illite with 100 mM  $CaCl_2$  Experiments: 17 up to 24

Figure 4.8: Head velocities experiment 1 up to 24

For comparison, the head velocities of 10, 50, and 100 g/L with different salinity were plotted in figure 4.9. For the low amount of clay, it shows that the head velocity is reduced when salt is added; this is in contradiction with Baker et al. (2017). With illite amounts of 50 and 100 g/L, there is no clear distinction about the difference in head velocity seen in figure 4.9. However, with the maximum speed and time to reach the end is determined, some things can be concluded, see table 4.7. The time to reach the end is always the lowest when no salt is added.

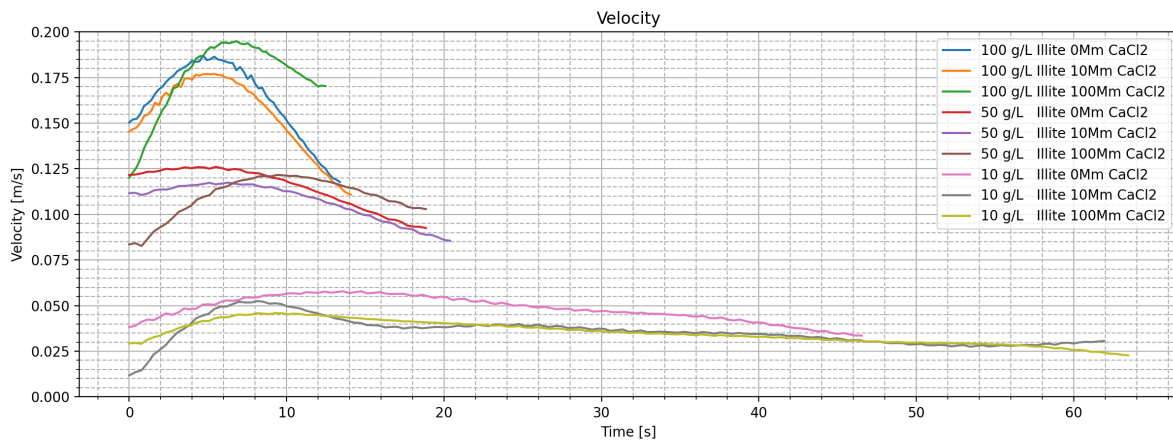


Figure 4.9: Head velocities experiments: 10, 50 and 100 g/L of illite with different salinity's

	0 mM		10 mM		100 mM	
	Time to reach end [s]	Max velocity [m/s]	Time to reach end [s]	Max velocity [m/s]	Time to reach end [s]	Max velocity [m/s]
10 g/L	46,9	0,055	62,7	0,052	63,9	0,046
20 g/L	31,4	0,083	36,7	0,075	34,9	0,085
30 g/L	23,5	0,111	29,1	0,100	27,7	0,100
40 g/L	21,2	0,127	22,5	0,115	23,5	0,117
50 g/L	18,8	0,126	20,5	0,117	19,2	0,121
75 g/L	14,7	0,171	16,2	0,176	15,9	0,160
100 g/L	13,4	0,187	14,0	0,177	12,6	0,195
125 g/L	10,6	0,224	10,4	0,216	11,0	0,250

Table 4.7: Comparison time to reach end and maximum head velocity of experiments 1 tm 24

The difference in density between the mixture in the mixing section and the water in the outflow section is of great importance when considering the behavior of the current. The densities are always higher in the mixing section as there the clay is added. The density differences between the mixing section and the outflow section are shown in 4.8. The table shows that with an increase of illite, the density difference increases. No significant difference is established between the densities created by the salinity.

	0 mM [kg/m <sup>3</sup> ]	10 mM [kg/m <sup>3</sup> ]	100 mM [kg/m <sup>3</sup> ]
10 g/L	6.4	6.4	6.3
20 g/L	12.7	12.7	12.6
30 g/L	19.0	19.1	19.0
40 g/L	25.5	25.4	25.3
50 g/L	31.8	31.8	31.6
75 g/L	47.7	47.7	47.4
100 g/L	63.6	63.6	63.2
125 g/L	79.5	79.5	79.0

Table 4.8: Density different mixing section with outflow section for illite

#### Additional experiments with pre-existing bed

Additional experiments were done to find out if a pre-existing bed influences the head velocity. Three possibilities of beds are compared: (a) no bed (experiments 1, 5, and 7), (b) a bed which is made 24 hours before, and (c) a bed which is made 48 hours before. The experimental details are shown in table 4.9.

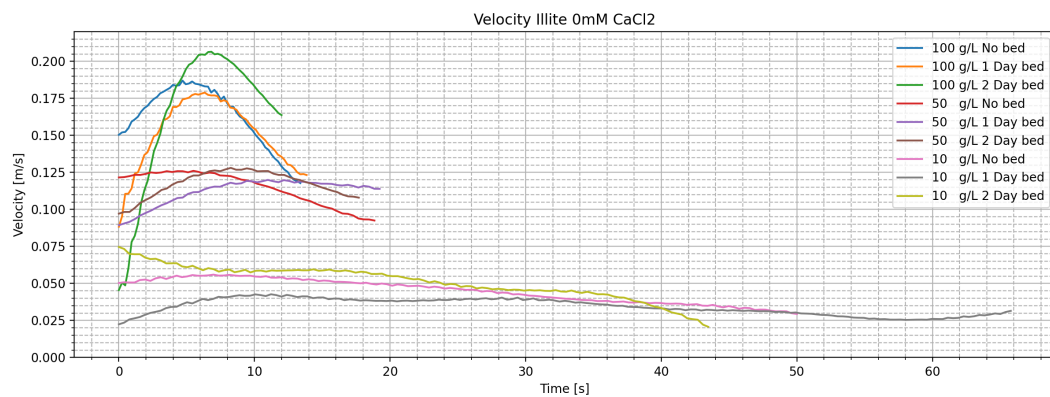
#	Mass concentration illite [g/L]	Concentration $CaCl_2$ [mM]	Frames per measurement	Fs [Hz]	Temperature [° C]	pH	TDS [mg/L]
25_1	10	0	50	2,6	15,2	8,00	273
25_2	10	0	50	2,6	18,4	7,89	274
26_1	50	0	50	4,3	16,3	8,01	265
26_2	50	0	50	4,3	17,5	7,92	278
27_1	100	0	30	4,3	16,4	7,78	231
27_2	100	0	30	4,3	18,7	7,91	282
28_1	10	10	50	2,6	16,5	8,27	1612
28_2	10	10	50	2,6	19,3	7,50	2071
29_1	50	10	50	4,3	23,8	7,78	1918
29_2	50	10	50	4,3	23,1	7,67	1577
30_1	100	10	30	4,3	18,0	7,65	1724
30_2	100	10	30	4,3	19,6	7,76	1538

Table 4.9: Experimental details pre-existing bed. With \_1 indicates 24 hours and \_2 indicates 48 hours.

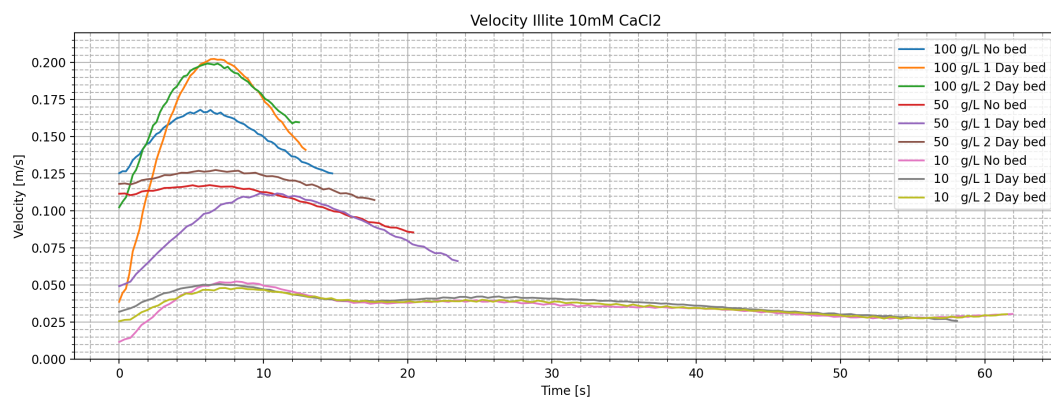
As Nogueira et al. (2013) noted that the roughness of the bed plays a vital role in the current kinematics, particularly in decreasing the front velocity due to extra drag at the bed. Increasing the bed roughness made the transition to the self-similar phase happen earlier.

Alternatively, sediment may be entrained if the current is passing sufficiently rapidly over an erodible bed, which increases the particle concentration and driving buoyancy force. Both the settling and entrainment rates depend on the velocity and dimensions of the gravity current. So there is a strong coupling between the sediment transport and the dynamics of the flow (Bonnetcaze et al., 1993).

Both cases are observed; see figure 4.10.



(a) Velocities 0 mM  $CaCl_2$  without a bed, with 1 day bed and with 2 day bed



(b) Velocities 10 mM  $CaCl_2$  without a bed, with 1 day bed and with 2 day bed

Figure 4.10: Head velocities of experiments with pre-existing bed

Table 4.10 shows the maximum velocities and time the current needed to reach the end of the video compared to experiments without salt and bed. It clearly shows an increase of time considering one-day beds, however with two-day beds; it is different. A gravity current moving over a two-day bed almost always indicates a decrease of time to reach the end. This is also clear regarding the maximum velocity. At a one-day bed, the maximum speed decreases in all cases, except for experiment 30. The maximum speed of the two-day beds are more incredible except for the experiment of 10 g/L of illite in a 10 mM two-day bed (experiment 28 – 2)

The initial concentration in the outflow section depends on the time the sediment had to settle. Figure 4.11 shows the initial transparency of the outflow section. There is more sediment in the outflow section at a one-day bed than the two-day bed, demonstrated by more white/ light blue areas, which corresponds with a shorter settling time.

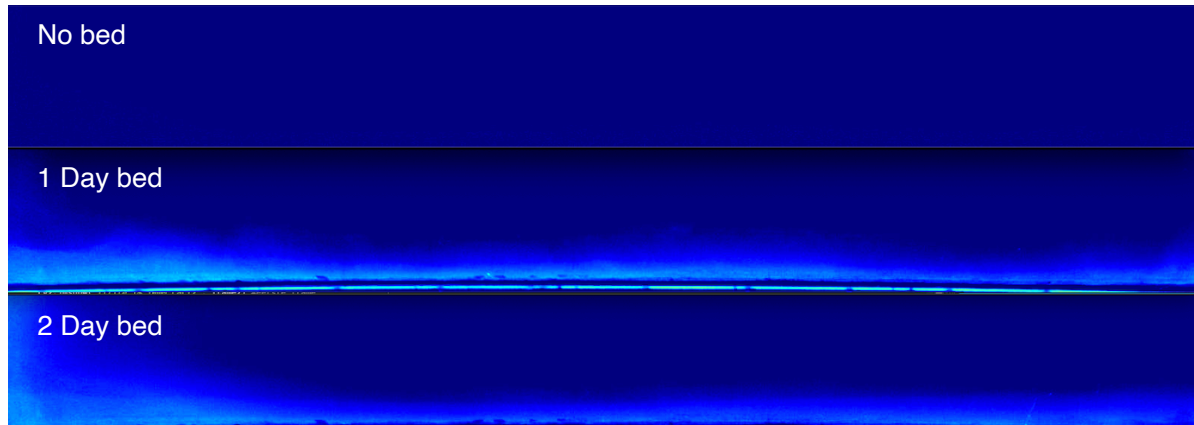


Figure 4.11: Initial transparency of illite in the tank before test is done

	0 mM		0 mM 1 day bed		0 mM 2 day bed	
	Time to reach end [s]	Max velocity [m/s]	Time to reach end [s]	Max velocity [m/s]	Time to reach end [s]	Max velocity [m/s]
10 g/L	46,9	0,058	66,5	0,042	44,1	0,074
50 g/L	18,8	0,126	19,5	0,120	18,0	0,128
100 g/L	13,4	0,187	14,4	0,179	12,1	0,206

	10 mM		10 mM 1 day bed		10 mM 2 day bed	
	Time to reach end [s]	Max velocity [m/s]	Time to reach end [s]	Max velocity [m/s]	Time to reach end [s]	Max velocity [m/s]
10 g/L	62,7	0,052	58,6	0,051	62,4	0,048
50 g/L	20,5	0,117	23,5	0,112	12,9	0,128
100 g/L	14,0	0,177	18,0	0,202	12,8	0,199

Table 4.10: Comparison time to reach end and maximum velocity of experiments 25 tm 30

#### Additional experiments with flocculant

Two kinds of experiments were done. One was mixing the flocculant with the mixture in the mixing section, and the second by mixing the flocculant in the outflow section. The experimental details are shown in 4.11

#	Mass concentration illite [g/L]	Concentration $CaCl_2$ [mM]	Frames per measurement	Fs [Hz]	Temperature [° C]	pH	TDS [mg/L]
31	10	0	50	2,6	13,7	7,84	259
32	100	0	30	4,3	11,8	8,01	255
33	10	0	50	2,6	23,1	7,83	195
34	100	0	30	4,3	23,1	7,83	195
35	10	0	50	2,6	22,0	8,23	211
36	100	0	30	4,3	22,0	8,19	196
37	10	0	50	2,6	22,0	8,32	202
38	100	0	30	4,3	22,0	8,27	200
39	10	10	50	2,6	22,0	8,02	1470
40	100	10	30	4,3	17,9	8,08	1458
41	10	10	50	2,6	22,0	8,13	1304
42	100	10	30	4,3	13,7	8,00	1777

Table 4.11: Experimental details experiments with flocculant.

From the six experiments where flocculant is added to the mixing section, only two reached the end of the camera visibility, see figure 4.12. All experiments with Zetag 4120 stop before 1.25 meters; when salt is added, it stops before 0.5 meters. As told in paragraph 3.4.2 Zetag 4120 is anionic. Due to the ions in the tap water, flocculation can occur.

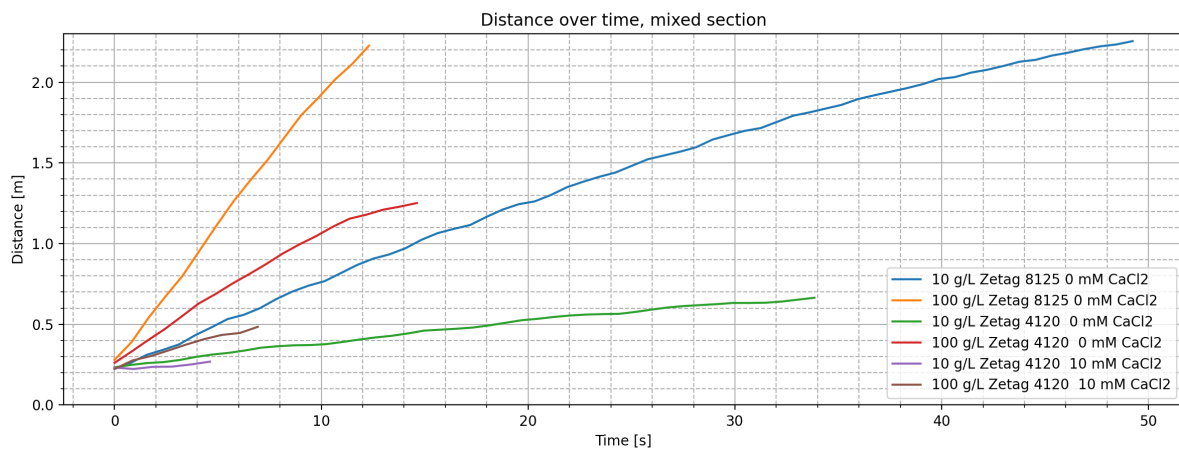
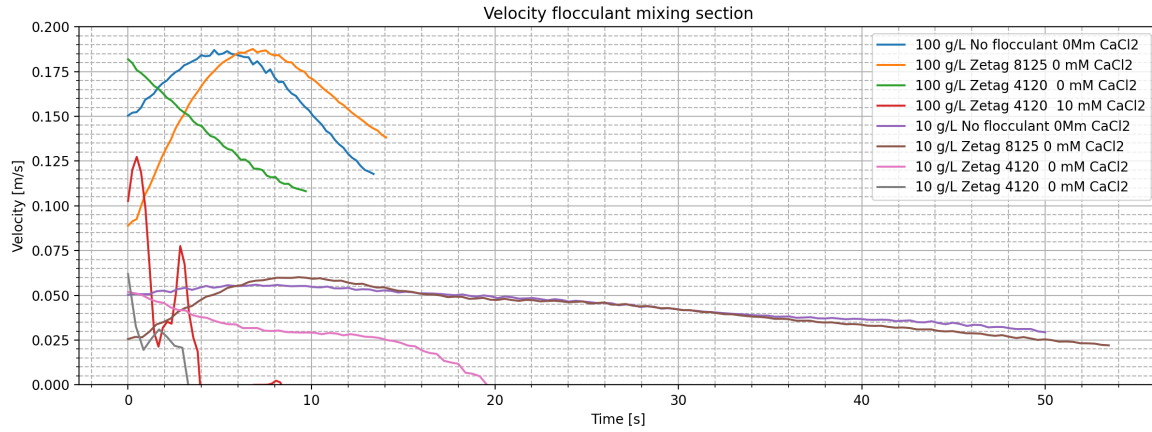


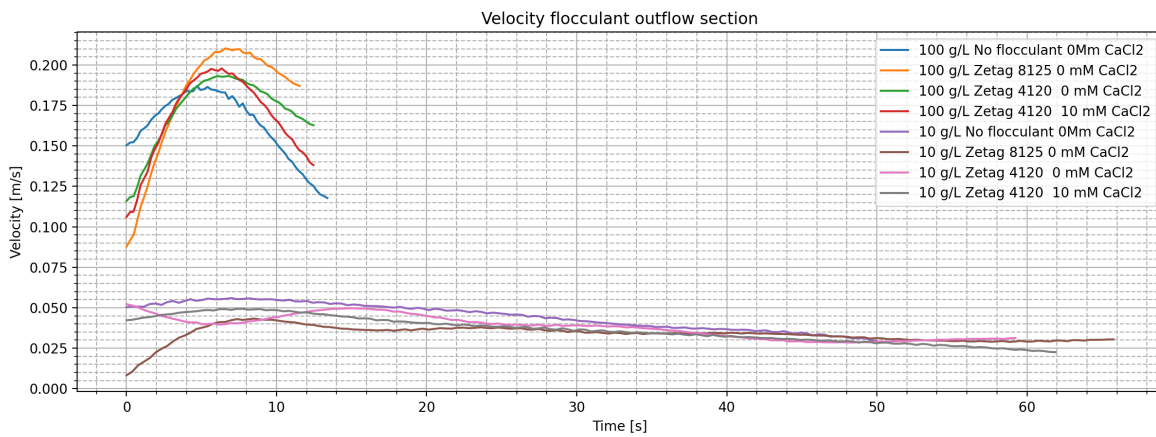
Figure 4.12: Distance travelled of the current created with flocculant mixed in the mixing section. Experiments: 33, 34, 35,36,39 and 40

All experiments done with mixing the flocculant in the outflow section result in currents that reach the end. The head velocities of the experiments, compared to the benchmark experiments, are shown in figure 4.13. Figure 4.13a shows no direct influence of flocculant regarding Zetag 8125. A big difference is shown when Zetag 4120 is used. A sharp decline in velocity is shown, which corresponds with the fact that the current not reaches the end, shown in figure 4.12. The experiments with Zetag 4120 in 10 mM  $CaCl_2$  are very slow and are influenced by the standing wave.

Figure 4.13b shows that with 100 g/L of illite, flocculant in all cases increases the head velocity. Experiments with 10 g/L show a decrease in head velocity when flocculant is added.



(a) Head velocities of flocculant mixed in the mixing section. Experiments: 7, 34, 36, 40, 1, 33, 35, 39



(b) Head velocities of flocculant mixed in the outflow section. Experiments: 7, 32, 38, 42, 1, 31, 37, 41

Figure 4.13: Head velocities of experiments with added flocculant

No essential differences were determined for Zetag 8125; see figure 4.13a this is indeed the case when we look at table 4.12. Only a longer time to reach the end is noticed and increases by a small amount. For Zetag 4120 0mM, it is remarkable that it has a semi-similar maximum velocity as it doesn't reach the end. Table 4.13 shows the outcomes of the flocculant mixed in the outflow section. It shows, as told, the decrease of maximum velocity for 10 g/L and an increase for 100 g/L. The time to reach the end was at all times greater when flocculant is added to 10 g/L of Illite. The time it took to reach the end of the 100 g/L experiments declined with added flocculant.

	0 mM		0 mM Zetag 8125		0 mM Zetag 4120		10 mM Zetag 4120	
	Time to reach end [s]	Max velocity [m/s]	Time to reach end [s]	Max velocity [m/s]	Time to reach end [s]	Max velocity [m/s]	Time to reach end [s]	Max velocity [m/s]
10 g/L	46,9	0,058	53,8	0,060	-	0,052	-	0,062
100 g/L	13,4	0,187	14,2	0,187	-	0,182	-	0,127

Table 4.12: Comparison time to reach end and maximum velocity of mixed in mixing section



	0 mM		0 mM Zetag 8125		0 mM Zetag 4120		10 mM Zetag 4120	
	Time to reach end [s]	Max velocity [m/s]	Time to reach end [s]	Max velocity [m/s]	Time to reach end [s]	Max velocity [m/s]	Time to reach end [s]	Max velocity [m/s]
10 g/L	46,9	0,058	66,0	0,044	59,3	0,052	62,2	0,049
100 g/L	13,4	0,187	11,6	0,210	12,4	0,193	12,5	0,198

Table 4.13: Comparison time to reach end and maximum velocity of mixed in outflow section

#### Additional experiments with artificial Clarion Clipperton zone clay

To make sure the experiments were not too idealized, experiments were done with artificial CCZ sediment. Six experiments were done to see if the head velocity and time to reach the end are comparable with the experiments above. Table 4.14 show the experimental details.

#	Mass concentration mixture [g/L]	Concentration CaCl <sub>2</sub> [mM]	Frames per measurement	Fs [Hz]	Temperature [° C]	pH	TDS [mg/L]
43	10	0	50	2,6	14,0	8,12	243
44	50	0	50	4,3	16,2	8,01	197
45	100	0	30	4,3	17,9	7,98	215
46	10	10	50	2,6	18,2	7,65	1986
47	50	10	50	4,3	18,4	7,84	1764
48	100	10	30	4,3	18,2	7,71	1842

Table 4.14: Experimental details CCZ sediment

Two experiments with CCZ sediment also did not reach the end. The distance the currents travelled are shown in figure 4.14. It shows similar behaviours for sediment with and without added salt.

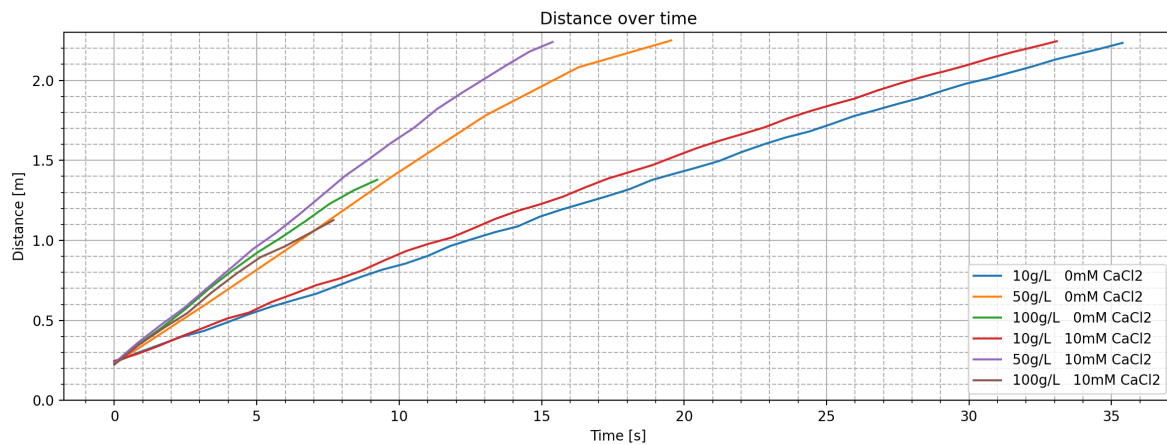


Figure 4.14: Distance travelled of the current with CCZ sediment. Experiment: 43, 44, 45, 46, 47 and 48.

The head velocities are shown in figure 4.15. The head velocities of 10 g/L show a slight increase in head velocity when salt is added. The 50 g/L experiments show a more significant increase in head velocity compared to 50 g/L of illite without salt. It reaches even higher than the 100 g/L experiments.



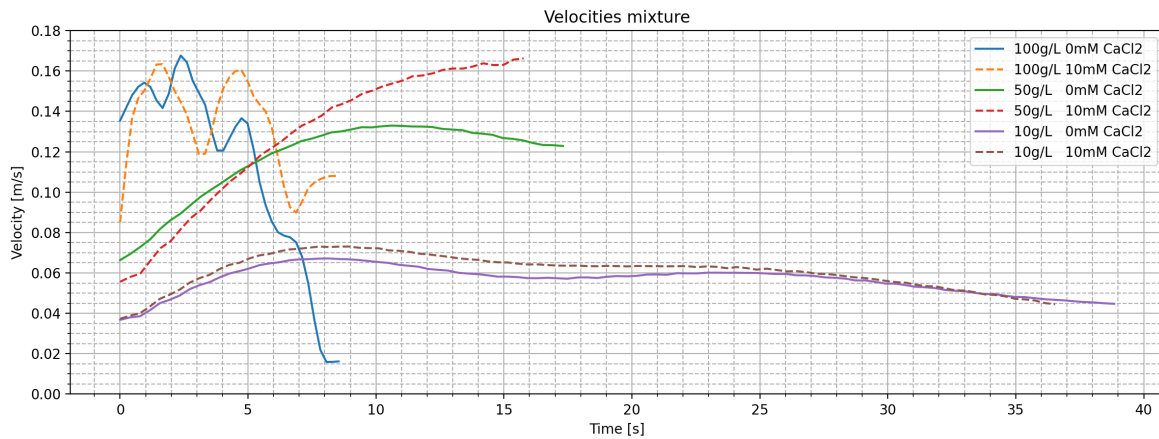


Figure 4.15: Head velocities of artificial CCZ mixture

The maximum velocity and time to reach the end are shown in graph 4.15. It shows, as stated before, with added salt, higher head velocities are found compared to no added salt for 10 and 50 g/L. The head velocities of 100 g/L are similar. The time to reach the end for 10 g/L and 50 g/L is lower for the added salt.

	0 mM		10 mM	
	Time to reach end [s]	Max velocity [m/s]	Time to reach end [s]	Max velocity [m/s]
10 g/L	39,3	0,067	36,7	0,073
50 g/L	17,5	0,132	16,2	0,166
100 g/L	-	0,167	-	0,163

Table 4.15: Comparison time to reach end and maximum velocity of the CCZ sediment

The density differences between with and without  $CaCl_2$  are shown in table 4.16. It shows that there is no significant difference observed when comparing experiments with no salt and added salt.

	0 mM	10 mM
10 g/L	4.3	4.3
50 g/L	21.4	21.4
100 g/L	42.8	42.9

Table 4.16: Density different mixing section with outflow section for artificial CCZ clay

### Froude number

The densimetric Froude number is calculated for each experiment. All the experiments run with illite have a densimetric Froude number below 0.8, which means a sub-critical flow; see appendix C for the plots. For experiments with artificial CCZ sediment, the Froude number is higher; see figure 4.16. This is especially the case for experiment 46, where 10g/L of artificial CCZ sediment is run with 10 mM  $CaCl_2$  added to the water. This experiment has, as noted above, a much faster head velocity than comparable illite experiments, which influences the densimetric Froude number. At some point, it nearly reaches 1, which is the point the flow gets in critical condition.

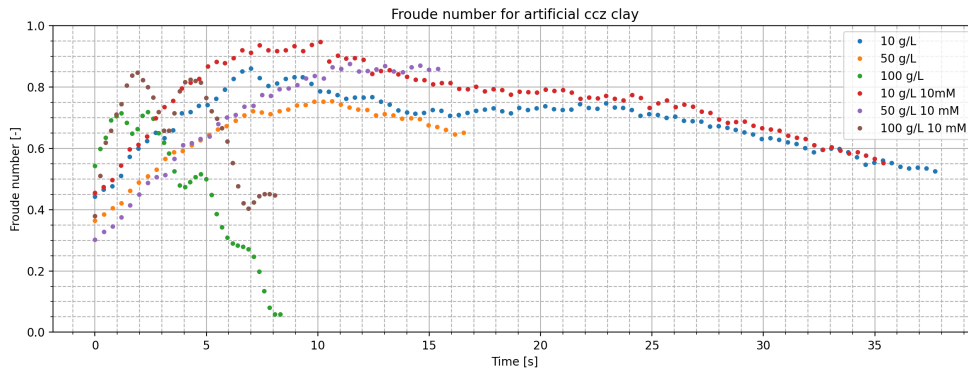


Figure 4.16: Densimetric Froude number experiments with artificial CCZ sediment. Exp 43 up to 48.

### Summary of the Illite results

The following two pages show tables, table 4.17 and table 4.19, with all the illite experiments combined. Underneath these tables are tables 4.18 and 4.20, which compare the experiments with 0 mM added  $CaCl_2$ . Standard deviations were only executed for experiments with 10 and 100 g/L of illite. The mean values of experiments 1 and 7 are shown in these tables to make better comparisons.

Table 4.18 shows in almost all cases an increase of time to reach the end for the low mass concentrations of added  $CaCl_2$ . Increasing the mass concentration results in experiments that are most of the time inside the standard deviation, which makes it hard to say something about. Table 4.20 shows the comparison of the maximum head velocities. Most of the time, there is a decrease in velocity observed for low concentrations. Increasing the concentration shows experiments in the standard deviation zone. Note: only 10 g/L and 100 g/L had multiple experiments to calculate the standard deviation.

	0 mM	10 mM	100 mM	0 mM 1 day bed	0 mM 2 day bed	10 mM 1 day bed	10 mM 2 day bed	Zetag 8125 mixing section	Zetag 8125 outflow section	Zetag 4124 mixing section 0 mM	Zetag 4124 outflow section 0 mM	Zetag 4124 mixing section 10 mM	Zetag 4124 outflow section 10 mM
10 g/L	46,9	62,7	63,9	66,5	44,1	58,6	62,4	53,8	66,0	-	59,3	-	62,2
20 g/L	31,4	36,7	34,9										
30 g/L	23,5	29,1	27,7										
40 g/L	21,2	22,5	23,5										
50 g/L	18,8	20,5	19,2	19,5	18,0	23,5	18,0						
75 g/L	14,7	16,2	15,9										
100 g/L	13,4	14,0	12,6	14,4	12,1	12,9	12,8	14,2	11,6	-	12,4	-	12,5
125 g/L	10,6	10,4	11,0										

Table 4.17: Time to reach end [s]

	0 mM	10 mM	100 mM	0 mM 1 day bed	0 mM 2 day bed	10 mM 1 day bed	10 mM 2 day bed	Zetag 8125 mixing section	Zetag 8125 outflow section	Zetag 4124 mixing section 0 mM	Zetag 4124 outflow section 0 mM	Zetag 4124 mixing section 10 mM	Zetag 4124 outflow section 10 mM
10 g/L	bm	+34%	+36%	+42%	-6%	+25%	+33%	+14%	+41%	+∞%	+26%	+∞%	+33%
20 g/L	bm	+17%	+11%										
30 g/L	bm	+24%	+18%										
40 g/L	bm	+6%	+11%										
50 g/L	bm	+9%	+2%	+4%	-4%	+25%	-4%						
75 g/L	bm	+10%	+8%										
100 g/L	bm	+4%	-6%	+7%	-10%	-4%	-4%	+6%	-13%	+∞%	-7%	+∞%	-7%
125 g/L	bm	-2%	+4%										

Table 4.18: Time to reach end, compared with benchmark settings of 0 mM  $CaCl_2$ . Green: positive effect on plume dispersion, red: negative effect on dispersion, yellow: undecided effect as it lays in the standard deviation zone.

	0 mM	10 mM	100 mM	0 mM 1 day bed	0 mM 2 day bed	10 mM 1 day bed	10 mM 2 day bed	Zetag 8125 mixing section	Zetag 8125 outflow section	Zetag 4124 mixing section 0 mM	Zetag 4124 outflow section 0 mM	Zetag 4124 mixing section 10 mM	Zetag 4124 outflow section 10 mM
10 g/L	0,058	0,052	0,046	0,043	0,075	0,051	0,048	0,060	0,043	0,052	0,052	0,062	0,049
20 g/L	0,083	0,075	0,085										
30 g/L	0,111	0,100	0,100										
40 g/L	0,127	0,115	0,117										
50 g/L	0,126	0,117	0,121	0,120	0,128	0,112	0,128						
75 g/L	0,171	0,176	0,160										
100 g/L	0,187	0,177	0,195	0,179	0,206	0,202	0,199	0,188	0,210	0,182	0,193	0,127	0,198
125 g/L	0,224	0,216	0,250										

Table 4.19: Maximum head velocities illite [m/s]

	0 mM	10 mM	100 mM	0 mM 1 day bed	0 mM 2 day bed	10 mM 1 day bed	10 mM 2 day bed	Zetag 8125 mixing section	Zetag 8125 outflow section	Zetag 4124 mixing section 0 mM	Zetag 4124 outflow section 0 mM	Zetag 4124 mixing section 10 mM	Zetag 4124 outflow section 10 mM
10 g/L	bm	-10%	-21%	-26%	+30%	-12%	-17%	+3%	-26%	-10%	-10%	+7%	-16%
20 g/L	bm	-10%	+2%										
30 g/L	bm	-10%	-10%										
40 g/L	bm	-9%	-8%										
50 g/L	bm	-7%	-4%	-5%	+2%	-11%	+2%						
75 g/L	bm	+3%	-6%										
100 g/L	bm	-5%	+4%	-4%	+10%	+8%	+6%	+1%	+13%	-3%	+3%	-32%	+6%
125 g/L	bm	-4%	+12%										

Table 4.20: Maximum head velocities illite, compared with benchmark settings of 0 mM  $CaCl_2$ . Green: positive effect on plume dispersion, red: negative effect on plume dispersion, yellow: undecided effect as it lays in the standard deviation zone.

### 4.2.2. Mass calculation

The mass can be calculated for experiments one till 24 as three calibration curves were made for illite for the different salinities. The mass values in this paragraph give a misleading impression as they only show the minimum mass in the current, as told in paragraph 3.5. The current is cut into five sections to determine the mass per part. This is done to see if there are differences in the head, the body, and the tail of the current. The five parts are shown in figure 4.17. The mass will only be calculated with the head visible. So part 5 will have less time to be measured than four and so on. The darker the red will indicate a higher mass concentration than the green and green. The dark blue is zero mass.

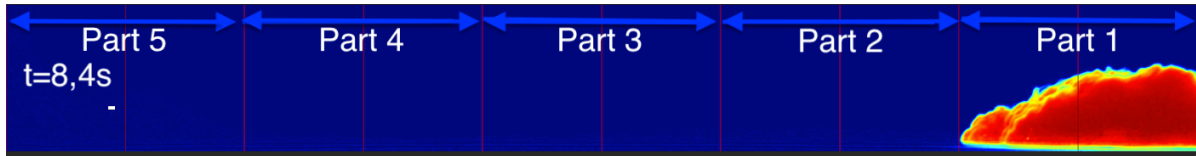


Figure 4.17: Velocities of flocculant mixed in the outflow section

The additional experiments have no mass calculations; however, it is possible to visually say something about the experiments. I only investigated 10, 50, and 100 g/L of illite in this paragraph.

Figure 4.18 shows the mass distribution in the whole stream. It shows that there is a big difference in mass when for mass concentrations of 10 g/L.

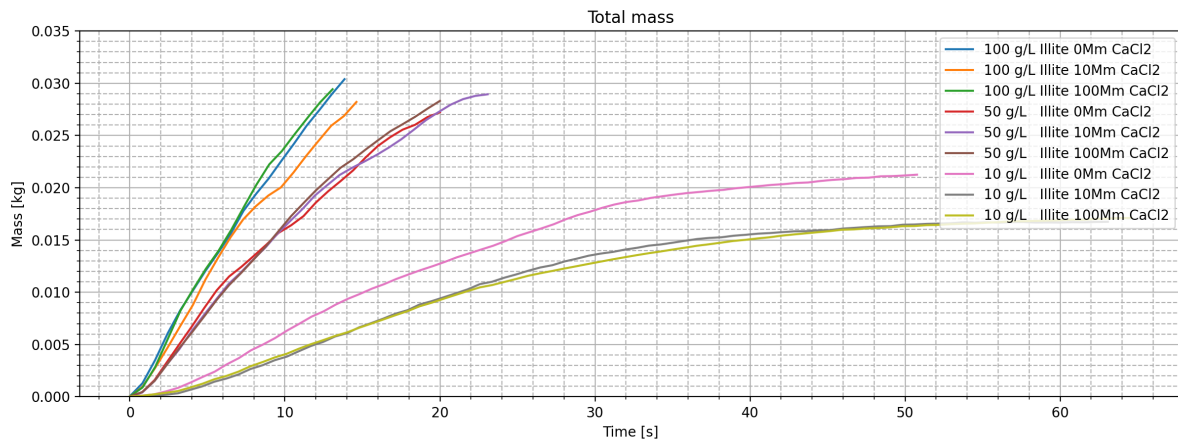


Figure 4.18: Results for mass measurement

The big difference can be derived from figure 4.19. It shows the color map made of the current reaching the end. The heads of the currents show a similar image. The body and the tail show significant differences. Less Kelvin-Helmholtz instabilities are shown with added  $CaCl_2$  compared to without added  $CaCl_2$ . The biggest differences are shown in part1, part 2, and part 3.

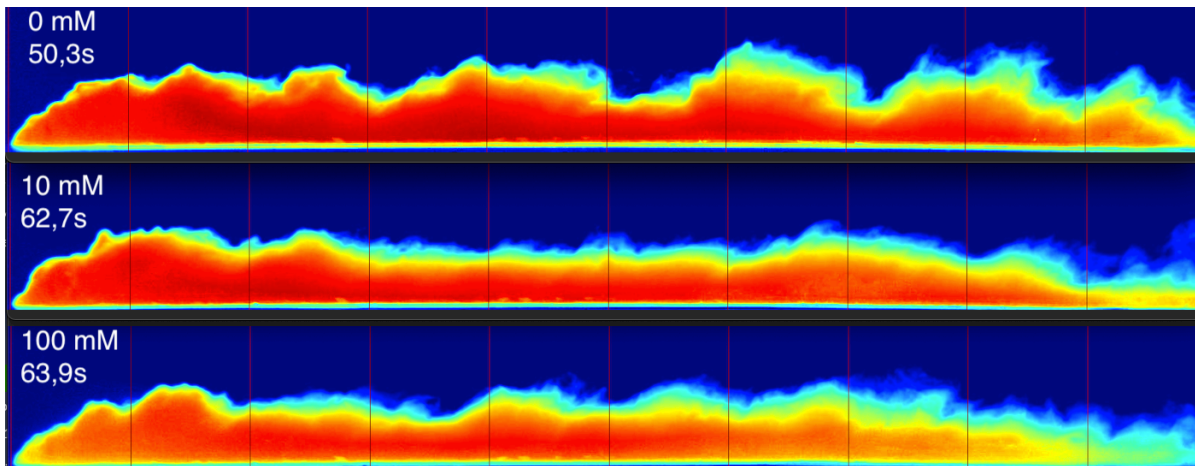


Figure 4.19: Color maps of 10 g/L. Exp 1, 9 and 17.

Figure 4.20 shows the mass for the first three sections for 10 g/L and 50 g/L. For the 50 g/L, not much can be concluded, however for 10 g/L; it can. For all three parts, there is a higher peak of mass visible when no  $\text{CaCl}_2$  is added, as also shown in the color map above, which means that there is more mass in the head, which explains the higher head velocity. In part 1, from 20 to 40 seconds, the mass of 10 mM is higher than 0 mM. In part two, from 30 seconds, 100 mM has more mass than 0 mM.

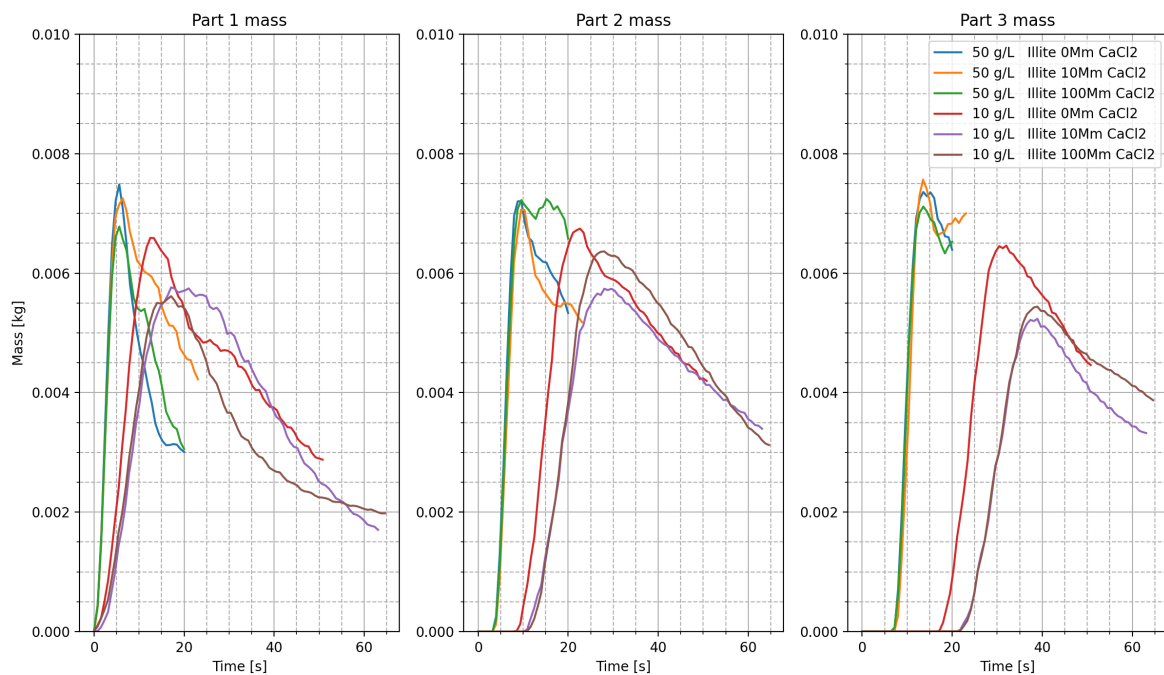


Figure 4.20: Mass in 3 parts for 10 and 50 g/L with different salinity's

#### Additional experiments with pre-existing bed

The experiments with a pre-existing bed are not conclusive. As figure 4.21 shows, there are a lot of color fluctuations in the current. This is because first, the initial picture is subtracted to filter out imperfections for making the color maps. When for example, figure 4.11 is subtracted, there is a big difference if you subtract a picture without a bed or with a bed. These images can only give shape differences. The color maps are misleading as the pre-existing bed is subtracted.



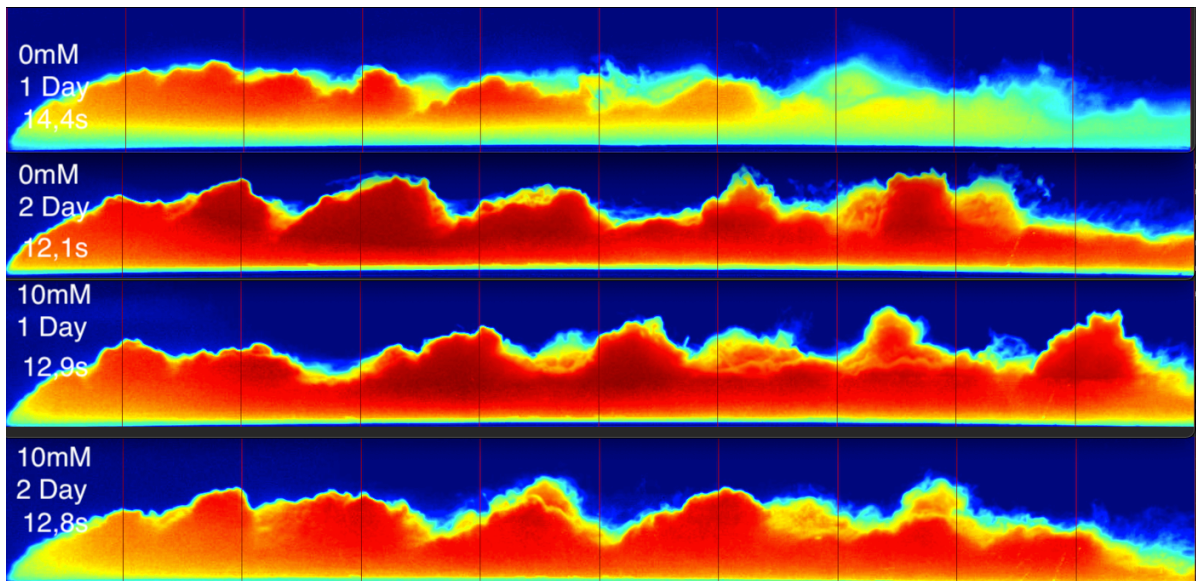


Figure 4.21: Color maps of 100 g/L with pre-existing beds. Exp 27, exp 27-2, exp 30 and exp 30-2

#### Additional experiments with flocculant

No calibration curve was made for flocculant, as it has a very different effect on clay than salt. These experiments are compared to the benchmark experiments 1 & 7.

Figure 4.22 shows the comparison of experiment 1 with the experiments done with flocculant and 10 g/L of illite. Significant differences are visible in the tail and the body of the current. Experiments 31 and 41 are already settled in the tail. Experiment 31 also shows a much earlier start of the body compared to the others.

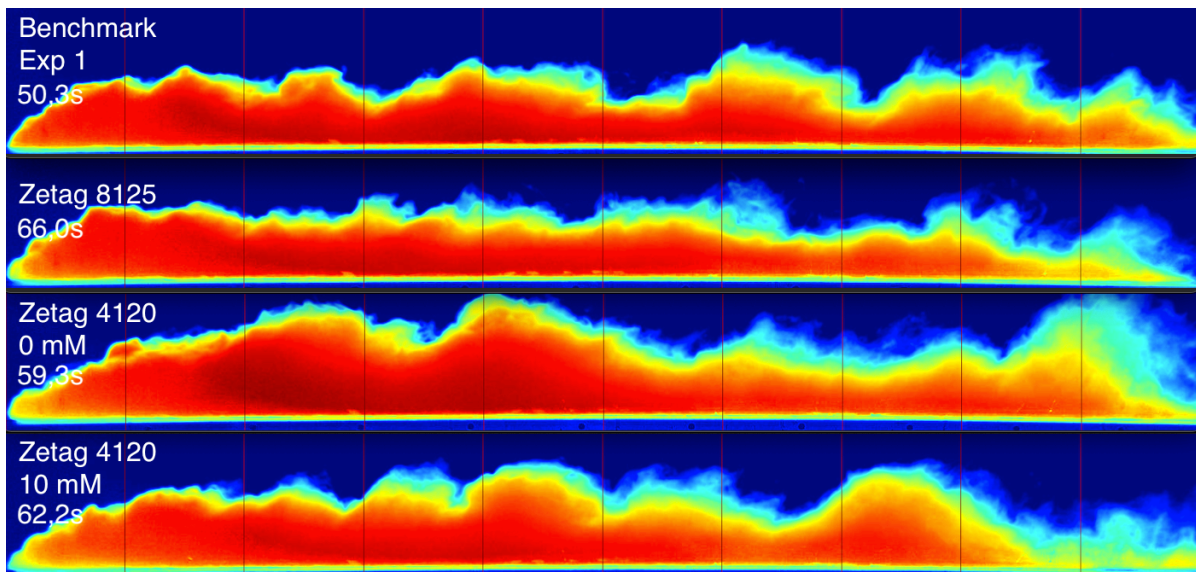


Figure 4.22: Color maps of 10 g/L illite mixed in outflow section. Exp 1, exp 31, exp 37 and exp 41

Figure 4.23 shows experiments with 100 g/L of illite with flocculant mixed in the outflow section. Much more minor differences are shown in these color maps. The benchmark experiments show darker colours.

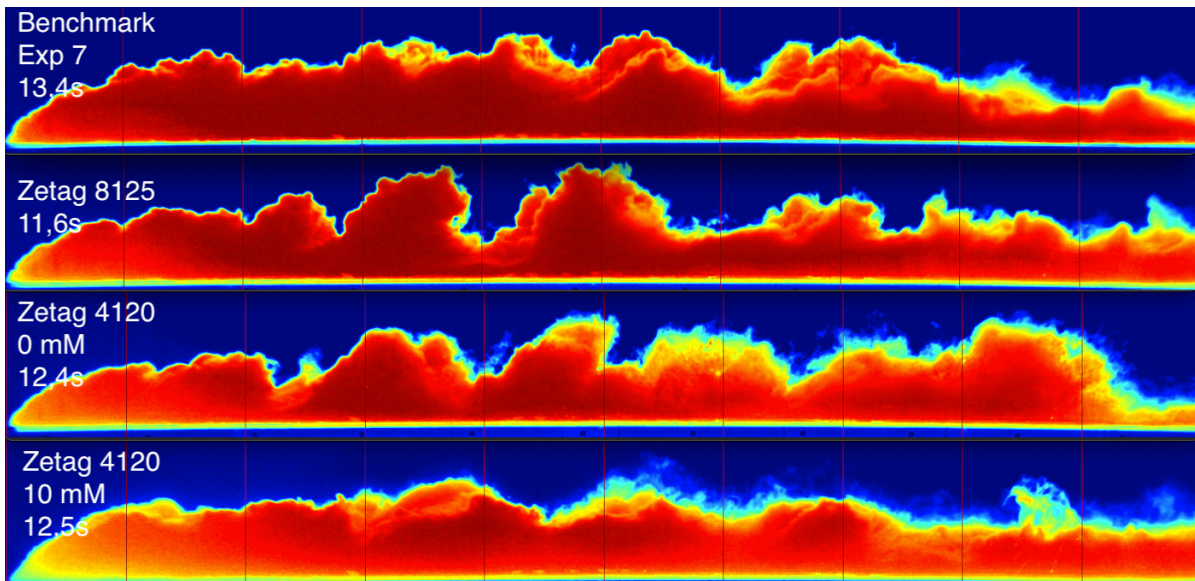


Figure 4.23: Color maps of 100 g/L illite mixed in outflow section. Exp 7, exp 32, exp 38 and exp 42

The color maps of the mixing of flocculant on the mixing section are shown in figure 4.24 and figure 4.25. For the 10 g/L of illite, it shows clearly the effect to multiple extents the effect. Zetag 8125 has a more minor impact than Zetag 4120. Zetag 4120 flocculates directly and is already partly settled in the mixing section.

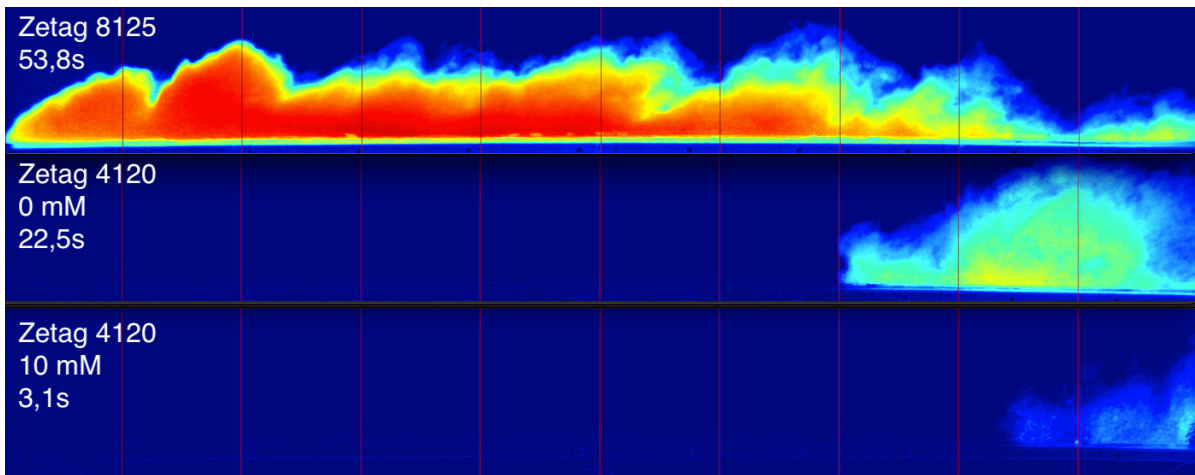


Figure 4.24: Color maps of 10 g/L illite mixed in mixing section. Exp 33, exp 35 and exp 39

When the illite is increased to 100 g/L, there is still a big difference. Again Zetag 4120 has a more significant effect on flocculation than Zetag 8125. In the color map from experiment 36, there are large flocs shown.



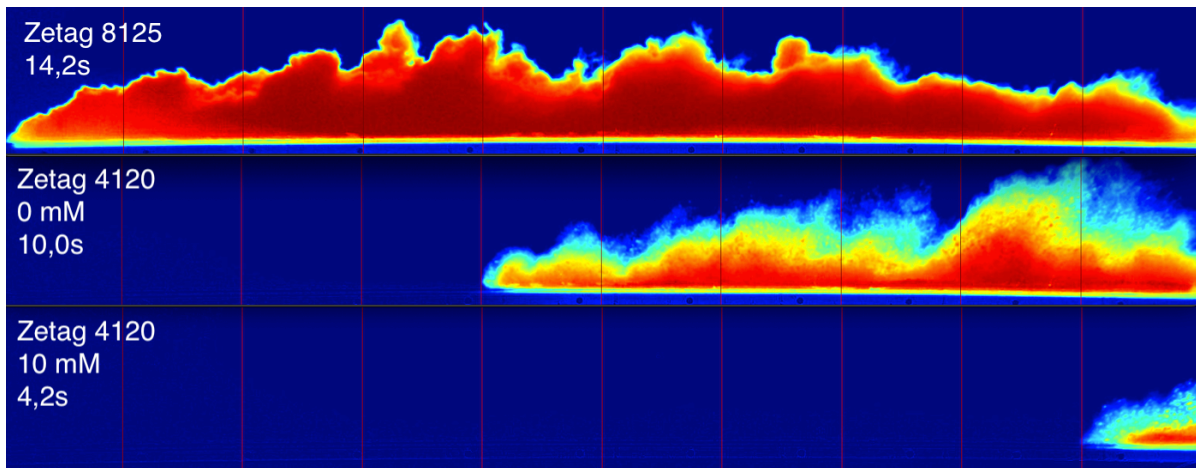


Figure 4.25: Color maps of 100 g/L illite mixed in mixing section. Exp 34, exp 36 and exp 40

#### Additional experiments with artificial Clarion Clipperton zone clay

Again no calibration curve was made for the CCZ clay as this a very time-consuming process. An earlier start of the tail is noticed for the experiments with 10 and 50 g/L, figures 4.26 and 4.27. The big difference is shown with 100 g/L, see 4.28. These are the last parts they reach. Experiment 48 has had a significant influence by  $CaCl_2$  as compared with experiment 45. More minor Kelvin-Helmholtz instabilities are shown for 10 g/L of artificial CCZ sediment compared to illite.

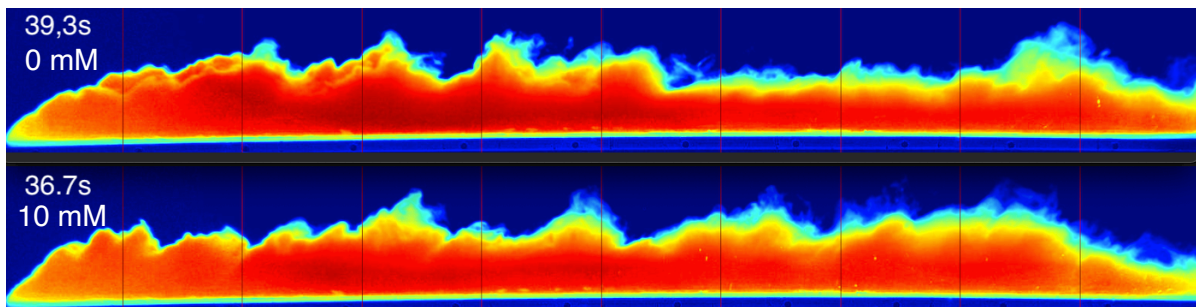


Figure 4.26: Color maps of 10 g/L artificial clay. Exp 43 and exp 46

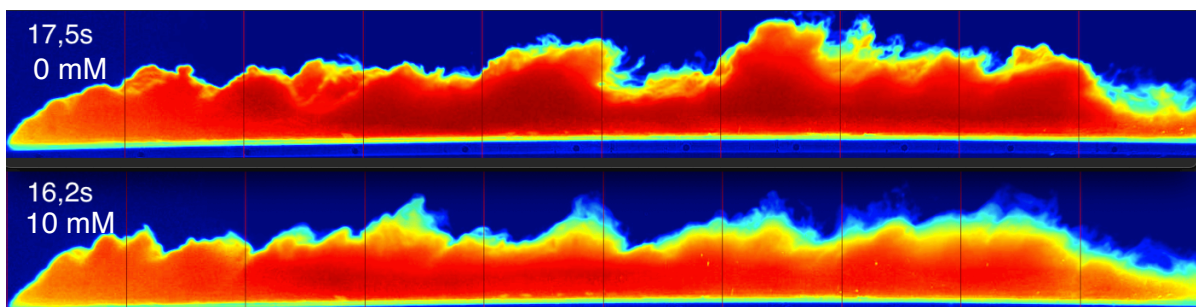


Figure 4.27: Color maps of 50 g/L artificial clay. Exp 44 and exp 47

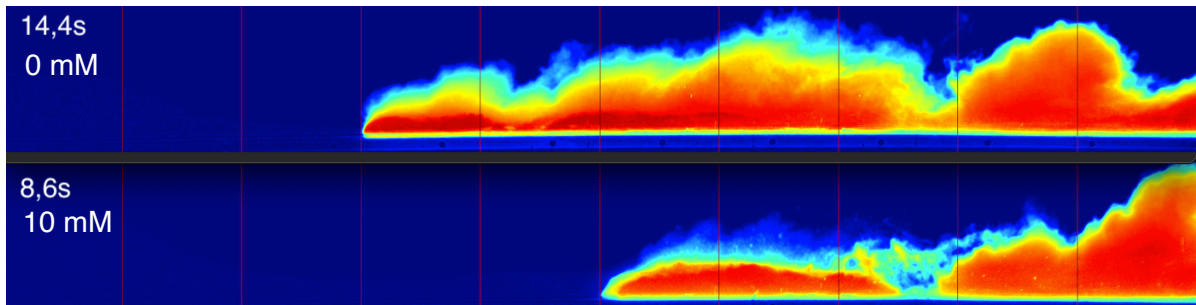


Figure 4.28: Color maps of 100 g/L artificial clay. Exp 45 and exp 48

The last two experiments, 45 and 48, both experiments with 100g/L of CCZ mixture, behave in different ways than all experiments with illite. They show no to weak internal turbulence in the head; see figure 4.29.

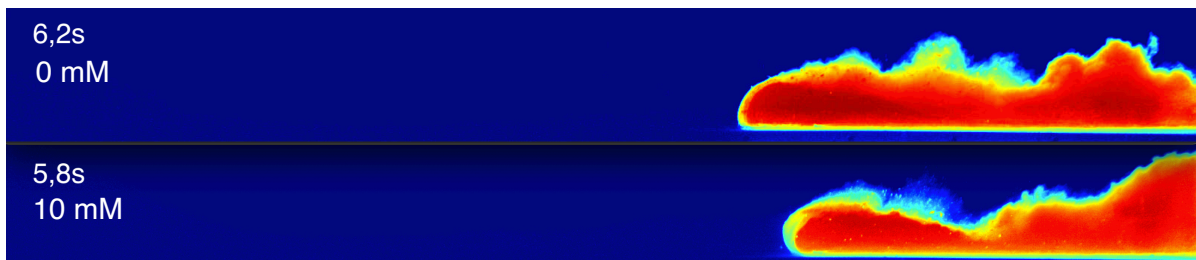


Figure 4.29: Color maps of 100 g/L artificial clay. Exp 45 and exp 48

## 4.3. Discussion

### 4.3.1. Settling column experiments

The settling column shows that with the addition of  $CaCl_2$ , flocculation is induced up to a point of 75 g/L of illite. From this point, hindered settlement prevails over flocculation. Flocculation plays a significant role when the sediment concentration is increased as Winterwerp (2002) predicted. There is a big difference in the way the illite settles. When investigating the difference of settling velocity between 10 mM and 100 mM, I found marked differences, especially for 10 and 20 g/L of illite. As stated in chapter 3, the 100 mM would not dissolve entirely, and undissolved particles of  $CaCl_2$  will be floating in the cylinder. These extra particles will contribute to the hindered settling and so decrease the settling velocity of these experiments.

As the density difference between illite and water declines when salt is added, the settling velocity should also decline with increasing salinity. However, this is not shown due to the effect that the density difference was not significant as shown in table 4.8.

### 4.3.2. Lock exchange experiments

Lock exchange experiments develop more head velocity when more clay is added due to a higher density difference in the mixing section and the outflow section. Flocculation is also induced in lock exchange experiments by adding  $CaCl_2$  in contradiction with what Baker et al. (2017) told. The flocculation is most visible at low mass concentrations of illite. The head velocities decline with added  $CaCl_2$ , and a decrease in mass is observed. The mass declines the most for parts one up to part three, the body and the tail. It shows that flocculation is happening the furthest from the head, which is in agreement with what Spearman et al. (2020) and Gillard et al. (2019) predicted. No density differences are shown, so the less head velocity should be due to the effect of clay forming by aggregation, which will slow down the head velocity.

#### Additional experiments with pre-existing bed

As Nogueira et al. (2013) noted is shown in the experiments with a one-day bed, the bed is not entirely settled. This makes for horizontal hindered settlement, which reduces the head velocity, especially for low mass concentrations of illite.

For experiments with a bed of two days, a decrease in head velocity is observed; this is due to the effects mentioned by Bonneau et al. (1993). The current is passing sufficiently rapidly over an erodible bed. Sediment may be entrained, which increases the particle concentration and driving buoyancy force. Only experiment 28-2, 10 g/L of illite with 10 mM of  $CaCl_2$  on a two-day bed, does not behave as predicted; this can be an erroneous experiment, or 25-2 can be inaccurate. It is impossible to say if the current is moving fast enough; it is hard to say which one is erroneous.

#### Additional experiments with flocculant

Adding flocculant to either the mixing section or the outflow section will induce flocculation. When flocculant is added to the outflow section, a similar effect can be shown with added  $CaCl_2$  for low mass concentrations of illite. The time to reach the end increases, and the mass visually decreases in part 1. Looked at higher mass concentrations of illite, the time to reach the end decreases, but just very slightly and sits inside the standard deviation zone. Comparing the color maps shows a reduction of high concentrations of mass as the image becomes lighter from color. No difference is shown in the behavior of the current compared to the benchmark experiment.

With flocculant added to the mixing section, different effects are shown. The time to reach the end is only given for Zetag 8125, as Zetag 4120 never reaches the end. Remarkable differences are shown when looked at the color maps. Zetag 4120 with added  $CaCl_2$  doesn't even reach part 2. The flocculation effect is very evident. When mixed in the lock, clay particles already start to aggregate and will form large flocks. When the lock is opened, the current almost immediately settles.

#### Additional experiments with artificial Clarion Clipperton zone clay

Experiments with artificial CCZ clay lead, in contradiction with the theory odd effects and show that the experiments with illite are strongly idealized. The current is much faster than the same mass concentration of illite for mass concentrations of 10 g/L, which corresponds with Marr et al. (2001). The current consists partially out of bentonite, which is strongly coherent between 7 and 50 g/L as the grains are held fixed within the fine-grained matrix.

The Froude number reaching just under one indicates that the experiments with mass concentrations of

10g/L are near-critical conditions, which means that the flow velocity is equal to the speed generated by a disturbance. This disturbance can be the opening of the lock. This will also explain high head velocities of the low concentrations, where they were not expected. With adding salt to these experiments, the time to reach the end decreases, which is also not comparable to the illite experiments. The experiments with mass concentrations of 50 g/L need a little less time to reach the end but differ not much.

With mass concentrations of 100g/L of the CCZ clay, the current doesn't reach the end. The experiment with added  $CaCl_2$  shows similar behavior to with added salt and settles faster. This all can be due to the effect that this is a mixture of bentonite. The greater cohesive strength of bentonite producing flows with a significantly higher molecular viscosity and yield stress than illite flows. The currents seem to show no internal turbulence in the head, which was also demonstrated by Baker et al. (2017), but this was for volume concentration of bentonite of  $18\% \leq C \leq 19\%$ . This could be due to the effect of gelling, where flow deceleration by gelling exceeds flow acceleration by density difference, but Baker et al. (2017) only experienced this at volume concentrations of  $C \geq 10\%$ . However, Winterwerp (2002) showed that gelling effects of cohesive sediment could take place at sediment concentration  $\geq 40$  g/L, which explains the gelling at a concentration of 100g/L.

# 5

## Conclusion and recommendations

### 5.1. Conclusions

- Experiments with illite with mass concentrations between 10 and 75 g/L, in  $CaCl_2$  water solution, show an increase in time before the end of the tank is reached. The maximum head velocity shows a decrease in almost all these experiments, except for 20g/L of illite, in which case, 100 mM  $CaCl_2$  is added to the water and 75 g/L of illite which case 10 mM  $CaCl_2$  is added to the water. This all can be ascribed to flocculation as there are no density differences and the height of the water column stayed the same. Adding  $CaCl_2$  to 10 and 20 g/L of illite visually shows flocculation in the tails of currents as the mass decreases. The most significant decline in plume scatter is observed for currents with 10 g/L of illite.
- Running illite mixture currents over preexisting beds made of illite gives different results when looked at when the bed had to settle. With a bed, which had 24-hours to settle, an increase is shown when the current reached the end, except for the experiment where 100 g/L of illite is run, in which case 10 mM  $CaCl_2$  is added to the water.  
With a bed, which had 48-hours to settle, different observations are made. The time the current reaches the end is decreased at all times.
- Adding additives as a flocculant in the outflow section shows a decrease of head velocity and an increase of settlement in the tail for 10 g/L of illite. Adding 100 g/L of illite shows an increase of head velocity, no change in shape is shown compared to experiments without flocculant.  
Adding additives as a flocculant in the mixing section show a decrease of head velocity and an increase of time to reach the end, for Zetag 8125. It also shows a lot of settling in the tail of the current. When adding Zetag 4120, the plume will almost immediately settle when leaving the mixing section. The effect is more significant when this experiment is performed in water with added salt.  
When looked at 100 g/L of illite, the time to reach the end is also increased, but no conclusion can be made on flocculation. Zetag 4120 flocculates a lot and settles before the end is reached. The effect is more prominent when this experiment is performed in water with added salt.
- The outcomes of experiments with illite are not comparable with CCZ sediment. The artificial CCZ clay for mass concentrations of 10 g/L give much higher head velocities and decrease in time to reach the end, compared to similar mass concentrations of illite. Experiments with 100 g/L of artificial CCZ clay undergo gelling, which was not shown with the illite experiments. With added salt, the stream settles earlier than without added salt.  
To minimize the plume dispersion created by deep-sea mining, a concentration between the 50 and 100 g/L of artificial CCZ sediment should be ideal. Gelling will occur and will increase the settling time.
- The speed of the current fluctuates over the traveled trajectory to the end. The maximum velocity does not dominate the time needed to reach the end of the tank.

## 5.2. Recommendations

- Experiments should be performed with genuine CCZ sediment, as artificial CCZ sediment already showed marked differences compared to illite. It would be interesting to find out with which concentration the gelling effect starts.
- A wide-angle lens should be better appropriate to film the tank to ensure the hole tank is visible underneath the dark cloth.
- There should be investigated at what influence opening the lock has, the opening procedure should be standardized because the opening differs each time. Opening the lock creates a surface wave which affects the measurements. Standardizing the process with actuators will fix this variable.
- Experiments can be done with a reduced height of the water column so that every experiment settles before the back wall is reached. The Froude number can be extracted and compared with these experiments to see if they are consistent. Also, samples can be removed and sieved to find out the particle size distribution in the tank.
- Experiments can be done with different concentrations of flocculant to see what the effect is. The results now for Zetag 4120 in the mixing section are extreme; it would be nice to have control over the flocculation. Floccs can be extracted using a pipette to not hinder the flow and measure the floc sizes.
- a further analyses technique should be used; the used method is not sufficient to measure the volume concentration above 0.015. The used analyses give a misleading image of the mass profiles as the calibration technique is based on light permeability. The mass profiles now only show the minimum of mass inside the current.
- Experiments with sediment with organic material should be done. This can then be compared with the experiments with flocculant. Using Zetag 4120 and Zetag 8125 will probably never be used in the deep-sea environment.
- Experiments can be done in a different setup, where the current can also disperse to the side.
- All experiments should be done multiple times, to see which standard deviation is expected for all concentrations.

# References

- Altinakar, M, W Graf, and E Hopfinger (1996). "Flow structure in turbidity currents". In: *Journal of Hydraulic Research* 34.5, pp. 713–718. ISSN: 00221686. DOI: 10.1080/00221689609498467.
- Atkinson, John (2007). *The mechanics of soils and foundations*. London ; Taylor & Francis, xxxi, 442 pages : ISBN: 9780415362566.
- Baas, Jaco, James Best, and Jeff Peakall (2016). "Comparing the transitional behaviour of kaolinite and bentonite suspension flows". In: *Earth Surface Processes and Landforms* 41.13, pp. 1911–1921. ISSN: 10969837. DOI: 10.1002/esp.3959.
- Baker, Megan, Jaco Baas, Jonathan Malarkey, Ricardo Silva Jacinto, Melissa Craig, Ian Kane, and Simon Barker (2017). "The Effect of Clay Type On the Properties of Cohesive Sediment Gravity Flows and Their Deposits". In: *Journal of Sedimentary Research* 87.11, pp. 1176–1195. ISSN: 1527-1404. DOI: 10.2110/jsr.2017.63.
- Benjamin, T (1968). "Gravity currents and related phenomena". In: *Journal of Fluid Mechanics* 31.2, pp. 209–248. ISSN: 14697645. DOI: 10.1017/S0022112068000133.
- Best, J, A Kirkbride, and J Peakall (Mar. 2009). "Mean Flow and Turbulence Structure of Sediment-Laden Gravity Currents: New Insights using Ultrasonic Doppler Velocity Profiling". In: *Particulate Gravity Currents*. Blackwell Publishing Ltd., pp. 157–172. DOI: 10.1002/9781444304275.ch12.
- Bischoff, J, R Heath, and M Leinen (1979). *Geochemistry of Deep-Sea Sediments from the Pacific Manganese Nodule Province: DOMES Sites A, B, and C*. January 2016, pp. 397–436. ISBN: 9781468435184. DOI: 10.1007/978-1-4684-3518-4{\\_}12.
- Bonnecaze, R, Huppert E, and J Lister (1993). "Particle-driven gravity currents". In: pp. 339–369.
- Brandt, M, M Johnson, E Andrew, and D Ratnayaka (2015). "Twort's Water Supply". In: 4, pp. 155–159. DOI: 10.1016/B978-0-12-814348-3.00010-1.
- Buckee, C, B Kneller, and J Peakall (2001). *Turbulence structure in steady, solute-driven gravity currents*.
- Buhler, J, S Wright, and Y Kim (2016). "Gravity currents advancing into a coflowing fluid". In: July. DOI: 10.1080/00221689109499007.
- Burban, P, W Lick, and J Lick (1989). "The flocculation of fine-grained sediments in estuarine waters". In: *Journal of Geophysical Research* 94.C6, pp. 8323–8330. ISSN: 0148-0227. DOI: 10.1029/JC094iC06p08323.
- Camenen, B and D van Bang (2011). "Modelling the settling of suspended sediments for concentrations close to the gelling concentration". In: *Continental Shelf Research* 31.10 SUPPL. Pp. 106–116. ISSN: 02784343.
- Chassagne, C, F Mietta, and J Winterwerp (2009). "Electrokinetic study of kaolinite suspensions". In: *Journal of Colloid and Interface Science* 336.1, pp. 352–359. ISSN: 00219797. DOI: 10.1016/j.jcis.2009.02.052.
- Chikita, K (1990). "Sedimentation by river-induced turbidity currents: field measurements and interpretation". In: *Sedimentology* 37.5, pp. 891–905. ISSN: 13653091. DOI: 10.1111/j.1365-3091.1990.tb01832.x.
- D'Alessio, S, T Moodie, J Pascal, and G Swaters (1996). "Gravity currents produced by sudden release of a fixed volume of heavy fluid". In: *Studies in Applied Mathematics* 96.4, pp. 359–385. ISSN: 00222526. DOI: 10.1002/sapm1996964359.
- Dankers, P (2006). *On the hindered settling of suspensions of mud and mud-sand mixtures*, p. 112. ISBN: 9789090210117.
- Dankers, P and J Winterwerp (2007). "Hindered settling of mud flocs: Theory and validation". In: *Continental Shelf Research* 27.14, pp. 1893–1907. ISSN: 02784343. DOI: 10.1016/j.csr.2007.03.005.
- Drake, DE (1967). "Suspended sediment transport and mud deposition on continental shelves". In: *Wiley New York*.
- Eisma, D (1986). "Flocculation and de-flocculation of suspended matter in estuaries". In: *Netherlands Journal of Sea Research* 20.2-3, pp. 183–199. ISSN: 00777579. DOI: 10.1016/0077-7579(86)90041-4.
- Elerian, Mohamed, Rudy Helmons, and Cees Van Rhee (n.d.). "Near-field analysis of turbidity flows generated by seafloor mining tools". In: ().
- Ellison, T and J Turner (1959). "Turbulent entrainment in stratified flows". In: *Journal of Fluid Mechanics* 6.3, pp. 423–448. ISSN: 14697645. DOI: 10.1017/S0022112059000738.

- Federal Ministry for Economic Affairs and BGR Energy (2018). “Environmental Impact Assessment for the testing of a pre-prototype manganese nodule collector vehicle in the Eastern German licence area (Clarion-Clipperton Zone) in the framework of the European JPI-O MiningImpact 2 research project.” In: p. 204.
- Ferguson, R and M Church (2004). “A simple universal equation for grain settling velocity”. In: *Journal of Sedimentary Research* 74.6, pp. 933–937. ISSN: 15271404. DOI: 10.1306/051204740933.
- GarcôÃa, M (1993). “Hydraulic jumps in sediment-driven bottom currents”. In: 119.10, pp. 1094–1117.
- (1994). “Depositional turbidity currents laden with poorly sorted sediment”. In: 120.11, pp. 1240–1263.
- Gillard, Benjamin (2019). “Towards Deep Sea Mining – Impact of mining activities on benthic pelagic coupling in the Clarion Clipperton Fracture Zone Dissertation”. In: July.
- Gillard, Benjamin, Kaveh Purkiani, Damianos Chatzievangelou, Annemiek Vink, Morten H Iversen, and Laurenz Thomsen (2019). “Physical and hydrodynamic properties of deep sea mining-generated, abyssal sediment plumes in the Clarion Clipperton Fracture Zone (eastern-central Pacific)”. In: DOI: 10.1525/elementa.343.
- Gladstone, C, J Phillips, and R Sparks (1998). “Experiments on bidisperse, constant-volume gravity currents: Propagation and sediment deposition”. In: *Sedimentology* 45.5, pp. 833–843. ISSN: 00370746. DOI: 10.1046/j.1365-3091.1998.00189.x.
- Glover, Adrian, C Smith, G Paterson, G Wilson, L Hawkins, and M Shearer (2002). “Polychaete species diversity in the central Pacific abyss: Local and regional patterns, and relationships with productivity”. In: *Marine Ecology Progress Series* 240, pp. 157–170. ISSN: 01718630. DOI: 10.3354/meps240157.
- Gollner, Sabine, Stefanie Kaiser, Lena Menzel, Daniel Jones, Alastair Brown, Nelia C. Mestre, Dick van Oevelen, Lenaick Menot, Ana Colaço, Miquel Canals, Daphne Cuvelier, Jennifer Durden, Andrey Gebruk, Great A. Egho, Matthias Haeckel, Yann Marcon, Lisa Mevenkamp, Telmo Morato, Christopher Pham, Autun Purser, Anna Sanchez-Vidal, Ann Vanreusel, Annemiek Vink, and Pedro Martinez Arbizu (2017). “Resilience of benthic deep-sea fauna to mining activities”. In: *Marine Environmental Research* 129, pp. 76–101. ISSN: 18790291. DOI: 10.1016/j.marenvres.2017.04.010.
- Gonda, Ryoko, Masashi Tomoda, Noriko Shimizu, and Mieko Kanari (1990). *Characterization of Polysaccharides Having Activity on the Reticuloendothelial System from the Rhizome of Curcuma longa*. Vol. 38. 2, pp. 482–486. ISBN: 9789279479373. DOI: 10.1248/cpb.38.482.
- GSR (2007). “Environmental Impact Assessment”. In: pp. 1–19.
- (2018). “Environmental impact statement”. In: *Nuclear Plant Journal* 18.1. ISSN: 08922055. DOI: 10.1007/978-3-642-79940-2\_{\\_}11.
- Halbach, P and R Fellerer (1980). “The metallic minerals of the Pacific Seafloor”. In: *GeoJournal* 4.5, pp. 407–421. ISSN: 03432521. DOI: 10.1007/BF01795925.
- Hamilton, K (1997). “Gravity currents in the environment and the laboratory”. In: *Eos, Transactions American Geophysical Union* 79.6, pp. 71–71. ISSN: 0096-3941. DOI: 10.1029/98eo00052.
- Hein, James, Andrea Koschinsky, and Thomas Kuhn (2020). “Deep-ocean polymetallic nodules as a resource for critical materials”. In: *Nature Reviews Earth & Environment* 1.3, pp. 158–169. ISSN: 2662-138X. DOI: 10.1038/s43017-020-0027-0.
- Helmons, Rudy (2019). “Development and Testing of a Hydraulic Nodule Collector while minimizing its Environmental Impact, Preliminary Results of Discharge Experiments (Blue Harvesting project)”. In: Sanya, China.
- Hillel, Daniel (2003). “Introduction to Environmental Soil Physics”. In:
- Hiscott, R, K Pickering, A Bouma, B Hand, B Kneller, G Postma, and W Soh (Apr. 1997). “Basin-Floor Fans in the North Sea: Sequence Stratigraphic Models vs. Sedimentary Facies: Discussion”. In: *AAPG Bulletin* 81 (1997).4, pp. 662–665. ISSN: 0149-1423. DOI: 10.1306/522b4401-1727-11d7-8645000102c1865d.
- Huppert, H and J Simpson (1980). “The slumping of gravity currents”. In: *Journal of Fluid Mechanics* 99.4, pp. 785–799. ISSN: 14697645. DOI: 10.1017/S0022112080000894.
- International Seabed Authority (2014). “Decision of the Assembly of the International Seabed Authority Relating to the Regulations on Prospecting and Exploration for Polymetallic Nodules in the Area (Isba/6/A/18, the “Mining Code”) (suppl.)” In: *United Nations Convention on the Law of the Sea* 40403.July, pp. 115–166. DOI: 10.1163/ej.laos\_{\\_}9789004215634\_{\\_}115-166.
- Jiménez, José and Ole Madsen (2004). “Closure to “simple formula to estimate settling velocity of natural sediments””. In: *Journal of Waterway, Port, Coastal and Ocean Engineering* 130.4, pp. 220–221. ISSN: 0733950X. DOI: 10.1061/(ASCE)0733-950X(2004)130:4(220).
- Keulegan, G (1957). *Thirteenth progress report on model laws for density currents : an experimental study of the motion of saline water from locks into fresh water channels*.



- Kneller, Ben (1995). "Beyond the turbidite paradigm: Physical models for deposition of turbidites and their implications for reservoir prediction". In: *Geological Society Special Publication* 94.94, pp. 31–49. ISSN: 03058719. DOI: 10.1144/GSL.SP.1995.094.01.04.
- Kneller, Ben and Clare Buckee (2000). "The structure and fluid mechanics of turbidity currents: A review of some recent studies and their geological implications". In: *Sedimentology* 47.SUPPL. 1, pp. 62–94. ISSN: 00370746. DOI: 10.1046/j.1365-3091.2000.047s1062.x.
- Kneller, C, Sean Bennett, and William Mccaffrey (1999). "in Experimental Gravity Currents". In: *Velocity structure, turbulence and fluid stresses in experimental gravity currents* 104.1998, pp. 5381–5391.
- Kooistra, A, P.N.W. Verhoef, W Broere, D.J.M. Ngan-Tillard, and A.F. van Tol (1998). "Appraisal of Stickiness of Natural Clays From Laboratory Tests". In: *Engineering Geology and Infrastructure* April 2014, pp. 101–113.
- Koschinsky, Andrea, Ulrich Fritsche, and Andreas Winkler (2001). "Sequential leaching of Peru Basin surface sediment for the assessment of aged and fresh heavy metal associations and mobility". In: *Deep-Sea Research Part II: Topical Studies in Oceanography* 48.17-18, pp. 3683–3699. ISSN: 09670645. DOI: 10.1016/S0967-0645(01)00062-5.
- Krone, R B (1963). "A study of rheologic properties of estuarial sediments". In: September, pp. 1–41.
- Kuenen, H (1951). "Properties of Turbidity Currents of High Density". In:
- Kuhn, T, A Wegorzewski, C Rühlemann, and A Vink (2017). *Deep-sea mining: Resource potential, technical and environmental considerations*, pp. 1–535. ISBN: 9783319525570. DOI: 10.1007/978-3-319-52557-0.
- Kyrousi, Foteini, A Leonardi, F Roman, V Armenio, F Zanello, J Zordan, C Juez, and L Falcomer (2018). "Large Eddy Simulations of sediment entrainment induced by a lock-exchange gravity current". In: *Advances in Water Resources* 114, pp. 102–118. ISSN: 03091708. DOI: 10.1016/j.advwatres.2018.02.002.
- La Rocca, Michele, Claudia Adduce, Giampiero Sciortino, and Allen Bateman Pinzon (2008). "Experimental and numerical simulation of three-dimensional gravity currents on smooth and rough bottom". In: *Physics of Fluids* 20.10. ISSN: 10706631. DOI: 10.1063/1.3002381.
- Lagaly, G (1989). "Principles of flow of kaolin and bentonite dispersions". In: *Applied Clay Science* 4.2, pp. 105–123. ISSN: 01691317. DOI: 10.1016/0169-1317(89)90003-3.
- Lang, Aleksandra, Siemen Dasselaar, Kurt Aasly, and Erik Larsen (2019). "Blue Nodules Deliverable report D3 . 4 Report describing the process flow overview PU". In: 688975, pp. 1–23.
- Le Quéré, Corinne, Robbie Andrew, Pierre Friedlingstein, Stephen Sitch, Julia Pongratz, Andrew Manning, Jan Ivar Korsbakken, Glen Peters, Josep Canadell, Robert Jackson, Thomas Boden, Pieter Tans, Oliver Andrews, Vivek Arora, Dorothee C Bakker, Leticia Barbero, Meike Becker, Richard Betts, Laurent Bopp, Frédéric Chevallier, Louise Chini, Philippe Ciais, Catherine Cosca, Jessica Cross, Kim Currie, Thomas Gasser, Ian Harris, Judith Hauck, Vanessa Haverd, Richard Houghton, Christopher Hunt, George Hurtt, Tatiana Ilyina, Atul Jain, Etsushi Kato, Markus Kautz, Ralph Keeling, Kees Klein Goldewijk, Arne Körtzinger, Peter Landschützer, Nathalie Lefèvre, Andrew Lenton, Sebastian Lienert, Ivan Lima, Danica Lombardozzi, Nicolas Metz, Frank Millero, Pedro Monteiro, David Munro, Julia Nabel, Shin-ichiro Nakaoka, Yukihiro Nojiri, X. Antoni Padín, Anna Peregon, Benjamin Pfeil, Denis Pierrot, Benjamin Poulter, Gregor Rehder, Janet Reimer, Christian Rödenbeck, Jörg Schwinger, Roland Séférian, Ingunn Skjelvan, Benjamin Stocker, Hanqin Tian, Bronte Tilbrook, Ingrid van der Laan-Luijckx, Guido van der Werf, Steven van Heuven, Nicolas Viovy, Nicolas Vuichard, Anthony Walker, Andrew Watson, Andrew Wiltshire, Sönke Zaehle, and Dan Zhu (2018). "Global Carbon Budget". In: *Earth System Science Data Discussions* pre print. November, pp. 1–54. ISSN: 1866-3591. DOI: 10.5194/essd-2017-123.
- Leussen, W van (1994). *Estuarine macroflocs and their role in fine-grained sediment transport*.
- Luckham, Paul and Sylvia Rossi (1999). "Colloidal and rheological properties of bentonite suspensions". In: *Advances in Colloid and Interface Science* 82.1, pp. 43–92. ISSN: 00018686. DOI: 10.1016/S0001-8686(99)00005-6.
- Lutz, Michael, Ken Caldeira, Robert Dunbar, and Michael Behrenfeld (2007). "Seasonal rhythms of net primary production and particulate organic carbon flux to depth describe the efficiency of biological pump in the global ocean". In: *Journal of Geophysical Research: Oceans* 112.10. ISSN: 21699291. DOI: 10.1029/2006JC003706.
- Maciag, Tuskasz and Jan Harff (2020). "Application of multivariate geostatistics for local-scale lithological mapping – case study of pelagic surface sediments from the Clarion-Clipperton Fracture Zone, north-eastern equatorial Pacific (Interoceanmetal claim area)". In: *Computers and Geosciences* 139. ISSN: 00983004. DOI: 10.1016/j.cageo.2020.104474.
- Maggi, Federico (2005). "Flocculation dynamics of cohesive sediment". In: *Communications on Hydraulic and Geotechnical Engineering* 5.1, pp. 1–139. ISSN: 01696548.

- Manning, Andrew James and Keith Richard Dyer (2002). "The use of optics for the in situ determination of flocculated mud characteristics". In: *Journal of Optics A: Pure and Applied Optics* 4.4. ISSN: 14644258. DOI: 10.1088/1464-4258/4/4/366.
- Marr, J, G Shanmugam, and G Parker (2001). "Experiments on subaqueous sandy gravity flows: The role of clay and water content in flow dynamics and depositional structures". In: *Bulletin of the Geological Society of America* 113.11, pp. 1377–1386. ISSN: 00167606. DOI: 10.1130/0016-7606(2001)113<1377:E0SSGF>2.0.CO;2.
- Matousek, Vaclav (2004). "Dredge Pumps and Slurry Transport". In: September, pp. 1–18.
- McAnally, W (1999). *Aggregation and Deposition of Estuarial Fine Sediment*. URL: [https://www.researchgate.net/publication/235166248\\_Aggregation\\_and\\_Deposition\\_of\\_Estuarial\\_Fine\\_Sediment](https://www.researchgate.net/publication/235166248_Aggregation_and_Deposition_of_Estuarial_Fine_Sediment).
- Middleton, G (1993). "Sediment deposition from turbidity currents". In: *Annual Review of Earth & Planetary Sciences* 21, pp. 89–114. ISSN: 0084-6597. DOI: 10.1146/annurev. ea.21.050193.000513.
- Middleton, Gerard (Aug. 1966). "Experiments in density and turbidity currents: Motion of the head". In: *Canadian Journal of Earth Sciences* 3.4, pp. 523–546. ISSN: 0008-4077. DOI: 10.1139/e66-038. URL: <https://ui.adsabs.harvard.edu/abs/1966CaJES...3..523M/abstract>.
- (June 1967). "Experiments on density and turbidity currents III." In: *Canadian Journal of Earth Sciences* 4.3, pp. 475–505. ISSN: 0008-4077. DOI: 10.1139/e67-025.
- Mietta, F, C Chassagne, and J Winterwerp (2009). "Shear-induced flocculation of a suspension of kaolinite as function of pH and salt concentration". In: *Journal of Colloid and Interface Science* 336.1, pp. 134–141. ISSN: 00219797. DOI: 10.1016/j.jcis.2009.03.044.
- Mietta, Francesca, Claire Chassagne, Andrew Manning, and Johan Winterwerp (2009). "Influence of shear rate, organic matter content, pH and salinity on mud flocculation". In: *Ocean Dynamics* 59.5, pp. 751–763. ISSN: 16167341. DOI: 10.1007/s10236-009-0231-4.
- Mietta, Francesca (TU Delft) (2010). *Evolution of the floc size distribution of cohesive sediments Ontwikkeling van de vloggrootteverdeling van cohesief sediment*. ISBN: 9789088911583.
- Migniot, C (1968). "Étude Des Propriétés Physiques De Différents Sédiments Très Fins Et De Leur Comportement Sous Des Actions Hydrodynamiques". In: *La Houille Blanche* 7, pp. 591–620. ISSN: 0018-6368. DOI: 10.1051/1hb/1968041.
- Miller, Kathryn, Kirsten Thompson, Paul Johnston, and David Santillo (2018). "An overview of seabed mining including the current state of development, environmental impacts, and knowledge gaps". In: *Frontiers in Marine Science* 4.JAN. ISSN: 22967745. DOI: 10.3389/fmars.2017.00418.
- Mohn, Christian, Paul Vercrujse, Wiebe Boomsma, Christian Mohn, Paul Vercrujse, and Phil Weaver (2019). "Blue Nodules Deliverable report D2. 8 Detailed design of SWOE return systems and water management". In: 688975, pp. 1–4.
- Moodie, T (2002). "Gravity currents". In: *Journal of Computational and Applied Mathematics* 144.1-2, pp. 49–83. ISSN: 03770427. DOI: 10.1016/S0377-0427(01)00551-9.
- Moodie, T, J Pascal, and G Swaters (1998). "Sediment transport and deposition from a two-layer fluid model of gravity currents on sloping bottoms". In: *Studies in Applied Mathematics* 100.3, pp. 215–244. ISSN: 00222526. DOI: 10.1111/1467-9590.00076.
- Nogueira, Helena, Claudia Adduce, Elsa Alves, and Mário Franca (2013). "Analysis of lock-exchange gravity currents over smooth and rough beds". In: *Journal of Hydraulic Research* 51.4, pp. 417–431. ISSN: 00221686. DOI: 10.1080/00221686.2013.798363.
- Oebius, Horst, Hermann Becker, Susanne Rolinski, and Jacek Jankowski (2001). "Parametrization and evaluation of marine environmental impacts produced by deep-sea manganese nodule mining". In: *Deep-Sea Research Part II: Topical Studies in Oceanography* 48.17-18, pp. 3453–3467. ISSN: 09670645. DOI: 10.1016/S0967-0645(01)00052-2.
- Olphen, H. van (1964). "Internal mutual flocculation in clay suspensions". In: *Journal of Colloid Science* 19.4, pp. 313–322. ISSN: 00958522. DOI: 10.1016/0095-8522(64)90033-9.
- Park, K (2011). "Deep-Sea pH". In: *American Association for the Advancement of Science* 154.3756, pp. 1540–1542.
- Parsons, Jeffrey, Carl Friedrichs, Peter Traykovski, David Mohrig, Jasim Imran, James Syvitski, Gary Parker, Pere Puig, James Buttles, and Marcelo Garca (2009). *The Mechanics of Marine Sediment Gravity Flows*. October 2017, pp. 275–337. ISBN: 9781444304398. DOI: 10.1002/9781444304398.ch6.
- Partheniades, Emmanuel (2009a). "Forces between Clay Particles and the Process of Flocculation". In: *Cohesive Sediments in Open Channels* 1, pp. 47–88. DOI: 10.1016/b978-1-85617-556-2.00003-2.

- Partheniades, Emmanuel (2009b). "The Mineralogy and the Physicochemical Properties of Cohesive Sediments". In: *Cohesive Sediments in Open Channels*, pp. 11–45. DOI: 10.1016/b978-1-85617-556-2.00002-0.
- Peakall, Jeff, Bill McCaffrey, and Ben Kneller (2000). *A process model for the evolution, morphology, and architecture of sinuous submarine channels*. DOI: 10.1306/2DC4091C-0E47-11D7-8643000102C1865D.
- Peukert, Anne, Timm Schoening, Evangelos Alevizos, Kevin Köser, Tom Kwasnitschka, and Jens Greinert (2018). "Understanding Mn-nodule distribution and evaluation of related deep-sea mining impacts using AUV-based hydroacoustic and optical data". In: *Biogeosciences* 15.8, pp. 2525–2549. ISSN: 17264189. DOI: 10.5194/bg-15-2525-2018.
- Richardson, J and W Zaki (1997). "Sedimentation and fluidization: Part I". In: *Process Safety and Environmental Protection: Transactions of the Institution of Chemical Engineers, Part B* 75.Suppl, S82–S100. ISSN: 09575820. DOI: 10.1016/S0263-8762(97)80006-8. URL: [http://dx.doi.org/10.1016/S0263-8762\(97\)80006-8](http://dx.doi.org/10.1016/S0263-8762(97)80006-8).
- Roels, Oswald (1974). "Environmental Impact of Manganese Nodule Mining." In: April, pp. 156–163.
- Rottman, James and John Simpson (1983). "Gravity currents produced by instantaneous releases of a heavy fluid in a rectangular channel". In: *Journal of Fluid Mechanics* 135, pp. 95–110. ISSN: 14697645. DOI: 10.1017/S0022112083002979.
- Rowe, P (Jan. 1987). "A convenient empirical equation for estimation of the Richardson-Zaki exponent". In: *Chemical Engineering Science* 42.11, pp. 2795–2796. ISSN: 00092509. DOI: 10.1016/0009-2509(87)87035-5. URL: <https://scinapse.io/papers/1996055377>.
- Shakeel, Ahmad, Zeinab Safar, Maria Ibanez, Leon van Paassen, and Claire Chassagne (2020). "Flocculation of clay suspensions by anionic and cationic polyelectrolytes: A systematic analysis". In: *Minerals* 10.11, pp. 1–24. ISSN: 2075163X. DOI: 10.3390/min10110999.
- Sharma, R (2017). *Deep-Sea Mining*. ISBN: 9783319525563.
- Simpson, J (1982). "Gravity currents in the laboratory, atmosphere, and ocean." In: *Annual Review of Fluid Mechanics* 14, M. Va.Hoult 1972. ISSN: 00664189.
- Simpson, J and R Britter (1980a). "A laboratory model of an atmospheric mesofront". In: *Quarterly Journal of the Royal Meteorological Society* 106.449, pp. 485–500. ISSN: 1477870X. DOI: 10.1002/qj.49710644907.
- (1980b). "Experiments on the dynamics of the front of a gravity current." In: 88.
- Simpson, John (1972). "Effects of the lower boundary on the head of a gravity current". In: 53.
- Spearman, Jeremy, Jonathan Taylor, Neil Crossouard, Alan Cooper, Michael Turnbull, Andrew Manning, Mark Lee, and Bramley Murton (2020). "Measurement and modelling of deep sea sediment plumes and implications for deep sea mining". In: DOI: 10.1038/s41598-020-61837-y.
- Sutherland, Bruce, Kai Barrett, and Murray Gingras (2014). "Clay settling in fresh and salt water". In: *Environmental Fluid Mechanics* 15.1, pp. 147–160. ISSN: 15677419. DOI: 10.1007/s10652-014-9365-0.
- Tan, Xiao Ling, Guo Ping Zhang, Hang Yin, Allen H. Reed, and Yoko Furukawa (2012). "Characterization of particle size and settling velocity of cohesive sediments affected by a neutral copolymer". In: *International Journal of Sediment Research* 27.4, pp. 473–485. ISSN: 10016279. DOI: 10.1016/S1001-6279(13)60006-2. URL: [http://dx.doi.org/10.1016/S1001-6279\(13\)60006-2](http://dx.doi.org/10.1016/S1001-6279(13)60006-2).
- The World Bank (2017). *The Growing Role of Minerals and Metals for a Low Carbon Future*. Tech. rep. June. DOI: 10.1596/28312.
- Thistle, David (2003). "The deep-sea floor: an overview". In: *Ecosystems of the deep oceans*, pp. 5–39. ISSN: 0167-4579.
- Ungarish, Marius (2009). *An Introduction to Gravity Currents and Intrusions*. January 2009. ISBN: 9781584889045. DOI: 10.1201/9781584889045.
- Valioulis, Iraklis Anestis (1983). "Particle Collisions and Coalescence in Fluids." In: *California Institute of Technology, W. M. Keck Laboratory of Hydraulics and Water Resources, Repor KH-R-44*. ISSN: 02725002.
- Vane, Leland and Gwen Zang (1997). "Effect of aqueous phase properties on clay particle zeta potential and electro-osmotic permeability: Implications for electro-kinetic soil remediation processes". In: *Journal of Hazardous Materials* 55.1-3, pp. 1–22. ISSN: 03043894. DOI: 10.1016/S0304-3894(97)00010-1.
- Vanreusel, Ann, Ana Hilario, Pedro Ribeiro, Lenaick Menot, and Pedro Martínez Arbizu (2016). "Threatened by mining, polymetallic nodules are required to preserve abyssal epifauna". In: *Scientific Reports* 6, pp. 1–6. ISSN: 20452322. DOI: 10.1038/srep26808.
- Vasquez, A A Bedon (2020). *Quantifying the dispersion of turbidity currents generated by seafloor mining operations Section of Dredging Engineering*. Tech. rep.

- Volz, Jessica, José Mogollón, Walter Geibert, Pedro Martínez Arbizu, Andrea Koschinsky, and Sabine Kastten (2018). “Natural spatial variability of depositional conditions, biogeochemical processes and element fluxes in sediments of the eastern Clarion-Clipperton Zone, Pacific Ocean”. In: *Deep-Sea Research Part I: Oceanographic Research Papers* 140. December 2017, pp. 159–172. ISSN: 09670637. DOI: 10.1016/j.dsr.2018.08.006. URL: <https://doi.org/10.1016/j.dsr.2018.08.006>.
- Wang, Yan (2019). *China's deep-sea mining, a view from the top*. URL: <https://chinadialogueocean.net/10891-china-deep-sea-exploration-comra/>.
- Wikipedia (n.d.). *Mining implications*. URL: [https://upload.wikimedia.org/wikipedia/commons/1/18/Mining\\_implications\\_figure.png](https://upload.wikimedia.org/wikipedia/commons/1/18/Mining_implications_figure.png).
- Wilson, Richard, Heide Friedrich, and Craig Stevens (2017). “Turbulent entrainment in sediment-laden flows interacting with an obstacle”. In: *Physics of Fluids* 29.3. ISSN: 10897666. DOI: 10.1063/1.4979067. URL: <http://dx.doi.org/10.1063/1.4979067>.
- Winterwerp, J (2002). “On the flocculation and settling velocity of estuarine mud”. In: *Continental Shelf Research* 22.9, pp. 1339–1360. ISSN: 02784343. DOI: 10.1016/S0278-4343(02)00010-9.
- Winterwerp, J and W Kesteren (2004). *Introduction to the physics of cohesive sediment in the marine environment*.
- Wishner, K, C Ashjian, C Gelfman, M Gowing, L Kann, L Levin, L Mullineaux, and J Saltzman (1995). “The lower interface of the eastern tropical pacific oxygen minimum zone”. In: *Deep-Sea Research. Part I: Oceanographic Research Papers* 42.1, pp. 93–115. ISSN: 0967-0637. DOI: 10.1016/0967-0637(94)00021-J. URL: [http://dx.doi.org/10.1016/0967-0637\(94\)00021-J](http://dx.doi.org/10.1016/0967-0637(94)00021-J).
- Yong, R, M Nakano, and R Pusch (2012). “Swelling Clays”. In: *Environmental Soil Properties and Behaviour*, pp. 133–161. DOI: 10.1201/b11658-5.
- Zawadzki, Dominik, Łukasz Maciag, Tomasz Abramowski, and Kevin McCartney (2020). “Fractionation Trends and Variability of Rare Earth Elements and Selected Critical Metals in Pelagic Sediment from Abyssal Basin of NE Pacific (Clarion-Clipperton Fracture Zone)”. In: *Minerals* 10.4. ISSN: 2075163X. DOI: 10.3390/min10040320.

# **Appendices**

# A

## Sediment properties of illite and bentonite

### A.1. Illite

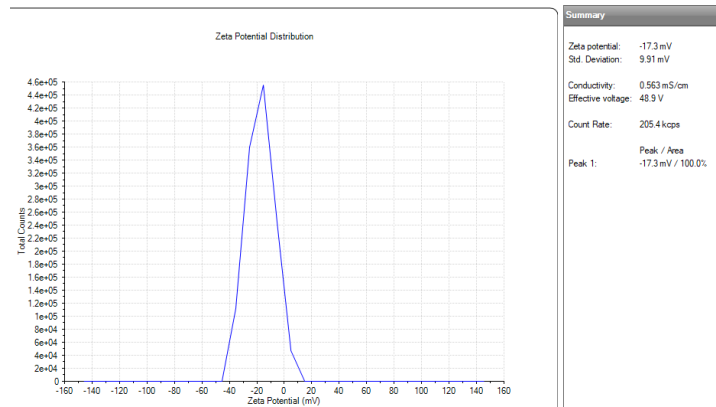


Figure A.1: Zeta potential illite

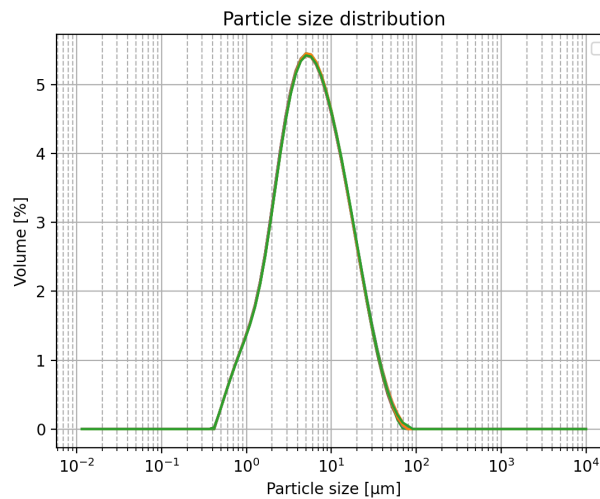


Figure A.2: Particle size distribution illite

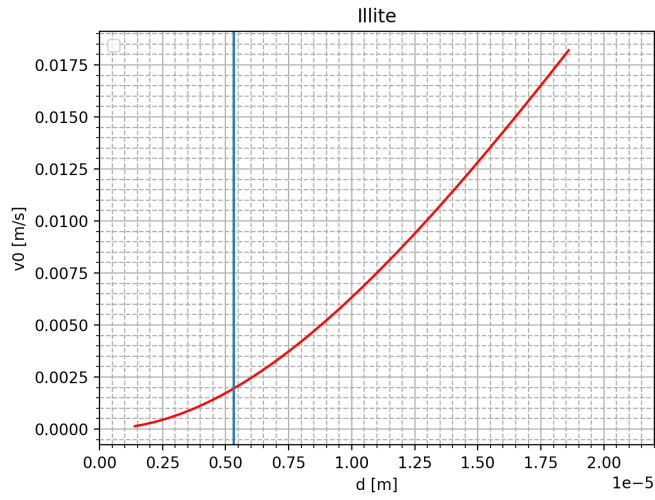


Figure A.3: Settling velocity with increased grain size. Blue line is size illite used

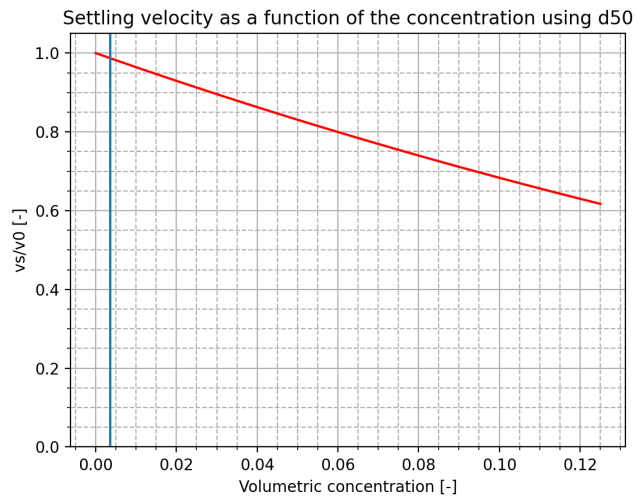


Figure A.4: Settling velocity with hindered settlement. Blue line is mass concentration of 10 g/L of illite.

## A.2. Bentonite

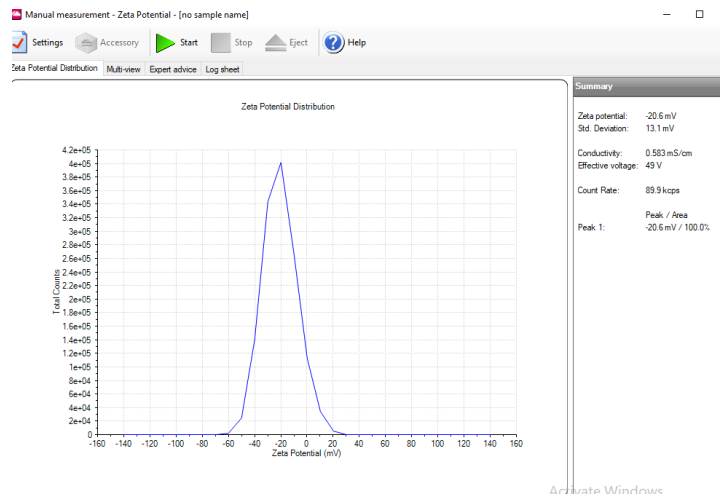


Figure A.5: Zeta potential bentonite

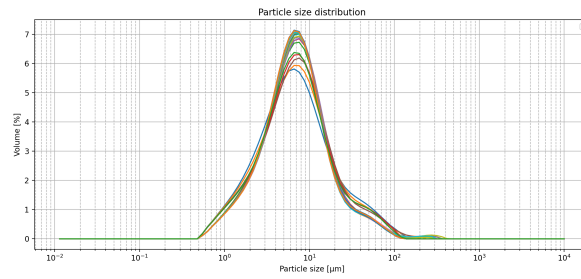
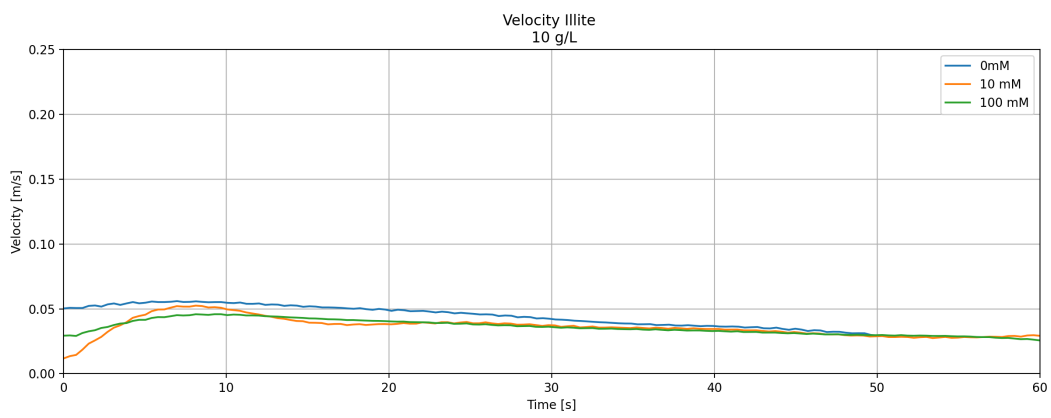


Figure A.6: Particle size distribution bentonite

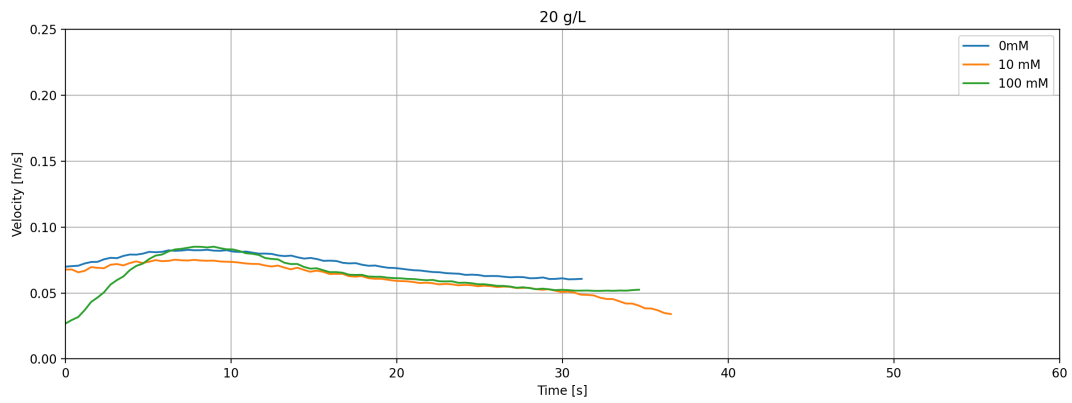


# B

## Head velocities

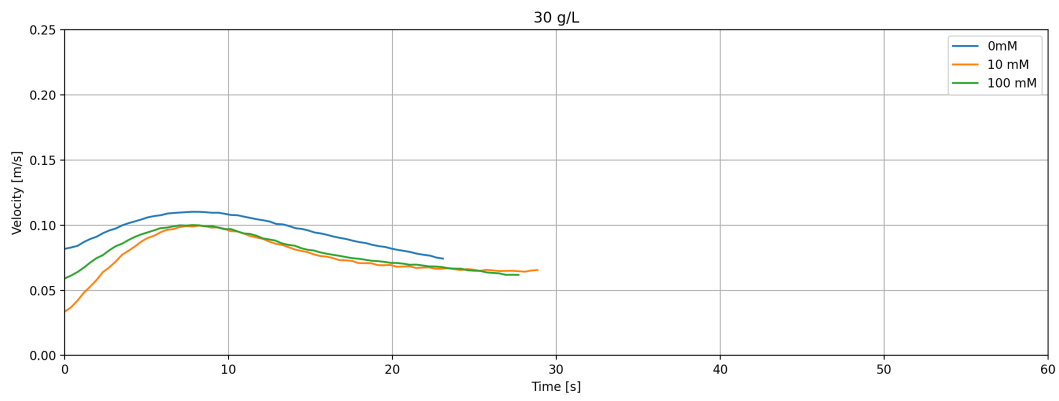


(a) Head velocity experiments with 10 g/L of Illite

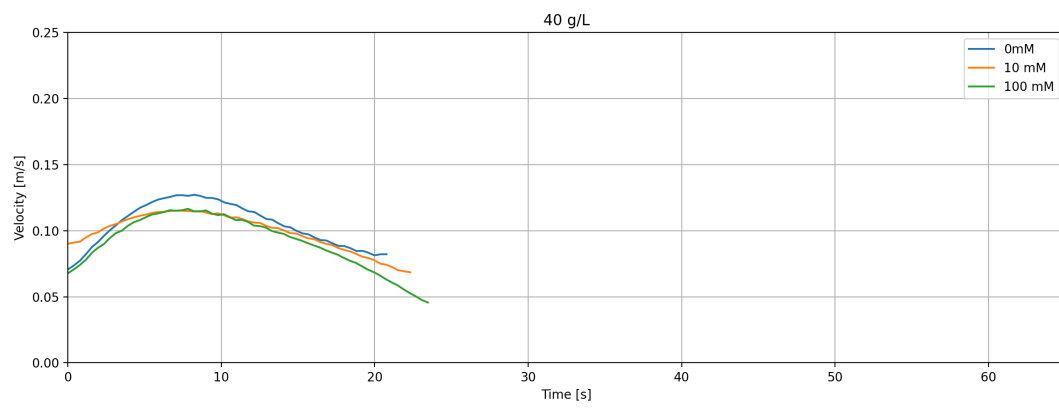


(b) Head velocity experiments with 20 g/L of Illite

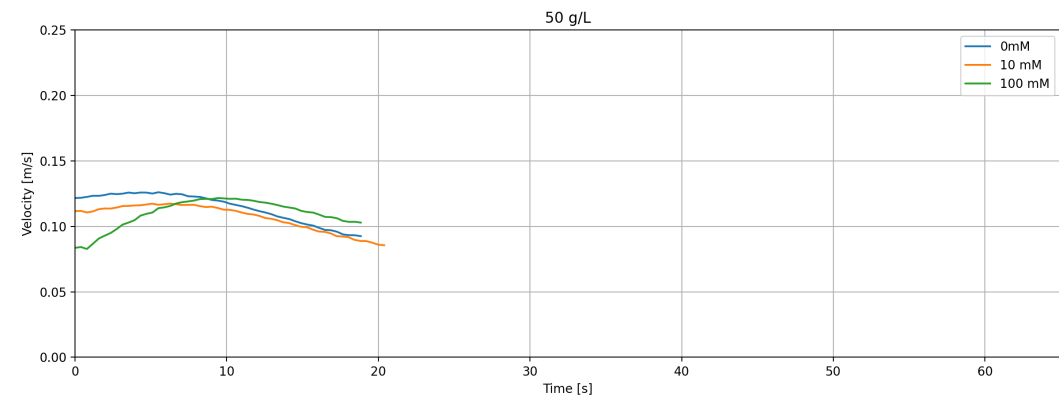
Figure B.1: Head velocities experiments: 1, 2, 9, 10, 17 and 18



(a) Head velocity experiments with 30 g/L of Illite

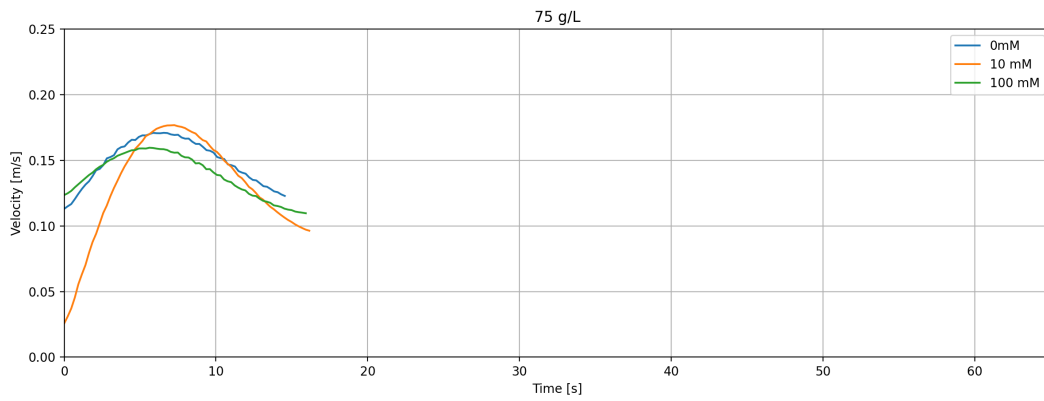


(b) Head velocity experiments with 40 g/L of Illite

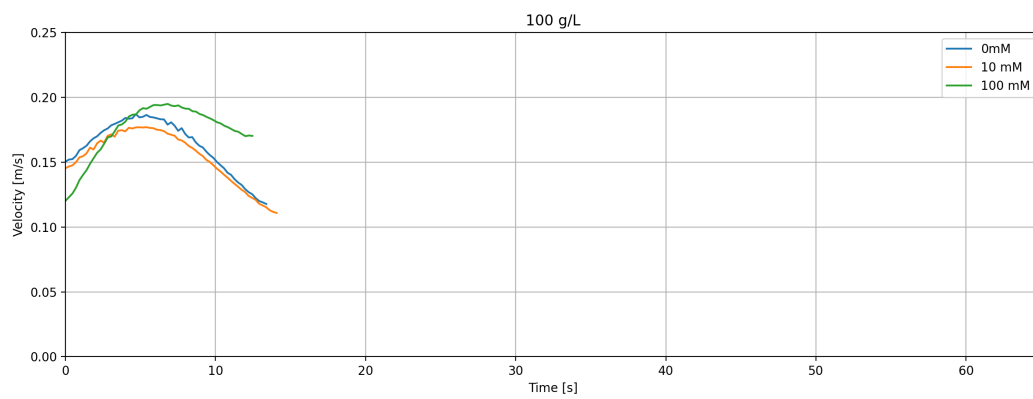


(c) Head velocity experiments with 50 g/L of Illite

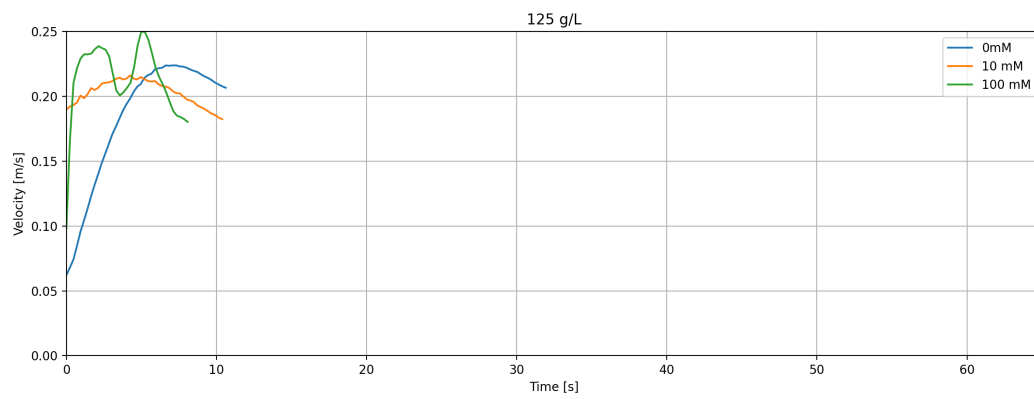
Figure B.2: Head velocities experiments: 3, 4, 5, 11, 12, 13, 19, 20 and 21



(a) Head velocity experiments with 75 g/L of Illite



(b) Head velocity experiments with 100 g/L of Illite



(c) Head velocity experiments with 125 g/L of Illite

Figure B.3: Head velocities experiments: 6,7,8, 14, 15, 16, 22, 23 and 24

# C

## Froude plots

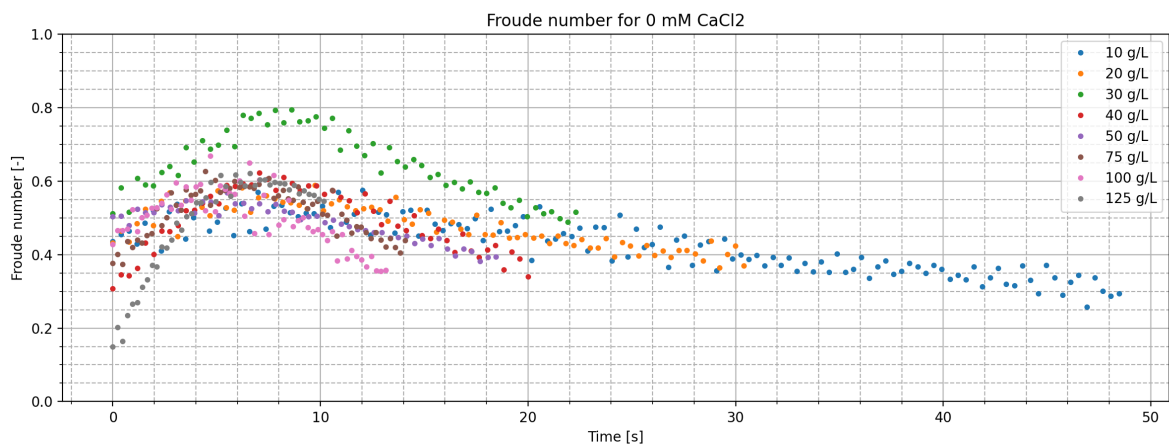


Figure C.1: Densimetric Froude number, experiment 1 up to 8

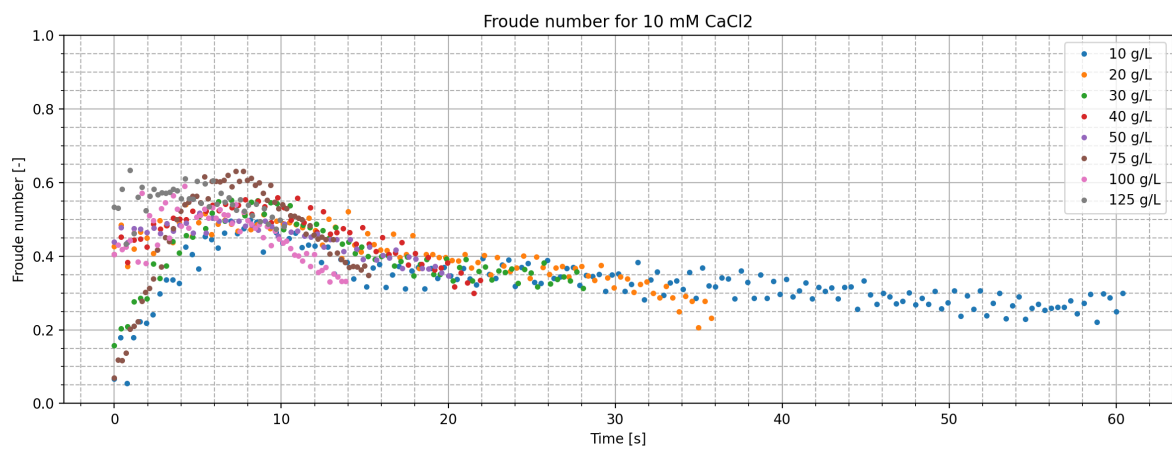


Figure C.2: Densimetric Froude number, experiments 9 up to 16

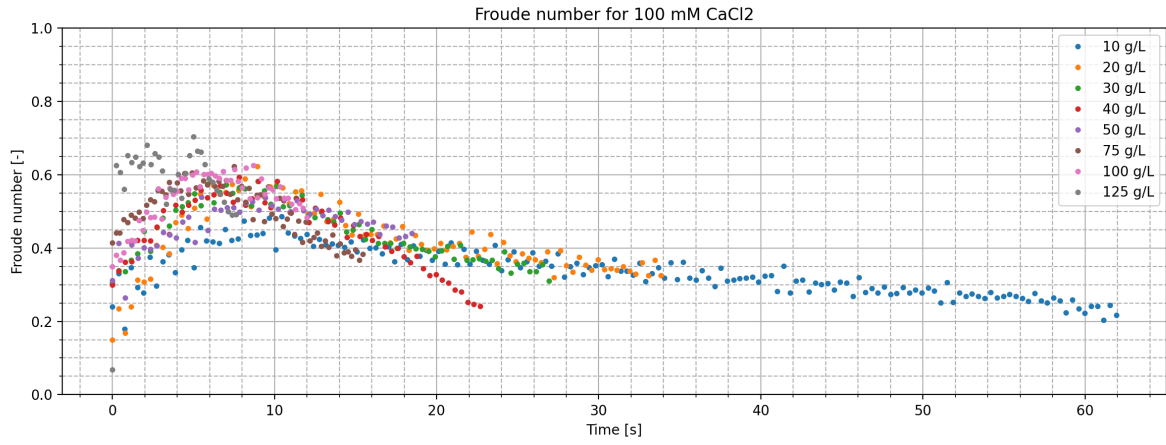


Figure C.3: Densimetric Froude, number experiments 17 up to 24

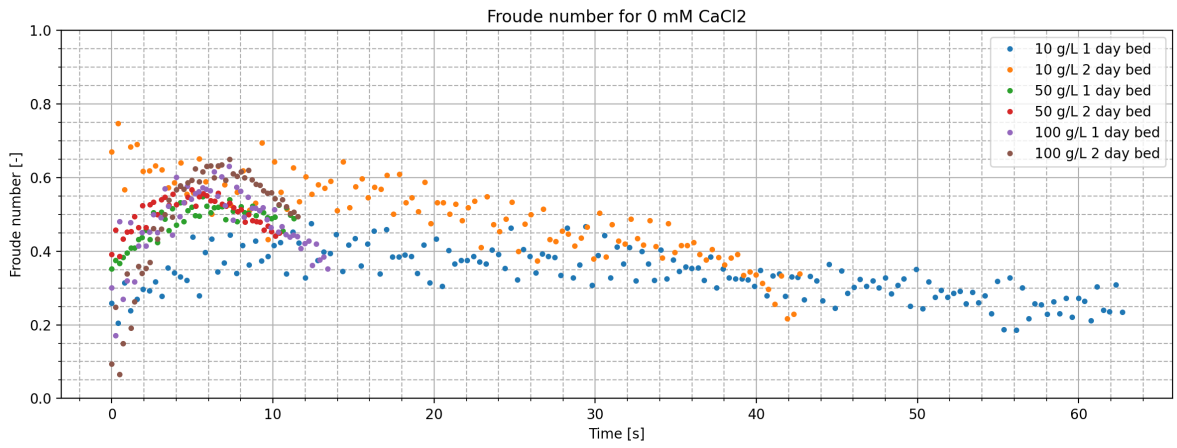


Figure C.4: Densimetric Froude number, experiments 25 up to 27-2

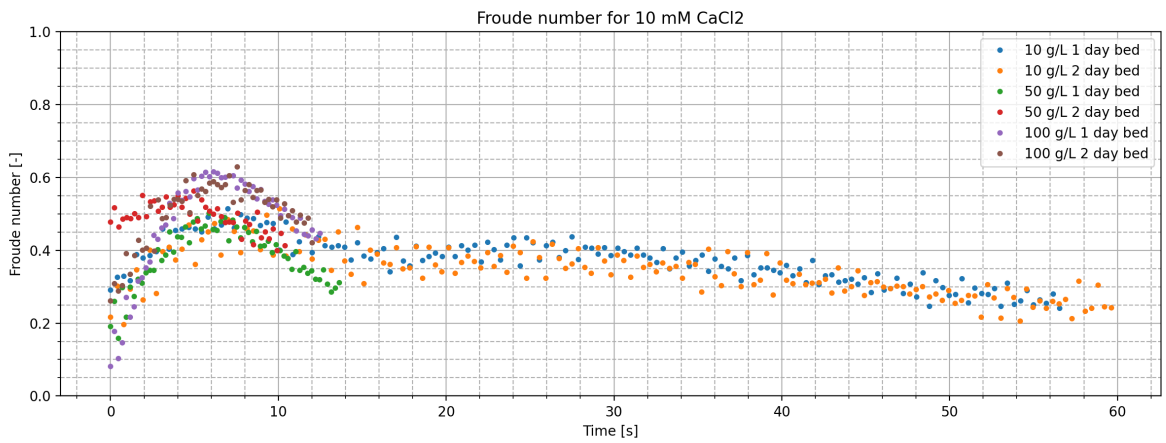


Figure C.5: Densimetric Froude number, experiments 28 up to 30-2

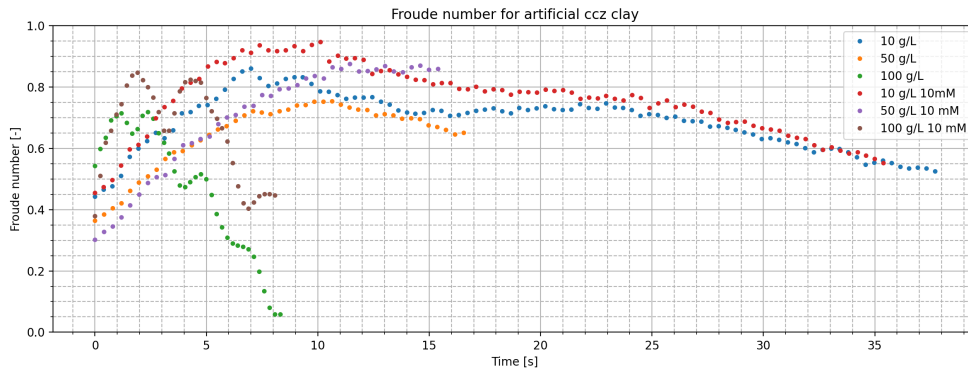


Figure C.6: Densimetric Froude number, experiments 43 up to 48

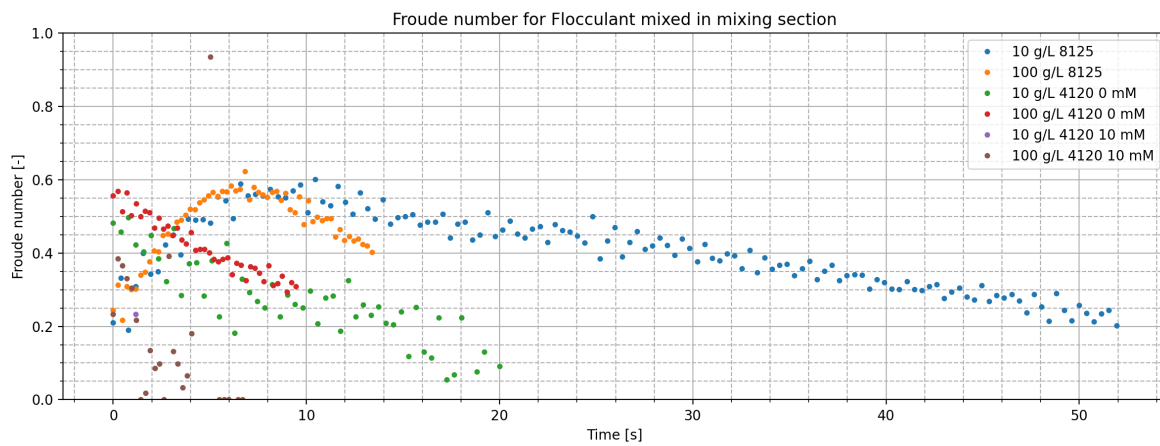


Figure C.7: Densimetric Froude number, experiments 33, 34, 35, 36, 39 and 40

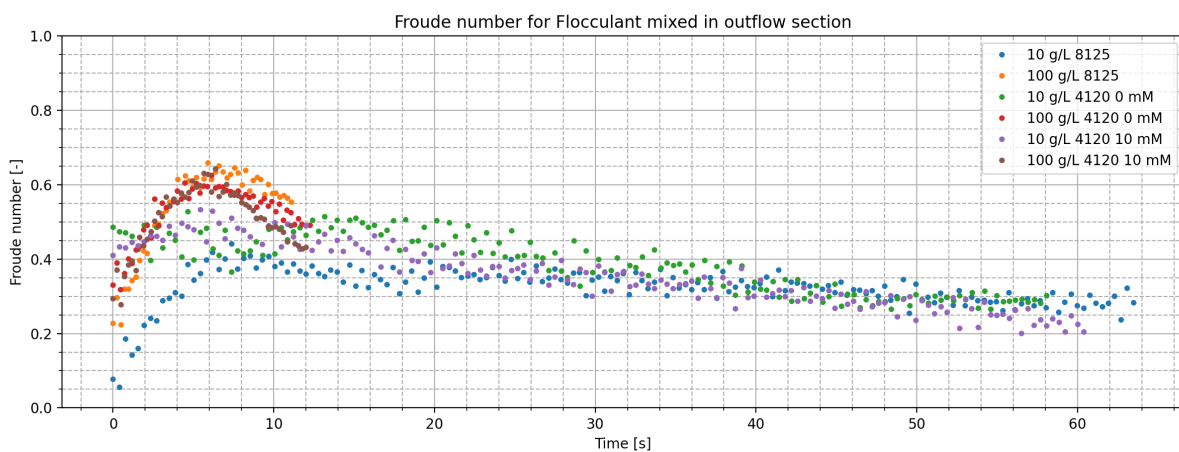
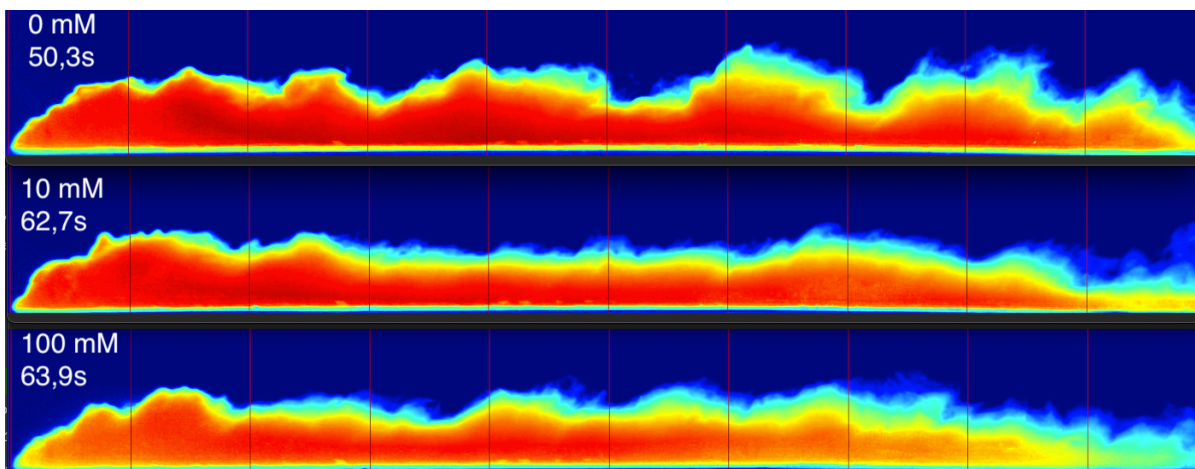


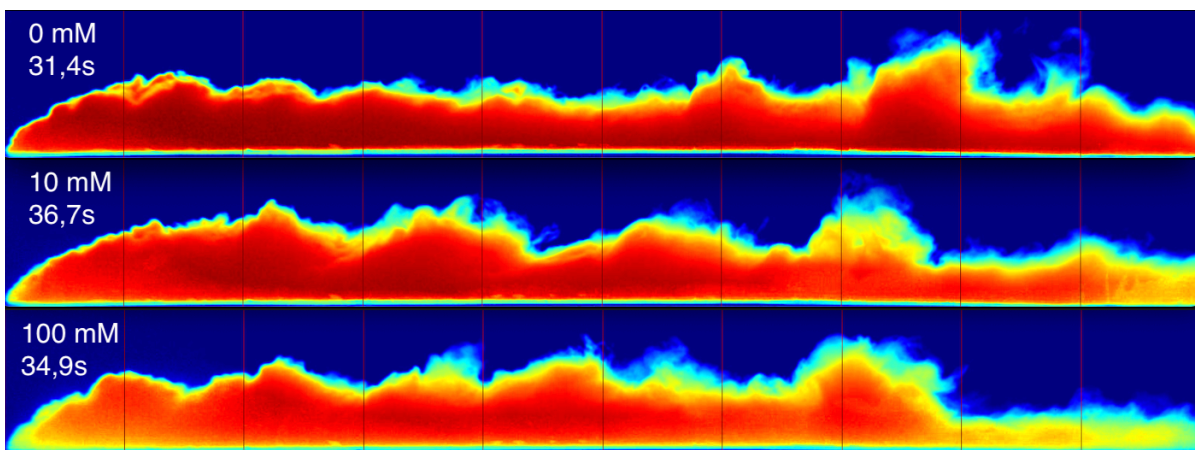
Figure C.8: Densimetric Froude number, experiments 31, 32, 37, 38, 41 and 42

# D

## Color maps



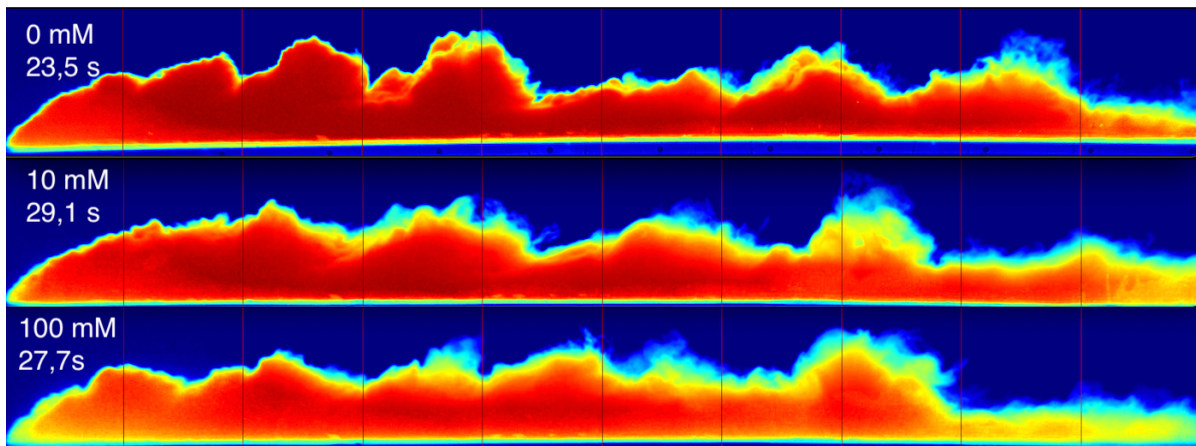
(a) Color maps 10 g/L of Illite. Exp 1, 19 and 17.



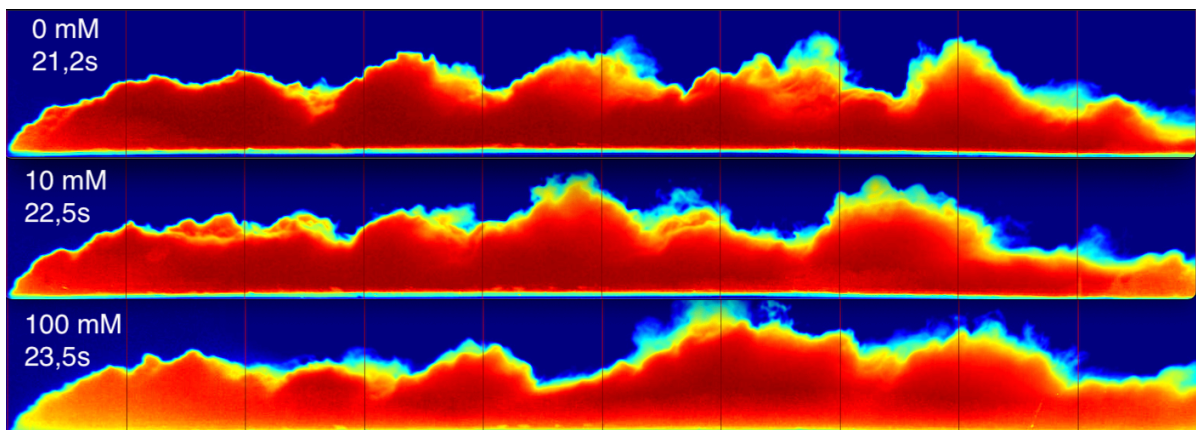
(b) Color maps 20 g/L of. Exp 2, 10 and 18. Illite

Figure D.1: Color maps of experiments: 1, 2, 9, 10, 17 and 18

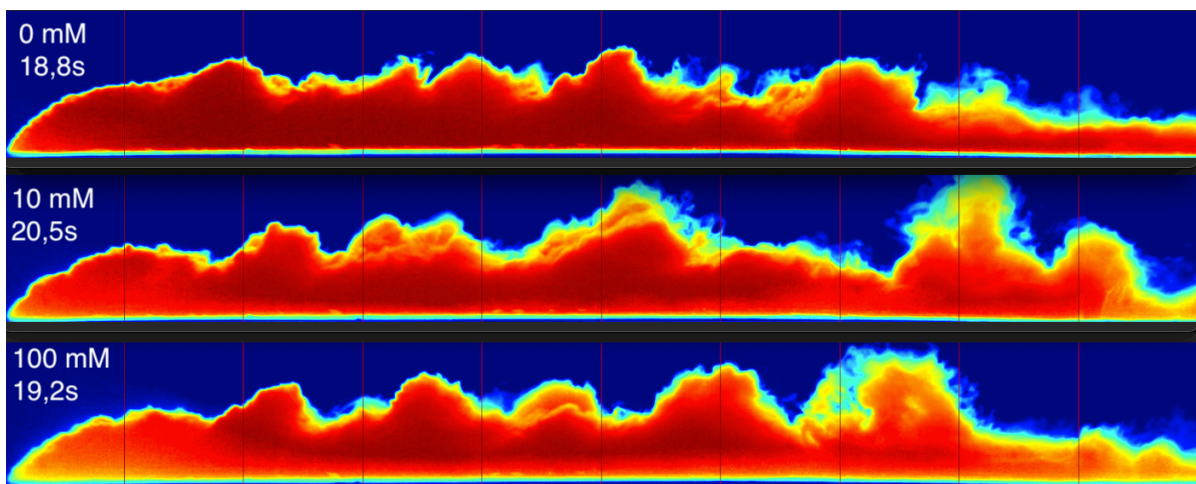




(a) Color maps 30 g/L of Illite. Exp 3, 11 and 19.



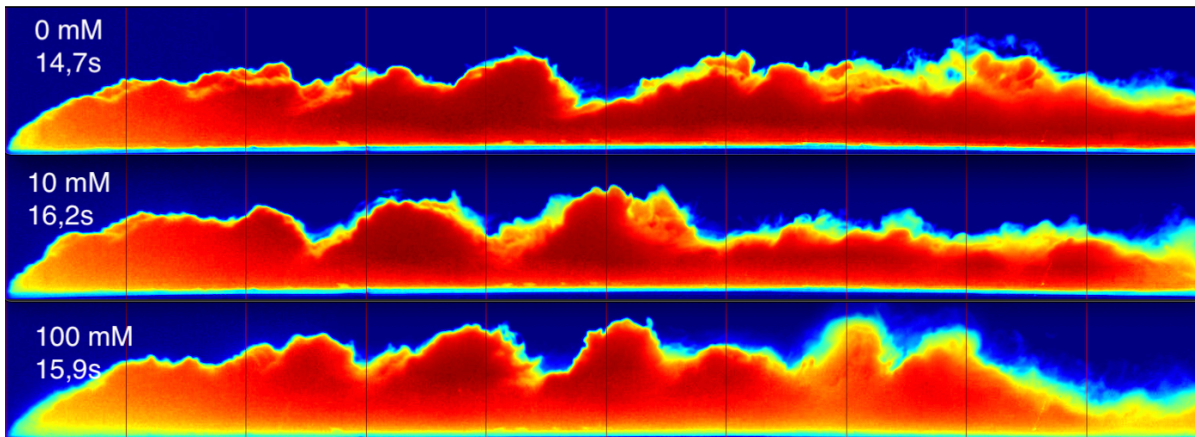
(b) Color maps 40 g/L of Illite. Exp 4, 12 and 20.



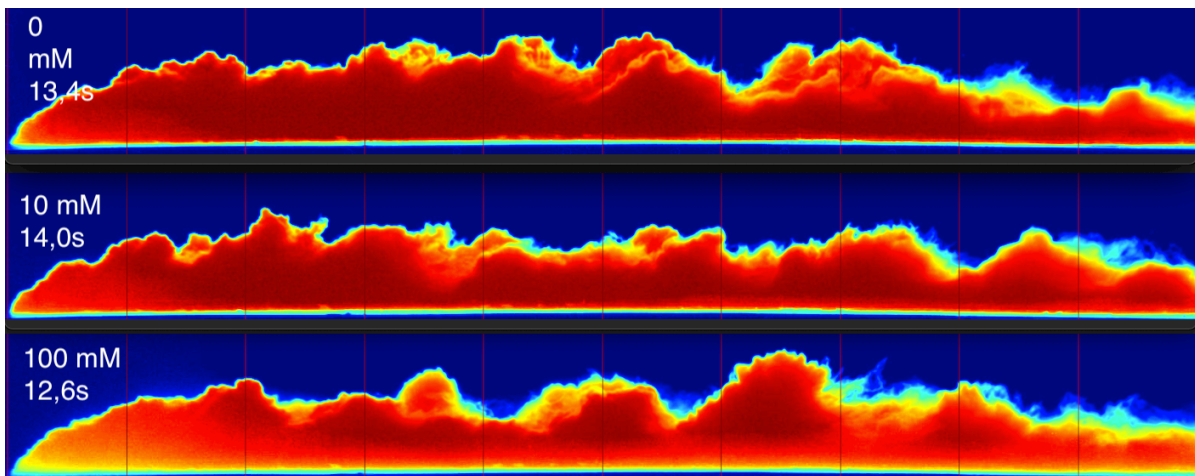
(c) Color maps 50 g/L of Illite. Exp 5, 13 and 21.

Figure D.2: Color maps of experiments: 3, 4, 5, 11, 12, 13, 19, 20 and 21

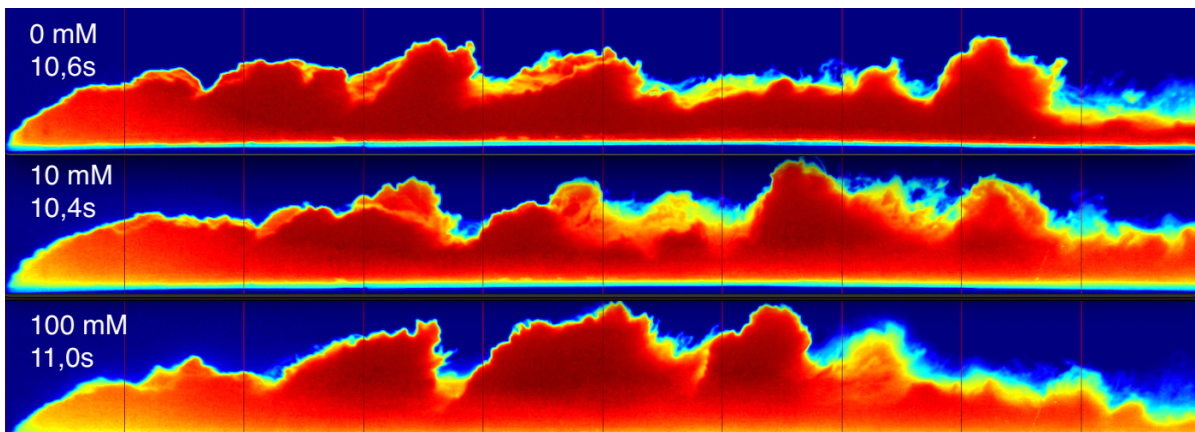




(a) Color maps 75 g/L of Illite. Exp 6, 14 and 22.



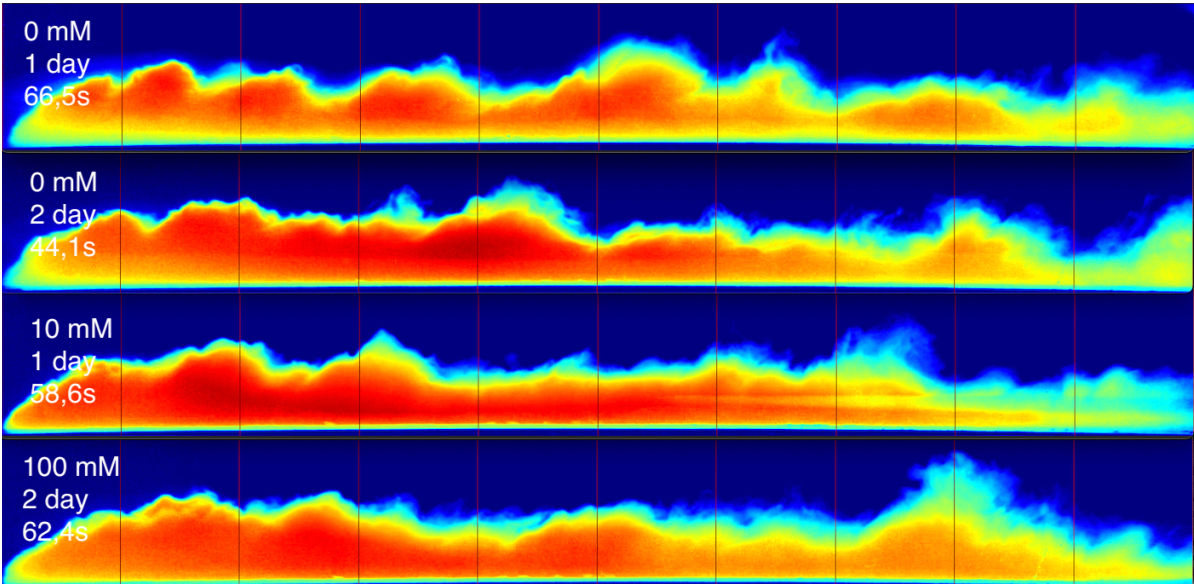
(b) Color maps 100 g/L of Illite. Exp 7, 54 and 23.



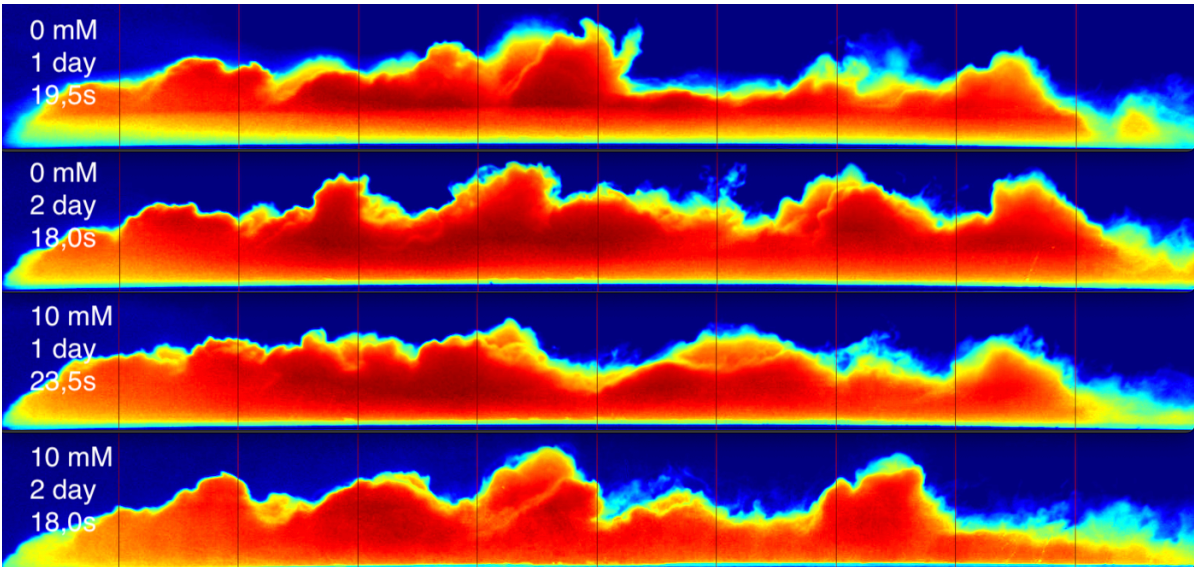
(c) Color maps 125 g/L of Illite. Exp 8, 16 and 24.

Figure D.3: Color maps of experiments: 6,7,8, 14, 15, 16, 22, 23 and 24

### D.1. Additional experiments with preexisting bed



(a) Color maps 10 g/L of Illite. Exp 25-1, 25-2, 28-1 and 28-2.



(b) Color maps 50 g/L of Illite. Exp 26-1, 26-2, 29-1 and 29-2. Illite

Figure D.4: Color maps of experiments with preexisting bed



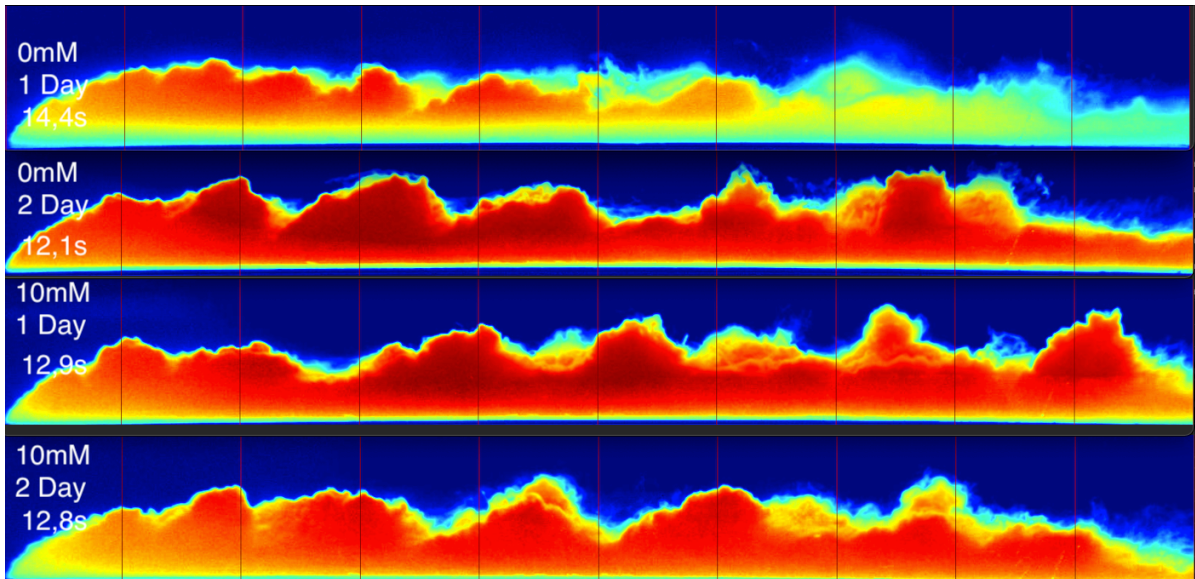
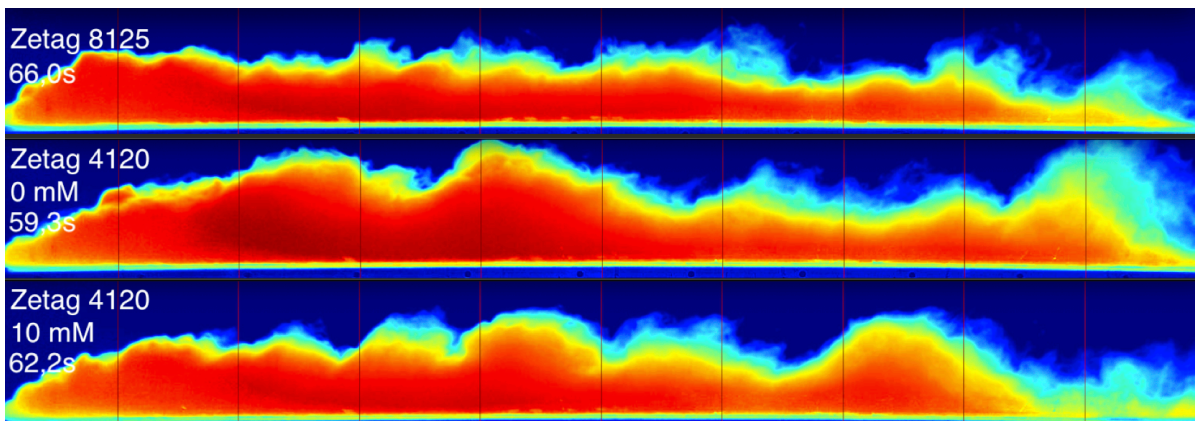
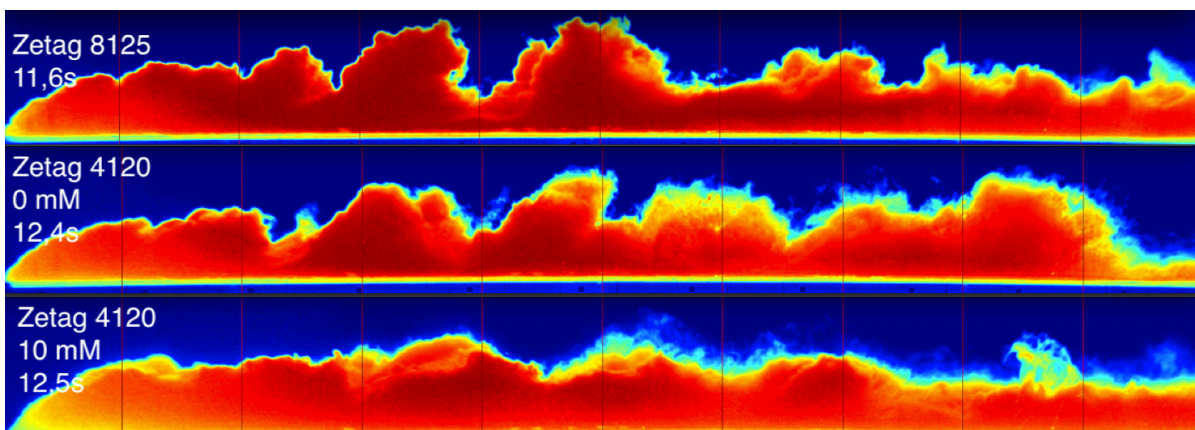


Figure D.5: Color maps 100 g/L of Illite with preexisting bed. Exp 27-1, 27-2, 30-1 and 30-2

## D.2. Additional experiments with flocculant

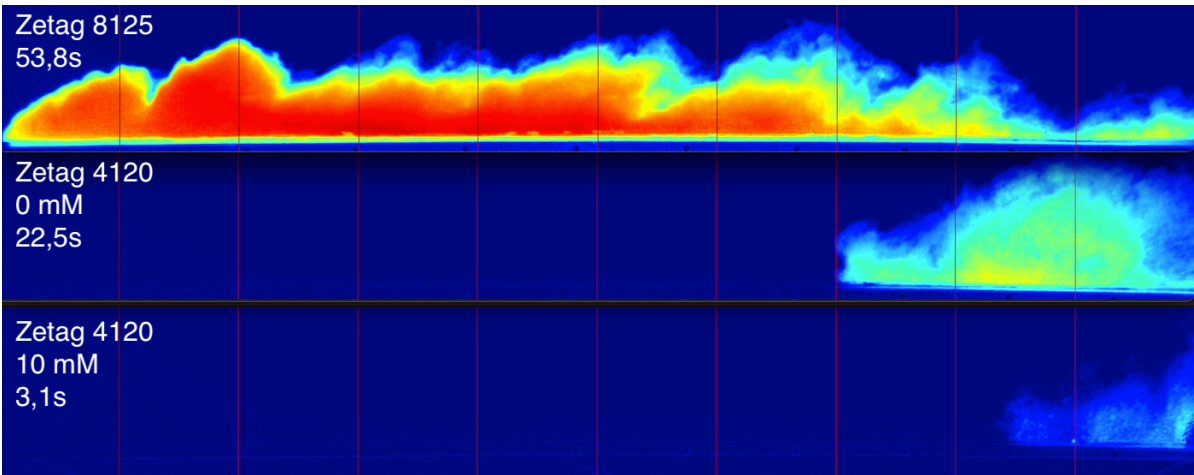


(a) Color maps 10 g/L of Illite. Exp 31, 37 and 41

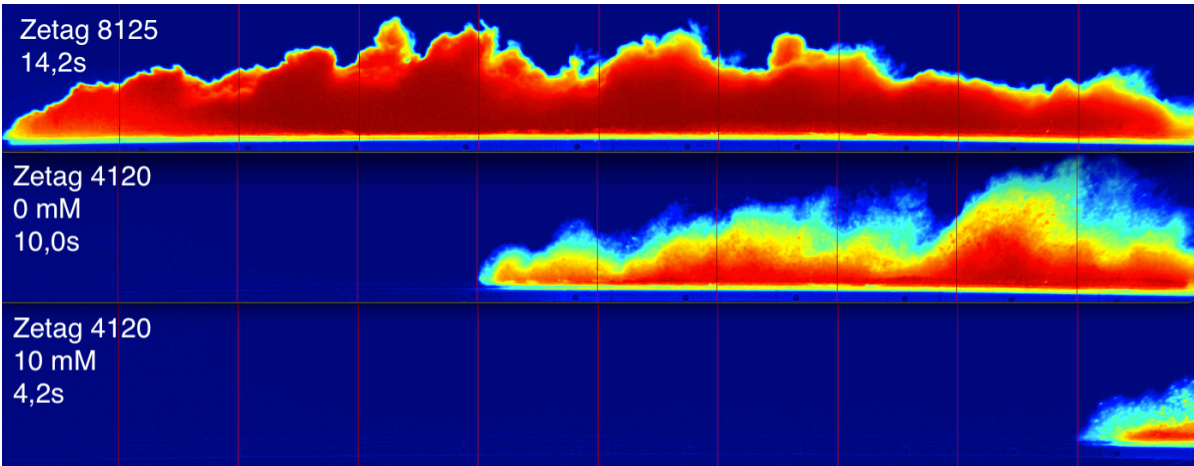


(b) Color maps 100 g/L of Illite. Exp 32, 38 and 42

Figure D.6: Color maps of experiments with flocculant mixed in outflow section

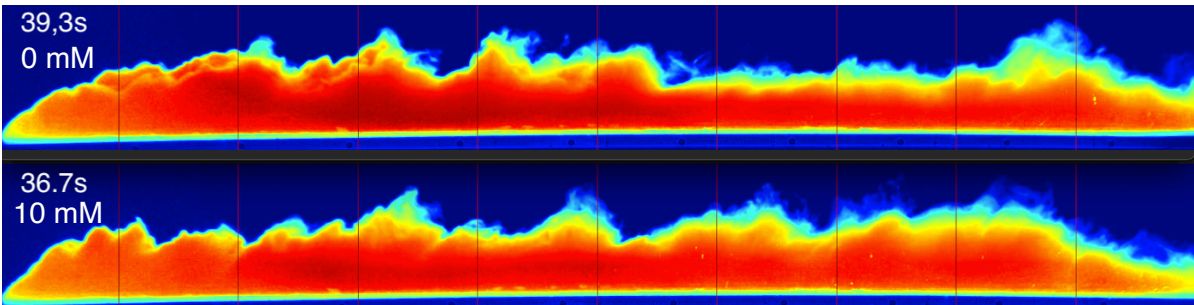


(a) Color maps 10 g/L of Illite. Exp 33, 35 and 39

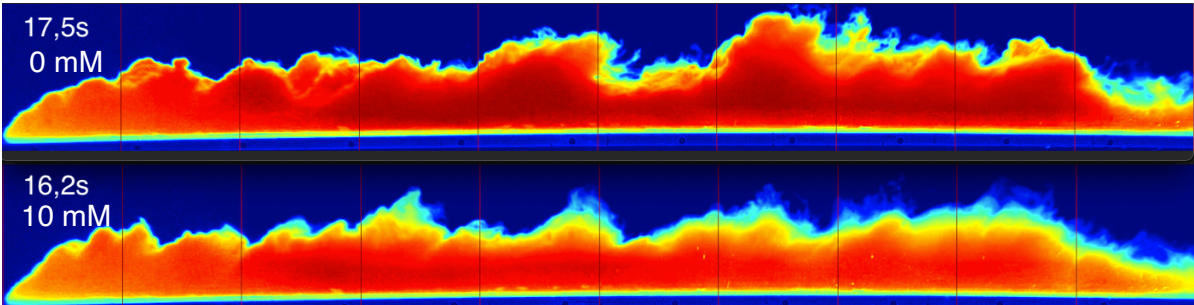


(b) Color maps 0.10 g/L of Illite. Exp 34, 36 and 40

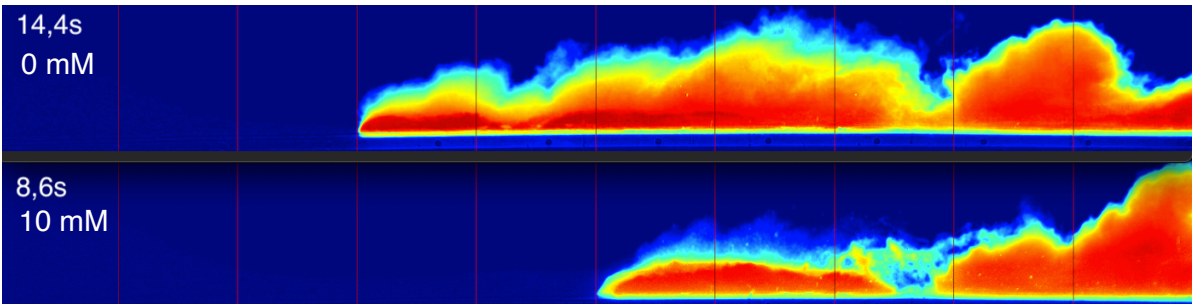
Figure D.7: Color maps of experiments with flocculant mixed in mixing section



(a) Color maps 10 g/L of mixture.



(b) Color maps 50 g/L of mixture.

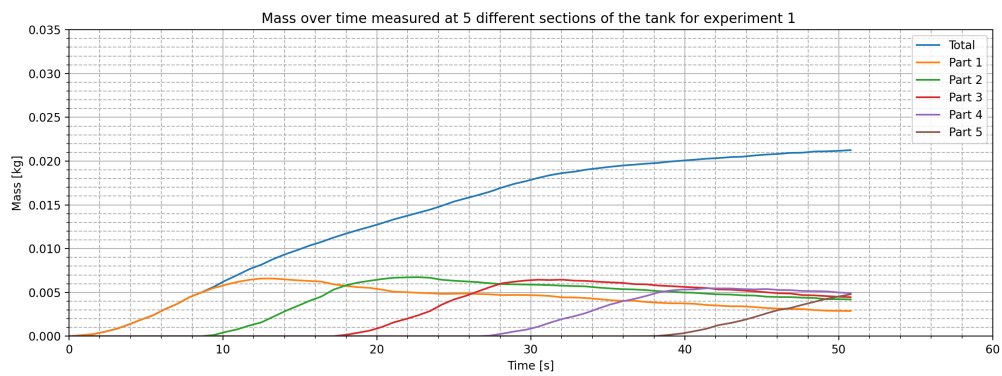


(c) Color maps 100 g/L of mixture.

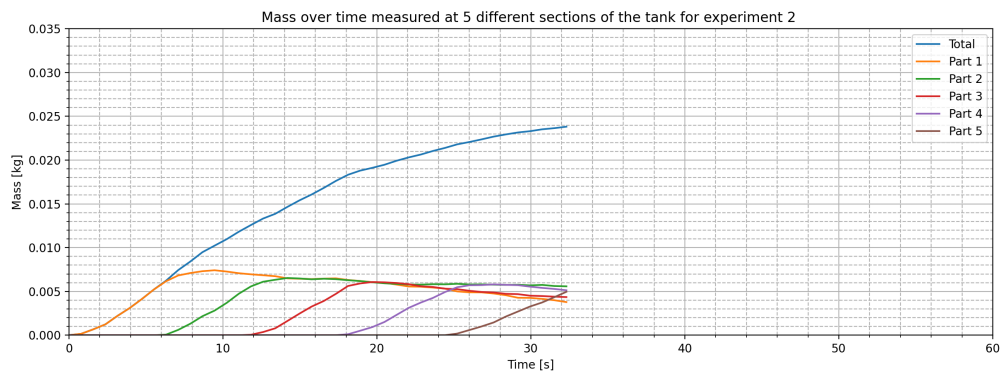
Figure D.8: Color maps of experiments with artificial CCZ sediment

# E

## Mass over time



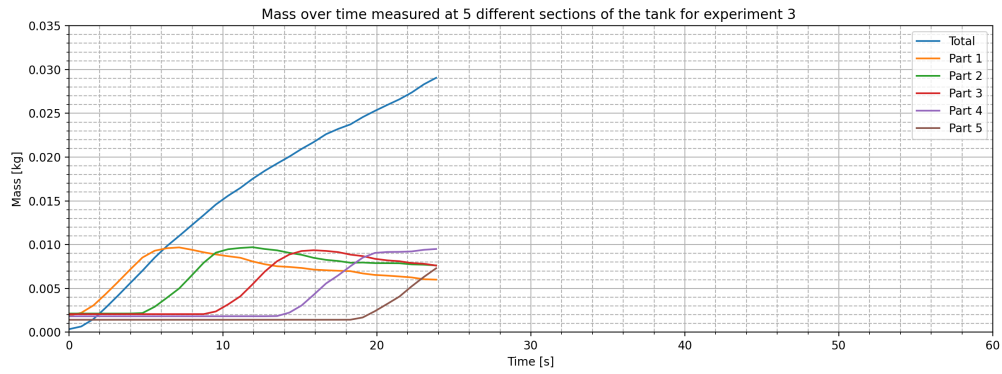
(a) Mass over time measured at 5 different sections of the tank for experiment 1



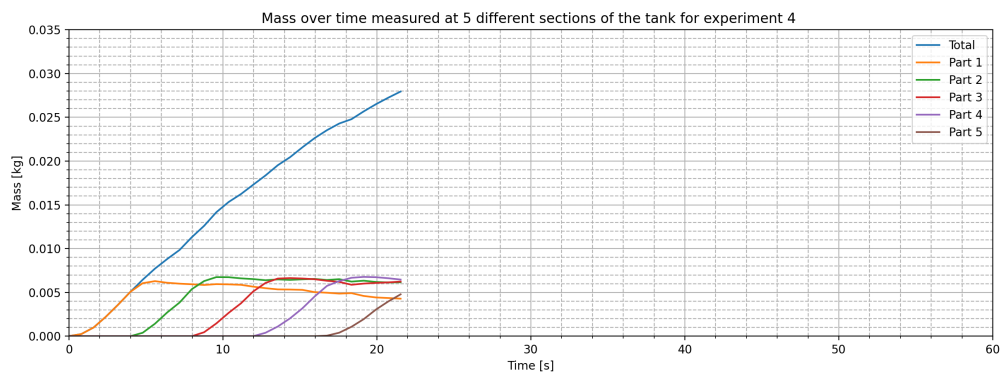
(b) Mass over time measured at 5 different sections of the tank for experiment 2

Figure E.1: Mass over time experiments 1 and 2

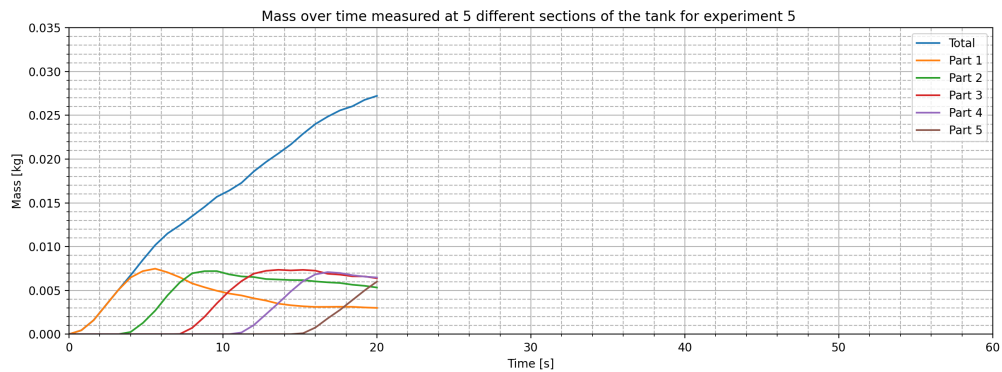




(a) Mass over time measured at 5 different sections of the tank for experiment 3

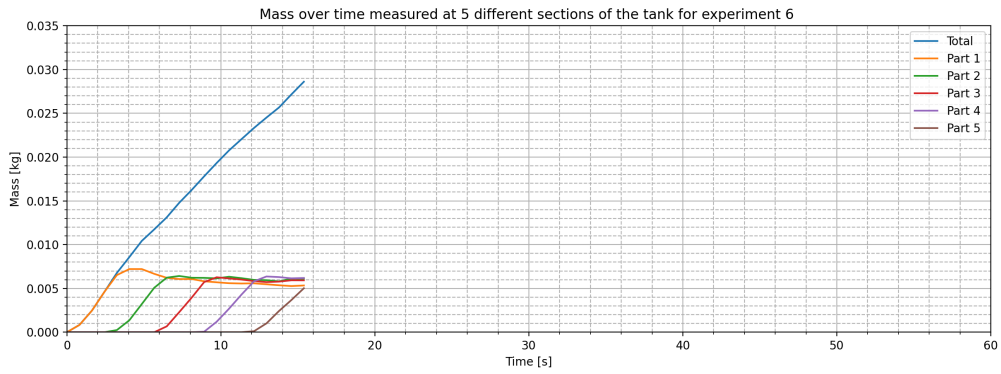


(b) Mass over time measured at 5 different sections of the tank for experiment 4

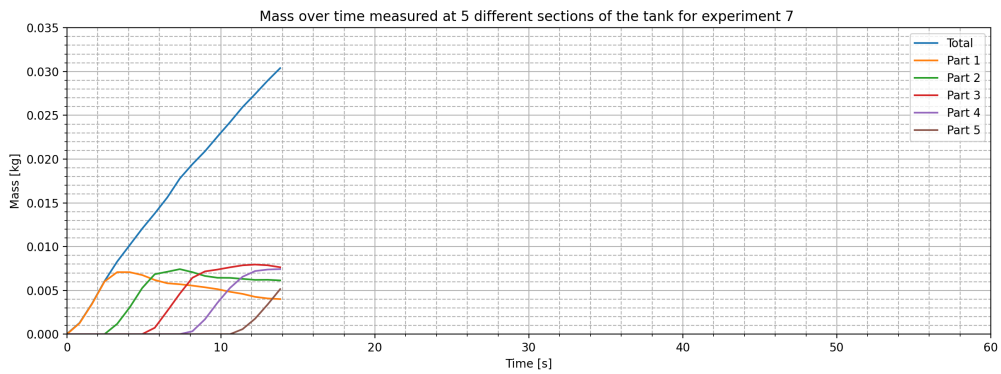


(c) Mass over time measured at 5 different sections of the tank for experiment 5

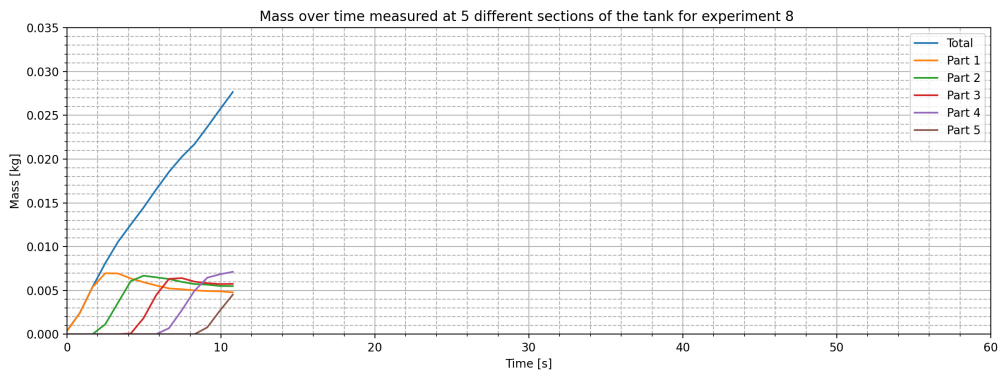
Figure E.2: Mass over time experiments 3, 4 and 5



(a) Mass over time measured at 5 different sections of the tank for experiment 6



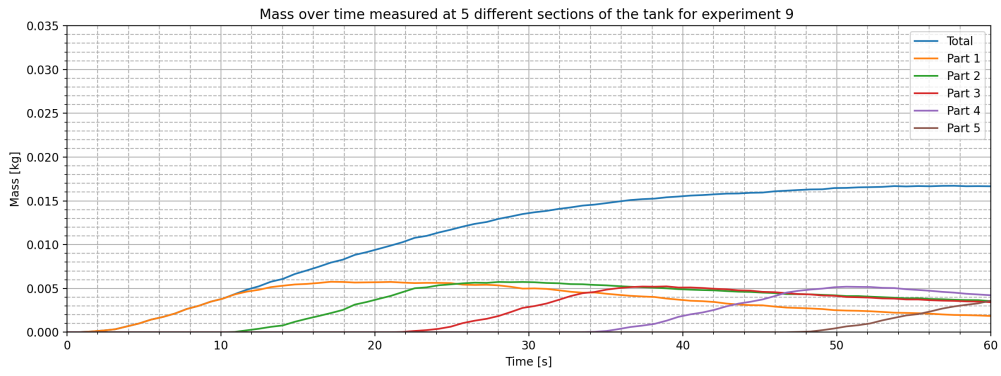
(b) Mass over time measured at 5 different sections of the tank for experiment 7



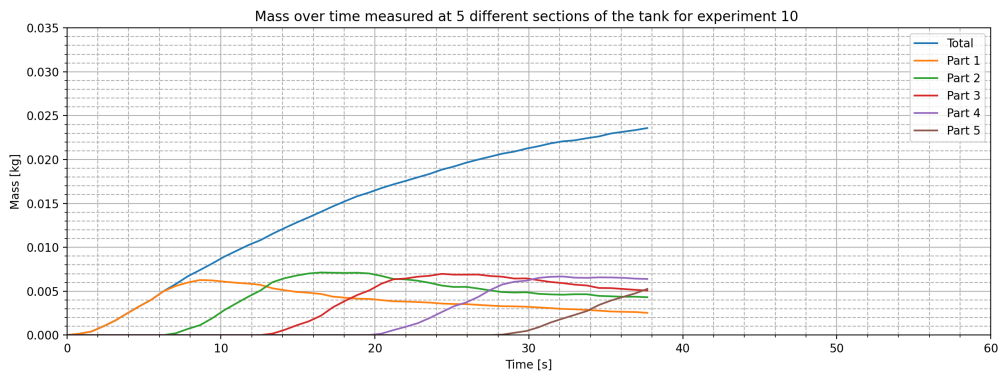
(c) Mass over time measured at 5 different sections of the tank for experiment 8

Figure E.3: Mass over time experiments 6, 7 and 8

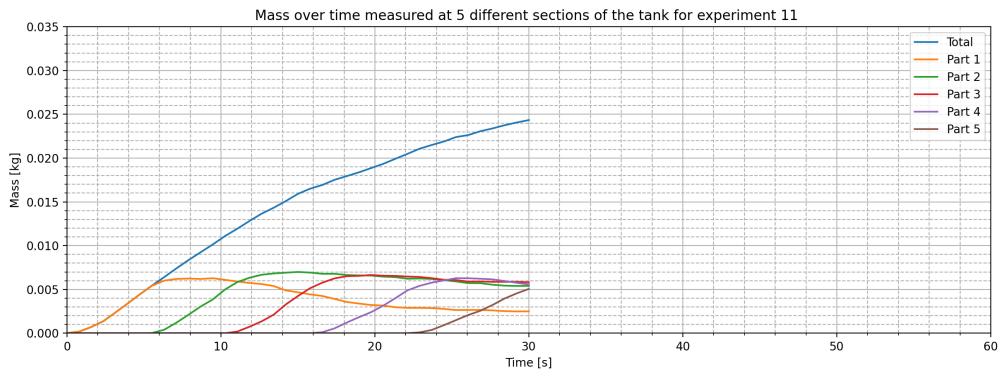




(a) Mass over time measured at 5 different sections of the tank for experiment 9

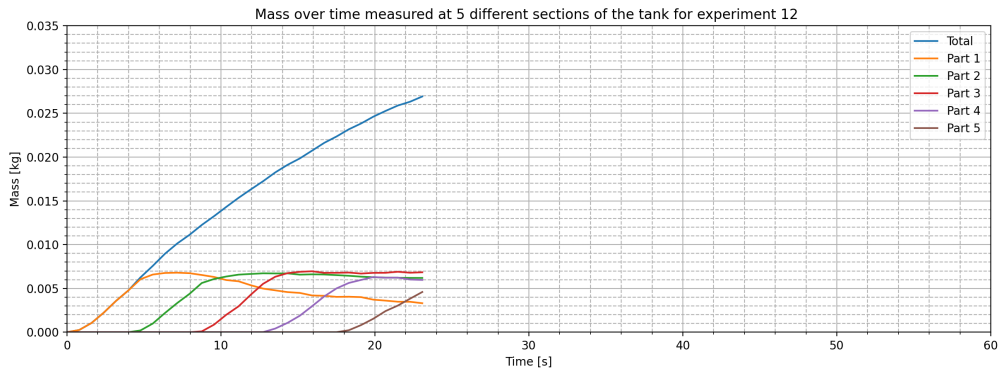


(b) Mass over time measured at 5 different sections of the tank for experiment 10

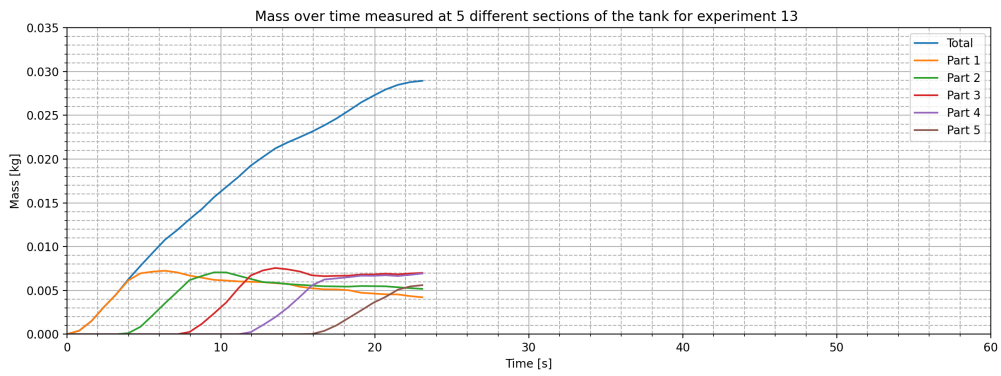


(c) Mass over time measured at 5 different sections of the tank for experiment 11

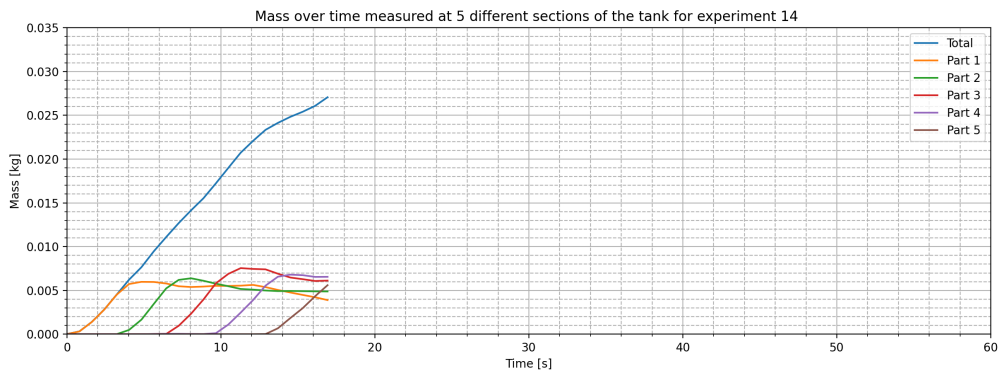
Figure E.4: Mass over time experiments 9, 10 and 11



(a) Mass over time measured at 5 different sections of the tank for experiment 12

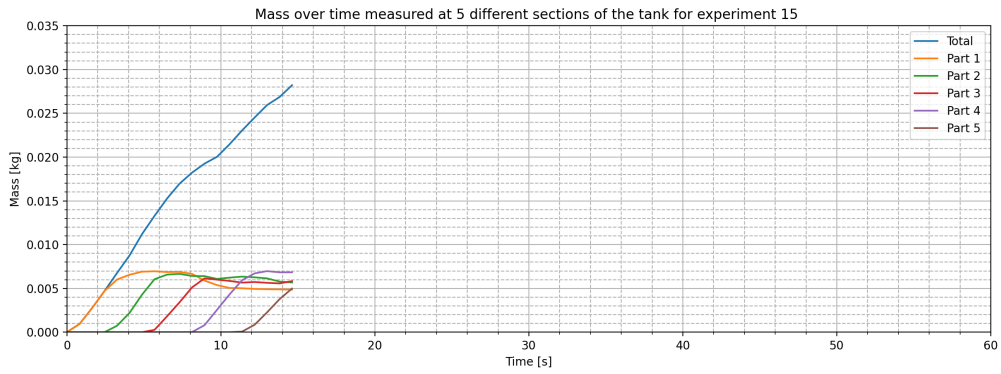


(b) Mass over time measured at 5 different sections of the tank for experiment 13

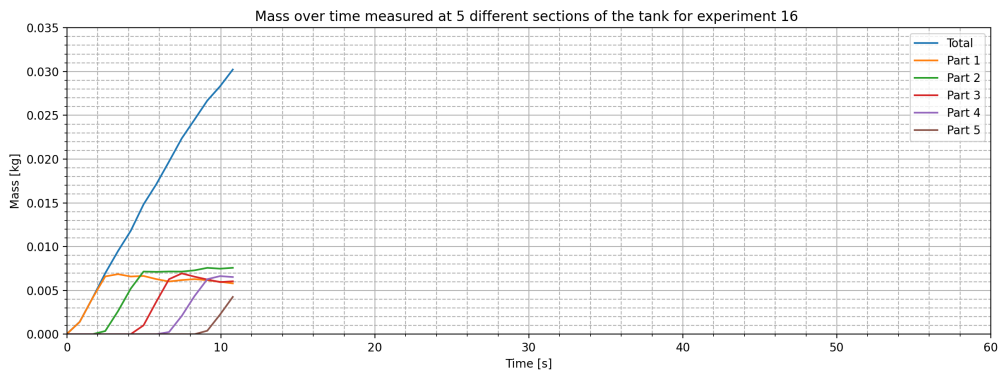


(c) Mass over time measured at 5 different sections of the tank for experiment 14

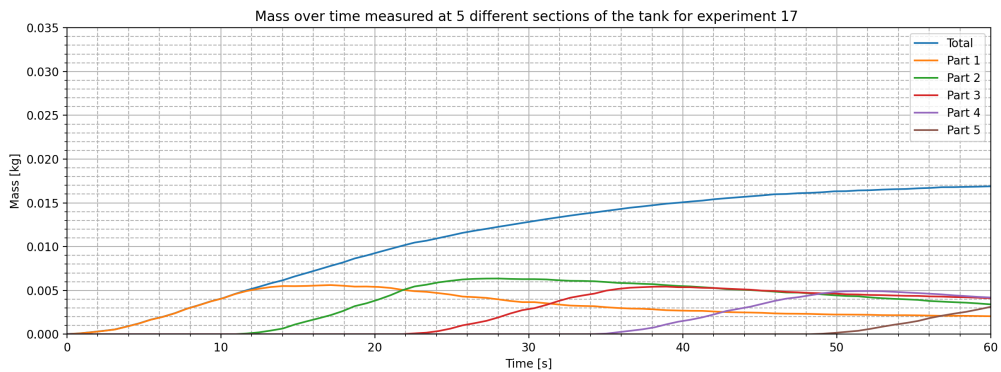
Figure E.5: Mass over time experiments 12, 13 and 14



(a) Mass over time measured at 5 different sections of the tank for experiment 15

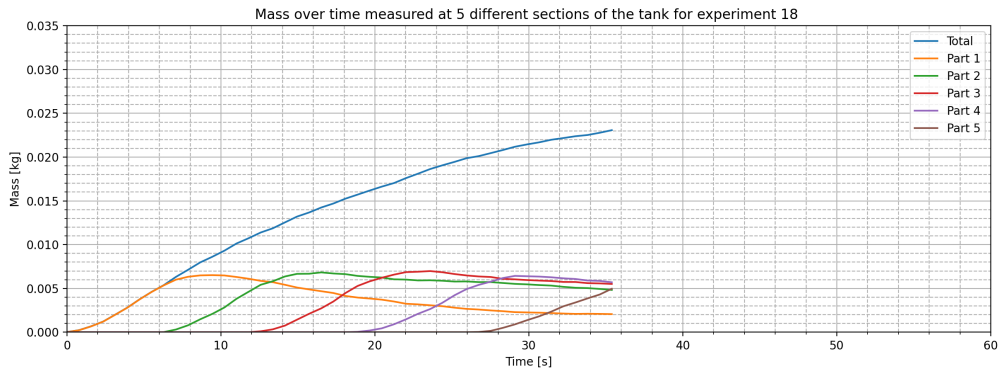


(b) Mass over time measured at 5 different sections of the tank for experiment 16

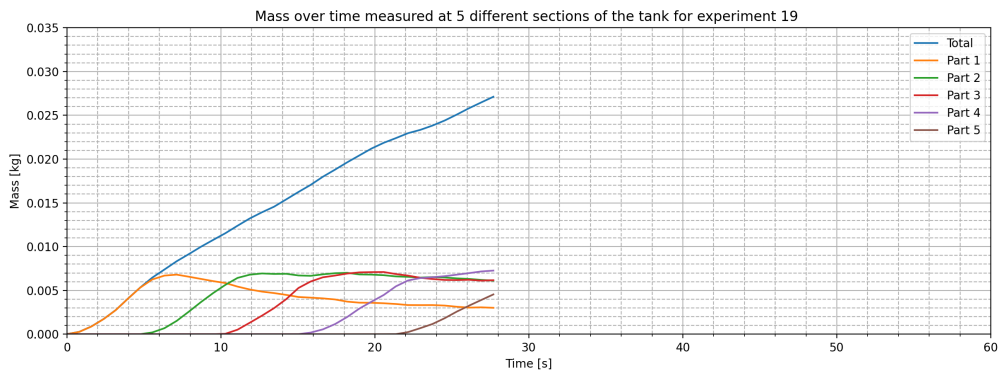


(c) Mass over time measured at 5 different sections of the tank for experiment 17

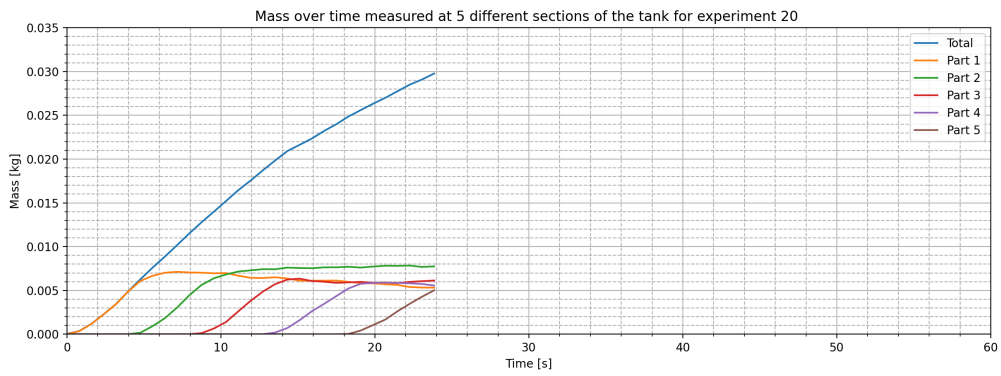
Figure E.6: Mass over time experiments 15, 16 and 17



(a) Mass over time measured at 5 different sections of the tank for experiment 18

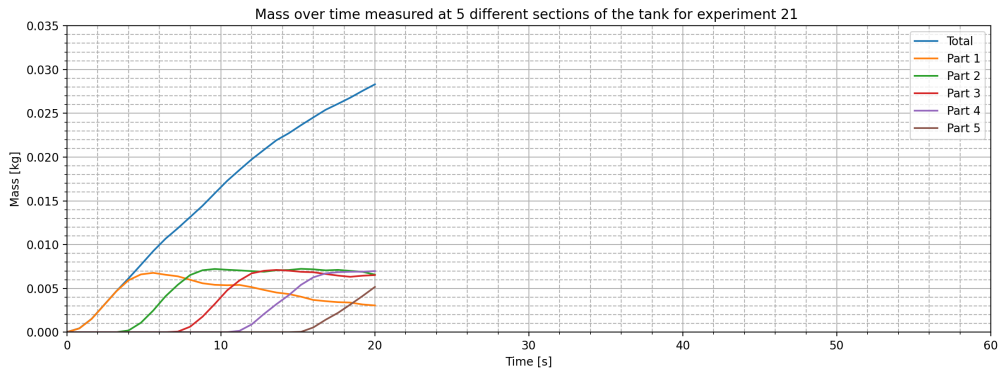


(b) Mass over time measured at 5 different sections of the tank for experiment 19

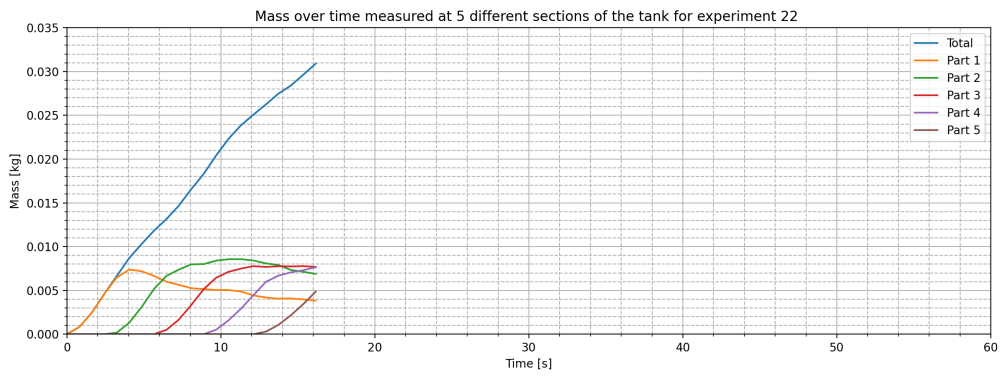


(c) Mass over time measured at 5 different sections of the tank for experiment 20

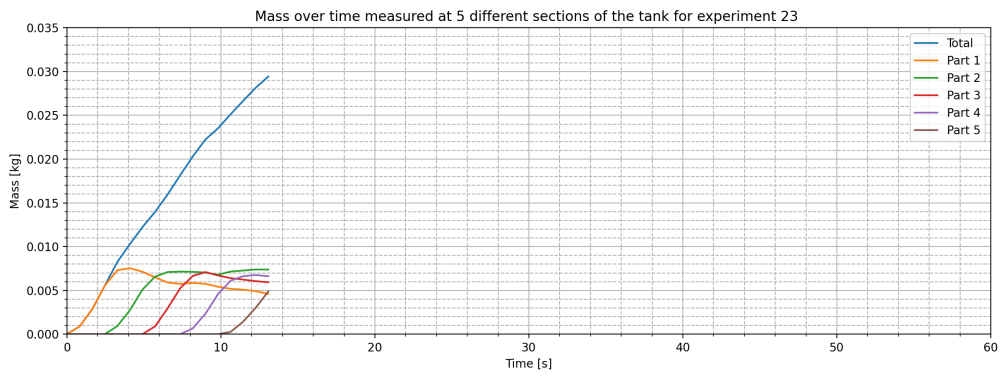
Figure E.7: Mass over time experiments 18, 19 and 20



(a) Mass over time measured at 5 different sections of the tank for experiment 21



(b) Mass over time measured at 5 different sections of the tank for experiment 22



(c) Mass over time measured at 5 different sections of the tank for experiment 23

Figure E.8: Mass over time experiments 21, 22 and 23

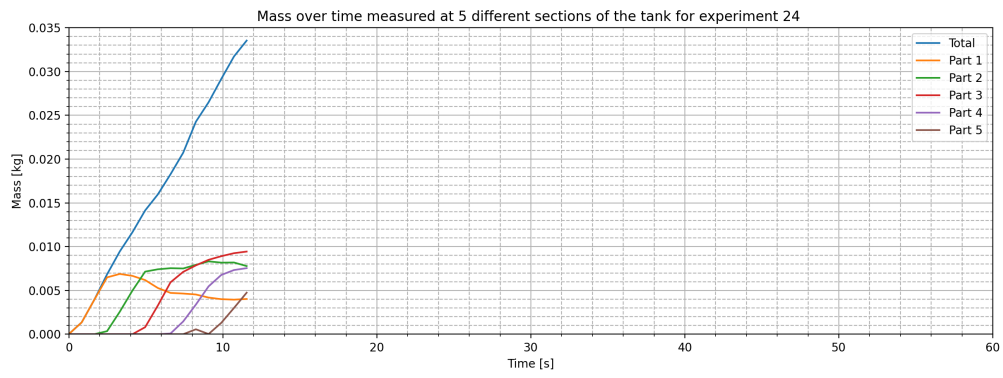
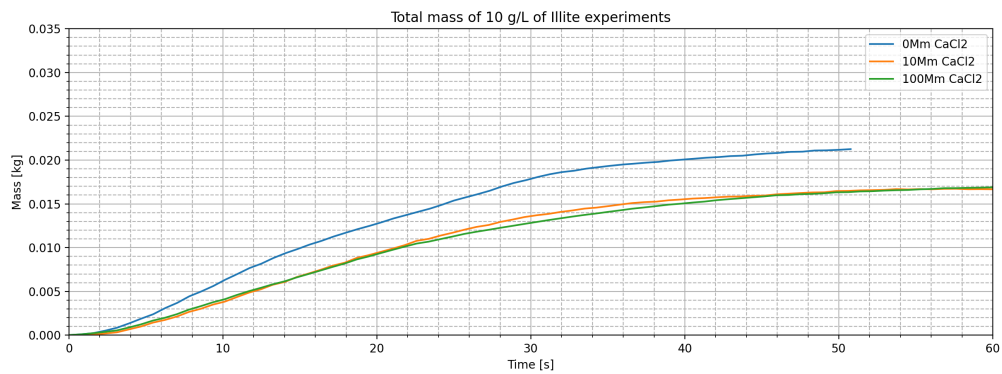


Figure E.9: Mass over time experiments 24

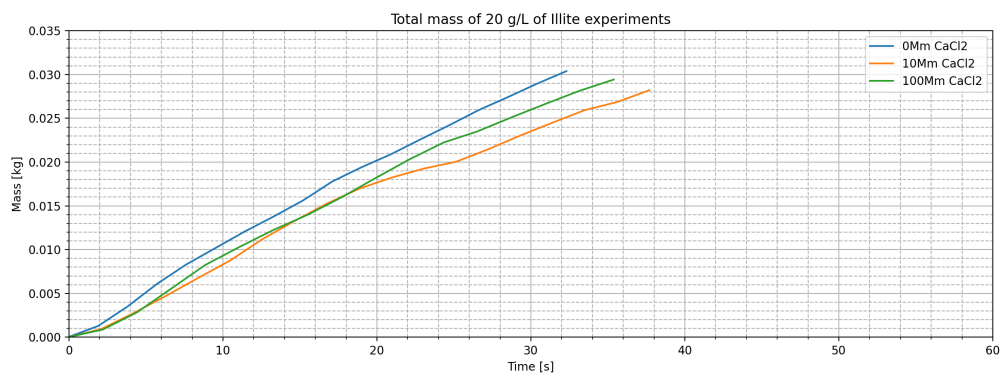
# F

## Mass over time compared with comparable experiments

### F.1. Total mass

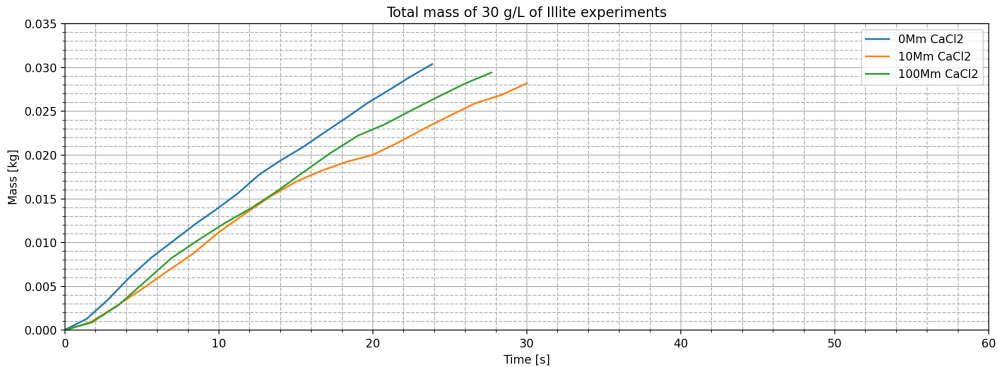


(a) Total mass of the experiments with 10 g/L of Illite

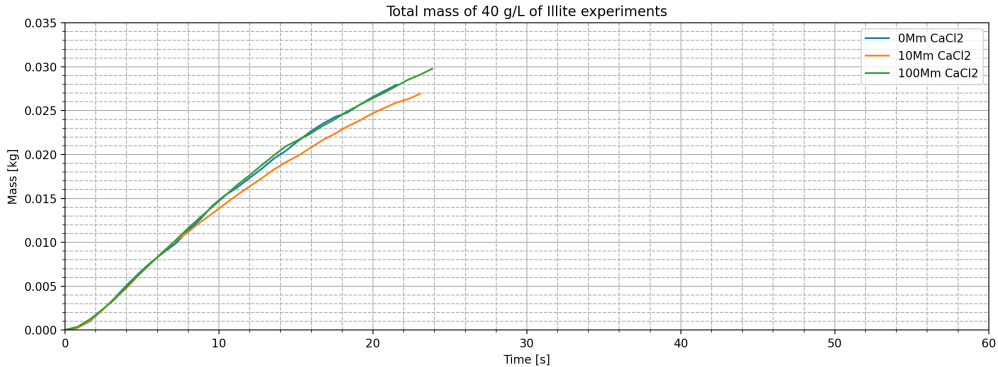


(b) Total mass of the experiments with 20 g/L of Illite

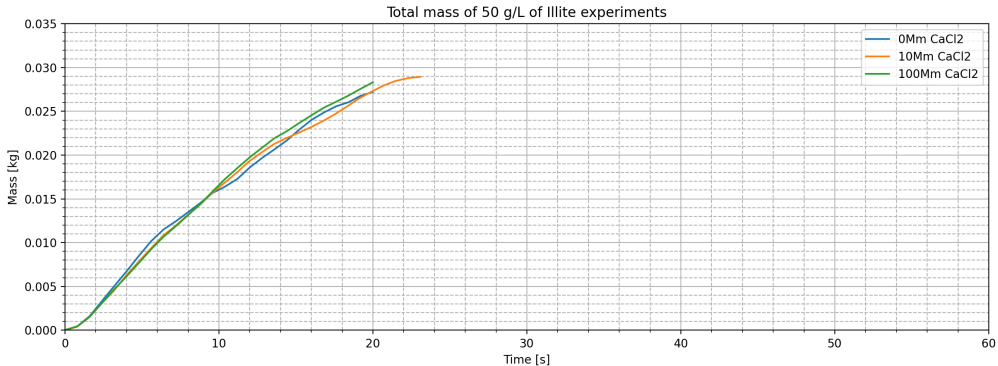
Figure F1: Total mass of experiments: 1, 2, 9, 10, 17 and 18



(a) Total mass of the experiments with 30 g/L of Illite



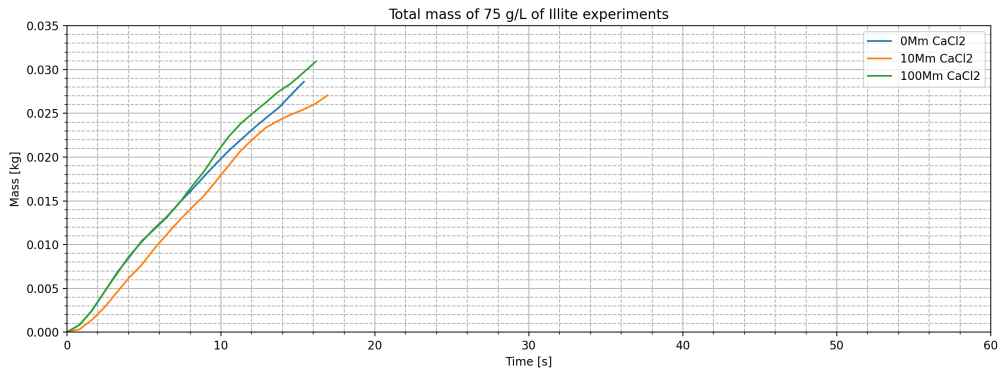
(b) Total mass of the experiments with 40 g/L of Illite



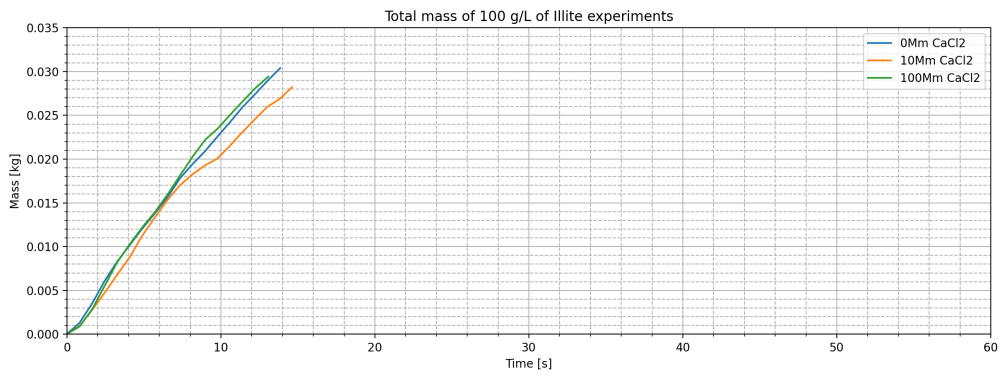
(c) Total mass of the experiments with 50 g/L of Illite

Figure E2: Total mass of experiments: 3, 4, 5, 11, 12, 13, 19, 20 and 21

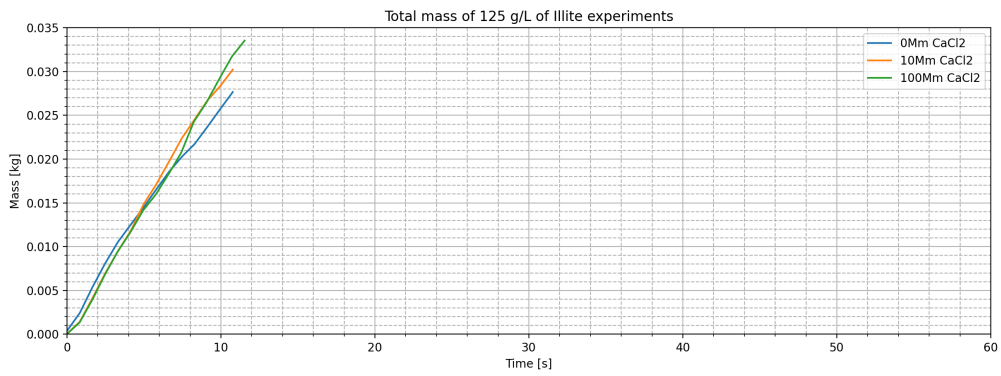




(a) Total mass of the experiments with 75 g/L of Illite



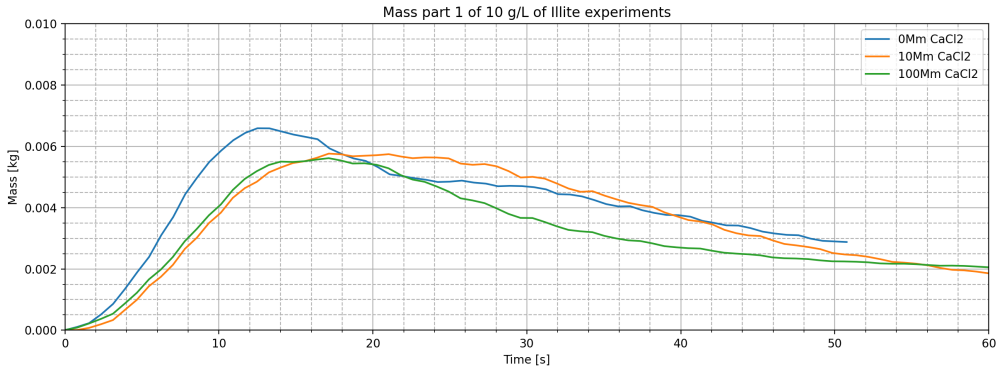
(b) Total mass of the experiments with 100 g/L of Illite



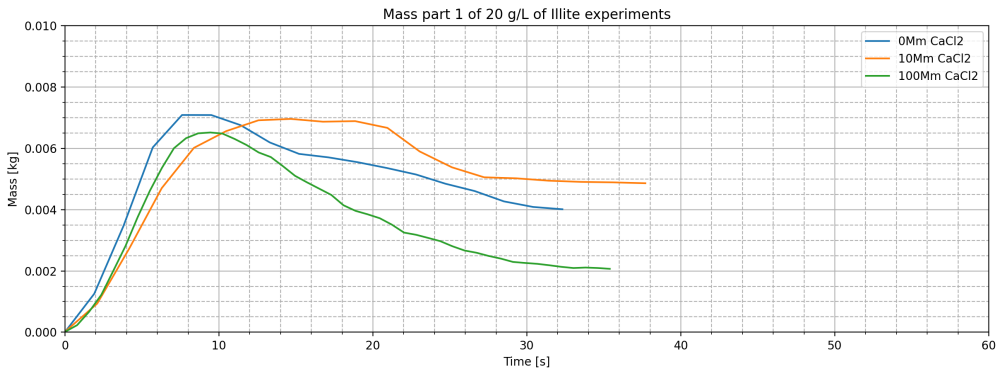
(c) Total mass of the experiments with 125 g/L of Illite

Figure E3: Total mass of experiments: 6,7,8, 14, 15, 16, 22, 23 and 24

F2. Part 1

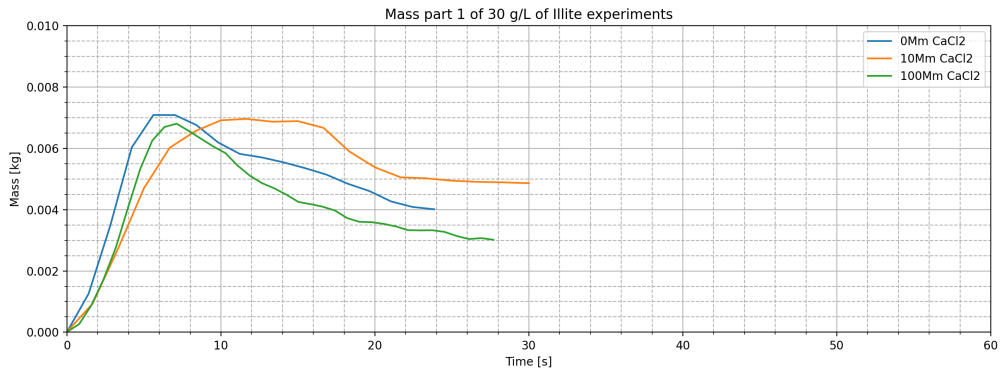


(a) Mass part 1 of the experiments with 10 g/L of Illite

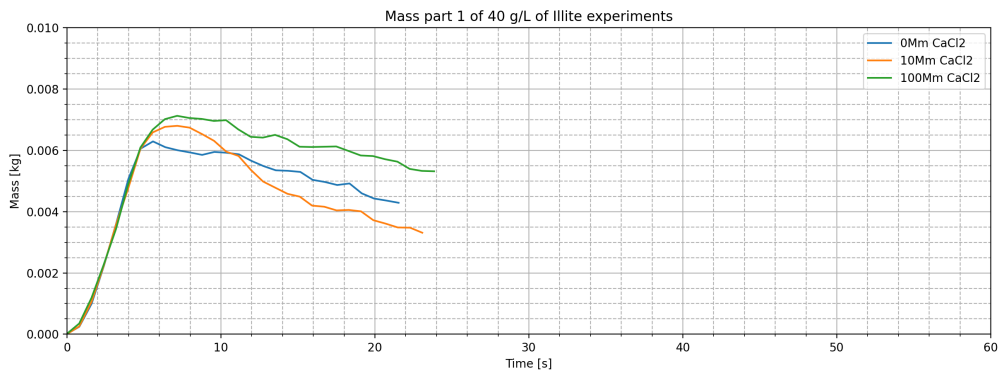


(b) Mass part 1 of the experiments with 20 g/L of Illite

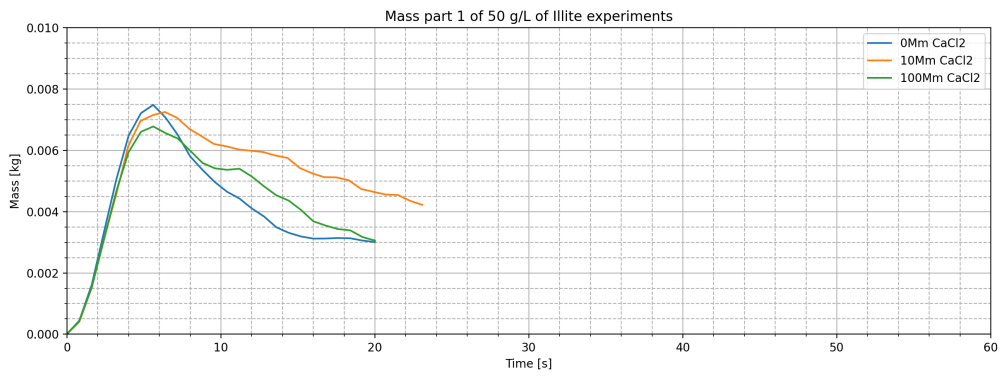
Figure F4: Mass part 1 of experiments: 1, 2, 9, 10, 17 and 18



(a) Mass part 1 of the experiments with 30 g/L of Illite

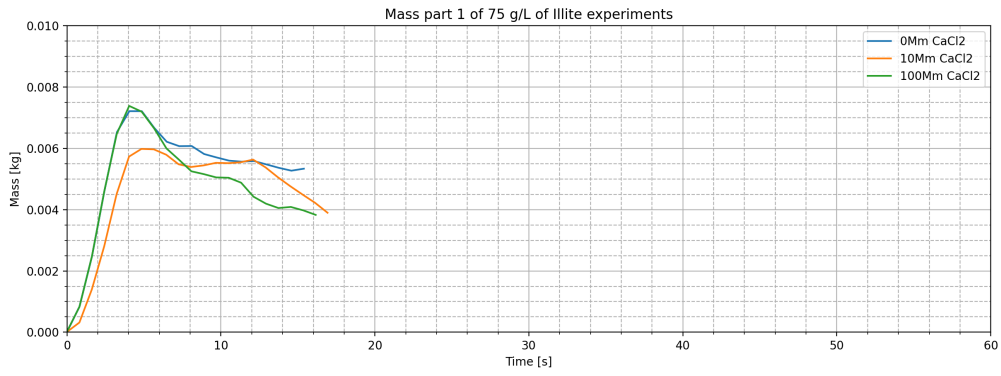


(b) Mass part 1 of the experiments with 40 g/L of Illite

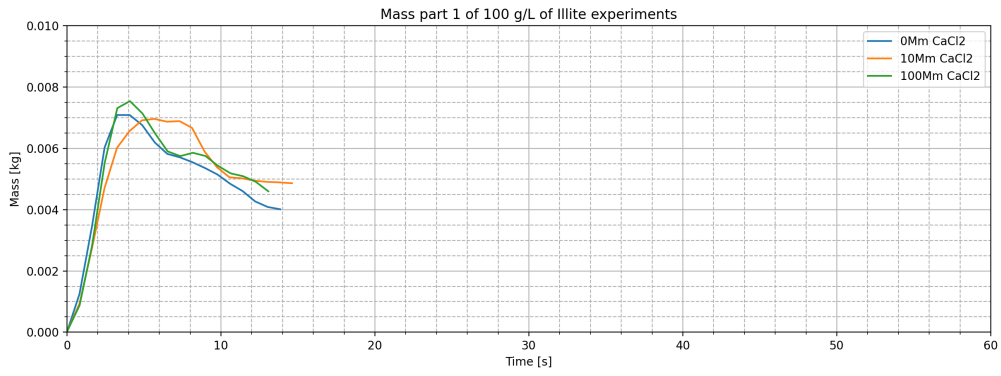


(c) Mass part 1 of the experiments with 50 g/L of Illite

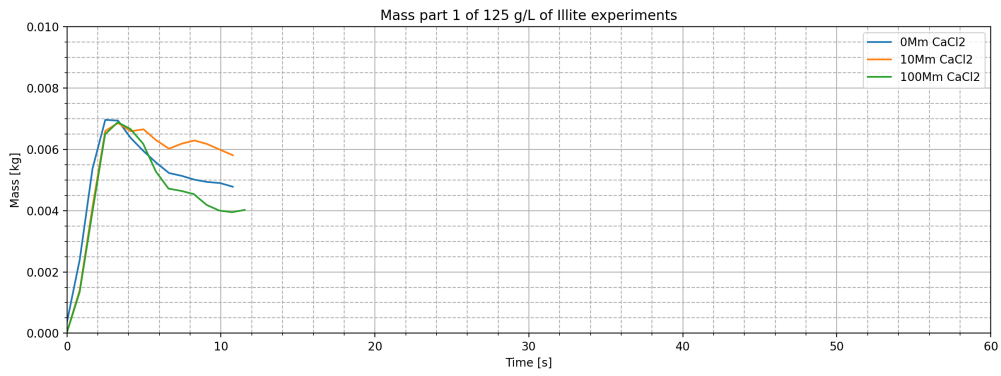
Figure E5: Mass part 1 of experiments: 3, 4, 5, 11, 12, 13, 19, 20 and 21



(a) Mass part 1 of the experiments with 75 g/L of Illite



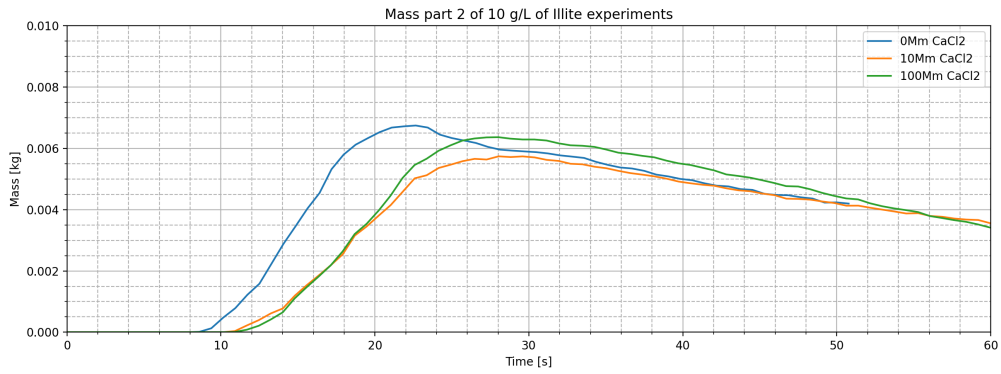
(b) Mass part 1 of the experiments with 100 g/L of Illite



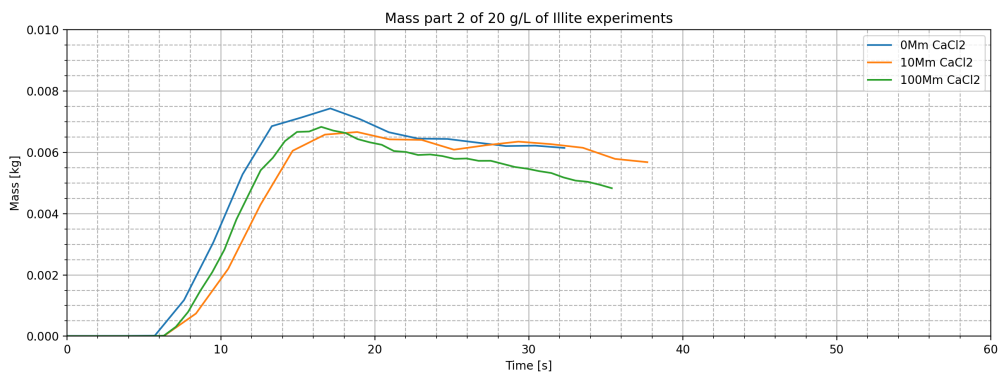
(c) Mass part 1 of the experiments with 125 g/L of Illite

Figure E6: Mass part 1 of experiments: 6,7,8, 14, 15, 16, 22, 23 and 24

**E3. Part 2**

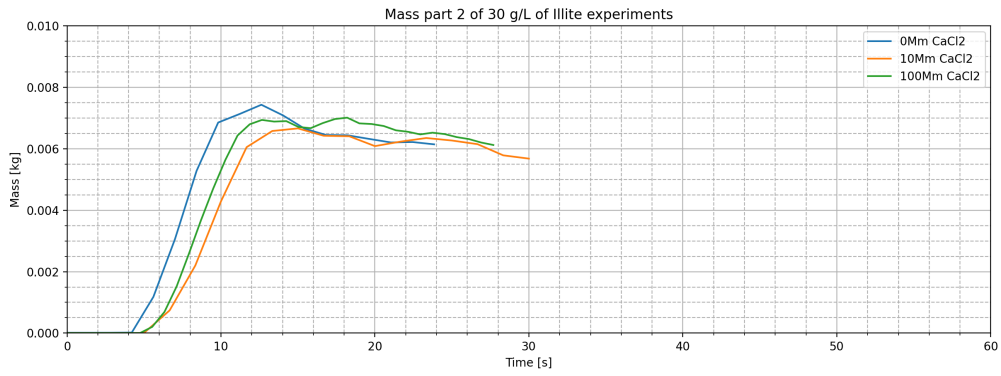


(a) Mass part 2 of the experiments with 10 g/L of Illite

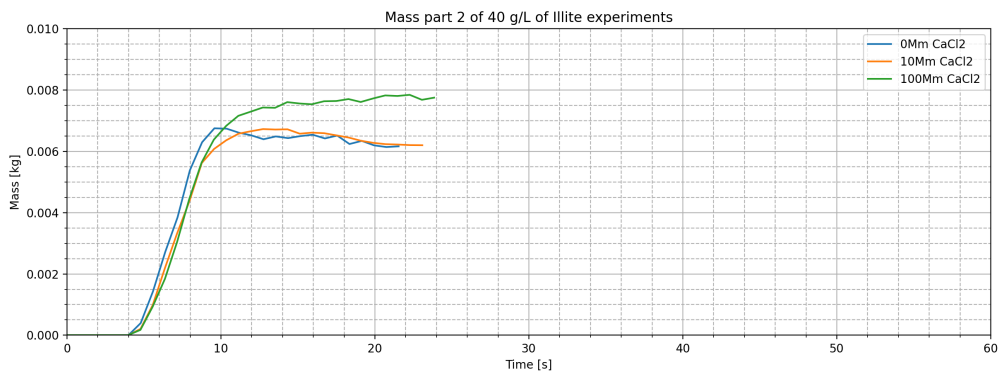


(b) Mass part 2 of the experiments with 20 g/L of Illite

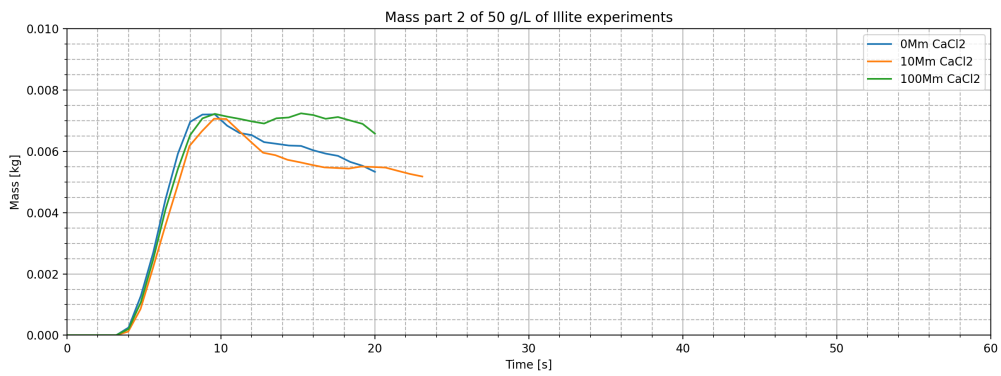
Figure E7: Mass part 2 of experiments: 1, 2, 9, 10, 17 and 18



(a) Mass part 2 of the experiments with 30 g/L of Illite

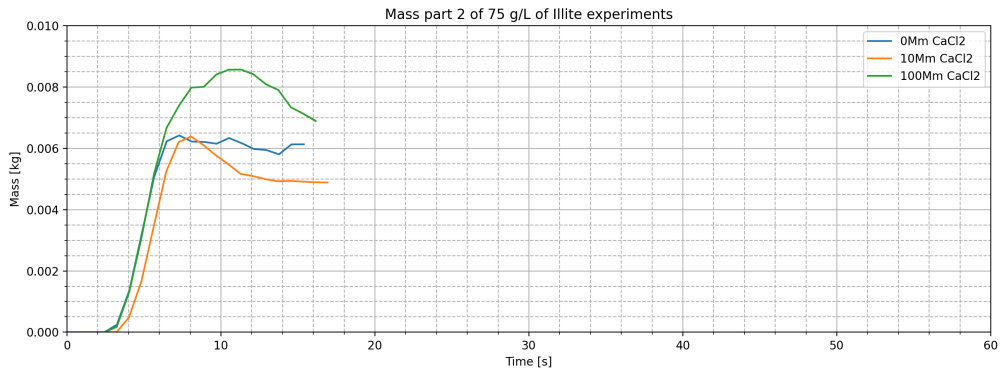


(b) Mass part 2 of the experiments with 40 g/L of Illite

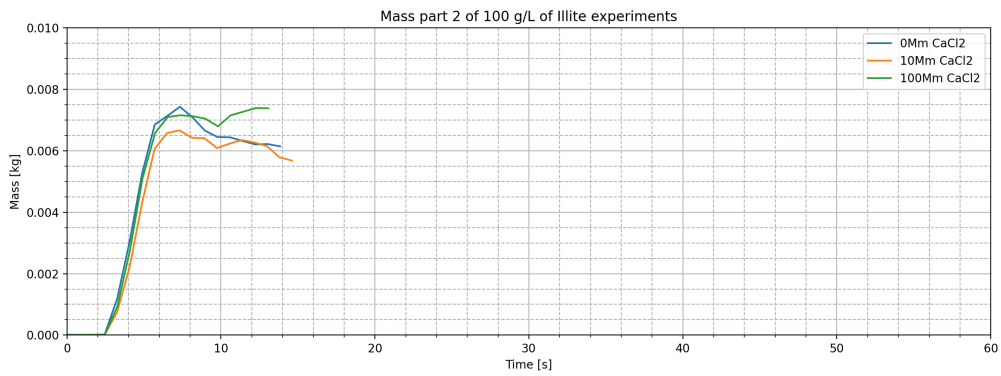


(c) Mass part 2 of the experiments with 50 g/L of Illite

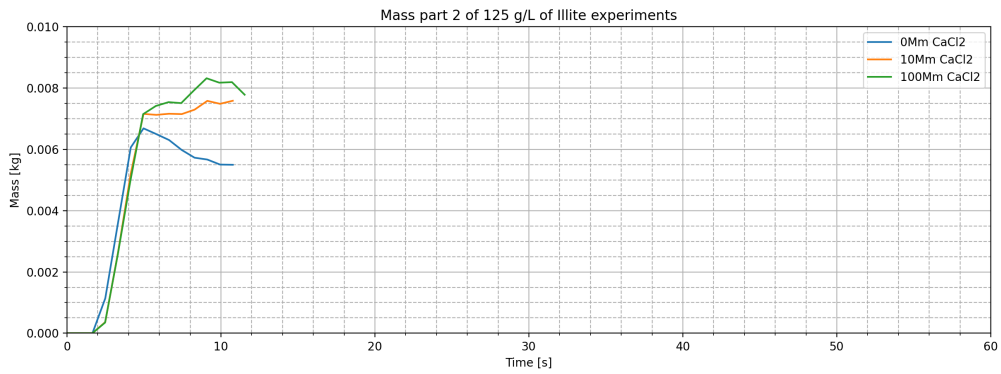
Figure E8: Mass part 2 of experiments: 3, 4, 5, 11, 12, 13, 19, 20 and 21



(a) Mass part 2 of the experiments with 75 g/L of Illite



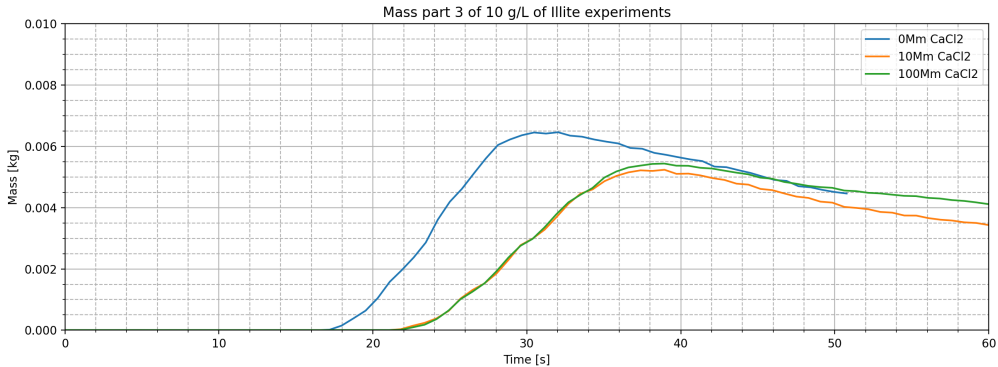
(b) Mass part 2 of the experiments with 100 g/L of Illite



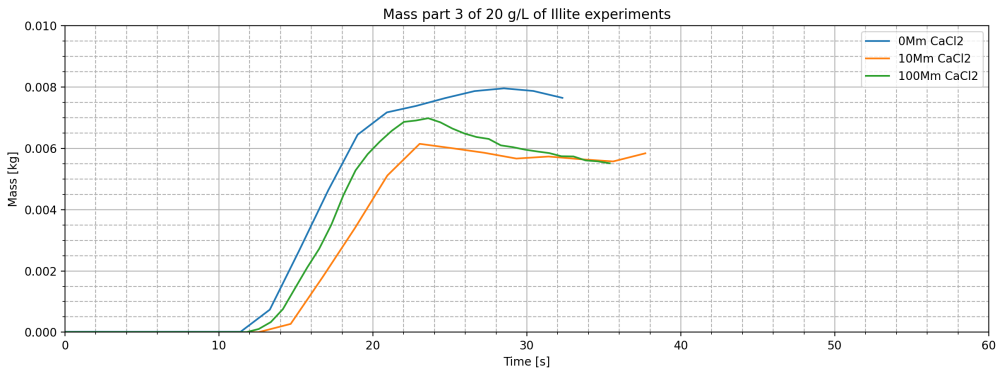
(c) Mass part 2 of the experiments with 125 g/L of Illite

Figure E9: Mass part 2 of experiments: 6,7,8, 14, 15, 16, 22, 23 and 24

### F4. Part 3



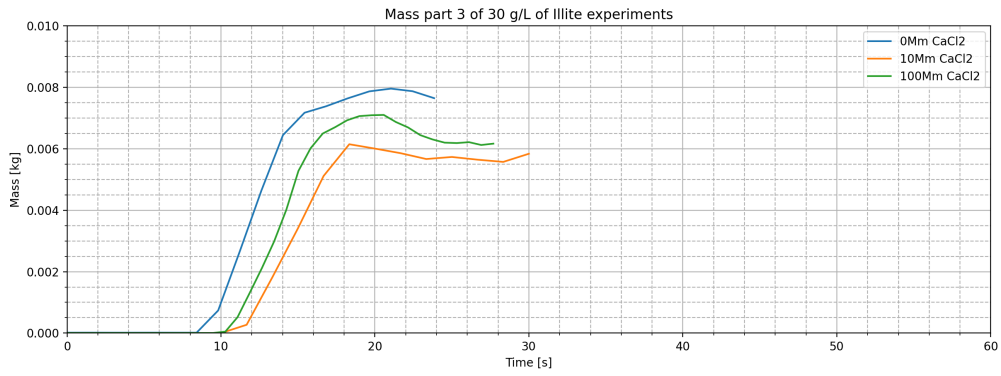
(a) Mass part 3 of the experiments with 10 g/L of Illite



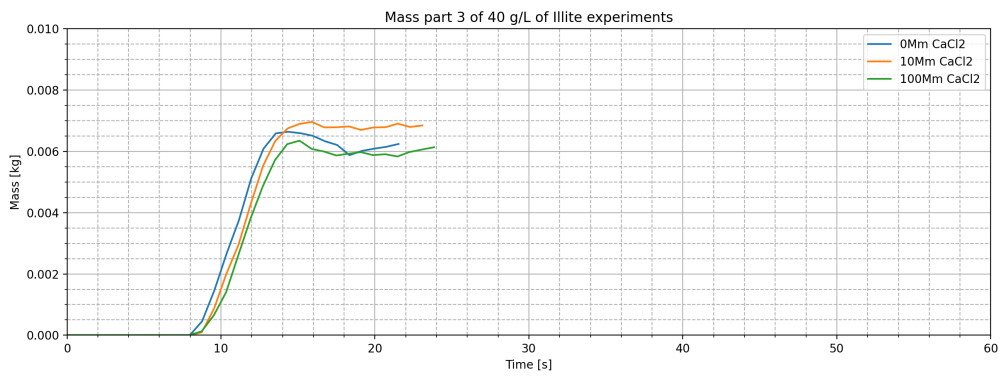
(b) Mass part 3 of the experiments with 20 g/L of Illite

Figure F10: Mass part 3 of experiments: 1, 2, 9, 10, 17 and 18

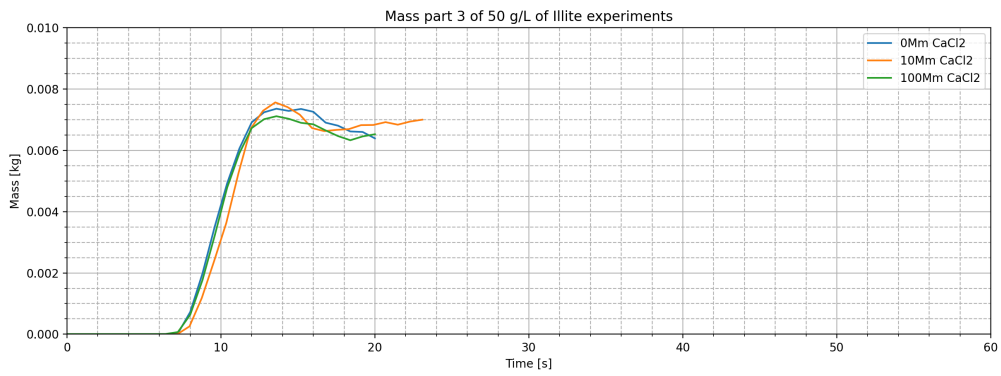




(a) Mass part 3 of the experiments with 30 g/L of Illite

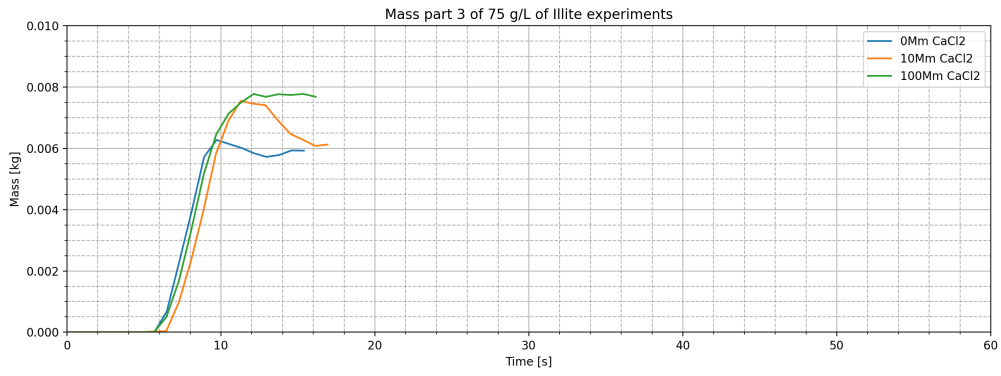


(b) Mass part 3 of the experiments with 40 g/L of Illite

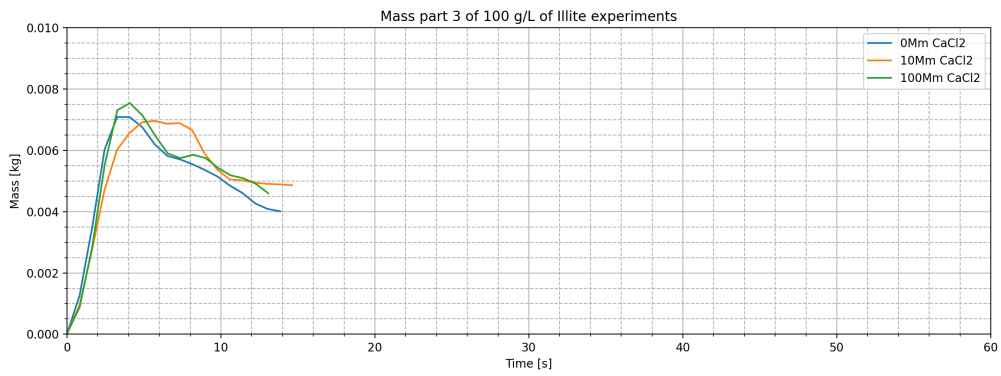


(c) Mass part 3 of the experiments with 50 g/L of Illite

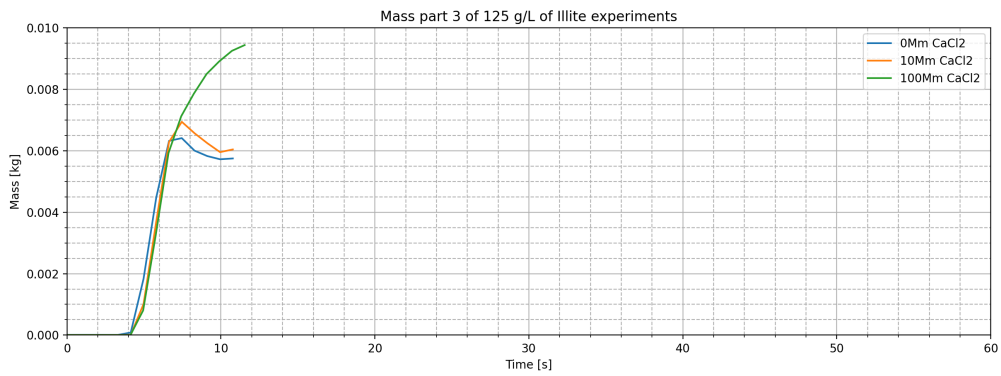
Figure E11: Mass part 3 of experiments: 3, 4, 5, 11, 12, 13, 19, 20 and 21



(a) Mass part 3 of the experiments with 75 g/L of Illite



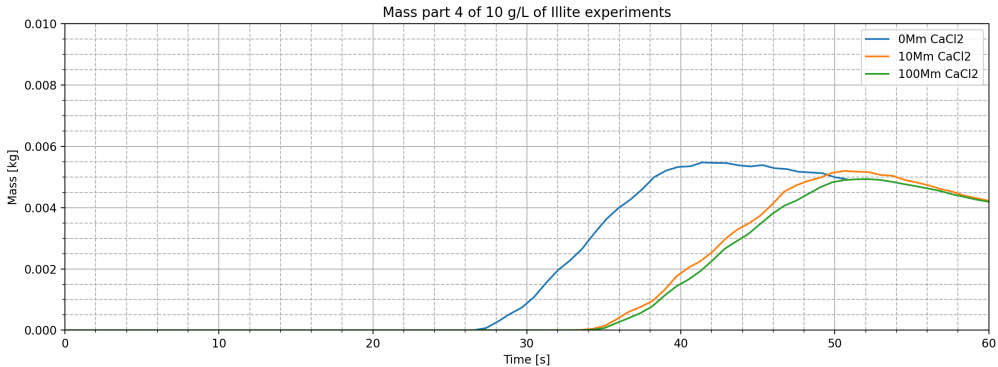
(b) Mass part 3 of the experiments with 100 g/L of Illite



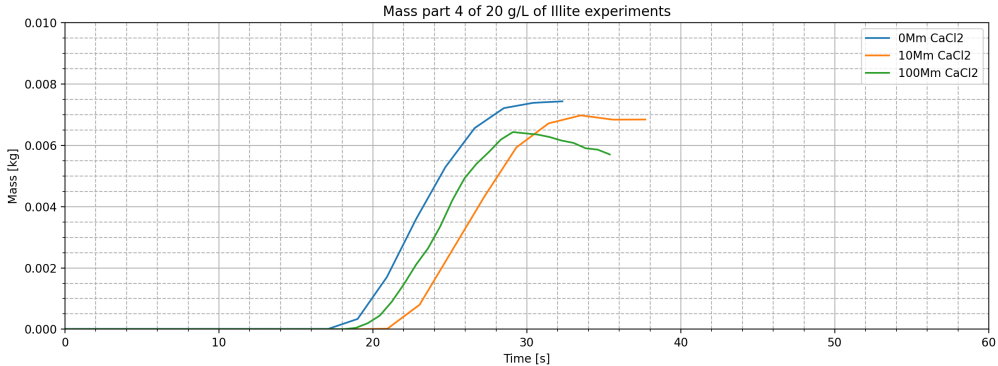
(c) Mass part 3 of the experiments with 125 g/L of Illite

Figure E12: Mass part 3 of experiments: 6,7,8, 14, 15, 16, 22, 23 and 24

### E5. Part 4

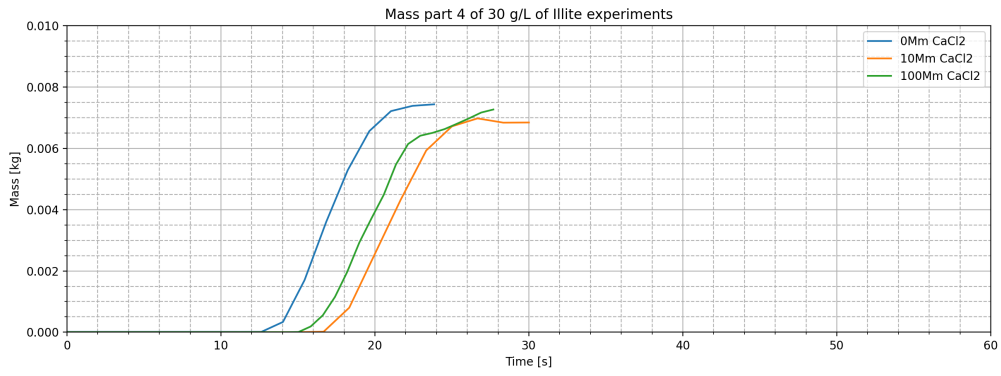


(a) Mass part 4 of the experiments with 10 g/L of Illite

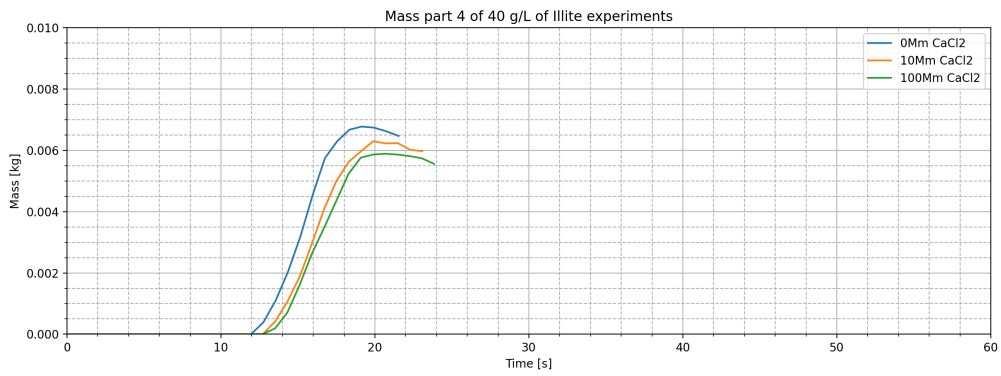


(b) Mass part 4 of the experiments with 20 g/L of Illite

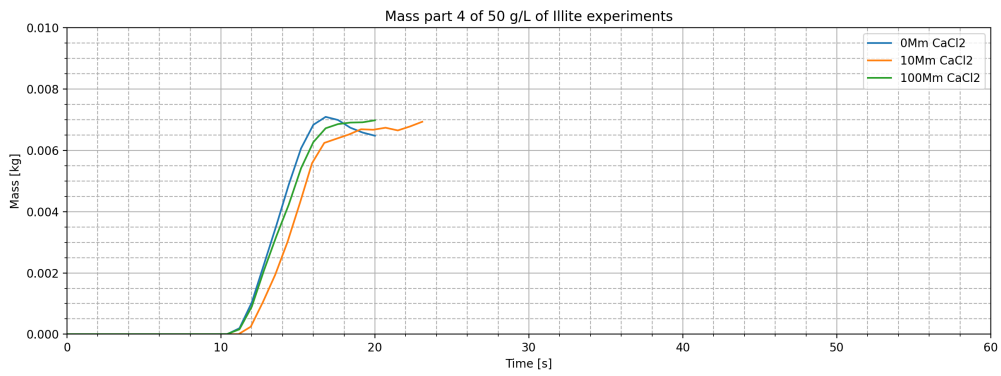
Figure E13: Mass part 4 of experiments: 1, 2, 9, 10, 17 and 18



(a) Mass part 4 of the experiments with 30 g/L of Illite

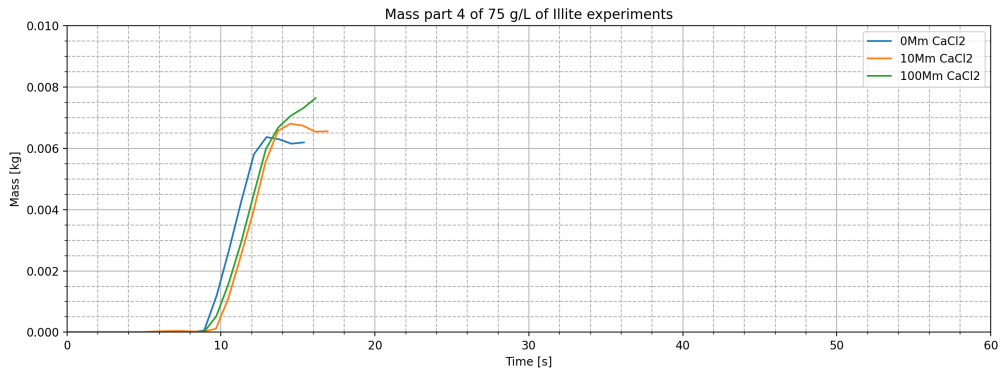


(b) Mass part 4 of the experiments with 40 g/L of Illite

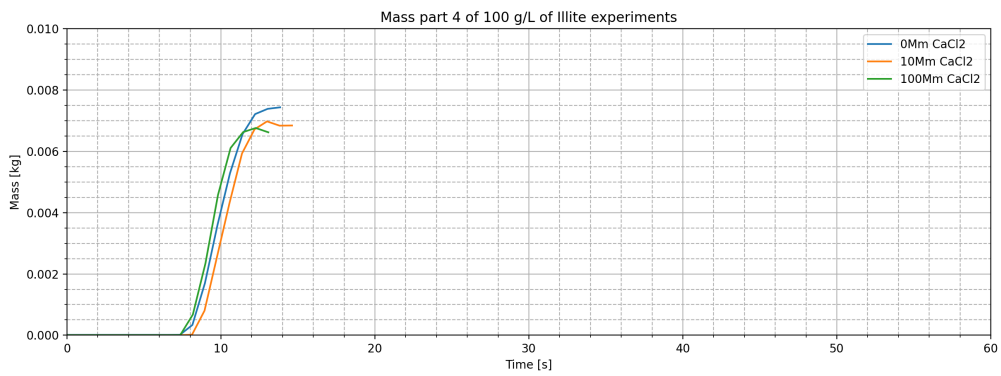


(c) Mass part 4 of the experiments with 50 g/L of Illite

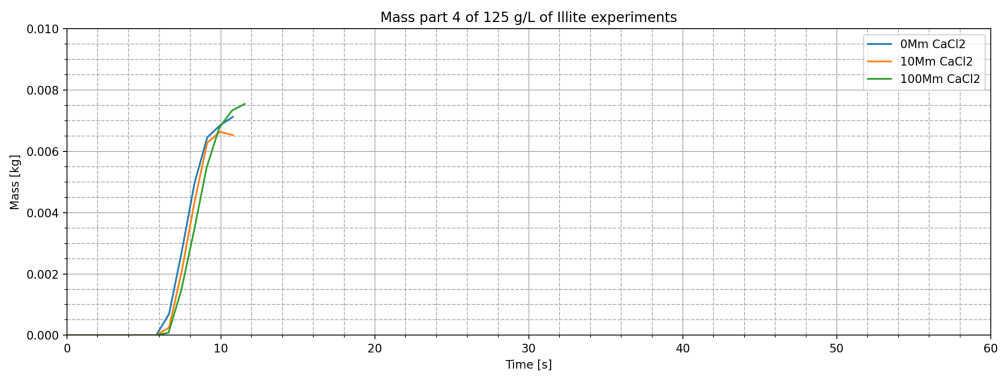
Figure E14: Mass part 4 of experiments: 3, 4, 5, 11, 12, 13, 19, 20 and 21



(a) Mass part 4 of the experiments with 75 g/L of Illite



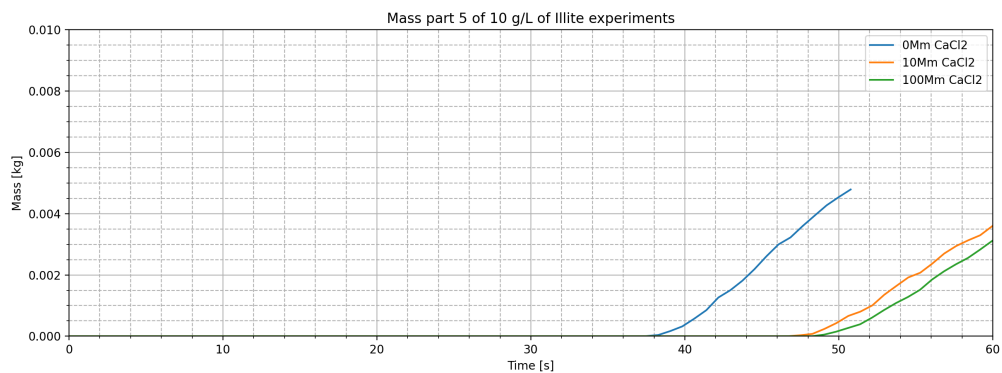
(b) Mass part 4 of the experiments with 100 g/L of Illite



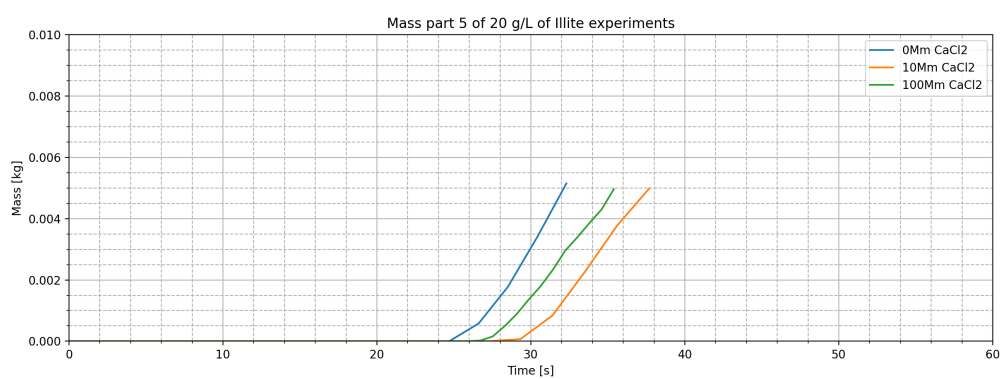
(c) Mass part 4 of the experiments with 125 g/L of Illite

Figure E15: Mass part 4 of experiments: 6,7,8, 14, 15, 16, 22, 23 and 24

### F6. Part 5

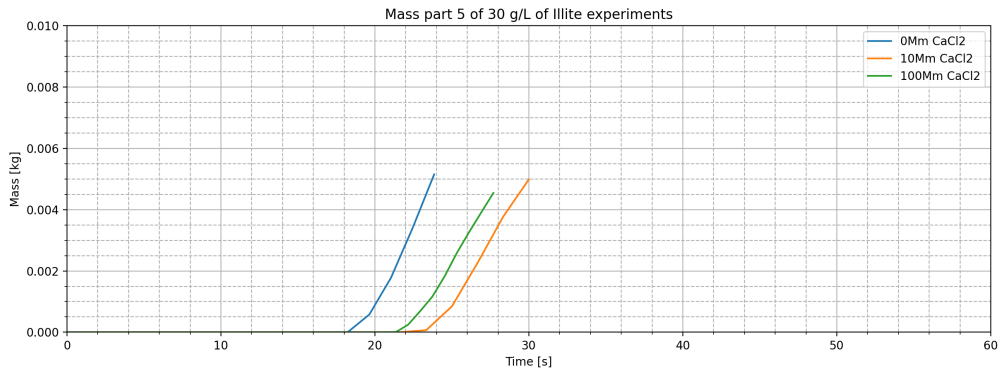


(a) Mass part 5 of the experiments with 10 g/L of Illite

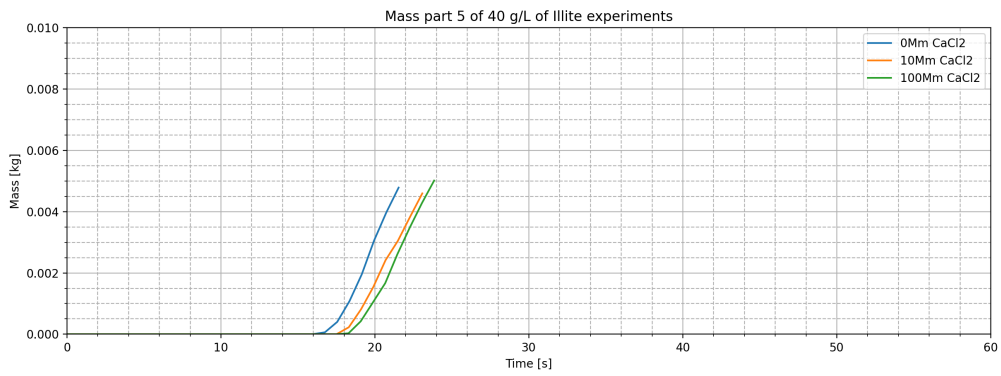


(b) Mass part 5 of the experiments with 20 g/L of Illite

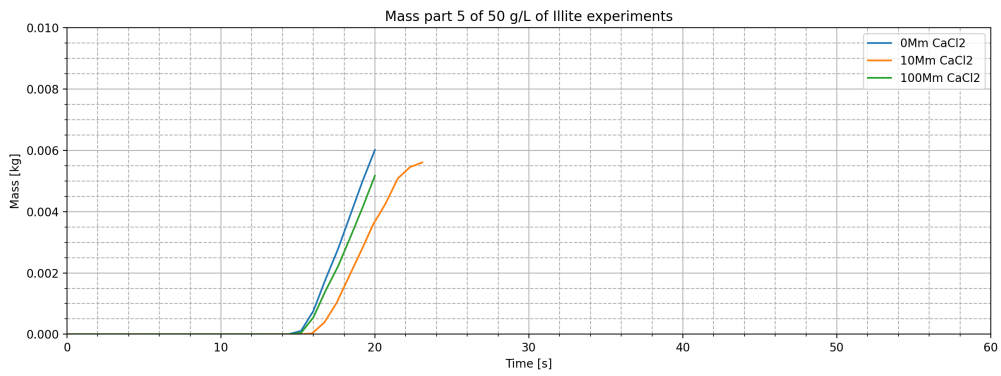
Figure F16: Mass part 5 of experiments: 1, 2, 9, 10, 17 and 18



(a) Mass part 5 of the experiments with 30 g/L of Illite

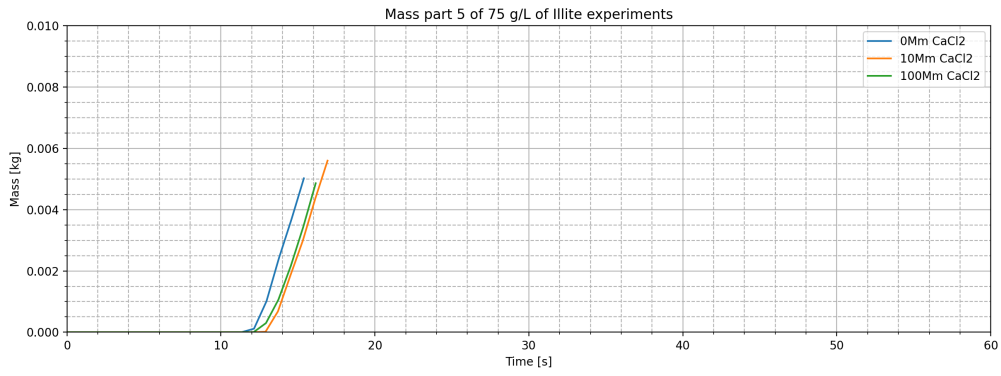


(b) Mass part 5 of the experiments with 40 g/L of Illite

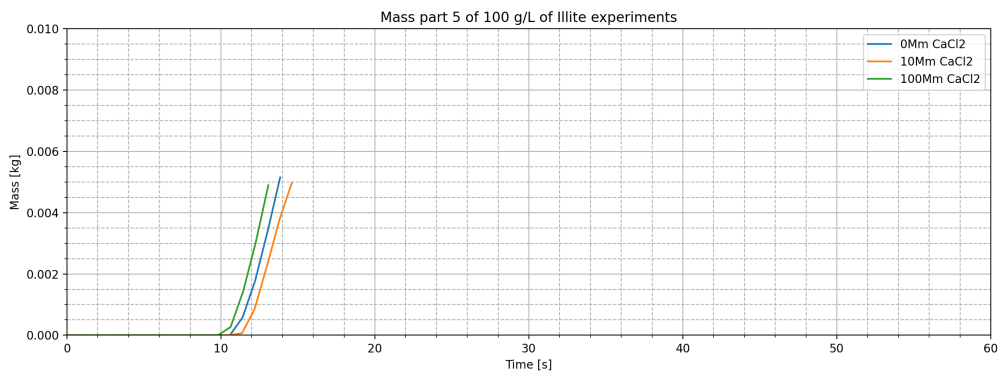


(c) Mass part 5 of the experiments with 50 g/L of Illite

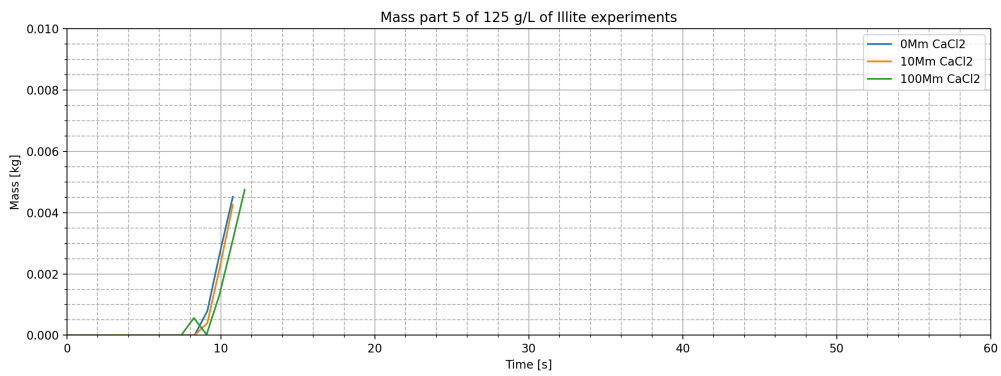
Figure E17: Mass part 5 of experiments: 3, 4, 5, 11, 12, 13, 19, 20 and 21



(a) Mass part 5 of the experiments with 75 g/L of Illite



(b) Mass part 5 of the experiments with 100 g/L of Illite



(c) Mass part 5 of the experiments with 125 g/L of Illite

Figure E18: Mass part 5 of experiments: 6,7,8, 14, 15, 16, 22, 23 and 24



# G

Average height head

	0 mM	10 mM	100 mM	0 mM 1 day bed	0 mM 2 day bed	10 mM 1 day bed	10 mM 2 day bed	Zetag 8125 mixing section	Zetag 8125 outflow section	Zetag 4124 mixing section 0 mM	Zetag 4124 outflow section 0 mM	Zetag 4124 mixing section 10 mM	Zetag 4124 outflow section 10 mM
10 g/L	0,181	0,191	0,179	0,168	0,173	0,175	0,181	0,174	0,180	0,204	0,156	0,183	0,170
20 g/L	0,185	0,184	0,179										
30 g/L	0,182	0,189	0,176										
40 g/L	0,184	0,187	0,175										
50 g/L	0,180	0,185	0,179	0,175	0,175	0,179	0,194						
75 g/L	0,183	0,178	0,168										
100 g/L	0,172	0,183	0,173	0,164	0,174	0,180	0,191	0,178	0,179	0,183	0,171	0,230	0,177
125 g/L	0,177	0,177	0,174										

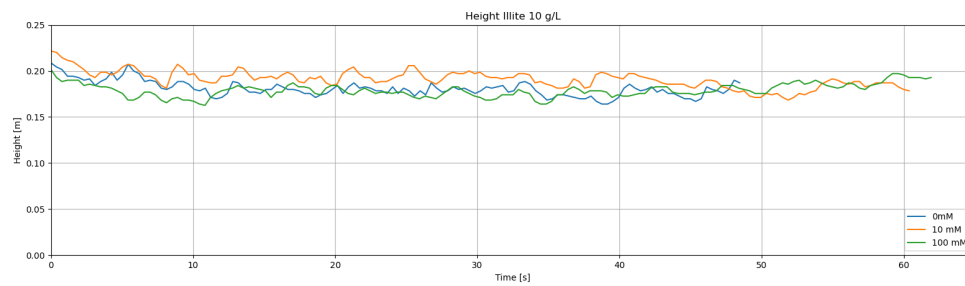
Table G.1.: Average height head [m]

	0 mM	10 mM	100 mM	0 mM 1 day bed	0 mM 2 day bed	10 mM 1 day bed	10 mM 2 day bed	Zetag 8125 mixing section	Zetag 8125 outflow section	Zetag 4124 mixing section 0 mM	Zetag 4124 outflow section 0 mM	Zetag 4124 mixing section 10 mM	Zetag 4124 outflow section 10 mM
10 g/L	bm	+6%	-1%	-7%	-4%	-3%	0%	-4%	0%	+13%	-14%	+1%	-6%
20 g/L	bm	0%	-3%										
30 g/L	bm	+4%	-3%										
40 g/L	bm	+2%	-5%										
50 g/L	bm	+3%	0%	-3%	-3%	0%	+8%						
75 g/L	bm	-3%	-8%										
100 g/L	bm	+6%	+1%	-5%	+1%	+5%	+11%	+3%	+4%	+6%	-1%	+33%	+3%
125 g/L	bm	0%	-2%										

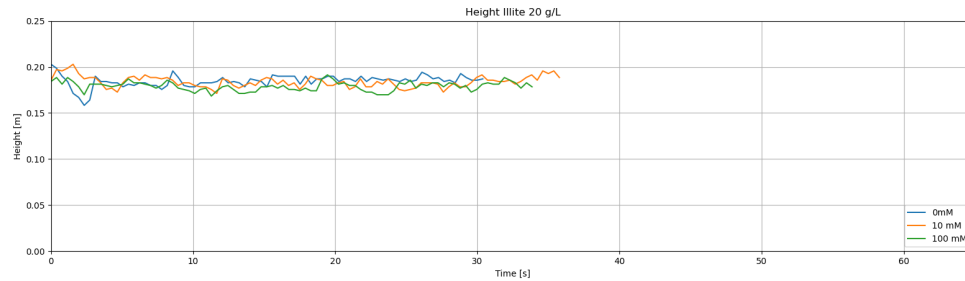
Table G.2.: Average height head [m], compared with benchmark settings of 0 mM CaCl<sub>2</sub>

# H

## Height profiles head

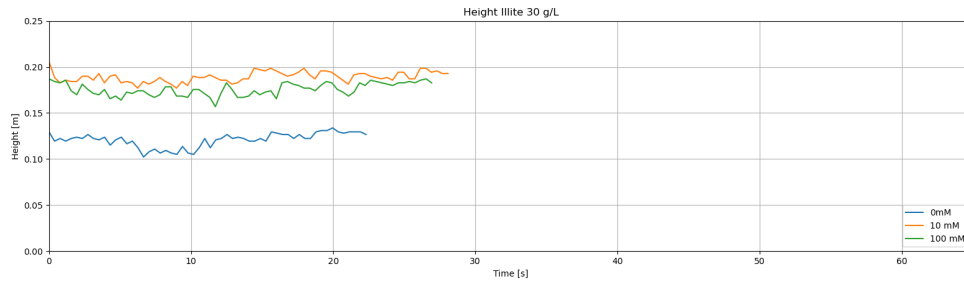


(a) Height head experiments with 10 g/L of Illite

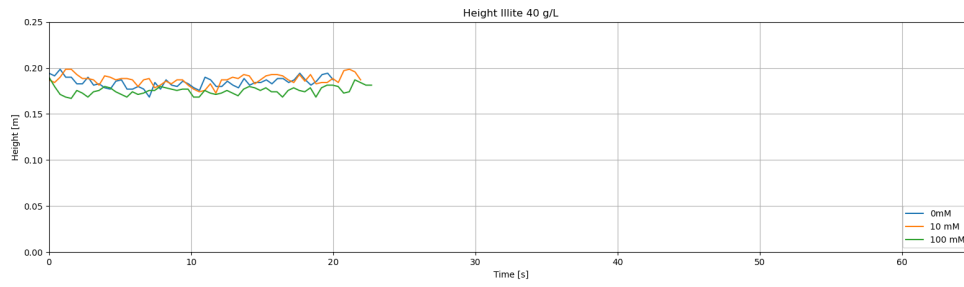


(b) Height head experiments with 20 g/L of Illite

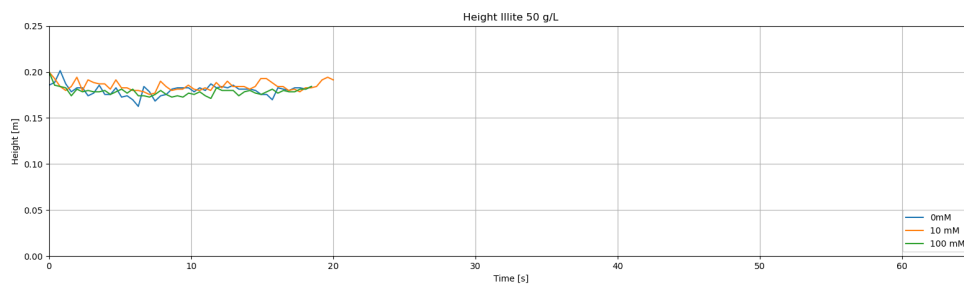
Figure H.1: Height heads experiments: 1, 2, 9, 10, 17 and 18



(a) Height head experiments with 30 g/L of Illite

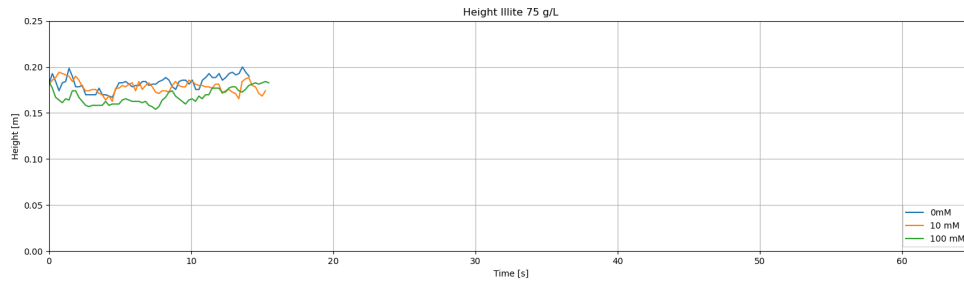


(b) Height head experiments with 40 g/L of Illite

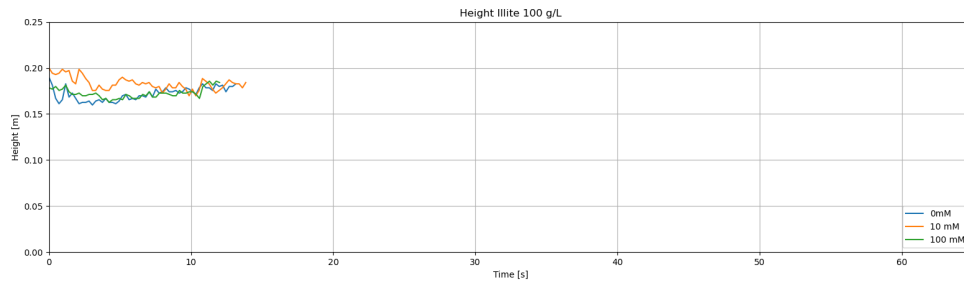


(c) Height head experiments with 50 g/L of Illite

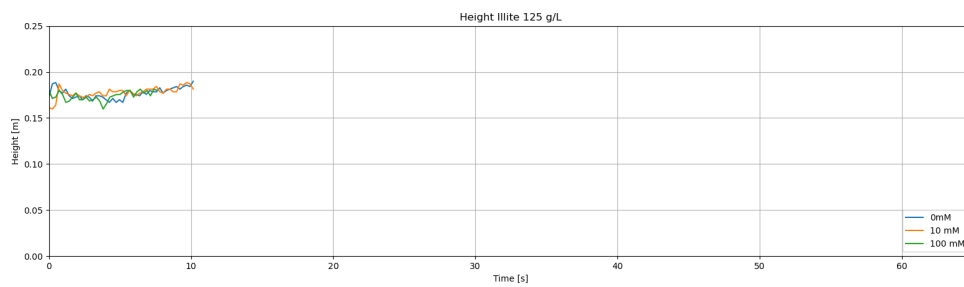
Figure H.2: Height heads experiments: 3, 4, 5, 11, 12, 13, 19, 20 and 21



(a) Height head experiments with 75 g/L of Illite

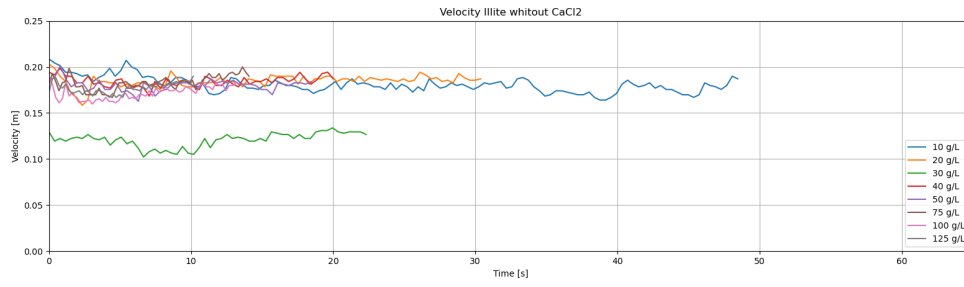


(b) Height head experiments with 100 g/L of Illite

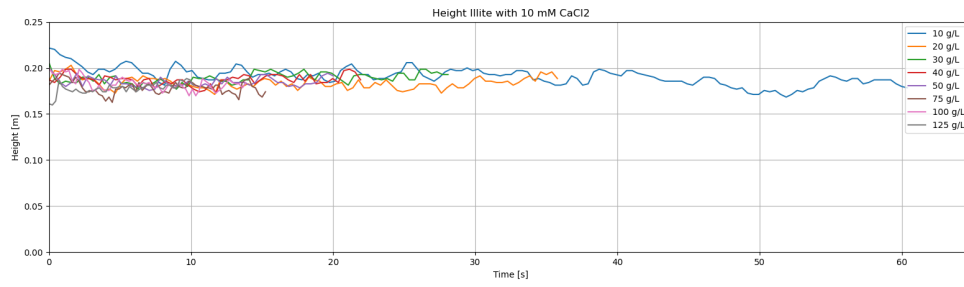


(c) Height head head experiments with 125 g/L of Illite

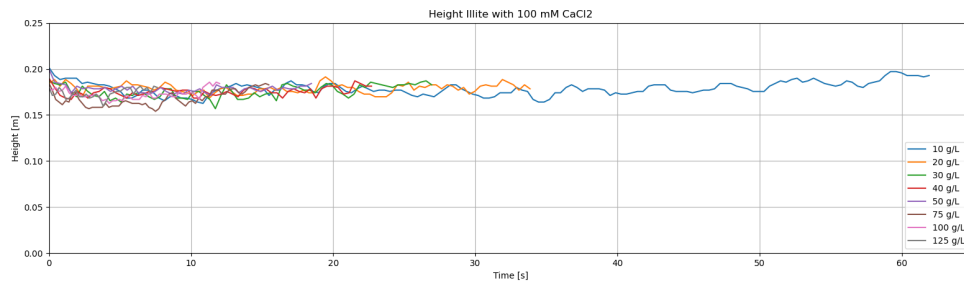
Figure H.3: Height heads experiments: 6,7,8, 14, 15, 16, 22, 23 and 24



(a) Height head experiments with 0 mM  $CaCl_2$

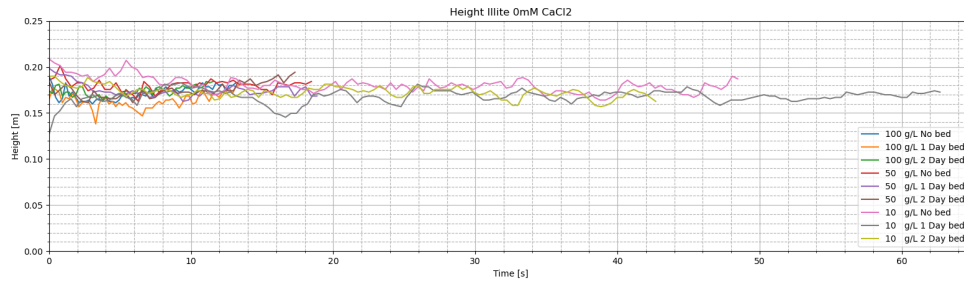


(b) Height head experiments with 10 mM  $CaCl_2$

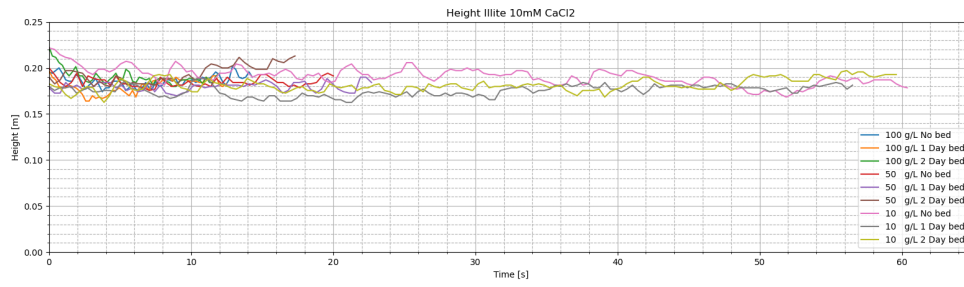


(c) Height head experiments with 100 mM  $CaCl_2$

Figure H.4: Height heads experiments: 1 up to 24

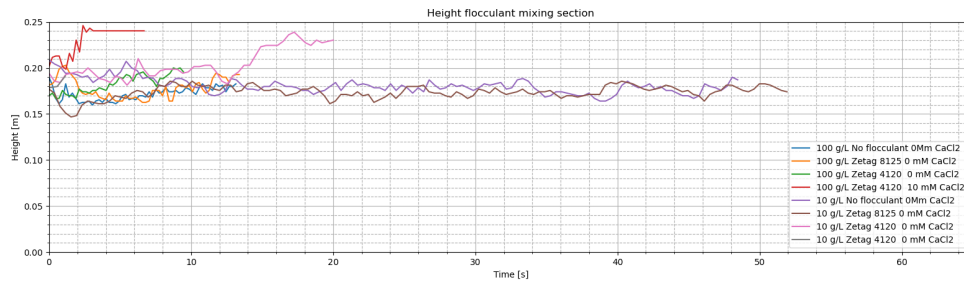


(a) Height head experiments with 0 mM  $CaCl_2$

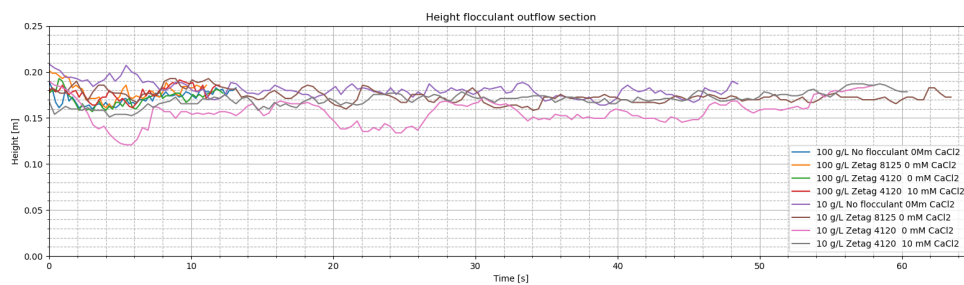


(b) Height head experiments with 10 mM  $CaCl_2$

Figure H.5: Height heads experiments with pre-existing bed: 25 up to 30<sub>2</sub>



(a) Height head experiments with flocculant in mixing section



(b) Height head experiments with flocculant in outflow section

Figure H.6: Height heads experiments with flocculant: 31 up to 42

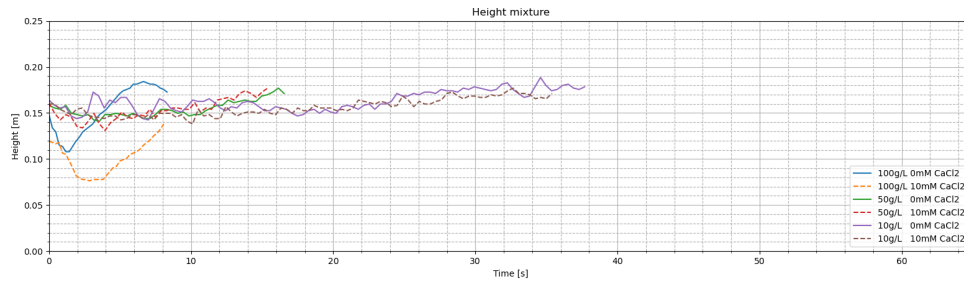


Figure H.7: Height heads experiments with artificial mixture: 43 up to 48





# Calibration curves

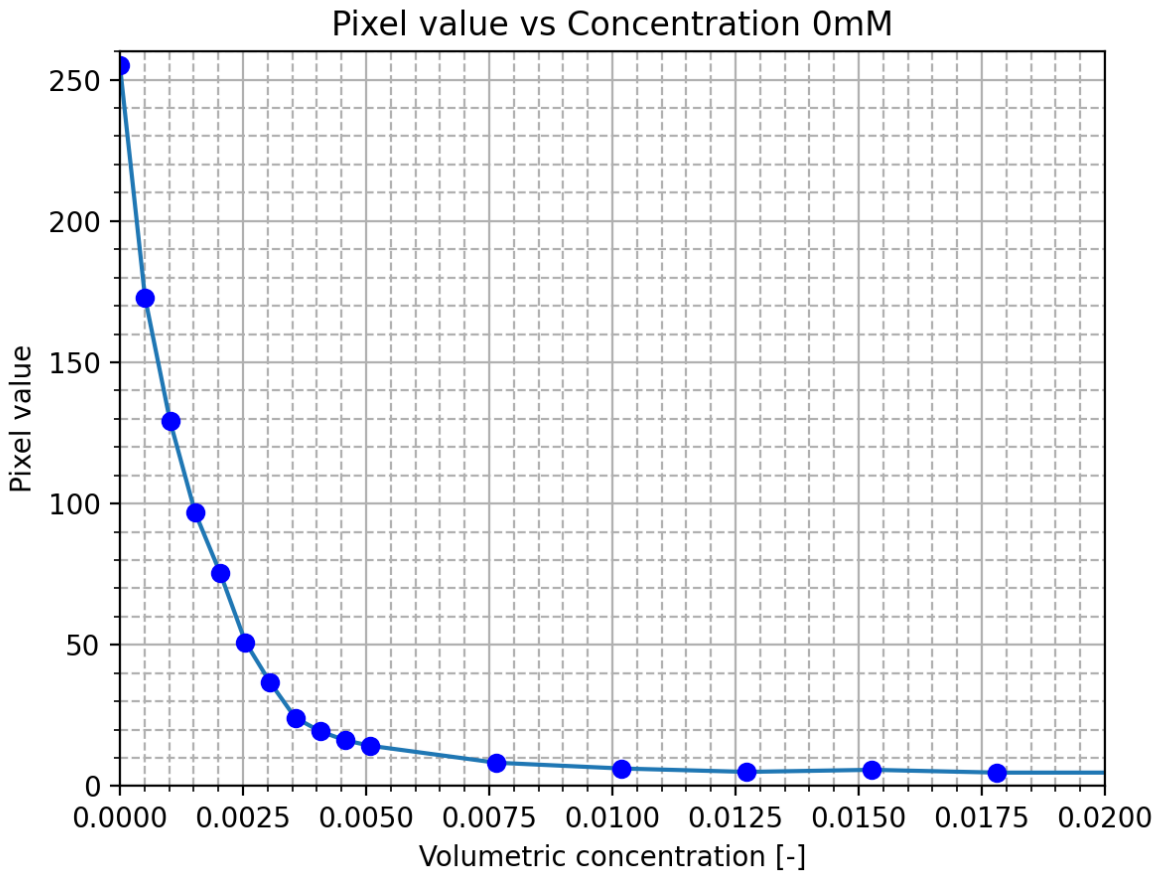


Figure I.1: Calibration curve without  $CaCl_2$

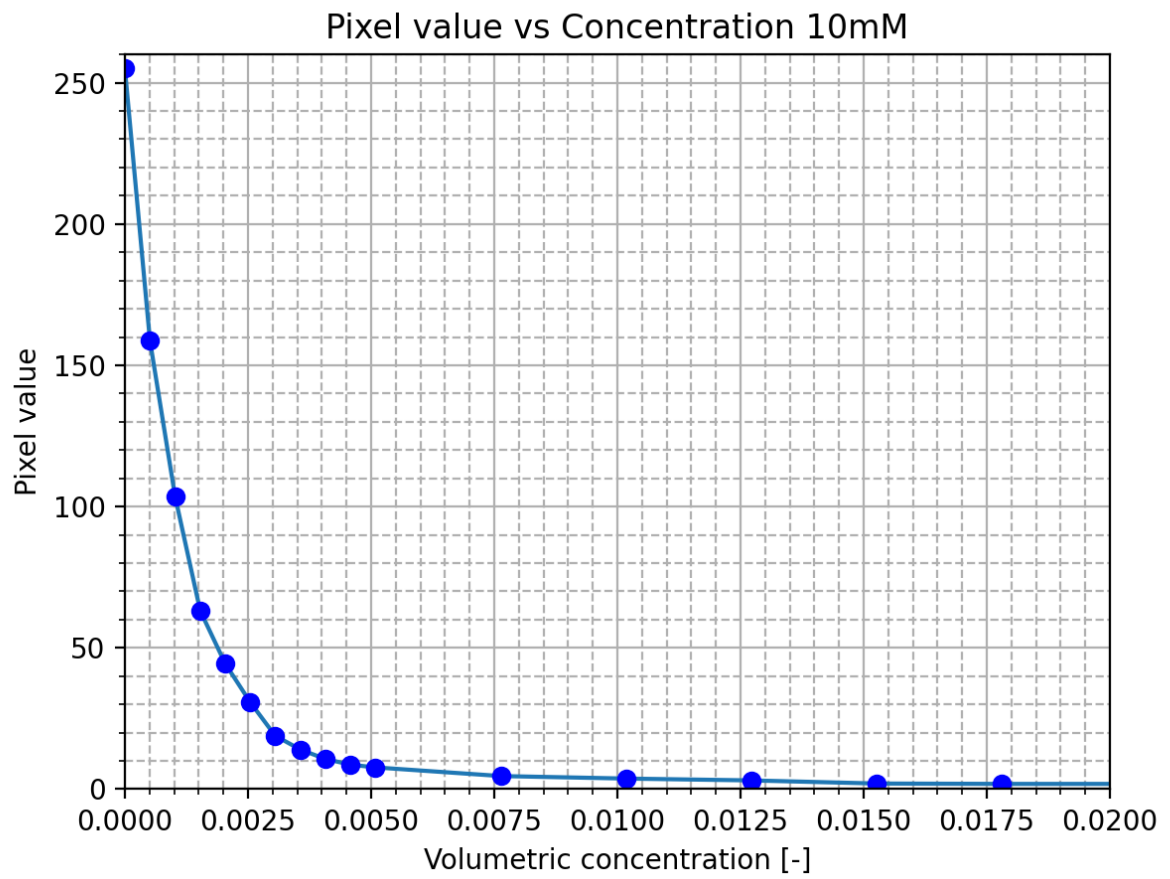


Figure I.2: Calibration curve with 10 mM  $CaCl_2$

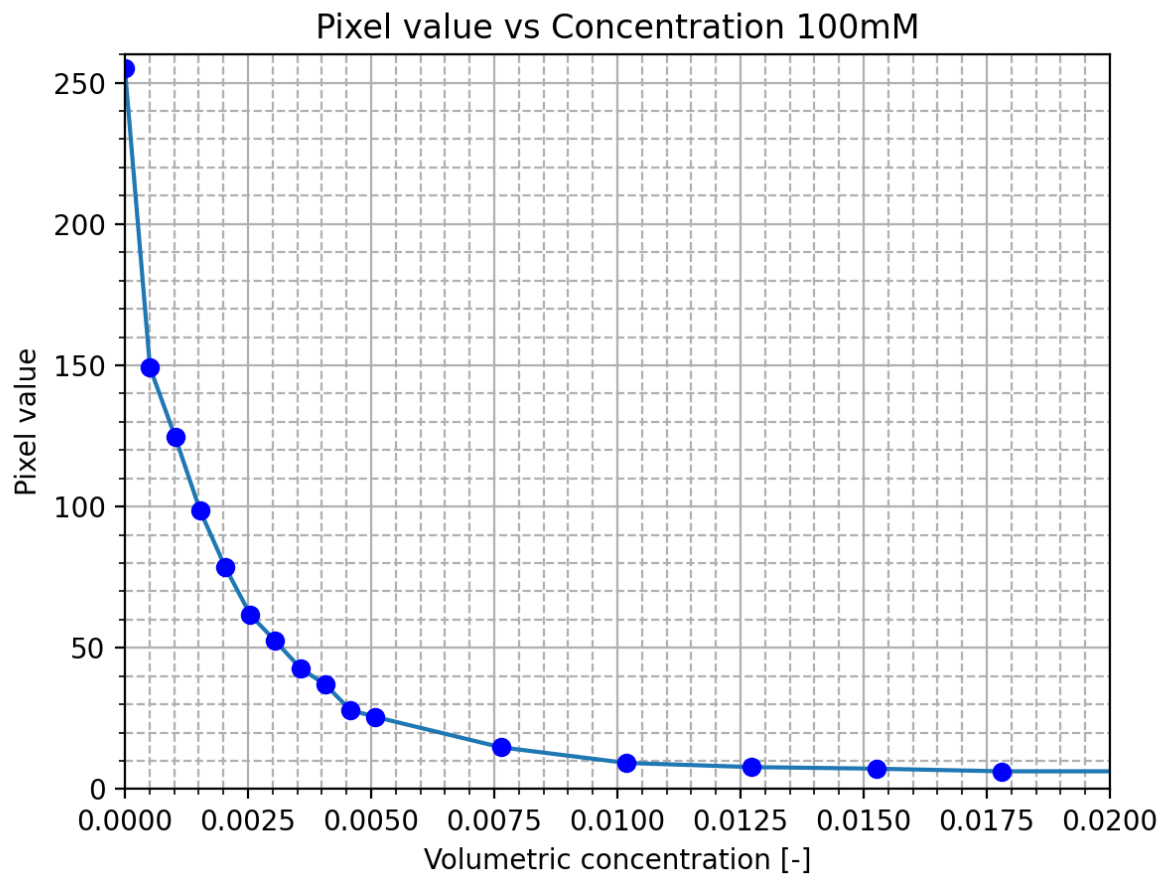


Figure I.3: Calibration curve with 100 mM  $CaCl_2$

# J

## Logbook of experiments

### J.1. Settling column experiments

#	Date	Temperature [° C]	TDS [mg/L]
1	11-01-2021	20.2	509.4
2	11-01-2021	20.1	498.3
3	07-01-2021	19.9	502.1
4	07-01-2021	20.3	500.7
5	07-01-2021	19.8	506.4
6	19-02-2021	18.4	491.3
7	19-02-2021	18.0	495.2
8	19-02-2021	17.4	554.9
9	16-02-2021	17.5	1336
10	16-02-2021	17.4	1157
11	18-02-2021	16.5	1244
12	17-02-2021	11.6	1049
13	11-01-2021	18.8	1425
14	17-02-2021	11.9	1040
15	17-02-2021	14.9	1044
16	28-02-2021	14.1	1191
17	13-01-2021	19.6	8049
18	13-01-2021	19.3	7900
19	13-01-2021	19.1	7993
20	13-01-2021	19.6	8155
21	23-02-2021	20.2	7839
22	23-02-2021	23.8	6208
23	23-02-2021	23.8	7311
24	23-02-2021	23.8	7353

## J.2. Lock exchange experiments

#	Mass concentration sediment [g/L]	Sediment	Concentration CaCl <sub>2</sub> [mM]	Preexisting bed [days]	Zetag 4120 mixing section	Zetag 4120 outflow section	Zetag 8125 mixing section	Zetag 4129 outflow section	Date	Temperature [°C]	pH	TDS [mg/L]
1	10	Illite	0	-	-	-	-	-	19-03-2021	23,2	8,00	259
2	20	Illite	0	-	-	-	-	-	05-02-2021	10,7	8,02	270
3	30	Illite	0	-	-	-	-	-	23-04-2021	10,9	8,04	267
4	40	Illite	0	-	-	-	-	-	05-02-2021	10,9	7,99	269
5	50	Illite	0	-	-	-	-	-	05-02-2021	10,1	8,09	299
6	75	Illite	0	-	-	-	-	-	24-02-2021	10,4	8,08	267
7	100	Illite	0	-	-	-	-	-	16-02-2021	10,1	8,01	179
8	125	Illite	0	-	-	-	-	-	24-02-2021	11,6	8,03	192
9	10	Illite	10	-	-	-	-	-	12-02-2021	10,4	8,12	1538
10	20	Illite	10	-	-	-	-	-	12-02-2021	9,4	8,00	1455
11	30	Illite	10	-	-	-	-	-	12-02-2021	9,2	8,33	1535
12	40	Illite	10	-	-	-	-	-	12-02-2021	9,1	8,32	1443
13	50	Illite	10	-	-	-	-	-	12-02-2021	9,6	8,32	1476
14	75	Illite	10	-	-	-	-	-	24-02-2021	10,7	8,31	1579
15	100	Illite	10	-	-	-	-	-	18-02-2021	10,1	8,25	1622
16	125	Illite	10	-	-	-	-	-	24-02-2021	11,0	8,24	1546
17	10	Illite	100	-	-	-	-	-	19-02-2021	17,5	7,24	7205
18	20	Illite	100	-	-	-	-	-	19-02-2021	17,3	7,74	5957
19	30	Illite	100	-	-	-	-	-	24-02-2021	19,0	7,55	7059
20	40	Illite	100	-	-	-	-	-	24-02-2021	19,1	7,60	7084
21	50	Illite	100	-	-	-	-	-	19-02-2021	17,5	7,45	7106
22	75	Illite	100	-	-	-	-	-	25-02-2021	16,3	7,19	7448
23	100	Illite	100	-	-	-	-	-	28-02-2021	17,4	7,69	6237
24	125	Illite	100	-	-	-	-	-	25-02-2021	16,7	7,23	7577

#	Mass concentration sediment	Sediment	Concentration CaCl <sub>2</sub> [mM]	Preexisting bed [days]	Zetag 4120 mixing section	Zetag 4120 outflow section	Zetag 8125 mixing section	Zetag 4129 outflow section	Date	Temperature [°C]	pH	TDS [mg/L]
25_1	10	Illite	10	1	-	-	-	-	17-02-2021	15,2	8,00	273
25_2	10	Illite	10	2	-	-	-	-	12-03-2021	18,4	7,89	274
26_1	50	Illite	50	1	-	-	-	-	18-02-2021	16,3	8,01	265
26_2	50	Illite	50	2	-	-	-	-	15-03-2021	17,5	7,92	278
27_1	100	Illite	100	1	-	-	-	-	25-02-2021	16,4	7,78	231
27_2	100	Illite	100	2	-	-	-	-	09-03-2021	18,7	7,91	282
28_1	10	Illite	10	1	-	-	-	-	19-02-2021	16,5	8,27	1612
28_2	10	Illite	10	2	-	-	-	-	22-03-2021	19,3	7,50	2071
29_1	50	Illite	50	1	-	-	-	-	23-02-2021	23,8	7,78	1918
29_2	50	Illite	50	2	-	-	-	-	09-04-2021	23,1	7,67	1577
30_1	100	Illite	100	1	-	-	-	-	26-02-2021	18,0	7,65	1724
30_2	100	Illite	100	2	-	-	-	-	14-07-2021	19,6	7,76	1538
31	10	Illite	10	-	-	-	-	x	17-03-2021	13,7	7,84	259
32	100	Illite	100	-	-	-	-	x	17-03-2021	11,8	8,01	255
33	10	Illite	10	-	-	-	x	-	22-03-2021	23,1	7,83	195
34	100	Illite	100	-	-	-	x	-	22-03-2021	23,1	7,83	195
35	10	Illite	10	-	x	-	-	-	22-03-2021	22,0	8,23	211
36	100	Illite	100	-	x	-	-	-	22-03-2021	22,0	8,19	196
37	10	Illite	10	-	-	x	-	-	22-03-2021	22,0	8,32	202
38	100	Illite	100	-	-	x	-	-	22-03-2021	22,0	8,27	200
39	10	Illite	10	-	x	-	-	-	22-03-2021	22,0	8,02	1470
40	100	Illite	100	-	x	-	-	-	23-03-2021	17,9	8,08	1458
41	10	Illite	10	-	-	x	-	-	22-03-2021	22,0	8,13	1304
42	100	Illite	10	-	-	x	-	-	23-03-2021	13,7	8,00	1777
43	10	Artificial ccz	0	-	-	-	-	-	15-04-2021	14,0	8,12	243
44	50	Artificial ccz	0	-	-	-	-	-	19-04-2021	16,2	8,01	197
45	100	Artificial ccz	0	-	-	-	-	-	22-04-2021	17,9	7,98	215
46	10	Artificial ccz	10	-	-	-	-	-	20-04-2021	18,2	7,65	1986
47	50	Artificial ccz	10	-	-	-	-	-	22-04-2021	18,4	7,84	1764
48	100	Artificial ccz	10	-	-	-	-	-	23-04-2021	18,2	7,71	1842

# K

## Used equipment and materials



Figure K.1: Mixing rod settling column experiments



Figure K.2: Left: Fastec camera. Right: Mixing rod lock exchange experiments



Figure K.3: Left: Elmetron pH/ Conductivity meter. Right: Vos stirrer





Figure K.4: Left: Illite/ Right:  $CaCl_2$



# Camera settings

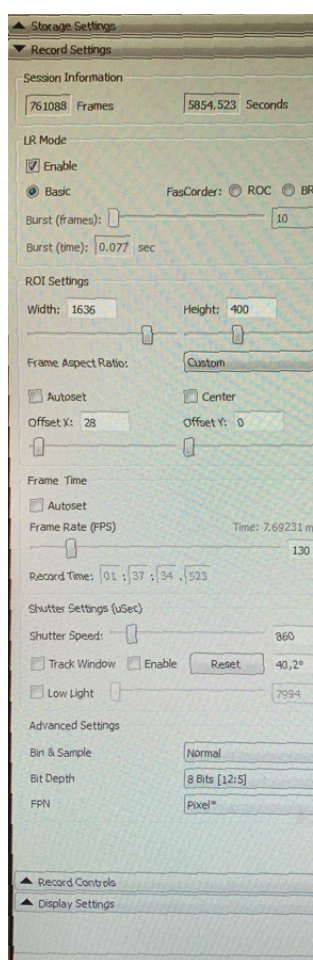


Figure L.1: Camera settings

# M

## Python script settling column experiments

```
2  # -*- coding: utf-8 -*-
3  """
4  Created on Tue Dec  8 10:51:49 2020
5
6  @author: dolfenthoven
7  """
8  # import packages
9  import cv2
10 import numpy as np
11 import matplotlib.pyplot as plt
12 import os
13 import sys
14
15 from scipy.ndimage.filters import gaussian_filter1d
16
17 os.system("clear")
18
19
20
21 def nothing(x):
22     pass
23 cnt = []
24 cap = cv2.VideoCapture('/Volumes/Dolf_afstud/Maatcilinder/Il-lite/0.Illite_12,5%_0CaCl2/output.mp4') #import video from map
25 length = int(cap.get(cv2.CAP_PROP_FRAME_COUNT)) #How many frames
26 print ('length =',length) #Print how many frames
27
28
29 # First frame
30 # ret, frame1 = cap.read()
31 # frame1 = cv2.cvtColor(frame1, cv2.COLOR_BGR2GRAY)
32
33 #Settings pixels/distance
34 width_low = 1760 #left
35 height_low = 1272 # up
36 width_high = 1830 #right
37 height_high = 2772 #down
38 bg = None #achtergrond reference eerste frame
39
40 # Settings
41 active_line = None
42 frame_counter = 0
43 last_frame_number = 0
44
45
46 dT = 30 # Time between the frames
47 m_per_pixel = (0.10/430)*100 # Distance from pixel in cm
48
49 # Initialize result lists
50 lengte = list() #Length from the pixels
51 Speed = list() #Velocity before filter
52 verschil2= list() #Difference between pixels values before filter
53 lengte2 = 0 #initial value next length
54 Differencefilt = list() #Difference between pixels values after filter
55 speedfilt = list() #Velocity after filter
56
57 #Choose the pixel values to filter
58 cv2.namedWindow('Trackbars')
59 cv2.createTrackbar("L - H", "Trackbars", 0, 179, nothing)
60 cv2.createTrackbar("L - S", "Trackbars", 0, 255, nothing)
61 cv2.createTrackbar("L - V", "Trackbars", 0, 255, nothing)
62 cv2.createTrackbar("U - H", "Trackbars", 179, 179, nothing)
63 cv2.createTrackbar("U - S", "Trackbars", 0, 255, nothing)
64 cv2.createTrackbar("U - V", "Trackbars", 255, 255, nothing)
65
66 while(cap.isOpened() and frame_counter <= (length-2)):
```

```

65
66 while(cap.isOpened() and frame_counter <= (length -2)):
67
68     ret, frame = cap.read()
69     contour_sum = 0
70     frame_counter = frame_counter + 1
71     Old = lengte2
72     filt = Differencefilt
73
74
75
76     l_h = cv2.getTrackbarPos("L - H", "Trackbars")
77     l_s = cv2.getTrackbarPos("L - S", "Trackbars")
78     l_v = cv2.getTrackbarPos("L - V", "Trackbars")
79     u_h = cv2.getTrackbarPos("U - H", "Trackbars")
80     u_s = cv2.getTrackbarPos("U - S", "Trackbars")
81     u_v = cv2.getTrackbarPos("U - V", "Trackbars")
82
83
84     lower = np.array([l_h, l_s, l_v])
85     upper = np.array([u_h, u_s, u_v])
86
87
88     if ret:
89         #Grray scale
90         hsv = cv2.cvtColor(frame, cv2.COLOR_BGR2GRAY)
91         cropped = frame[height_low:height_hei, width_low:widht_hei]
92         cv2.imshow('cropped',cropped)
93         p = cropped.shape
94
95
96     # Save first image
97     if bg is None:
98         bg = cropped
99         #bg = frame
100
101     if active_line is None:
102         active_line = cropped.shape[1]
103
104
105
106     # Haal nieuwe plaatje van eerste plaatje af
107     subtracted = cv2.subtract(cropped, bg)
108     cv2.imshow('subtracted',subtracted)
109     # define a threshold, 128 is the middle of black and white in grey scale, 255 white, 0 black
110     thresh = 150
111
112     # assign blue channel to zeros, 0 is black 255 is white
113     ret, tresh = cv2.threshold(subtracted, thresh, 255, 0)
114     cv2.imshow('tresh',tresh)
115     mask=cv2.inRange(tresh, lower, upper)
116     cv2.imshow('mask',mask)
117
118     img_height, img_width = mask.shape
119

```

```

120
121     #count the white pixels in the frame
122     nzCount = cv2.countNonZero(mask)
123     # print(nzCount)
124     lengte2 = (nzCount / (width_high - width_low)) * m_per_pixel
125     print('lengte in cm=', lengte2)
126     # pickle.dump(lengte, open("lengte.dat", "wb"))
127     lengte.append(lengte2)
128
129     verschil = Old - lengte2
130     print('verschil', verschil)
131     verschil2.append(verschil)
132
133     Speed2 = verschil / dT
134     print('Speed = ', Speed2)
135     Speed.append(Speed2)
136
137     # plt.plot(lengte)
138     # plt.plot(np.linspace(0, len(lengte), num=len(lengte)), lengte)
139     # ysmoothed = gaussian_filter1d(lengte, sigma=2)
140     ysmoothed2 = gaussian_filter1d(lengte, sigma=4)
141     Ylist = ysmoothed2.tolist()
142     # plt.plot(ysmoothed, ':', label='filtered, sigma=2')
143     plt.plot(ysmoothed2, '--', label='filtered, sigma=4')
144
145     Differencefilt = [j-i for i, j in zip(ysmoothed2[:-1], ysmoothed2[1:])]
146     Speedfilt2 = [-(x / dT) for x in Differencefilt]
147     np.savetxt('/Volumes/Dolf afstud/Maatcilinder/CSV/8_150.csv', ysmoothed2, delimiter=',', fmt="%1.10f")
148
149
150     if frame_counter == (length - 2):
151         sys.exit()
152
153     key = cv2.waitKey(1)
154     if key == ord('d'):
155         break
156     if key == ord('p'):
157         cv2.waitKey(-1)
158
159
160
161     plt.ylabel("Height[cm]")
162     plt.xlabel("Time(s)")
163
164
165
166     cap.release()
167     cv2.waitKey(0)
168
169     cv2.destroyAllWindows()

```